COMPUTATIONAL FLUID DYNAMICS AND FLUID STRUCTURE INTERACTION OF YACHT SAILS

Jonathan Paton, MEng

Thesis submitted to the University of Nottingham
for the degree of Doctor of Philosophy

June 2011

APPENDIX 1
NOT COPIED

ON INSTRUCTION FROM THE UNIVERSITY

ABSTRACT

This thesis focuses on the numerical simulation of yacht sails using both computational fluid dynamics (CFD) and fluid structure interaction (FSI) modelling.

The modelling of yacht sails using RANS based CFD and the SST turbulence model is justified with validation against wind tunnel studies (Collie, 2005; Wilkinson, 1983). The CFD method is found to perform well, with the ability to predict flow separation, velocity and pressure profiles satisfactorily. This work is extended to look into multiple sail interaction and the impact of the mast upon performance.

A FSI solution is proposed next, coupling viscous RANS based CFD and a structural code capable of modelling anistropic laminate sails (RELAX, 2009). The aim of this FSI solution is to offer the ability to investigate sails' performance and flying shapes more accurately than with current methods. The FSI solution is validated with the comparison to flying shapes of offwind sails from a bespoke wind tunnel experiment carried out at the University of Nottingham. The method predicted offwind flying shapes to a greater level of accuracy than previous methods.

Finally the CFD and FSI solution described here above is showcased and used to model a full scale Volvo Open 70 racing yacht, including multiple offwind laminate sails, mast, hull, deck and twisted wind profile. The model is used to demonstrate the potential of viscous CFD and FSI to predict performance and aid in the design of high performance sails and yachts. The method predicted flying shapes and performance through a range of realistic sail trims providing valuable data for crews, naval architects and sail designers.

LIST OF PUBLICATIONS

Journal – in print

PATON, J. AND MORVAN, H., 2007, The effect of mast rotation and shape on the performance of sails, *International journal of marine engineering,* Vol 149, Part A2

PATON, J. AND MORVAN, H., 2007C, Using computational fluid dynamics to model main and foresail interaction - the 'slot effect' revisited, *Journal of wind engineering and industrial aerodynamics*, Volume 97, Issues 11-12, 2009, 540-547

Conferences

PATON, J. AND MORVAN, H., 2007B, Yacht Sail Aerodynamics Using Computational Fluid Dynamics, *Marine 2007 – Computational methods in marine engineering, 5th-7th June 2007, Barcelona.*

PATON, J., MORVAN, H., AND HEPPEL, P., 2008, Fluid structure interaction of yacht sails, *International conference on innovation in high performance sailing yachts, 29-30 May 2008, Lorient.*

ACKNOWLEDGEMENTS

I would like to thank my supervisor Dr Herve Morvan for all his help and guidance throughout this thesis. Without him I would never have started my PhD, let alone finished it. I would also like to thank Dr Martin Smith and Dr Nicholas Kokkkas for all their effort through the experimental parts. I would also like to thank all the technicians that have helped me through the years included Pat and Andy in the labs. I would also like to thank Dr David Hargreaves for all his efforts to keep the computers and software up and running.

I would like to thank all of my peers that helped me through the years. Thanks to Faye for all her help and advice over numerous cups of coffee. Thanks to Dave for answering maths questions, Paolo for his Fortran skills, Mike for his programming skills and Neil for his help with CFX when I first started.

A special thank you must go to Peter Heppel for his help throughout the thesis and generously offering RELAX for the duration of the thesis. His help in both direction and technically has been invaluable. Thanks to Jeremy Elliot at North Sails for the creation of the model sails and for trimming them in the wind tunnel.

A final set of thank yous to my family and my partner Sarah. My family, especially my Dad has been tremendously helpful. Thanks to Sarah for putting up with me through the tough bits! Thanks.

LIST OF CONTENTS

LIST OF FIGURES

LIST OF TABLES

LIST OF SYMBOLS

Latin

C	Chord Length
E	Specific energy of a fluid
k	Materials conductivity
k	Turbulent kinetic energy per unit mass
p	Pressure
p′	Fluctuating pressure component
S_E	Source of energy per unit volume per unit time
S_M	Momentum source per unit volume per unit time
t	Time
T	Temperature
u	Instantaneous velocity component in the x–direction
u'	Fluctuating velocity component in the x–direction
u^+	Near wall velocity
u	Velocity vector
U	Velocity vector
u_*	Friction velocity
v	Instantaneous velocity component in the y–direction
v'	Fluctuating velocity component in the y–direction
V(z)	Velocity at height z
V(ref)	Reference velocity
w	Instantaneous velocity component in the z–direction
w'	Fluctuating velocity component in the z–direction
x	X co-ordinate
X	X co-ordinate (usually parallel to free stream)
y^+	Non dimensional distance to the first cell away from a wall
y	Distance to the first cell
y	y co-ordinate
z	z-co-ordinate
z	Height
z_0	Roughness height
z_{ref}	Reference height

Greek

α	True wind angle
β	Apparent wind angle
ε	Dissipation of k
κ	von Karman constant
ρ	Density
λ	Viscosity
μ	Dynamic viscosity
μ_t	Eddy viscosity
τ	Viscous stresses
τ_w	Wall shear stress
ν	Kinematic viscosity
ω	Rate of dissipation of turbulent kinetic energy
ϕ	Velocity potential

LIST OF ABBREVIATIONS

ACC	America's Cup Class
AWA	Apparent Wind Angle
AWS	Apparent Wind Speed
CAD	Computer Aided Design
CFD	Computational Fluid Dynamics
DES	Detached Eddy Simulation
DNS	Direct Numerical Simulation
DOE	Design of Experiments
FEA	Finite Element Analysis
FSI	Fluid Structure Interaction
GGI	General Grid Interface
GUI	Graphical User Interface
LES	Large Eddy Simulation
NACA	National Advisory Committee for Aeronautics
RANS	Reynolds Averaged Navier-Stokes
RMS	Root Mean Square
SST	Shear Stress Transport
TWA	True Wind Angle
TWS	True Wind Speed
VPP	Velocity Prediction Program

Chapter 1

Introduction

1.1. Sailing

The sport of sailing can boast the oldest active international sporting trophy, the America's Cup, dating back to 1851 (*New Zealand*, 2009). The America's Cup is one of the most famous and prestigious trophies in the world, consisting of a series of match races between yachts. Not surprisingly, in recent years technology has played an increasingly important role in the sail and boat design. Indeed, it is regattas and races such as the America's Cup that have driven the need for an ever improving understanding of sails and optimisation of their performance, as teams search exhaustively for any possible competitive advantage. However, before sails and their performance can be improved, the physics of sailing has to be better understood. For a long time sail design was empirical, but more recently optimisation has been undertaken with advanced experimental and computational methods.

This chapter provides a brief introduction to sailing and sail design. It then considers some of the complexities associated with sails and their performance. The chapter concludes by outlining the aims of this thesis and then detailing the objectives used to achieve them.

1.1.1. Points of Sailing

The physics of sailing is complex and varies greatly depending on the direction the vessel is travelling in, relative to the wind direction. The orientation of the boat to the wind is called the 'point of sailing'. Although there is a continuum of angles that a boat can travel in relative to the wind, these directions can be split up into five main points of sailing. The boat can also sail at any angle in between these points, on part of the continuum. The only angle that a boat cannot sail is directly into the wind, or close to it, as the physics of sailing prohibits this. The sector the boat cannot sail into is often called the 'no-go' zone and the nearest direction that the boat can sail towards the wind is termed 'close hauled'. In contrast, when the boat travels with the wind directly behind it, from the stern, this is called a 'dead run' or just a 'run'.

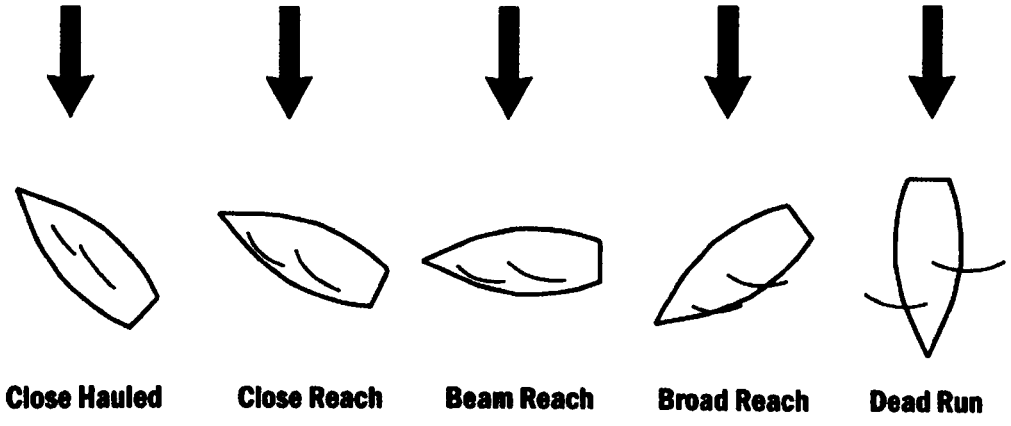

Figure 1.1.1.1 – The five points of sailing

The force on the boat can be considered as the resultant of two components: the drag, D, acting in line with the airflow, and the lift, L, acting at 90 degrees to this. From Figure 1.1.1.2, it can be seen that on a dead run, with the wind directly behind, the objective is to maximise the drag force, which is in line with the boat's direction, whilst minimising lift. In contrast, when sailing 'close hauled',

the aim is to sail with maximum lift, which has a component in line with the boat's direction, whilst minimising drag, which has a component opposing the boat's direction. However, with modern boats travelling faster and faster, the physics of sailing away from the wind are transforming as the influence of the boat speed transforms these physics. This will be discussed further later in this chapter in Section 1.1.3, where the concept of apparent wind is detailed. The physics and goals of travelling towards the wind, or 'upwind', and travelling away from the wind, or 'downwind', remain very different and can provide the designer with contrasting design goals and objectives. Consequently, most racing boats carry different sails to help meet the desired criteria for different points of sailing.

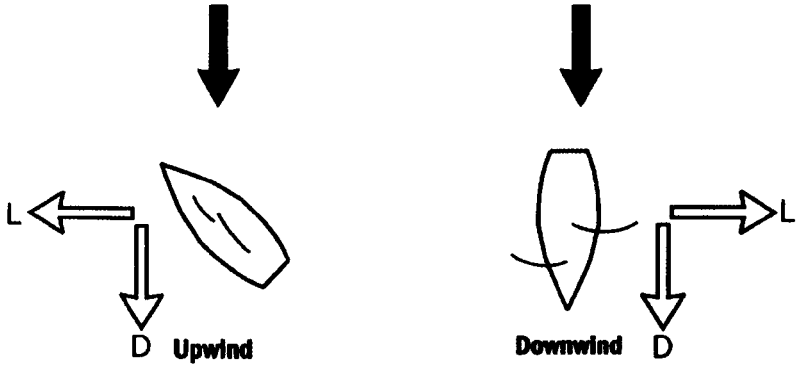

Figure 1.1.1.2 – Forces on a vessel for different legs of sailing (D = Drag, L = Lift)

1.1.2. Sailing Terminology

A typical 'sloop rigged' sailing yacht is shown in Figure 1.1.2.1. The figure highlights the main terms used to describe features of a sailing vessel. The two sails that can be seen in Figure 1.1.2.1 are the mainsail and the foresail. The mainsail is attached to the mast along its leading edge, the luff, and the foot of the sail travels parallel to the boom. The foot can either travel along a slot in the

boom or be attached at just the outer corner, called the clew. The foresail is attached to the front of the yacht at the bow and the luff of the foresail is held in place by the tension in the luff wire. The angles the sails are set to are controlled by the mainsheet and foresail sheet respectively. The mainsheet length controls how closely the boom, and hence the mainsail, lies relative to the centre line of the boat. The foresail is controlled by the foresail sheet, which can be sheeted in to bring the sail closer to the centreline or mast. There are many other control lines that can be used to set the shape of the sails but they will not be considered for this simplified introduction. Two other terms used are 'windward' and 'leeward'. 'Windward' refers to the side of the boat or sails facing the wind. Conversely the 'leeward' side is opposite the windward side.

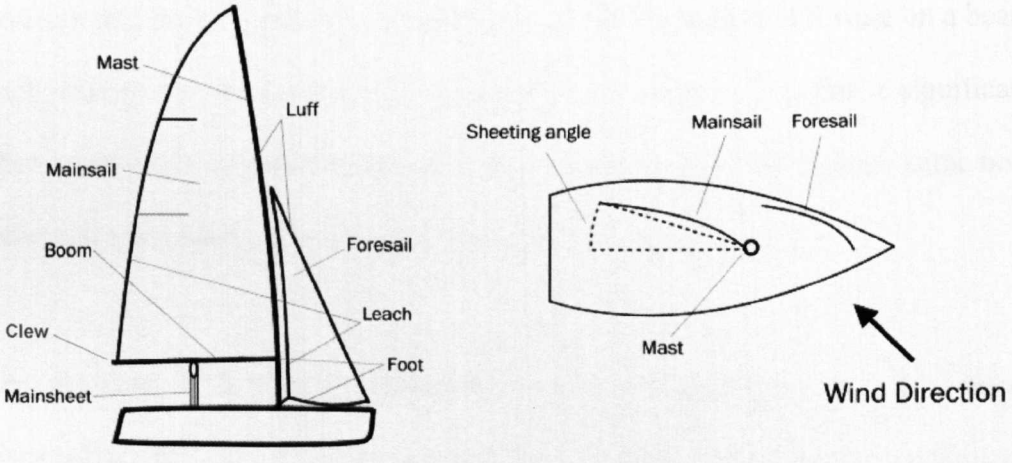

Fig. 1.1.2.1 - Common sailing terms

1.1.3. Wind and Wind Twist

Apparent wind is an effect that comes into play when the forward velocity of the boat is included in a vector triangle with the true wind velocity. These vectors are shown in Figure 1.1.3.1.

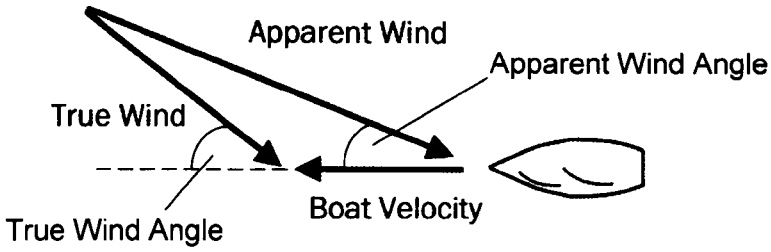

Figure 1.1.3.1 – The apparent wind triangle

By definition, the effect of apparent wind becomes greater as the boat speed increases. The larger the boat speed, the more the apparent wind will differ from the true wind. This is particularly so when sailing downwind, when boat speeds are typically higher than during upwind sailing. Modern boats can travel at and above the speed of the wind. Apparent wind acts to move the wind vector forward, towards the bow. As an example, a boat travelling quickly in the direction of a broad reach may actually have to set the sails as if it were on a beam reach, due to the direction of the apparent wind vector. This has a significant effect upon the design and operation of sails, as the need to retrim sails as the boat speed and wind changes is essential for optimum performance.

This problem is further complicated when the atmospheric boundary layer surrounding the Earth's surface is considered. A boundary layer, the region over which the velocity profile develops over a solid region, can be described using the Von Karman velocity profile, Equation 1.1.3.1. The fluid velocity immediately adjacent, to a solid surface is zero, which is often described as a no-slip condition. Away from the surface the velocity of the fluid increases, and the flow transitions from laminar to turbulent, until it reaches the free stream velocity, where the effect of the surface and the associated viscous shear are no longer felt. The

boundary layer surrounding the Earth's surface is more specifically known as the atmospheric boundary layer.

In sailing, the atmospheric boundary layer has an affect upon the true wind and as a result also affects the apparent wind velocity. Further away from the sea's surface, the boundary layer has less influence and the apparent wind therefore changes direction. This change in direction is known as wind twist. Close to the sea surface the true wind is small, hence the apparent wind is due primarily to boat speed. Further away from the sea's surface the true wind contribution increases, causing the wind twist, Figure 1.1.3.2.

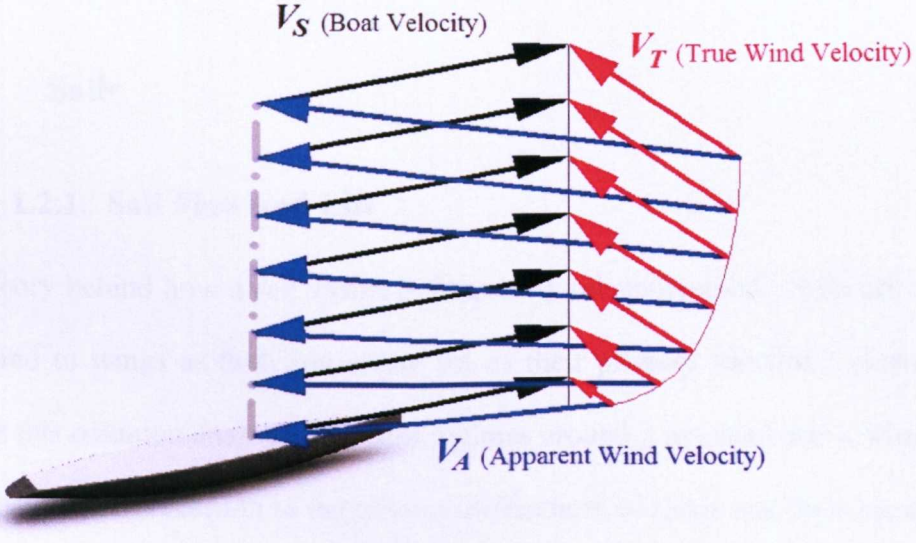

Figure 1.1.3.2 – Wind twist vectors (Collie, 2005)

The equation of the true wind velocity can be represented by Equation 1.1.3.1, where u_* is friction velocity, z is the vertical height, z_0 is the roughness length, k is the von Karman constant and $V_w(z)$ is the velocity at height z. (Schlichting and Gersten, 2000).

$$V_w(z) = \frac{u_*}{k} \ln\left(\frac{z + z_0}{z_0}\right) \qquad \textbf{Equation 1.1.3.1}$$

In the present thesis a value for $z_0 = 0.01$m was used throughout. More detail is provided in Section 6.3.

It is the apparent wind that is important when setting (aligning) the sails to produce the forward motion. The Apparent Wind Angle (AWA) is shown in Figure 1.1.3.1 and the magnitude of the apparent wind vector termed the Apparent Wind Speed (AWS). In a similar convention, the angle and speed of the true wind are denoted by TWA (see Figure 1.1.3.1) and TWS.

1.2. Sails

1.2.1. Sail Flow and Lift

The theory behind how a sail works is frequently misunderstood. Sails are often compared to wings as both can create lift as their primary function. However, despite this common analogy, the flow regimes around a mainsail and a wing are quite different. In addition to the obvious differences of shape and their operating speeds, the main difference between them is a feature called separation. This fundamental concept where the wind loses contact with the sail surface will be discussed throughout this thesis, as it affects both the performance and the computational modelling of sails.

The flow around a real mainsail attached to a mast always contains areas of separation. This is very different to the flow seen by aircraft wings where at small

angles of attack, the flow remains attached. Figure 1.2.1.1, shows the flow phenomena past wings and mainsails. The figure gives the flow patterns as well as pressure plots around the structures (Bethwaite, 2003).

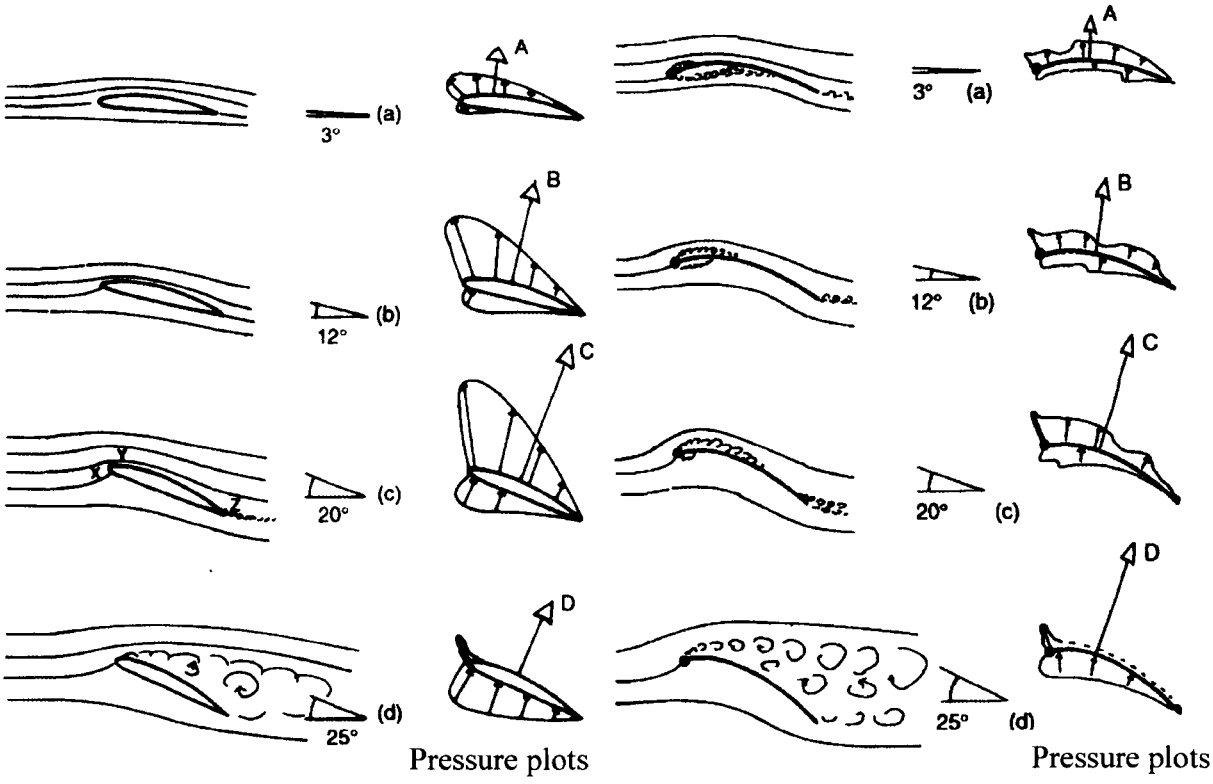

Figure 1.2.1.1 – Wing (left) and sail flow (right) at various angles of attack: (a) 3 degrees AWA, shallow angle of attack , (b) 12 degrees AWA, (c) 20 degrees AWA, (d) 25 degrees AWA, large angle of attack with resulting flow separation in the wake. (Bethwaite, 2003)

The group of images on the left of Figure 1.2.1.1 represent the flow past aerofoil sections whilst the images in the right represent a mainsail and mast combination at varying wind angles.

As can be seen the flow is very different and hence the commonly held assumption of their similarity can be misleading. Although there are differences, the general concept of lift can still be used with sails. The regions of separation seen in Figure 1.2.1.1 provide a significant difference in terms of their complexity for numerical modelling. This will be discussed further in Chapter 4.

Many books and papers have been written studying the flow around conventional sloop rigs (Bethwaite, 2003; Gentry, 1981). A typical pressure profile and flow pattern around a mainsail are shown in more detail in Figure 1.2.1.2 (Bethwaite, 2003).

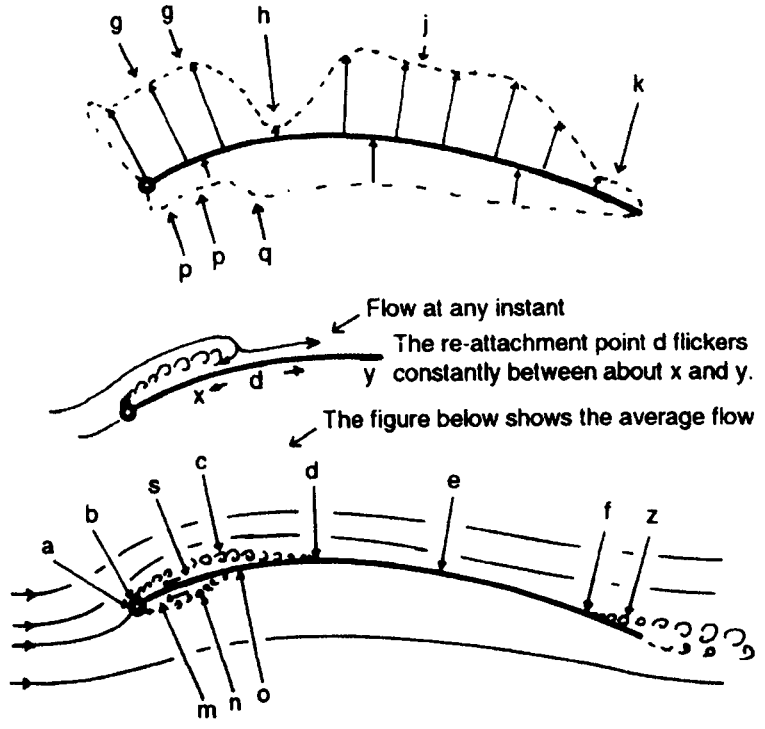

a Wind meets mast - stagnation point
b Flow separates from mast
c Free shear layer - over
s Separation bubble
d Flow re-attaches to sail (refer to inset)
e Zone of attached flow
f Flow separates from sail
z Free shear layer at leech
g Uniform reduced suction over s
h Greatly reduced suction near d
j Useful suction over e
k Zero suction over z
n Free shear layer
m Separation bubble
o Flow re-attaches to sail
p Uniform reduced pressure over m
q Pressure jump at 0

Figure 1.2.1.2 – Pressure (top) and flow patterns (middle and bottom) around a sail attached to a mast

(Bethwaite, 2003)

As can be seen above, the flow around a sail is complex even at shallow angles of attack, with multiple regions of separation on both sides of the sail. The point at the very front of the mast is called the 'stagnation point', **a**. As the flow is forced around the mast it separates due to the adverse pressure gradient. On the leeward

(top) side, the point at which the flow separates is termed the 'separation point', **b**. The region that follows in the lee of the mast forms a 'separation bubble', **s**. As the flow continues along the sail it reattaches at the 'reattachment point', **d.** The flow then remains in a region of 'attached flow', **e**. At **f**, the flow separates again, close to the leach of the sail. Flow on the windward side of the sail (bottom) is similar to that on the leeward (top) side. The flow separates and causes a 'separation bubble', **m**, and a 'reattachment point', **o**. The pressure variation can also be seen in Figure 1.2.1.2 (Bethwaite, 2003). The pressure on both sides of the sail is of great interest, as it is the pressure differences across the sail that creates the driving force. To maximise lift the leading edge separation must be minimised. It is the difference between the pressure on both sides of the sails, *dp* that creates the force of lift on the sail. It is this fundamental principal of lift that creates the movement of a yacht or dinghy (Bethwaite, 2003). The flow described is typical of a mainsail during upwind sailing. As the boat turns away from the wind (offwind sailing) the curvature of the sails increases, often with greater regions of separation. The added complexities of offwind sailing will be detailed later in the thesis.

1.2.2. Sail Performance

Predicting the performance of sails is a complex procedure. The components of lift and drag vary significantly depending on the point of sailing. At times through this thesis, these vectors will be resolved into a driving force vector, in the direction of the yacht, and a side force vector, at right angles. This helps to simplify the performance analysis of sails, as the desire to minimise side force whilst maximising driving force is always the requirement for maximum performance of yachts.

Throughout this thesis, the importance of being able to determine/predict the regions of separation is emphasised, as it is paramount when predicting the performance of sails.

A further complexity in sailing, is that the sails can create an undesirable heeling effect on the vessel. Clearly there is a limit to the righting moment that a given vessel possesses to counteract the heeling forces from the sails. In contrast, when designing the rear wing of a performance motorcar, the desire to increase downforce and reduce drag is uncompromised (within reason). However, for a sailing vessel excessive lift from sails could also create too much heeling force, reducing boat performance or, in the extreme, capsizing the boat. It is factors like this that make the design of sails for optimum performance especially complicated.

1.3. Motivation, Aims and Objectives

The motivation behind the research reported in this thesis is to be able to accurately model yacht sails numerically, and to remove the reliance on experimental testing, which can be costly, inaccurate and time consuming. Inherent inaccuracies in the measurement of sail shapes and forces, questions surrounding the flow conditions and the difficultly in manufacturing scale sails all add to issues surrounding wind tunnel testing and full scale testing.

In addition to the complexities discussed in the previous section, such as separation, apparent wind, wind twist and heeling moment, the fundamental factor that a sail is a flexible membrane and not a solid structure has to be considered. This means that the sail can move significantly and easily, changing its shape

under loading. This provides an interesting dimension to the problem, requiring the highly complex modelling of the interaction between the fluid flow analysis and the structural analysis, termed a Fluid-Structure Interaction (FSI) solution. Further justification for the aims laid out in Section 1.3.1 will be given in Chapter 2.

Until recently a significant proportion of computational sail modelling has been undertaken using inviscid codes. The ability of a full viscous CFD solution to predict flow separation is key to predicting sail performance. Sail design and boat performance prediction should consider the interaction between the sail structural performance and the resulting sail aerodynamic performance; yet there is little evidence for viscous FSI being performed in the field. Bridging these gaps would enable a 'right first time' design process and would limit the number of testing iterations.

1.3.1. Aim

The gaps in the current research into sail modelling lead to the following aim:

> *"To develop a viscous fluid-structure interaction model for the accurate modelling of yacht sails, capable of modelling and predicting the performance of upwind and offwind sails."*

1.3.2. Objectives

To achieve the above aim, a series of objectives are proposed, breaking down the aim into a series of achievable goals. Before improvements to the current modelling methods can be made, the current methods have to be fully understood

and their limitations appreciated. This provides the rationale for the first objective:

1. *To review the current research into modelling methods, suitable for sail flow analysis and determine their limitations.*

The use of viscous computational fluid dynamics is a relatively new tool for use with sail modelling applications. Its use for a complete range of sail flows needs to be justified and validated, which leads to the next objective:

2. *To validate the use of viscous computational fluid dynamics for the modelling of upwind and downwind sail sections and thus justify the use of viscous CFD over inviscid solutions.*

The third set of objectives are related to completing the fundamental aim to create a fluid-structure interaction model for the accurate modelling of yacht sails, which takes into account that the sail is a flexible membrane. These objectives are:

3. *The creation of a fluid-structure interaction solution for the modelling of sail flow problems.*
4. *The validation of the fluid-structure interaction solution.*

The fourth and final set of objectives relate to the application of the Fluid-Structure Interaction solution to real sailing applications, leading to the following objectives:

5. *The application of the Fluid-Structure Interaction solution to the modelling of real world sail flow scenarios.*

6. *The application of the fluid-structure interaction solution to the modelling of scenarios not currently within the capability of existing methods.*

1.4. Thesis Outline

There are five main chapters to reflect the four groups of objectives outlined above. Following this introductory chapter, the first objective is addressed in Chapter 2. This contains a detailed review of the currently available 'state of the art' methods of modelling yacht sails. It highlights where further research could add to the numerical modelling of sail flow. This chapter considers conventional inviscid modelling, the more computationally expensive viscous modelling and the experimental alternative to the numerical modelling methods. Chapter 3 details viscous CFD modelling and gives an overview of the techniques used within the remaining chapters.

Chapter 4 focuses on objective 2, showing how viscous CFD can be applied to the modelling of sails and rigs in a variety of situations. These applications range from simplified 2D models to more comprehensive models including multiple sails and masts. The chapter details the application of viscous CFD to a series of validation cases. It also outlines how viscous CFD can be used to model and predict the performance of sails, aid sail design and provide performance improvements. Viscous rigid CFD is discussed in relation to improvements offered over inviscid methods.

Chapter 5 deals with objectives 3 and 4, detailing the Fluid Structure Interaction (FSI) solution and the components that make up the FSI loop. Justification for the

method that is proposed in comparison with the existing alternatives is also detailed. The method is then compared to a bespoke validation case created from a series of wind tunnel experiments carried out in The University of Nottingham climatic wind tunnel.

Fulfilling objectives 5 and 6, Chapter 6 takes the method developed in Chapter 5 and applies it to scenarios where previous methods could not have been used accurately or reliably. The chapter includes performance prediction and the full scale modelling of downwind sails with comprehensive rigs

The final chapter summarises the work carried out during the PhD studies, highlighting the new contributions made to the field. It also draws conclusions from the objectives and includes suggestions for further research.

Chapter 2

Literature Review

2.1. Introduction

Knowledge and understanding of sailing boats and the physics behind sails has developed over many hundreds of years. Much of this understanding has been gained from 'hands on' or experimental methods. It has accelerated and become computational from the 1970's onward. More recently the development of cheaper and quicker computers has allowed for more intensive computational analysis to be implemented and potential performance gains to be better understood. However, the use of computational modelling to aid design is still relatively new and not fully accepted in the marine industry. The use of scaled models, full scale models and wind tunnel testing still remains a major part in the development of most boats.

The science behind sailing and its computational modelling brings together many different areas of expertise. Vast amounts of knowledge have been brought from the aeronautical industry, where computational modelling of aeroplane wings has been carried out for many years and adapted to model sails. Aerodynamics experts from this field, such as Arvel Gentry (1981), are know working as sail designers that have built sails based upon experience rather than science for many years.

Tom Whidden and Michael Levitt emphasise the contrasts in approach to sail design, in their intriguing text entitled 'The art and science of sails' (1998). This text details the fascinating contest between Hood and North. These were two of the top sail makers of their era (1970s onwards), both approaching sail design from opposing perspectives and backgrounds. Their contrast in approach highlights the complexity in trying to develop sails, showing how sails and the conditions they sail in are both varied and complex. Within Whidden and Levitt's book, Hood is described as 'the artist' using intuition and his experience in sailing to design his sails. North, in contrast, was a college educated engineer and disregarded the 'if it looks right' type design that had been used previously and so successfully by Hood. North carried out experimental testing of sail shapes and used these results, rather than his intuition, to help improve his sails. This revolution was the start of a technical approach to sail design.

This chapter aims to provide a broad review of previous attempts to further the scientific understanding and the computational modelling of sails. The chapter begins with a brief introduction to wind tunnel testing and sailing theory in general. The chapter then details computational modelling contributions and is split up into sections, including; inviscid fluid analysis, viscous fluid analysis and structural analysis, see Figure 2.1.1. These three sections feed logically into the overall objective of this thesis and the final section of the chapter, the fluid structure interaction of yacht sails.

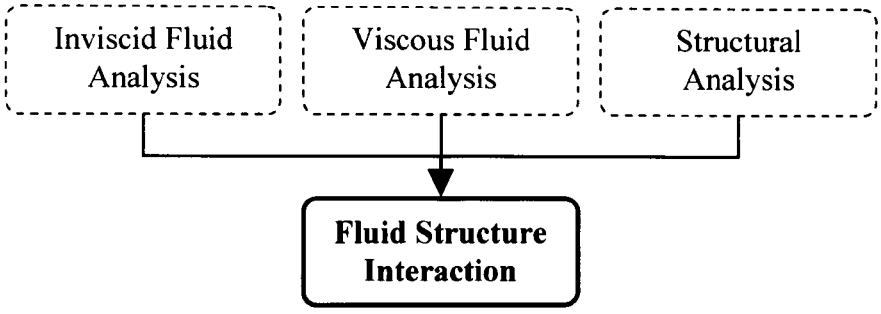

Figure 2.1.1 – Breakdown of literature review

2.2. Sailing Theory

It is difficult to identify precisely when sailing theory was initially approached in a scientific way, but some of the famous names in the initial understanding of sail flow include that of Milgram (1968, 1971, 1978), Marchaj (1964) and Gentry (1973).

Milgram was among the first to do both experimental and numerical analysis of yacht sails. His lifting line work and experimental analysis were among the first documented scientific approaches to sail performance (Milgram, 1968, 1978). Lifting line theory is a classical mathematical approach to estimating the lift generated from wings (Prandtl, 1918). This was further developed by Milgram to take into account the atmospheric boundary layer and resulting changes in velocity with height. Further details can be found in Milgram, 1968. During his analysis of sails he highlighted the similarities and differences to low speed aircraft, including that of velocity gradients and the substantial differences in lift coefficients created by both (Milgram, 1968). Milgram states 'a typical propeller blade might have a lift coefficient of about 0.4, whereas a typical sail would have a lift coefficient of about 1.4' (1968). The velocity gradient present on an aircraft

wing is limited to the root of the wing, whereas most sails operate in a region where the wind gradient is significant over the entire sail.

Milgram's (1971) experimental analysis included a series of water tunnel tests on thin cambered plates shaped to airfoil profiles developed by the National Advisory Committee for Aeronautics, commonly called NACA profiles. Milgram also investigated the effects of masts on sail flow which will be further extended in the following chapter. Milgram's work highlighted and detailed important features of sail flow including the separation zones behind the mast and at the trailing edge (Milgram, 1968).

The work of Marchaj has also established itself as highly acclaimed work (Marchaj, 1964; Marchaj, 2003). His 2003 text is based upon his 1964 text with updated thoughts and discussion. The text covers most aspects of sailing theory and the aerodynamics of sails. He discusses pressure distributions with the use of classical pressure distribution plots. He also discusses drag and the effect of various aspects of the rig. Marchaj makes his own discussion upon the 'slot effect controversy' surrounding the theory of sail interaction. The slot is the region between the main and foresail. The importance of this slot and the effect the sails have upon each other has long been discussed. Unlike a slot in an aircraft's wing, the slot within a sail changes shape constantly as the boat changes course, changing the slot size and the sails' relative location to each other. Marchaj also presents findings about the effects of the mast upon sail flow, providing useful insight into this area. The effect of the mast and the 'slot effect' are approached by this author later in this thesis. Marchaj also uses Wilkinson's experimental

data (1989), which is detailed in Section 2.3.1, to help reinforce his discussion on pressure distributions and mast effects (2003).

Arvel Gentry was another early pioneer to bring technology to the marine industry, using his experience as an aeronautical engineer. Gentry was an aerodynamicist for the Douglas company (later to become McDonnell Douglas) between the years of 1958-1977 and then later Boeing until he retired in 1995 (Gentry, 2007). Initially he used experimental techniques but later used computational methods to further understand the science behind sails.

Gentry's most famous work was probably that published in SAIL magazine in 1973. These articles were later reproduced to form part of the book, 'The best of SAIL trim', published by SAIL magazine (Mason, 2000). The reason these publications have lasted the test of time is the way in which they were written. Although Gentry was a technical aerodynamicist the articles were not written in a particularly technical manner but instead were aimed at the sailor.

Gentry concisely wrote about sail flow in his paper entitled, 'A review of modern sail theory', in 1981. In this paper he discusses previous explanations of lift and sail interaction (Gentry, 1981). He highlights errors in older theories; in particular he discusses theories such as 'it has a greater distance to travel...so must travel faster' and varying density theories and replaces them with more complete and accurate theories of lift. His theories on sail flow extend into the theory behind the interaction of multiple sails on a traditional yacht rig. He dismisses traditional theories such as the 'slot effect' and Venturi theory and replaces them with

modern theories of wing interaction. This contentious issue is still being debated today and this author's thoughts are presented in Chapter 4.

In contrast to the majority of Gentry's work, Bethwaite approaches the various aspects of sail flow in an experimental way, usually with bespoke 'low tech' examples of his own (2003). Most subjects are discussed and where appropriate modelled in full scale, giving details and pictorial examples to demonstrate the theory. An example of this is his experimental demonstration of wind twist explained in the previous chapter. For this demonstration, he used ribbons at various heights up the mast and then took photographs to show how the wind changed direction at various heights up the mast. Bethwaite highlights the importance of modelling sails with masts due to the inherent flow separation associated with their inclusion. Following Milgram's comments, Bethwaite also agrees on the comparison of sails with aeroplane wings. However, Bethwaite (2003) places more emphasis on the differences between the two and includes particular points on the difference in aspect ratio (6.4:1 for a dinghy sail and 30:1 for a glider), angle of attack (10-180 degrees for a sail and 1-2.5 degrees for a glider) and twist (up to 20 degrees for a sail and negligible for a wing).

2.3. Sail Modelling

The flexible nature of sails makes their analysis complex as changes in surface pressure result in changes to their shape and vice versa, meaning that shape and aerodynamic performance are fully interdependent. As a result a substantial amount of research has been carried out on rigid sails, both experimentally and computationally to help simplify the problem. The following sections detail contributions made to the aerodynamic modelling of sails, starting with

experimental modelling and finishing with numerical modelling. Numerical modelling is further divided into inviscid modelling and full viscous modelling, both of which are critically reviewed.

2.3.1. Wind Tunnel and Full Scale Testing

Historically, sail modelling has been carried out through experimental testing, either using wind tunnels or full scale testing. For wind tunnel testing, scale models are typically used. The complexity of experimental testing and wind tunnels varies considerably. Most wind tunnels are general purpose tunnels used by the automotive or aeronautical industries, but a few have been purpose-built with sailing applications in mind and include advanced features such as wind twist to help model boundary layer effects (Flay, 1996; Fallow, 1996; Collie, 2005).

One of the main sources of error for wind tunnel testing is the inaccuracy inherent in taking measurements of a flexible system at small scales. Trying to create scale sails is a complex task where manufacturing tolerances can be an issue. For example, a 1 mm error in a broadseam of a 5m chord sail is more acceptable than that of a similar error on a $1{:}20^{th}$ scale model, where the same construction inaccuracy would have a more significant impact upon the testing. The creation of laminate sails in model scale is also complex and challenging. The trimming of sails in model scale can also be difficult, as very small changes in trim can affect the sails' performance considerably. The difficulty in accurately recreating the atmospheric boundary layer is also a source of error for wind tunnels.

Wind tunnel testing of rigid sails can be beneficial, where the sail shapes are created using solid material (Wilkinson, 1990; Collie, 2005; Lasher *et al.*, 2005).

Although this may seem a distant relative of larger flexible sails, the rigid nature of these models helps to simplify and remove some sources of uncertainty and error. For example, this type of testing can remove the scale issues of the sail material, construction inaccuracies and the need to trim the sails. Collie (2005) attempted this as part of his PhD study to validate numerical methods, with mixed results. He chose to validate his numerical results against data from wind tunnels, although he did question the results from his wind tunnel testing, in particular blockage and 3D effects. The experimental set-up is shown in Figure 2.3.1.1. The testing included the study of a circular arc section with 24.7% camber, a radius of 200mm and a chord length of 319mm through a range of wind angles (5-30 degrees) at a wind speed of $25ms^{-1}$. At each end of the model end plates were positioned that span the height of the tunnel. These end plates were positioned 165.5mm inside the side walls of the tunnel to allow the boundary layer on the tunnel walls to pass without influencing the model.

Some of Collie's experimental results will be revisited in more detail in Chapter 4, where they are used as a validation exercise for viscous CFD.

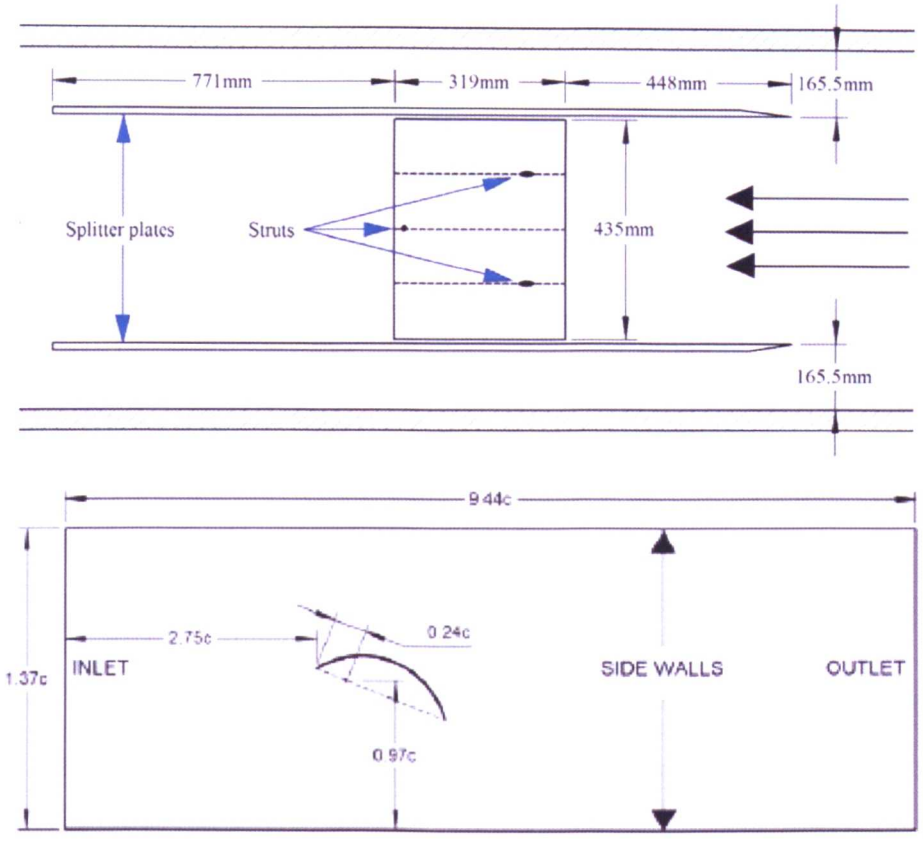

Figure 2.3.1.1 – Collie's experimental set up for his arc validation case (Collie, 2005)

Lasher *et al.*, (2005) could also see the attraction of rigid sail shapes and performed wind tunnel testing, purely for CFD validation, and made geometry and details available in the public domain. Lasher *et al*, took twelve parametric symmetric spinnaker models and studied them in a wind tunnel. They varied features of the spinnakers, such as camber and vertical distribution of sail width, and tested them at various angles of attack (35-90 degrees, with 90 degrees representing a run). Lasher *et al.* made all details of the sail geometries available in their publication to allow for future validation of numerical sail modelling (2005). They also highlighted some of the limitations of their testing. These included:

- The difficulty in matching Reynolds number due to the deflections in the rigid sails; the high tunnel speeds necessary to match the full scale Reynolds number results in deformations of the sail.
- The transient nature of the flow and its effect upon the rig; inherent to the flow around downwind sails is the transient shedding of the spinnaker wake.
- Testing of spinnakers in isolation; in reality spinnakers rarely operate in isolation but with a mainsail and mast.
- The lack of twist in the incoming free stream; important to the accurate modelling of downwind sails is the modelling of the atmospheric boundary layer which Lasher *et al.* were not capable of modelling in their tunnel.

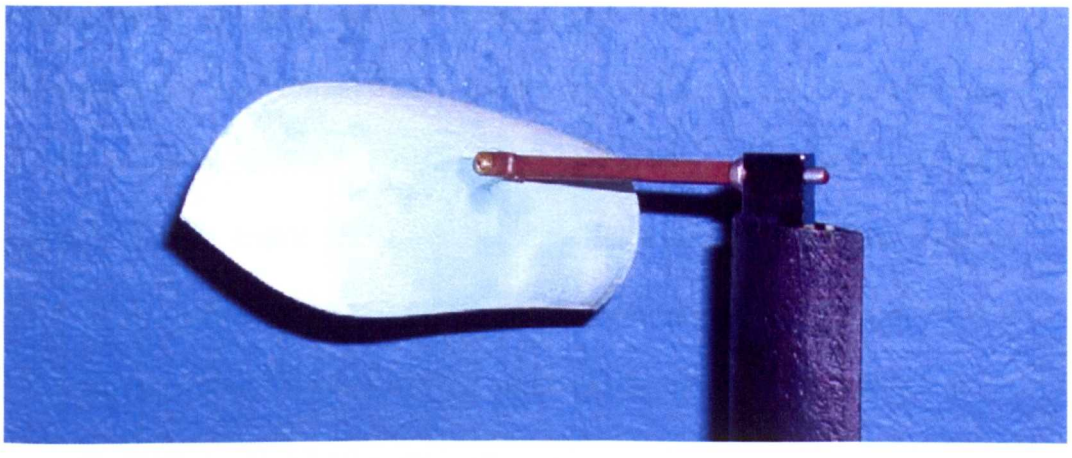

Figure 2.3.1.2 – Lasher *et al.* geometry mounted to dynamometer; typical sail area was of the order of 200cm^2

(Lasher *et al.*, 2005)

Other limitations include the inherent rigidity of the sail through all angles of attack. Rigid sails do not collapse if sailed at angles not physically possible for real sails. What results is an unrealistic performance of the sail at these angles of attack. This author's main concern over the study by Lasher *et al.* (2005), is the

geometric size of the experimental setup, Figure 2.3.1.2. The test section of the wind tunnel was 24"x24" and the blockage ratio was stated as being less than 5.5%. This equates to an extremely small sail area (~200cm$^{2)}$ and it is questionable that the accuracy of the experimental setup would be appropriate for such small scale models.

Replacing rigid sail shapes with their flexible alternative has both advantages and disadvantages. Some of the added complexities associated with flexible sails include: the creation of accurate model scale sails, the transient nature of some flows, the difficulty in obtaining actual flying shapes and the difficulty in trimming the sails in wind tunnel conditions.

The University of Auckland and the Twisted Flow Wind Tunnel provide some of the more advanced wind tunnel data that has been published (Flay, 1996; Richards *et al.*, 2001; Collie, 2005). Twisted wind tunnels have been used by many performance racing teams including the America's Cup Team New Zealand syndicate (Flay, 1996). The use of advanced wind tunnels and comprehensive models can help remove many of the problems highlighted by Lasher *et al.* (2005). Richards *et al.* (2001) used the Auckland tunnel to model downwind spinnakers with a mainsail present and with flexible sails. They used the model to test lift and drag on the system. With traditional and historical sailing vessels, sailing downwind was a question of maximising sail area to the wind and thus maximising drag. However, because vessel speed has increased over the years, their apparent wind angle can vary significantly from their true wind angle. America's Cup class yachts (AC32) sail downwind with apparent wind angles

between 90 and 135 degrees. Their paper concluded that America's Cup downwind spinnakers must be designed and trimmed to maximise lift to help achieve maximum thrust.

The thought of full scale testing is appealing given the inaccuracies in scale model wind tunnel testing. Full scale sails cannot be tested in even the largest of wind tunnels, so testing during real sailing conditions has been the only practical option. However, full scale testing at sea in real sailing conditions is not straight forward either. Changes to the environment, such as the constantly shifting wind velocity, in addition to the sea or water state, make full scale testing particularly challenging. For accurate data collection, details of all the relevant information must be captured simultaneously, including; wind data, sail shapes and forces etc. Attempts to capture this information, for comparison, include that of Masuyama and Fukasawa (1997) and of Hansen *et al.* (2002). Hansen *et al.* conclude that there are problems associated with both wind tunnel and full scale testing, stating the unsteady nature of the environment and the difficultly in measuring all relevant data accurately as being the main challenges. They found that the scatter for the full scale testing data was significant. They also highlight the need to account for the mast in the aerodynamic simulations, as its presence it not negligible.

The importance of including the mast in sail aerodynamic modelling has been known and documented for many years (Marchaj, 1964; Milgram, 1978). Wilkinson (1984) studied the effects of mast and sail interaction in detail, and highlighted flow regions common to all sail flows. He derived these regions from

extensive rigid model wind tunnel testing (Wilkinson, 1983). Wilkinson tested a sail and mast section in a wind tunnel. The ratio of mast diameter to sail chord was 4.03% with a camber to chord ratio of 12.5%. The angle of incidence of the sail was 5 degrees at a Reynolds number of 709,000. The camber distribution represents that of a NACA a=0.8. The sail was constructed from a 5mm thick aerofoil of 2.11m span and 0.7m chord, fitted horizontally across the wind tunnel (Wilkinson, 1990). He described the regions where separation occurs, Figure 2.3.1.3, which were later further documented by others in texts such as Bethwaite (2003) and Marchaj (2003). These regions include separation and reattachment points on both windward and leeward sail surfaces, in addition to 3 separated flow regions; the upper separation bubble, the lower separation bubble and the trailing edge separated region. Wilkinson (1987) also used these to try and calibrate various early computational methods which will be discussed further later in this chapter.

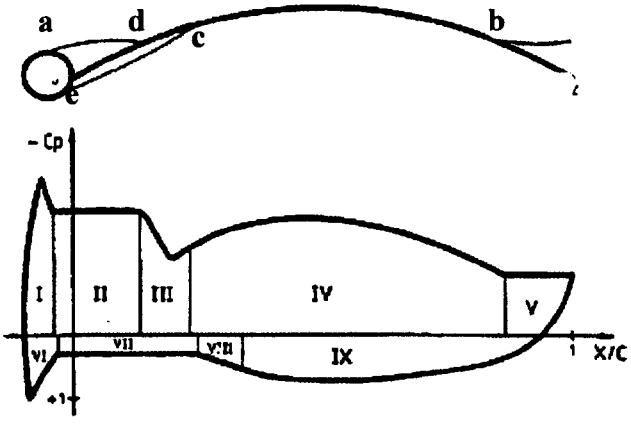

a, b, e – Separation points
c, d – Reattachment points
I – Upper mast attached flow region
II- Upper separation bubble
III- Upper reattachment point
IV – Upper foil attached flow region
V – Trailing edge separation point
VI – Lower mast attached flow region
VII – Lower separation bubble
VIII – Lower reattachment region
IX – Lower attached flow region

Figure 2.3.1.3 – Wilkinson's 9 regions of flow for a mast and sail geometry (Wilkinson, 1983)

Wilkinson (1990) also provided velocity profile data for a specific rigid mast and sail geometry. He supplied velocity profiles along the upper surface of the sail along with the pressure distributions seen in his other studies. This data is probably the most complete set of data, of good quality, available in the public domain to date. This experimental data is used later in this thesis as a validation case. A sample of the velocity profiles is shown in Figure 2.3.1.4. 5 different profiles were taken along the upper/leeward sail surface. This allows for a profile in the forward and trailing separation zones and one in the central lifting section. There is also a profile at, or as close as possible to, the reattachment and separation points.

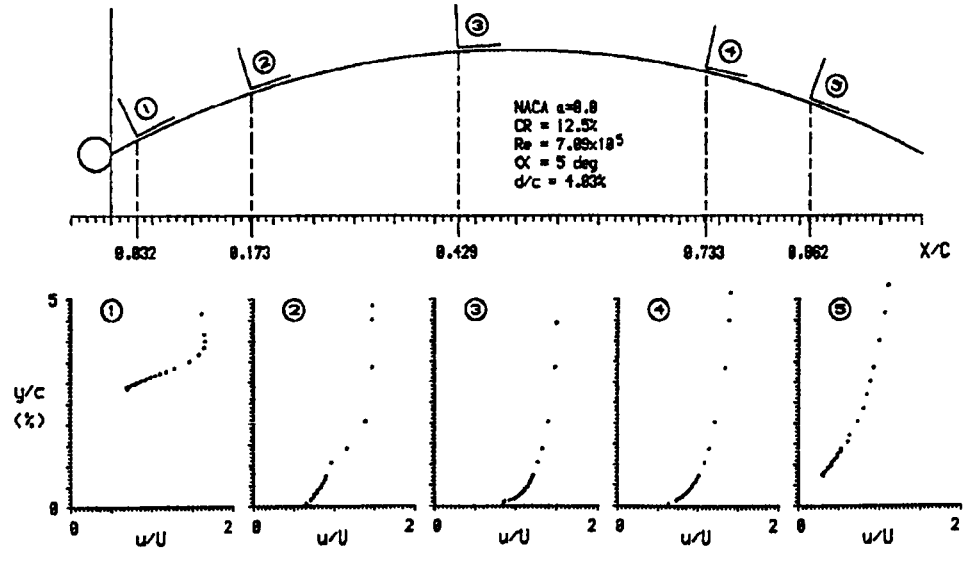

Figure 2.3.1.4 – Wilkinson's velocity boundary profile data (Wilkinson, 1990)

This section has detailed some of the wind tunnel tests carried out to date. In particular two simplified rigid sail models have been discussed (Collie, 2005; Wilkinson, 1990), which are used as validation cases later in the thesis. The scarcity of reliable data sets, which are not commercially sensitive, is apparent in the field.

2.3.2. Computational Modelling using Inviscid Codes

The vast majority of computational modelling to date has been carried out for rigid sails. The following section reports on the use of inviscid methods to model flow past rigid sails. The use of inviscid computational approaches has been common for many years. Early computers were only capable of basic, small size calculations, but as computers have increased in size (memory) and speed, so too has their potential for solving more complex fluid flow problems. Various assumptions can be made to simplify the Navier-Stokes equations. Assumptions of inviscid fluids and steady state flow are common and help make the problem computationally affordable. Details of the simplifications made to the Navier-Stokes equations are shown in the following chapter in Section 3.2. These solutions were initially used by the aeronautical industry for modelling plane wings (e.g. Hess, 1990). The disadvantage is that with each assumption made, a reduction in the potential accuracy of the flow is seen. The difficulty is deciding which assumptions can be justified, without making the analysis irrelevant or the duration of the analysis excessive.

Wilkinson was one of the early users of inviscid methods to model sails. His analysis of partially separated mast and sail flow (1987) uses a panel method combined with empirical input. Panel methods form one of the most basic CFD analysis tools available, based on the following assumptions: (1) That the fluid is inviscid; (2) The flow is incompressible. Further details on panel methods are given in Section 3.2. This empirical input, utilised in Wilkinson's method, allows separation and reattachment points to be inserted into the model to 'force' the solution to behave in a given manner, without the need to rely on complex

turbulence and boundary layer models. The results obtained show reasonable correlation but discrepancies are still present despite the empirical input. As expected the pressure distribution has greatest errors in the regions of the reattachment zones. A sample pressure plot of the sail with data from both experimental and inviscid numerical analysis is shown in Figure 2.3.2.1. In this plot X/C represents a fraction of the distance along the chord, where X is a chordwise coordinate and C is the chord length.

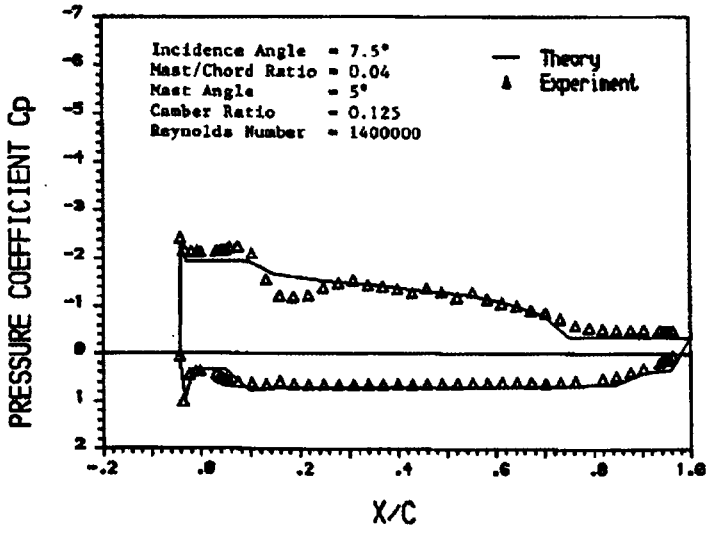

Figure 2.3.2.1 – Wilkinson's pressure analysis for a sail and mast configuration (Wilkinson, 1987)

Within Wilkinson's pressure analysis the windward (bottom) pressure surface is well captured. However the leeward surface is not so well represented. This is particularly true around X/C=0.2 and between X/C=0.7-8. These two regions are where the flow reattaches and separates from the sail. These errors are still apparent despite the empirical input of the separation and reattachment points necessary for this type of analysis. This highlights the difficulties in modelling flow separation and is one of the focuses of this thesis in the attempt to improve

sail performance and efficiency (Jones and Korpus, 2001; Chapin *et al.*, 2005a; Paton and Morvan, 2007). Additionally the practicality of such an approach is questionable, as it seriously restricts its predictive and design abilities as an input is required to drive the flow separation and re-attachment.

There are many different commercial flow simulation software solutions in the marine industry, which have been designed specifically for sail modelling. Examples include WINDFlow. (SMAR Azure Ltd, 2007) and PANSAIL (FLOW Solutions Ltd, 2007). Both packages use simplified inviscid flow solvers, although the details available to the public domain are somewhat brief due to their commercial nature. PANSAIL is a vortex-lattice code, details of which are described in Chapter 3 but can also be found in Wilkinson (1987) and Heppel (2002) for example. This type of analysis has progressed from the early panel methods as attempts are now made to estimate the wakes too, to help provide more accurate sail loads.

The main advantages of inviscid solvers is their ease of use and speed of calculation. Due to their incomplete nature and simplified form, solutions can be run within minutes. It has been argued by some that these types of calculation can provide acceptable results for solutions where little separation is found (Heppel, 2006, *personal communication*), for example flat sails when travelling to windward. However, the solutions become less reliable when masts or highly cambered sails are present, creating large areas of separation. For downwind sails, the use of this type of solver is questionable and a more complete fluid solver is needed, due primarily to the inherent flow separation. Leading sail

designers and consultants, such as North Sails and Peter Heppel Associates, use this type of inviscid approach in their design of sails (Elliot, 2008, *personal communication*, Heppel, 2006, *personal communication*). However, the limitations of this type of method restrict their use to upwind and close reaching sail modelling.

As well as the commercially available codes, the simplicity of this type of method results in some codes being available under the GNU General Public License. These solvers often fail to offer the user-friendliness of commercial codes, but can provide similar levels of accuracy. An example of this type of solver is the two dimensional XFOIL (XFOIL, 2007). Speer (2007) used XFOIL to look at the aerodynamics of teardrop wingmasts. He limits his use of XFOIL to applications he feels can be adequately modelled and chooses not to model wingmasts with blunt trailing edges. The results presented are interesting although the work is more of an experiment and has not been validated in any form, as highlighted by the author in his conclusions. With such large areas of separation, particularly on the windward side of rotated masts, the use of a more complete viscous code could perhaps be better suited as described in the following section.

2.3.3. Computational Modelling using Viscid Codes

The use of viscous CFD to model sail flow for the modelling of rigid sail shapes will be detailed in this section. Viscous CFD codes are now commonplace and there are numerous commercial CFD codes, such as FLUENT (FLUENT, 2009) and ANSYS CFX (ANSYS, 2009), in addition to opensource CFD codes, such as OpenFOAM (OpenCFD, 2009). There are also dedicated research codes usually confined to research institutes. The development of CFD and the increased

availability of numerous 'viscous' CFD codes has resulted in an increase in rigid viscous sail simulations over the last 15 years. For the sail designer, the use of viscous CFD enables the modelling of both upwind and downwind sails to become feasible, if not always practical.

In addition to the experimental work discussed previously in Section 2.3.1, Collie also did a significant amount of CFD work, including an in-depth look at the turbulence models available in the commercial domain (Collie *et al.*, 2001). Collie's PhD considered the application of CFD to two dimensional downwind sail flows (Collie, 2005). Although this sounds less advanced than some of the work presented later in this chapter, it is in fact some of the most advanced CFD carried out to date, with a great attention to detail. A systematic approach is adopted, with care and attention applied to both the mesh criteria and choice of turbulence model. Collie's work includes the modelling of the validation case replicated by this author and presented in Section 4.2.

Collie *et al.* (2001) published an internal report looking at various turbulence models available for practical sail flow applications. Their aim was '*not to develop a universal turbulence model, suitable for all flow situations. The intention of the research is to find a model that is suited to solving sail flows, while using minimum computational resources*' (Collie *et al.* 2001). They evaluate different types of model including: one equation (e.g. Spallart-Almaras model), two equations (e.g. $k-\varepsilon$ and $k-\omega$ model) and second order closure models (e.g. ASM model). Collie *et al.* conclude that the Shear Stress Transport (SST) turbulence model is '*the most accurate performer*' stating 'excellent results

for adverse pressure gradients and separated flow' found in both upwind and offwind sailing conditions. Further discussion on turbulence modelling is included in Chapters 3 and 4.

In 2004, Collie *et al.* looked at the parametric analysis of down-wind sails. Within this study they varied draft and camber within typical limits of an America's Cup Class (ACC) yacht. They highlighted the need to run three dimensional simulations due to the unrealistic high lift coefficients obtained in two dimensions, partly due to the unrealistic performance across the span, which cannot be maintained in 3 dimensions. Again the work was carried out with diligence. In particular, care was taken to ensure grid and timestep independence. The authors point out the loss of relevance to real sails due to the loss of the third dimension and inclusion of multiple foils; however it is this author's opinion that the simplicity of the study allows for research to be focussed onto particular aspects, in this case camber and draft, and the work therefore provides useful understanding. Although it may not be applicable to all sail shapes, it does help with fundamental understanding of sail flow. Collie *et al.* also demonstrate the importance of sail interaction, comprehensively demonstrated in Figures 2.3.3.1 and 2.3.3.2, showing the changes in flow field when modelled by viscous CFD (2004).

Similarly to Collie *et al.* (2004), Doyle *et al.* (2002) used computational techniques to carry out optimisation studies upon the sheeting angles of the sails for the mega yacht Maltese Falcon. This included the use of 2D RANS based numerical models coupled to an optimisation algorithm. Results from this can

then be used as an input for a velocity prediction program or VPP. This type of optimisation study is probably still too expensive for 3D simulations but provides an interesting insight into optimisation procedures.

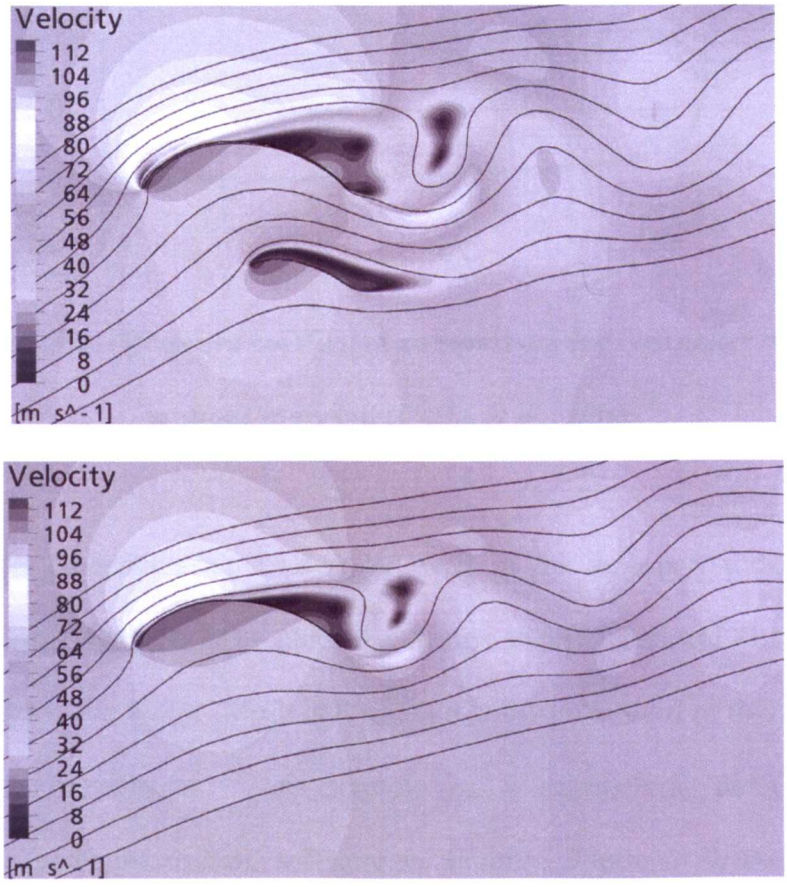

Figure 2.3.3.1 - Comparison of the flow streamlines and velocity contours for the gennaker / mainsail configuration (top) and the gennaker without the mainsail present (bottom) (Collie *et al.*, 2004)

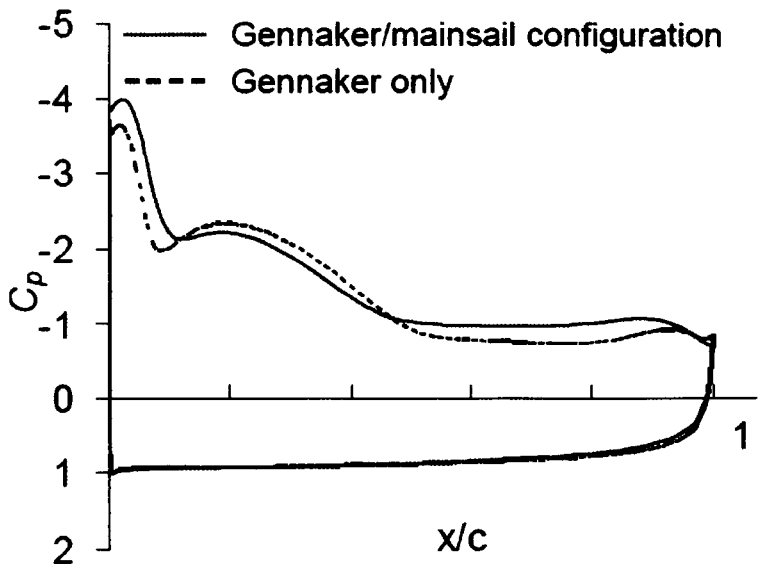

Figure 2.3.3.2 – Pressure coefficient comparison for Gennaker with and without mainsail (Collie *et al.*, 2004)

Optimisation procedures have advanced well in the autosport industry where extremely large budgets help push the design process forward (Lewis, 2009, *personal communication*). Mesh deformation software is used in this industry to parameterise movements. An example of a commercial piece of mesh deformation and optimisation software is Sculptor (Optimal Solutions, 2009). Within Sculptor control points can be moved around in a GUI creating new variations of the original mesh in real time. The deformations can be controlled, specified and parameterised by the user.

This technique is currently used for optimisation in motorsport (Seibert and Lewis, 2004). Seibert and Lewis use parametric mesh deformation to manipulate the front bodywork of a vehicle with the aim of maximising front downforce. The optimisation process led to an increase in front downforce of 75% (2004). The use of a design of experiments (DOE) combined with a response surface

formulation, which may then be searched for further refinement, can become a powerful design tool (Lewis, 2009, *personal communication*).

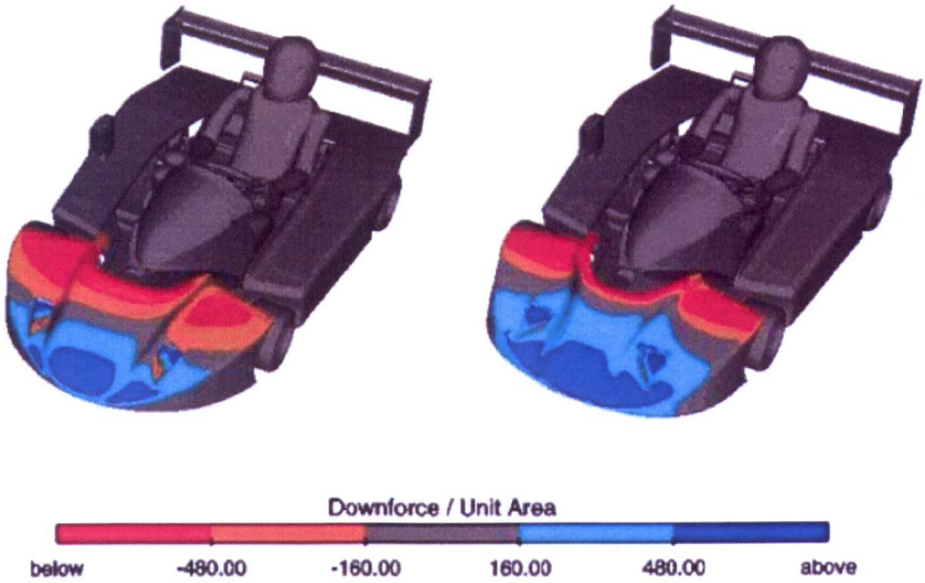

Figure 2.3.3.3 – Parametric optimisation of front bodywork

(Left – Baseline, Right – Optimised) (Seibert and Lewis, 2004)

Chapin *et al.* demonstrated and validated how viscous CFD can be used as a design tool for sailing yachts and rig development (2005a, 2005b). They included comprehensive validation of the commercial CFD code Fluent and the Spalart-Allmaras model via comparison to wind tunnel testing. Although this is a relatively basic, one equation model, Chapin *et al.* demonstrate impressive correlation for a range of sail scenarios. Their validation to Wilkinson's (1990) wind tunnel data of the mast and sail, demonstrates a very good correlation for the pressure coefficients. The ability for viscous RANS based CFD to accurately predict the separation and reattachment points is a key benefit over inviscid codes. Chapin *et al.*, demonstrate the potential for RANS based CFD to detect pressure profile trends for varying angle of attack, Figure 2.3.3.4.

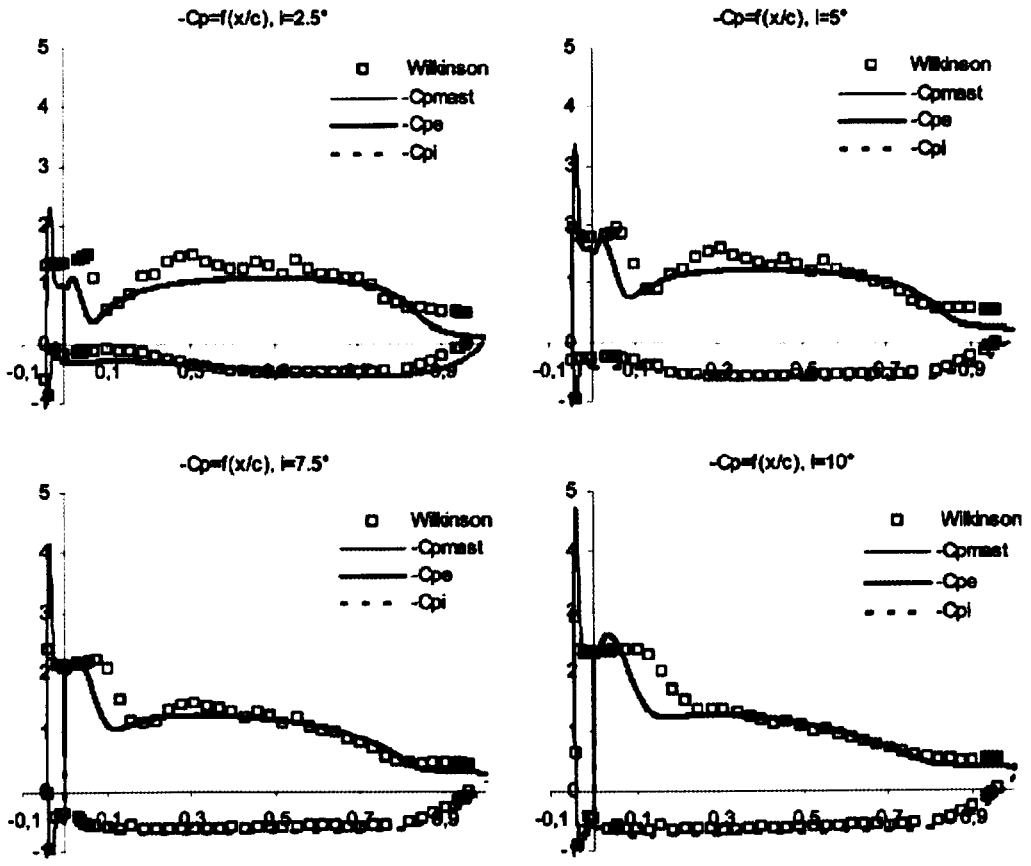

Figure 2.3.3.4 - Pressure coefficient distribution at four wind incidence angles; comparison between RANS based results and experimental data from Wilkinson 1984 (Chapin *et al.*, 2005a)

It is notable that within Chapin *et al.*'s (2005a) work the mesh created in the near wall regions was particularly refined. Although there are no quantitative figures for their refinement it is thought this will have contributed significantly to the performance of the CFD throughout the Wilkinson validation. Chapin *et al.* also detail their optimisation process, ADONF, in their 2006 paper, 'Analysis, design and optimisation of Navier-Stokes flow around interacting sails'. Chapin *et al.* (2006) also demonstrate the potential differences between RANS based models and an inviscid/viscid solution (Norris, 1993) with their comparison between the

two for the modelling of sails with various cambers. This is shown in Figure 2.3.3.5, again highlighting the importance of viscous analysis. Chapin *et al.* state *'RANS or URANS models are needed to predict flows around high camber sails like gennaker in reaching and downwind sailing conditions where separation and unsteadiness are commonplace.'*

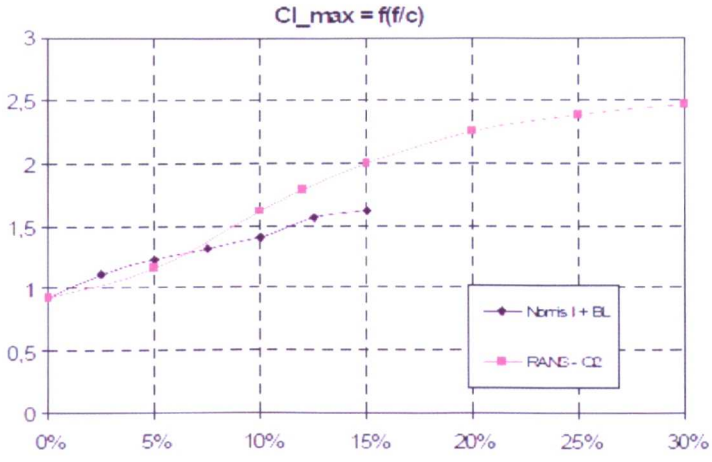

Figure 2.3.3.5 - Inviscid/viscous coupling and RANS prediction of the maximum lift coefficient versus sail camber (Chapin *et al*, 2006)

The advantages of viscous CFD can again be seen when offwind sails are modelled in 3 dimensions. Hedges *et al*, 1996, used the CFD code CFDS-FLOW3D to model downwind spinnakers. It is worth noting that the theory and application of CFD has moved on in the years since this study. The modelling of the spinnakers using CFDS-FLOW3D was then compared to wind tunnel tests. They obtained results with an error of 15% for lift and 3% for drag. Hedges *et al.* used the now superseded (Rumsey and Gatski, 2001), but still commonly used, $k-\varepsilon$ model. A more detailed look at turbulence modelling will be carried out in the following chapter.

Lasher and Sonnenmeier (2008) also attempted to model downwind sails when they tried to validate numerical methods against their experimental model described in an earlier Section, 2.3.1. They concluded that the realizable $k-\varepsilon$ model was the best turbulence model for modelling offwind sails. However, this author questions their CFD modelling and in particular the mesh resolution and their reported values of y^+, a measure of the mesh size adjacent to a surface (for a detailed explanation of y^+ please see Section 3.4.6). Lasher and Sonnenmeier briefly report convergence difficulties with their fine grid (330,000 cells; not a lot by today's CFD standard) but instead opt to use a coarser grid to eliminate these convergence issues (140,000). They also report y^+ values in the range of 30-200. To put these numbers in perspective, Collie *et al*, 2004, used a mesh with 55,340 cells in only two dimensions, did not use a wall function approach and had a y^+ as low as 1 (the laminar part of the boundary layer extends to a y^+ of approximately 5, therefore the first node of a CFD simulation which would attempt to resolve the boundary layer would need to be at $y^+ = 2$ to 3). The suitable range for y^+ is of course dependent upon the choice of turbulence model, as not all models are designed to resolve the boundary layer; some do indeed rely on wall functions, as was the case for Lasher and Sonnenmeier (2008), to bridge that gap but they cannot hope to capture the aerodynamic performance as well as others. As a result a single mesh cannot be suitable for all types of turbulence model. When using a wall function (see Section 3.4.9) the boundary layer velocity profile is assumed to be the same as the flow over a flat plate and the first computational node is well within the turbulence region. Consequences of this can be the erroneous prediction of local shear profiles and flow separation over a cambered surface and the miscalculation of resulting forces. The y^+ reported by Lasher and

Sonnenmeier is within the specified range for wall-function models such as the $k-\varepsilon$ model, so it is perhaps not surprising that the model performs comparably to others such as the SST. Their conclusion as to the superiority of the $k-\varepsilon$ model is therefore questioned by this author. Further explanations of boundary layer modelling and turbulence models can be found in Section 3.4.

In 2007, Lasher and Richards analysed a different set of downwind spinnakers through a range of apparent wind angles, using three different turbulence models in an attempt to validate their use for spinnakers in an atmospheric boundary layer. Their paper reported that at higher angles of attack (>30 degrees) the lift and drag forces were less well predicted than at lower angles of attack, partly due to the poor prediction of the onset of separation.

In an attempt to compare the inviscid models described in the previous section and the viscous methods detailed here, Fiddes and Gaydon (1996), provided a comparison between a new vortex lattice method and a Reynolds averaged Navier-Stokes based code. Fiddes and Gaydon used an International Americas Cup Class (IACC) rig including a mainsail and jib, without a mast, boom or hull for their comparison, during upwind sailing conditions at 15 degrees apparent wind angle. The comparison was between their own vortex lattice based PANSAIL code and the viscous RANS based PHOENIX code. The two codes at times predicted similar trends (Upper surface from x=0.2 onwards) for pressure distributions, but differences in values can be seen throughout the majority of Figure 2.3.3.6. However, the RANS model used, that at the time was modern, has now been superseded for applications with adverse pressure gradients (Rumsey

and Gatski, 2001), which make this author question the findings and conclusions drawn from this paper. The lack of experimental comparison also adds to the uncertainty surrounding any conclusions.

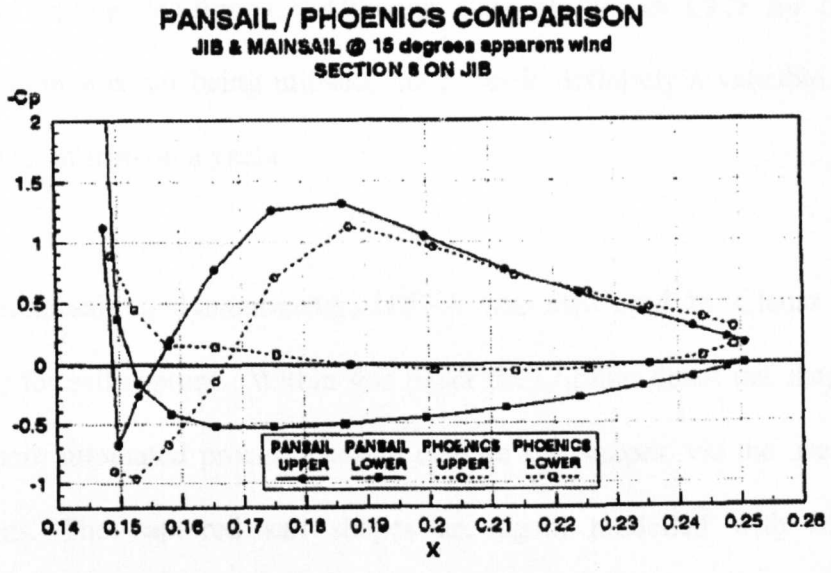

Figure 2.3.3.6 – Inviscid and viscid pressure profile comparison for an IACC jib during upwind sailing conditions (Fiddes and Gaydon, 1996)

Krebber and Hochkirch (2006) attempted to validate their CFD to full scale data. They detailed the effects of trim for a sailing yacht via the use of the full scale sailing dynamometer, DYNA. With the use of cameras located onboard and in-house software, the actual flying shapes can be recorded together with other data such as boat speed, heel angle and apparent wind angle.

The trim was then changed parametrically before being analysed numerically. The commercial CFD code ANSYS CFX was used for the computational simulations. The use of CFD created an insight into the changes in the flow due to the trim. Krebber and Hochkirch used the $k-\varepsilon$ model in a steady state

scenario with approximately 800,000 cells. No grid independence was discussed although the grid has been carefully created with a high level of refinement around the mast. The numerical comparison focused upon force coefficients and centre of effort. The AWA for this study was 28°, which for this vessel would be upwind sailing conditions. Although state of the art CFD for this type of application was not being utilised, the paper is definitely a valuable insight into the effect of trim on a yacht.

The same sailing dynamometer, DYNA was also used by Clauss and Heisen (2005) for sail capture. Within this paper they further detail the shape capturing and their automated process used to capture sail shapes, via the use of multiple cameras. The captured sail shapes are again modelled with RANS based simulations, utilising the $k-\varepsilon$, $k-\omega$, and *SST* models. They found reasonable agreement between their computational results and full scale data reporting errors between 0 and 30% (within the range of the experimental scatter).

Roux *et al.* (2002) provided an interesting contribution to yacht CFD analysis when they coupled their aerodynamic computations to a hydrodynamic computation in order to predict its performance in calm water. Their analysis allowed a given crew weight and righting moment to be pre specified and the heel angle allowed to change. This would again be a valuable addition to creating a more complete Velocity Prediction Program than deriving performance from a simple sail only simulation.

2.3.4. Summary

This section has highlighted the potential advantages and capabilities of viscous CFD and where possible given comparison to inviscid codes. The improved performance of the viscous codes has been evident for upwind, offwind and downwind sailing. The ability of viscous solutions to better model the effects of masts, separation and reattachment points form a key part of this. The ability of viscous solutions to also model sail interaction throughout different sailing conditions is again important. Viscous solutions are also capable of modelling sails with large camber and at larger angles of incidence than inviscid codes. The inability of inviscid codes to predict the onset of separation is their key weakness, given the inherent flow separation associated with sail flow.

2.4. Structural Analysis

The previous sections have detailed the computational modelling of the fluid flow around rigid sails. However the flexible nature of sails means that in practice designers are facing a very different problem. Research has therefore also been carried out into the modelling of yacht sails from a structural standpoint. Structural analysis can be carried out computationally and there are many pieces of software available. These can be split into 2 main categories; (1) those developed for general structural analysis and (2) those created for bespoke sail modelling.

By far the most common form of computational structural analysis uses Finite Element Analysis or FEA. This type of analysis assumes that a structure is an

assembly of elements with different forms of connections between these elements. The modelling of the elements of a sail can be challenging for FEA as particular features of a sail make their analysis differ from the majority of FEA applications such as beam and column design. These differences include: (1) the highly anisotropic nature of the materials used, (2) large deformations, (3) the ability of a membrane to wrinkle to remove compressive loads and (4) the membrane's inability to resist bending moments. These issues and others will be discussed further in Section 2.4.1 and again later in Chapter 5.

2.4.1. Sail Structural Modelling

The main feature of sails that make their analysis, using FEA, complicated is their thin nature and the materials from which they are made. Modern racing sails are made from laminate structures, with layers of synthetic fibres or yarn laid between two layers of mylar film (typical of a North Sails 3DL sail, North Sails, 2008). The yarns are laid in a specific layout to give the sails their required structural behaviour. As a result the structural behaviour of sails is highly anisotropic. The ability of a sail to change shape significantly with changes in wind angle also make the modelling of sails different to many other FEA applications. This is true even when strains are kept to a minimum.

The interaction of the sail and the mast is also challenging, as the sail is free (within some constraints) to move up and down the mast groove and is free to rotate relative to the mast. These very specific and complex needs, required for the structural modelling of sails, often render generic FEA codes inadequate, e.g. for the modelling of wrinkling (Jones, 2006, *personal communication)* and result in simplifications being made. Shankaran (2005) used the commercial FEA

software MSC Nastran (MSC Software, 2009) to model the structural deformations of the sails in his PhD thesis. For Shankaran's study (2005) the assumptions of an isotropic material without wrinkling limit the accuracy and potential applications for the model. Another disadvantage of the commercial FEA codes is the difficultly in trimming of the sails. Further details on the structural modelling of sails will be given in Chapter 5.

The majority of the sailing industry use bespoke sail modelling FEA packages, with many of the sail lofts using in-house codes. The most well known of these is Membrane, the North Sails FEA package (North Sails, 2008), used by North Sails designers throughout the world. North Sails have led the field in racing sail design, especially the Americas Cup in recent years. For the 2007 Americas Cup, the majority of boats used North Sails and as a result, Membrane, their structural code for sail modelling (Elliot, May 2007, *personal communication*). Membrane includes the features of the sails in a detailed manner (including thread structures, batten data and mast bend) and allows a comprehensive analysis to be performed. Limited details of the code and its working are available in the public domain due to its commercial sensitivity.

There are also commercial codes such as the analysis tools sold by SMAR Azure, AZURE Project (SMAR Azure Ltd, 2007) an integrated software suite for sail design and manufacture and the bespoke sail modelling code RELAX II (PHA, 2009). These codes are designed with sail modelling and analysis as their sole application, which help make simple tasks such as re-trimming sails far simpler than with a generic FEA package.

RELAX is capable of modelling the wrinkling of sails (Heppel, 2002) in addition to mast deflection, battens, fully anisotropic multiple sails and other features that would be complex, if not impossible, for standard FEA packages (Heppel, 2002). Heppel's 2002 paper, titled 'Accuracy in sail simulation: wrinkling and growing fast sails', focussed upon improving the accuracy of sail simulation in these specific conditions. He discusses how sails wrinkle to relieve compression within the membrane, and how to extend FEA models to achieve this. Heppel also discusses how to best generate grids and the use of wrinkling to best predict sail shapes. Other research based around the wrinkling of membranes includes that of Muttin, 1996.

2.5. Fluid Structure Interaction

The penultimate section within this chapter, draws together the material presented in the previous sections into an integrated solution. Fluid Structure Interaction (FSI) is the interaction between structural and fluid fields. The interaction between the two fields results in what is called a "coupled system" and terminology within these fields varies greatly. The following section will highlight a few basic terms used through this thesis.

A "system" consists of two or more "subsystems" (Felippa and Park, 2004). If there is no feedback between subsystems the interaction is termed one-way. If there is feedback the interaction is termed "two-way" or "multi-way" for two or more subsystems. This is demonstrated in Figure 2.5.1.

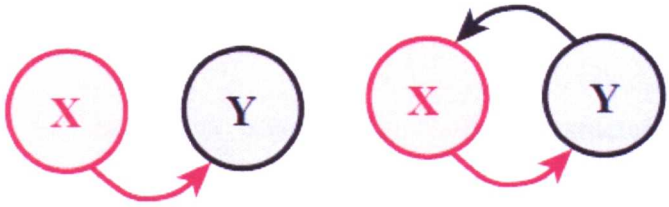

Figure 2.5.1 – Coupled subsystems (Park and Felippa, 2004)

(Left = one-way, Right = Two-way)

The FSI problem encountered with sail analysis is a two way coupled system and will be the focus of this thesis. Broadly classified, the system can either be modelled by a monolithic or partitioned approach. These approaches are often called "strong" and "weak" coupling respectively.

A monolithic approach treats the system as a single entity and is solved as such. With a partitioned approach the subsystems are treated as isolated entities with communication between the subsystems. They are solved independently. Despite this broad definition of two separate approaches there are many different variations that can form hybrids between the two approaches (Kamakoti and Shyy, 2004).

There are advantages and disadvantages to both approaches and these are discussed further in Chapter 5 once again.

2.5.1. Sail FSI Modelling

The nature of the interaction between the fluid and structural aspects of sail modelling, determines the type of FSI modelling that is most applicable. During upwind sailing conditions the sails form a predominantly steady shape (for well trimmed sails). This is not to say that the fluid flow is at a steady state, but the sails shapes themselves predominantly are. For offwind sails, the flow regime becomes truly time dependent as significant flow separation occurs. Despite this, the sail shape still remains relatively steady. However changes in the wind and boat motions can create more significant changes to the sail shape over time.

The fact that sails form predominantly steady shapes makes partitioned methods applicable. Further argument, for and against the use of partitioned methods will be given in Chapter 5. The remainder of this section highlights some of the partitioned FSI solutions used to date, with applications to sails.

Jackson and Christie were the first researchers known to the author to develop an FSI solution suitable for sail type analysis (1987). This solution coupled a potential flow solver, for the aerodynamic analysis, to a finite element representation of the membrane in a partitioned approach. Although within their paper the application is a simplified handglider, the method is equally applicable to yacht sails.

More recently Schoop *et al.* (1998, 2001) coupled a vortex lattice method to a finite element code with notable improvements from previous attempts, providing improved numerical accuracy and convergence. Their simulation has been

simplified by neglecting the anisotropy of the sails structural characteristics and any wrinkling. They believe their improvements over previous attempts could be put down to improved fluid solvers and the separate meshes for the vortex lattice and the finite element analysis. They do however question the utilisation of the potential flow theory for flow including masts, and mention future work including viscous flow solvers.

Coiro *et al.* (2002), used a similar methodology to Schoop *et al.* (2001), and developed the idea of an FSI solution, combining a FEA code and a Vortex lattice flow solver iteratively, in a partitioned approach, adding a boundary layer solution to add viscosity to the regions where viscosity is important, such as the separation bubble behind the mast. The aerodynamic results are validated against experimental results. They validate the completed solution with experimental data from a test rig in a wind tunnel to reasonable success, modelling flat upwind sails, however no quantitative performance values are given. Part of their conclusion states that the viscous effects do not play an important role in the sail deformations during upwind conditions. The experimental flying shapes were collected via the use of a laser scanner, capable of accuracies to within 1.5mm. A big disadvantage of this type of shape capture is the time taken for a complete scan of the sail.

Ranzenbach and Xu (2004) used their inviscid FSI method to demonstrate the effects of trim and luff sag upon sail performance. The work however was not validated and no estimate of the accuracy of the predictions is given. In 2005, Ranzenbach and Xu extended this work to study the sails of a 30' racing yacht.

They concluded that the primary load paths change with changes in trim and sailing conditions.

Shankaran took his NASTRAN model described in the previous section and coupled it to an Euler solver to create an FSI coupled solution (Shankaran *et al*, 2002; Shankaran, 2005). This was developed to provide a design tool for upwind sailing conditions, where attached flow is dominant. The Euler equations were discretised on unstructured tetrahedral grids to provide performance estimates. Shankaran concluded that the major influence of the head sail elasticity was to alter the pressure distribution at the leading edge of the head and mainsail alike. Similar work to Shankaran, by Sriram *et al.* (2003), demonstrates the potential of this type of solver to help improve understanding and reduce leading edge suction peaks. Controlling pressure profiles is essential in maximising performance throughout the operating conditions. The limitations of this solution include the isotropic assumption of the structural model and the inviscid solver, restricting its application to upwind sails.

Le Maitre *et al.* (1999) and Friedl (2002) both pushed the development of inviscid FSI a stage further as they attempted unsteady FSI. Le Maitre *et al.* (1999) used an inviscid unsteady solver coupled to an elastic membrane solver in 2D. This was further advanced by Friedl (2002) when he used an unsteady FSI tool utilising a potential flow code in 3D. However, the major drawback of all these previous FSI schemes is the assumption of inviscid flow.

As described previously the importance of viscosity when modelling real sail conditions, in particular offwind sailing, is paramount to obtaining accurate results. Mairs attempted to fill this area when he combined viscous commercial CFD to an FEA code in the attempt to model offwind sails (2003). He combined the commercial CFD code STAR-CD *(cd-adapco, 2009)*, using the $k-\varepsilon$ turbulence model, and the FEA code TENSION9. Although this set-up is close to providing a solution to the modelling of offwind or downwind sails, the solution actually produced results of mixed accuracy. This was most probably due to the poor performance of the $k-\varepsilon$ model when applied to highly cambered offwind sails, as described by others (Collie *et al*, 2001; Rumsey and Gatski, 2001). Other criticisms of the work include the way in which the sail shape data was collected. The use of a 'Romer', which involved the placement of a significant physical structure in the wind tunnel would undoubtedly affect the flow and pressures around it. The accuracy of the shape capture was estimated at a 'half inch', which is low for a scale model (luff length = 1.58m). Mairs studied two offwind sails; a code zero sail and a reaching asymmetric. Due to the relatively high camber of the sails combined with the poor choice of turbulence model and mesh limitations, the flying shapes were quite poorly predicted. The reaching asymmetric sail was more highly cambered than the code zero sail, resulting in poorer flying predictions. A sample of the reaching asymmetric sail shape comparison is shown below, Figure 2.5.1.1.

From Figure 2.5.1.1, two main features can be seen. The first is the reliability of the 'Romer' data. A closer look at the ¾ stripe shows the undulating nature of the predicted shapes, which is likely to be an artefact rather than genuine shape

features. The second feature is the poor prediction of the sail shapes by the FSI solution, "The two shapes are within a plus or minus one inch window of one another except at the trailing edge where there were some sizable computational irregularities". Although this analysis shows the limitations of the work done by Mairs, this work was at the forefront of viscous FSI modelling for yacht sails only a short time ago.

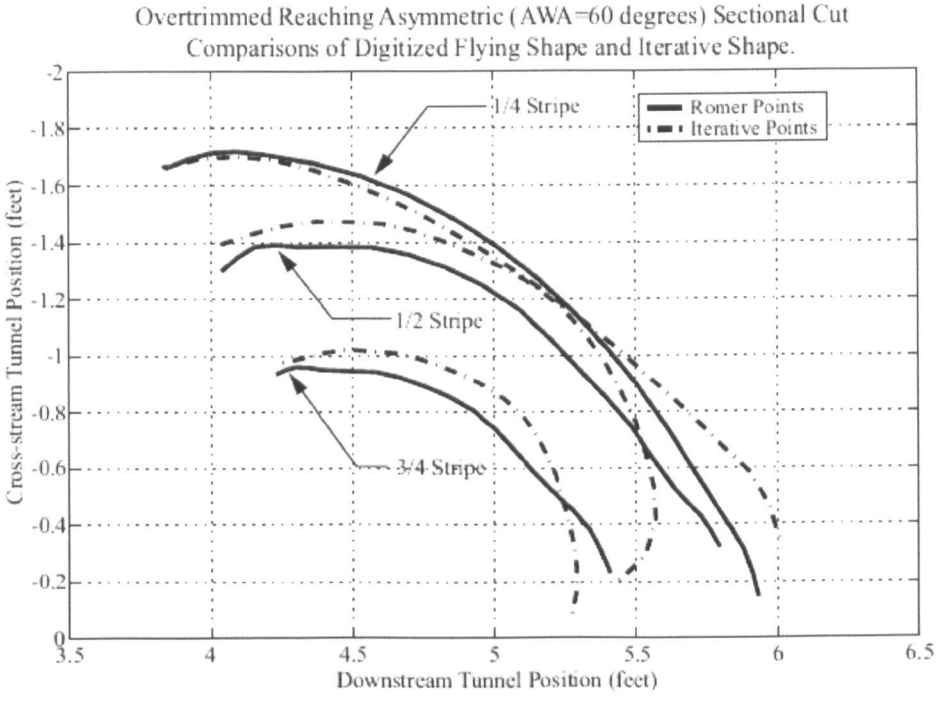

Figure 2.5.1.1 – Extract from Mairs, 2003, demonstrating predictions of flying shapes for a reaching asymmetric spinnaker (AWA=60 degrees)

Renzsch *et al.* (2008) used ANSYS CFX and an orthotropic membrane code for the modelling of downwind spinnakers. This used a finite element code written in Fortran 90 that was integrated into the CFX solver. The method used for the calculation of the deformation of the sail is based on several publications of Arcaro (2011A, 2011B). It assumes homogeneous and either iso- or orthotropic

linear elastic material. The solution was called FlexSail. This solution may appear to be one step closer toward a monolithic solution. However, despite the solution being calculated within the same solver, it is effectively a partitioned method, as the FE solver was called upon request. The $k-\omega$ turbulence model was used. Little discussion of the CFD grid is given. The work is one of the most advanced to date with its main limitation being that of the isotropic nature of the sail. There is also no discussion about the FEA treatment of wrinkling. Their validation of the code reported numerical results with "maximum deviation, normal to the sail, of wind tunnel results and FlexSail predictions are about three percent of the luff length." This equated to errors of approximately 54mm (based upon luff length of 1.8m). An example of the results from their validation exercise is shown in Figure 2.5.1.2.

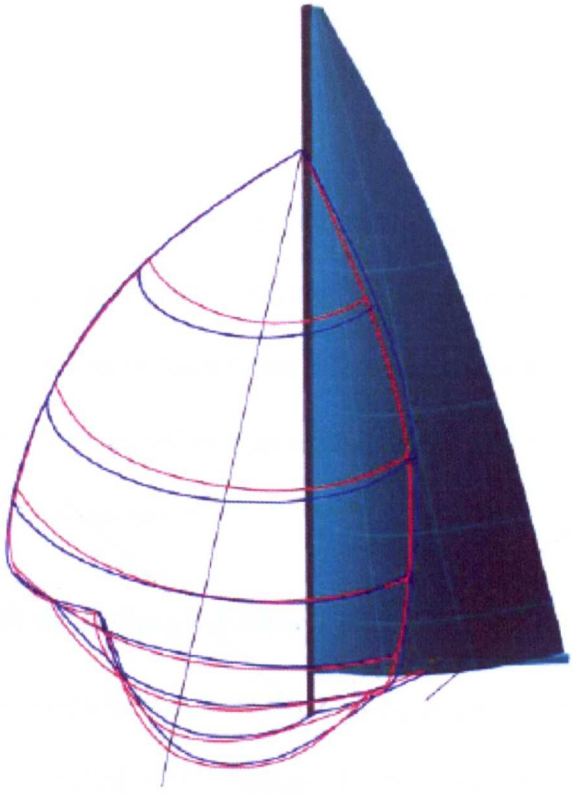

Figure 2.5.1.2 – FSI validation from Renzsch *et al.*, 2008

(Blue = FSI, RED = Wind tunnel)

The introduction of a third piece of software to couple two codes is also possible, and an example of this is MpCCI as utilised by Gluck *et al.* (2003). They utilised MpCCI to couple a finite volume code based on a RANS solver to a FEA code to model a membranous roof structure. The use of such software can simplify the coupling and interpolation process but can be less flexible than bespoke coding. This potentially reduces the amount of coding and development needed to get different pieces of software to communicate. However the coupling is mainly limited to the larger commercial codes.

An alternative to the FSI techniques shown above, where the mesh is moved around by the solver, was proposed by Richter and Horrigan, 2003. They proposed the modelling of downwind sails by using an automated remeshing strategy. Within this process they coupled Fluent and Membrane, with GAMBIT used for the remeshing process. In their process, following the structural solver, the new CFD mesh was created from automated journals (a series of pre recorded commands to recreate a similar state) that recreated a mesh from scratch based upon the '.iges' output from Membrane. The extra man hours potentially needed during a remeshing process rather than a mesh deformation process does not make this approach the most desirable.

2.5.2. FSI modelling – Other Fields

In addition to the developments in the marine industry, other fields have also developed and researched FSI. Some of the fields that have developed FSI include Civil, Mechanical and Aeronautical Engineering, Biomechanics and Motorsport.

Civil engineering has one of the most famous real world FSI cases with the collapse of the Tacoma Narrows bridge in 1940. This was a direct result of the wind blowing around the structure and has helped advance the field of FSI and knowledge about the aeroelastic behaviour of structures.

Gluck *et al.* (2001) state there are two main possibilities for fluid–structure interactions:

1. The wind load on the structure causes a steady deformation state.
2. The fluid flow leads to a time-dependent movement of the structure.

In the case of the Tacoma Narrows bridge the solution was clearly time dependent and this has lead to the development of transient CFD solutions being coupled.

Liaw (2005) used Large Eddy Simulation and Detached Eddy Simulation to model the time dependent flow around bluff bodies which is necessary when trying to predict the aeroelastic response of structures due to vortex shedding.

As mentioned earlier Gluck *et al.* (2001) used an iterative FSI approach for the modelling of a tent roof. The coupling software MpCCI was used to couple a Computational Structural Dynamics (CSD) code to their CFD code, FASTEST-3D. Their coupling schematic is shown below in Figure 2.5.2.1.

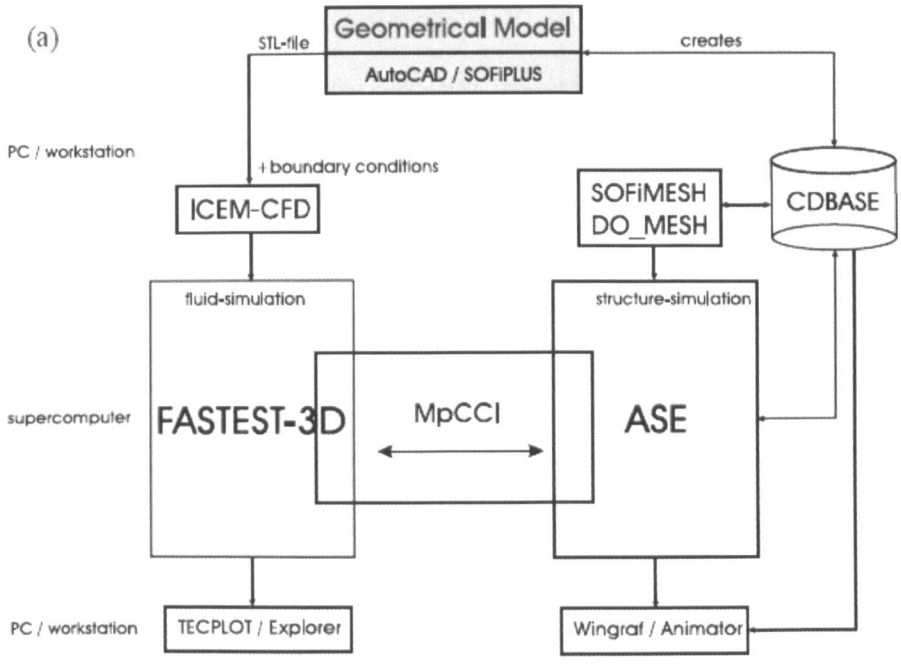

Figure 2.5.2.1 – Gluck *et al.* coupling schematic (Gluck *et al.*, 2001)

Kamakoti and Shyy (2004) discuss various coupling techniques for the aeroelastic applications in particular for modelling wing flutter. Their subdivision of coupling techniques is split into:

1. **Fully coupled model** - *"the governing equations are reformulated by combining fluid and structural equations of motion, which are then solved and integrated in time simultaneously"*
2. **Loosely coupled model – "***the structural and fluid equations are solved using two separate solvers. This can result in two different computational grids"*
3. **Closely coupled model** - **"***the fluid and structure equations are solved separately using different solvers but are coupled into one single module with exchange of information taking place at the interface or the boundary via an interface module thereby making the entire CAE model tightly coupled"*

This shows again the subtleties and complexity in terminology of FSI. The loose and closely coupled models are both partitioned methods with subtle changes between the approaches. Kamakoti and Shyy (2004) recognise the potential accuracy gains of a fully coupled model but this *"has limitations on grid size, and is currently limited to 2-D problems as they can be computationally expensive."* They also highlight the advantage of a partitioned approach, allowing for flexibility in the choice of solver. The added complexity of converting information between the CFD and structural model is also discussed.

The field of biomechanics also has multiple applications for FSI modelling including: Flow through elastic tubes, heart valves and heart chambers (Hron and Madlik, 2007; Bazilevs *et al.*, 2006; Hart *et al.*, 2003). Hron and Madlik (2007) chose an implicit approach, with simplified applications. An example is shown in Figure 2.5.2.2 for flow in a channel representative of a blood vessel. They note the added robustness from a non-partitioned solver but state that it comes with a computational expense.

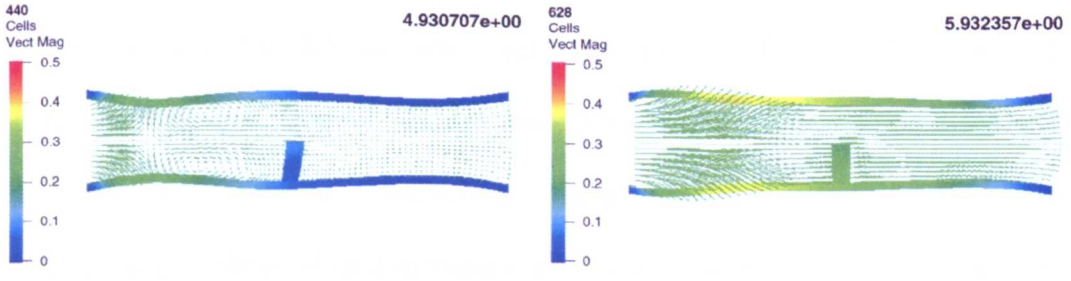

Figure 2.5.2.2 - Fluid flow during one pulse for flow in a channel with constriction (Hron and Madlik, 2007).

2.6. Conclusions and Summary

The advancement of computational power and numerical algorithms has lead to a recent shift towards viscous CFD software for the modelling of sail flows, particularly where areas of separation are involved. The current state of the art for computational fluid modelling for sail flow is that of comprehensive RANS based CFD as documented by Collie although this was in two dimensions (2005). For FSI of sails, the work of Mairs (2003) is one of the most advanced to date, with levels of accuracy exceeding others (+/- 1 inch for a scale model with luff length 1.8m, significantly more at the trailing edge), yet even this has been shown to be far from satisfactory. Within his work he coupled the commercial CFD code STAR-CD to the membrane code TENSION-9. Although STAR-CD is capable of comprehensive modelling of sail flow, Mairs did not model the flow to its full capability, utilising only a basic, and arguably unsuitable, turbulence model and relatively coarse meshes. The sails were also modelled as isotropic materials, which is unrealistic for modern racing sails.

The work of Renzsch *et al.* (2008) is also advanced, with a suitable choice of turbulence model for offwind sails. Again, the main limitation of the research is that of the isotropic nature of the sail representation. There is also no discussion about the FEA treatment of wrinkling. The maximum deviation, normal to the sail, of the experimental and numerical results was estimated at ~3% of the luff length (approximately 54mm for a scale model of luff length 1.8m).

The availability of experimental data for numerical validation is limited. The experimental work on rigid sails by Collie (2005) and Wilkinson (1990) are the

most complete and constitute the best source of data for validation purposes. However, this work is based on rigid sail sections. This will allow for the validation of the CFD but not for a FSI solution. The capturing of flying shape data is very hard to come by at both wind tunnel and full scale sizes. Krebber and Hochkirch did capture flying shape data using cameras mounted on the sailing vessel DYNA (2006). However the unknowns such as the instantaneous wind speeds and direction, in addition to the sea state and the sail design make this scenario unrepeatable numerically.

As discussed in this chapter, from the published literature available, there are significant limitations to the research which has previously been carried out in this field. There is clearly a need to create a FSI solution based upon viscous theory rather than inviscid theory, with an appropriate choice of turbulence model and mesh resolution. The need to model the anisotropic nature of the sails with wrinkling is also important. There is also the need to validate the FSI solution. This is the justification for the aim and objectives set out in Chapter 1.

"To develop a viscous fluid-structure interaction model for the accurate modelling of yacht sails, capable of modelling and predicting performance of upwind and offwind sails."

Chapter 3

Viscous CFD Modelling

3.1. Introduction

Inviscid numerical techniques have been used in the marine industry for many years, even for scenarios with known viscous effects, such as hull design in the field of naval architecture. Historically this was due to the lack of computing power to compute viscous flows. More recently they have been employed because of the overwhelming speed advantage they offer over their viscous counterparts, the rationale being that within the design cycle the use of an efficient inviscid code outweighs the benefits of a more complete but slower viscous code. Their near instantaneous turnaround times also allow for the quick computational retrimming of sails. The disadvantage of these codes is that they are based on inviscid theory and do not include viscous effects such as turbulence and the ability to predict flow separation. However, with the vast increase in computing power and the reduction in price of computing hardware, combined with advances in the ability to tackle turbulent flow phenomena over curved surfaces, comprehensive viscous CFD is becoming accessible and of interest for sail flow applications. The transfer to viscous CFD analysis results in potentially more accurate analysis with the capability to predict complex separated sail flow. The increase in potential accuracy comes at the price of increased computation times and potentially transient results due to the effects of viscosity.

This chapter begins by describing the fundamental differences between inviscid and viscous approaches to sail modelling, giving the advantages and disadvantages of each method. It then details further the viscous approach used throughout the remainder of the thesis.

3.2. Inviscid Codes

Full three dimensional viscous fluid flows can be mathematically described by the Navier-Stokes equations, Section 3.4.2. This section describes the fundamental differences between the various simplifications that can be made to reduce the complexity of the full Navier-Stokes equations.

The exclusion of viscosity from the Navier-Stokes equations leads to the formation of the Euler equations. The further assumption of irrotational flow creates a subset of these equations known as the Potential Flow equations. Figure 3.2.1 shows a simplified flow scenario. For incompressible flows the mass flow rate across AQP equals the mass flow rate ARP.

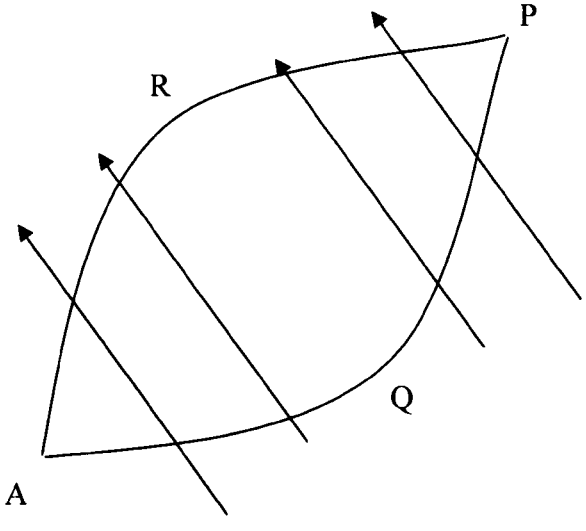

Figure 3.2.1 – Simplified flow scenario to demonstrate potential flow (Adapted from Abbott and Von Doenhoff, 1959)

The flow integral in equation 3.3.1 defines the velocity potential, ϕ (Massey, 1998).

$$-\phi = \int_{A}^{P} q_s ds \qquad \textbf{Equation 3.2.1}$$

Where q_s represents the component of velocity along an element *ds*. *ds* represents the length of an infinitesimal element of the curve joining *A* and *P*. The velocity potential is constant along lines perpendicular to streamlines and is independent of the path between A and *P*. The velocity components can be defined by Equations 3.2.2-3, Abbott and Von Doenhoff, (1959).

$$u = \frac{\partial \phi}{\partial x} \qquad \textbf{Equation 3.2.2}$$

$$v = \frac{\partial \phi}{\partial y} \qquad \textbf{Equation 3.2.3}$$

If these equations for the velocity components, Equations 3.2.1-3.2.2, are substituted into the continuity equation for two dimensional flow, Equation, 3.2.3 is created, Laplace's equation in two dimensions.

$$\frac{\partial u}{\partial x} + \frac{\partial v}{\partial y} = 0 \qquad \textbf{Equation 3.2.3}$$

$$\frac{\partial^2 \phi}{\partial x^2} + \frac{\partial^2 \phi}{\partial y^2} = 0 \qquad \textbf{Equation 3.2.4}$$

These simplifications to the Navier-Stokes Equations are shown in Figure 3.2.2.

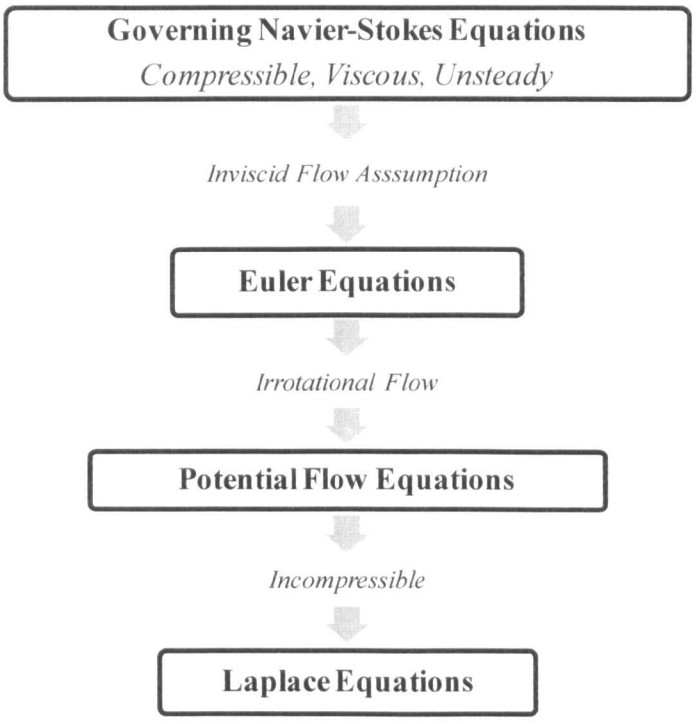

Figure 3.2.2 – Inviscid Simplifications to the Navier-Stokes Equations.

The solving of inviscid flow is often carried out by so called 'panel methods' (e.g. Wilkinson, 1987). These solutions involve the placement of 'panels' on surfaces. Linearised potential flow equations are then solved on the discretised surface panels. The solutions from this type of approach are both robust and efficient. This is the most basic type of inviscid solver but solutions can vary in their complexity (e.g. Fiddes and Gaydon, 1996). Often a high level of user knowledge and experience is required to help make this type of method more accurate. An alternative inviscid solution to panel methods is the Vortex Lattice Method. This approach is an extension of Prandtl's lifting line theory (Prandtl, 1918), where a lattice of horseshoe vortices are created (Falkner, 1943).

Inviscid codes, which neglect viscosity in their computations, are still the primary tool for analysing sails numerically in the marine industry today. Market leaders,

such as North Sails, rely upon the use of inviscid codes to fulfil the vast majority of their modelling needs (North Sails, 2007, *personal communication*). Although there is a great number of variants and codes, the majority of these inviscid methods are based upon potential flow theory and the Laplace equations.

The use of inviscid methods has many advantages over their viscid counterparts, most notably their speed and ease of use. The models can be set up and run very quickly (surface methods), with many automated solutions in existence (Pansail, 2007). The solvers can complete within seconds, giving an approximation of the surface pressures. Their fast turnaround times allow coupled Fluid Structure Interaction (FSI) solutions to be created with almost real time trimming of sails possible (Peter Heppel, 2006, *personal* communication; Jeremy Elliot, 2007, *personal* communication). Currently, this is not achievable with viscous codes, in a similar timescale, and this is unlikely to be possible for many years to come.

The codes can perform acceptably when flow remains attached and the viscous and turbulent effects are minimised. In regions of separation the models struggle and either fail to model it completely or approximations have to be made to make a numerical solution achievable, requiring prior user knowledge and input. The codes do not take account of turbulence and so any real scenario of a turbulent nature cannot be accurately modelled. The viscous codes also provide superior flow visualisation to that of the panel codes, an important tool in aiding understanding of complex flows and improving sail design.

The inviscid nature of panel based methods results in a solution that can give a crude, but near instantaneous flow prediction. If the mast is ignored, the flow during upwind sailing can remain predominantly attached (although regions of separation are always seen, Marchaj (1964)), allowing panel methods to be utilised and reasonably accurate results to be obtained. The limitations of the panel based methods become apparent when a mast is included or the modelling of downwind or offwind sails are attempted. Panel codes also struggle with multiple foils or sails, for example when a mainsail and a foresail are modelled in unison. It is known that the total forces on a rig are not the sum of the individual sails, but a complex scenario in which the two sails interact with each other (Paton and Morvan, 2007C). During these instances the more complete viscous solution can provide much improved accuracy. Inviscid codes also have inherent problems in accurately predicting drag forces.

Inviscid codes are common and there are many different codes available, both commercially and freely available as open source software. Commercial solutions such as Pansail are available cheaply, offering relatively advanced features such as twisted wind profiles (Pansail, 2007). There are also many open source solutions that are typically less advanced and less user friendly, but are free to the user. Xfoil is a common open source code that has been utilised in the aeronautical industry for many years (XFoil, 2007). XFoil was designed to combine the speed of panel methods with viscous modelling of the boundary layer. The Euler equations are discretised on a surface grid and are strongly coupled to a two-equation integral boundary-layer formulation (Drela and Giles, 1987).

3.3. Viscous Codes

Viscous solutions are based upon solving some variation of the Navier-Stokes equations. They can be split into three main categories:

- Reynolds Averaged Navier-Stokes (RANS)
- Large Eddy Simulation (LES)
- Direct Numerical Simulation (DNS)

The breakdown of the instantaneous velocity within the Navier-Stokes equations into a mean and fluctuating component and time averaging, lead to the so-called Reynolds Averaged Navier-Stokes equations, or RANS. These form the basis for all viscous simulations within this thesis. The RANS equations are detailed further in Section 3.4.

LES differs from RANS based solutions as they directly solve the large eddies that are bigger than the filter size, normally a function of the grid size; they typically resolve about 80% of the turbulent energy spectrum. The smaller eddies are then modelled using a sub-grid scale model. The third type of simulation, the simplest conceptually, is DNS. This involves the resolution of the full turbulence spectrum, on very fine grids determined by the Kolmogorov length scale, capable of solving the turbulence on all length and time scales.

Because of the nature of DNS, the computational expense inherent in the process becomes inappropriate for the large domains necessary for sailing applications.

DNS is in fact impractical for most, if not all, engineering problems. In practice LES is also currently too computationally expensive for industrial applications, although LES is progressing fast. This leaves RANS based simulations as the most advanced but practically viable solution.

A hybrid solution of RANS and LES has been developed, Detached Eddy Simulation or DES (Spalart, 2001). This attempts to use the best of both worlds, where RANS simulation is used in the near wall region and far field, and LES away from the wall in the turbulent wake. The model has shown potential in certain circumstances, where LES is too constraining and RANS fails to provide the accuracy. However, this type of turbulence modelling is still relatively in its infancy, and lacks the robust nature of RANS based solutions. It also relies on the same type of turbulence models used in this thesis for the near wall region.

The advantages and disadvantages of viscous codes over their inviscid counterparts are summarised below.

Advantages:

- They include the effects of viscosity.
- They offer the potential to model separation.
- They give a greater level of flow visualisation.
- They offer the potential to model offwind and downwind sails.
- They offer the potential to model multiple sails accurately.
- They give improved modelling of drag forces.
- They offer the potential to capture transient effects.

Disadvantages:

- They are more computationally expensive.
- The meshing procedure can be complex and time consuming.
- They are potentially less robust.

Lack of user knowledge and trust in what is considered as relatively unproven technology within the marine industry, have contributed to the slow spreading of this now maturing technology into the field of sailing. However other industries with similar requirements have accepted it. The performance automotive industry is a particular example where cars can enter production without the need for full scale testing (Robert Lewis, 2008, *personal* correspondence).

3.4. RANS and Turbulence Modelling

3.4.1. The CFD Process

The CFD process can be split into three distinct and separate parts. In modern commercial codes these processes get blurred into one, but should still be distinguished. The three elements are shown below and have to be carried out sequentially:

- Pre-processing (CAD, discretisation or meshing, physics/boundary conditions setup).
- Solving the equations to create the solution.
- Post-processing (data extraction and analysis, image and chart production).

The first part of the pre-processing phase begins within a CAD package or an advanced piece of meshing software. This involves the creation of the sail shapes and/or any aspects of the rig. Following this, the meshing process can begin. Initially this entails the creation of the geometry in and around the region of interest. The enclosing volume around the region of interest is called the domain. The next phase requires the splitting of the domain into a series of smaller cells or volumes.

Mesh generation is a time consuming process and is fundamental in determining the accuracy of the end solution. "In general, the larger the number of cells, the better the solution accuracy" (Versteeg and Malalasekera, 2007). However, in practice, the number of cells is limited by both the computational resources and the time available to solve the solution. For example, a workstation, with a specified amount of RAM, has a maximum capacity mesh that can be created upon it. Often it is necessary to work backwards from the total mesh capacity, to determine where the mesh needs to be refined in order to generate a solution as accurately as possible. If the maximum mesh size is not capable of accurately modelling the flow around the geometry and domain, this would dictate that a more simplified case must be considered.

It has been suggested that 50% of the CFD process within industry can be spent in the pre-processing phase (Versteeg and Malalasekera, 2007), particularly when complex geometries and CAD are involved. A great deal of judgement is needed to create a mesh that is both suitable and adequate for the given situation. Often

the mesh has to be refined around regions of interest or those with the largest gradients (McBeath, 2006).

Following this the physical and mathematical properties required to be modelled need to be specified, e.g. fluid properties, equations and models to be solved, boundary conditions, solver options, output storage etc.

The solving stage then follows the pre-processing stage. This involves the solving of the algebraic equations in an iterative manner throughout the domain.

Following the solution of the algebraic equations the final stage is post-processing. This involves the extraction of data from the solver and visualising this data in some form, whether it is total forces, contour plots or vector analysis. This concludes the brief summary of the CFD process, comprising of pre-processing, solving and post-processing.

3.4.2. Governing Equations of Fluid Flow

The governing equations of fluid flow represent mathematical statements of the conservation laws (Versteeg and Malalasekera, 2007):

- The conservation of mass.
- The rate of change of momentum equals the sum of the forces on a fluid particle (Newton's 2nd law).
- The conservation of energy.

The three dimensional mass conservation or continuity equation for a compressible fluid is given in Equation 3.4.2.1. (Versteeg and Malalasekera, *2007*),

$$\frac{\partial \rho}{\partial t} + div(\rho \mathbf{u}) = 0 \qquad \textbf{Equation 3.4.2.1}$$

where ρ is the density and **u** is the velocity vector.

The momentum equations are found by setting the rate of change of momentum of a fluid particle equal to the total force in a component direction due to surface stresses, plus the rate of increase in momentum due to sources, Equations 3.4.2.2-4 (Versteeg and Malalasekera, *2007*),

$$\rho \frac{Du}{Dt} = \frac{\partial(-\rho + \tau_{xx})}{\partial x} + \frac{\partial \tau_{yx}}{\partial y} + \frac{\partial \tau_{zx}}{\partial z} + S_{Mx} \qquad \textbf{Equation 3.4.2.2}$$

$$\rho \frac{Dv}{Dt} = \frac{\partial \tau_{xy}}{\partial x} + \frac{\partial(-\rho + \tau_{yy})}{\partial y} + \frac{\partial \tau_{zy}}{\partial z} + S_{My} \qquad \textbf{Equation 3.4.2.3}$$

$$\rho \frac{Dw}{Dt} = \frac{\partial \tau_{xz}}{\partial x} + \frac{\partial \tau_{yz}}{\partial y} + \frac{\partial(-\rho + \tau_{zz})}{\partial z} + S_{Mz} \qquad \textbf{Equation 3.4.2.4}$$

where τ denotes viscous stresses with suffix notation and S_M represents a momentum source per unit volume per unit time.

The third and final governing equation is the conservation of energy equation Equation 3.4.2.5 (Versteeg and Malalasekera, 2007),

$$\rho\frac{DE}{Dt} = -div(p\mathbf{u}) + \left[\begin{array}{l} \frac{\partial(u\tau_{xx})}{\partial x} + \frac{\partial(u\tau_{yx})}{\partial y} + \frac{\partial(u\tau_{zx})}{\partial z} + \frac{\partial(v\tau_{xy})}{\partial x} + \frac{\partial(v\tau_{yy})}{\partial y} + \\ \frac{\partial(v\tau_{zy})}{\partial z} + \frac{\partial(w\tau_{xz})}{\partial x} + \frac{\partial(w\tau_{yz})}{\partial y} + \frac{\partial(w\tau_{zz})}{\partial z} \end{array}\right] + div(k\ grad\ T) + S_E$$

Equation 3.4.2.5

where E is the specific energy of a fluid, k is the materials conductivity, T is the temperature and S_E is the source of energy per unit volume per unit time.

In a Newtonian fluid the viscous stresses are proportional to the rates of deformation. The viscous stress components are shown below in Equations 3.4.2.6-11 (Versteeg and Malalasekera, 2007),

$$\tau_{xx} = 2\mu\frac{\partial u}{\partial x} + \lambda\, div\,\mathbf{u} \qquad \textbf{Equation 3.4.2.6}$$

$$\tau_{yy=} 2\mu\frac{\partial v}{\partial y} + \lambda\, div\,\mathbf{u} \qquad \textbf{Equation 3.4.2.7}$$

$$\tau_{zz=} 2\mu\frac{\partial w}{\partial z} + \lambda\, div\,\mathbf{u} \qquad \textbf{Equation 3.4.2.8}$$

$$\tau_{xy} = \tau_{yx} = \mu\left(\frac{\partial u}{\partial y} + \frac{\partial v}{\partial x}\right) \qquad \textbf{Equation 3.4.2.9}$$

$$\tau_{xz} = \tau_{zx} = \mu\left(\frac{\partial u}{\partial z} + \frac{\partial w}{\partial x}\right) \qquad \textbf{Equation 3.4.2.10}$$

$$\tau_{yz} = \tau_{zy} = \mu\left(\frac{\partial v}{\partial z} + \frac{\partial w}{\partial y}\right) \qquad \textbf{Equation 3.4.2.11}$$

where μ is the dynamic viscosity and λ is the viscosity.

The substitution of these viscous stresses into Equations 3.4.2.2-4 leads to the Navier-Stokes equations. Rearranged this gives the equations shown below, Equations 3.4.2.12-3.4.2.14.

$$\rho\frac{Du}{Dt} = -\frac{\partial p}{\partial x} + div(\mu\ grad\ u) + S_{Mx} \qquad \textbf{Equation 3.4.2.12}$$

$$\rho\frac{Dv}{Dt} = -\frac{\partial p}{\partial y} + div(\mu\ grad\ v) + S_{My} \qquad \textbf{Equation 3.4.2.13}$$

$$\rho\frac{Dw}{Dt} = -\frac{\partial p}{\partial z} + div(\mu\ grad\ w) + S_{Mz} \qquad \textbf{Equation 3.4.2.14}$$

3.4.3. Reynolds Averaged Navier-Stokes Equations

Equations 3.4.1-3 show the incompressible form of the Navier-Stokes equations (source terms also removed for simplicity), where **u** is the velocity vector, comprising of Cartesian components u, v and w (Versteeg and Malalasekera, 2007).

$$\frac{\partial u}{\partial t} + div(u\mathbf{u}) = -\frac{1}{\rho}\frac{\partial p}{\partial x} + \nu\,\mathrm{div}(grad(u)) \qquad \textbf{Equation 3.4.3.1}$$

$$\frac{\partial v}{\partial t} + div(v\mathbf{u}) = -\frac{1}{\rho}\frac{\partial p}{\partial y} + \nu\,\mathrm{div}(grad(v)) \qquad \textbf{Equation 3.4.3.2}$$

$$\frac{\partial w}{\partial t} + div(w\mathbf{u}) = -\frac{1}{\rho}\frac{\partial p}{\partial z} + \nu\,\mathrm{div}(grad(w)) \qquad \textbf{Equation 3.4.3.3}$$

A subset of these equations is formed when the instantaneous components are broken into a mean and fluctuating component.

$\mathbf{u} = \mathbf{U} + \mathbf{u}'$ $\quad u = U + u'$ $\quad v = V + v'$ $\quad w = W + w'$ $\quad p = P + p'$

When the velocity vector **u** in Equations3.4.3.1-3 is replaced by it's mean and fluctuating component, and time averaging is taken, the 3 dimensional Reynolds Averaged Navier-Stokes (RANS) equations are formed, detailed below (Versteeg and Malalasekera, 2007),

$$\frac{\partial U}{\partial t} + div(U\mathbf{U}) = -\frac{1}{\rho}\frac{\partial P}{\partial x} + vdiv(grad(U)) + \frac{1}{\rho}\left[\frac{\partial(-\rho\overline{u'u'})}{\partial x} + \frac{\partial(-\rho\overline{u'v'})}{\partial y} + \frac{\partial(-\rho\overline{u'w'})}{\partial z}\right]$$

Equation 3.4.3.4

$$\frac{\partial V}{\partial t} + div(V\mathbf{U}) = -\frac{1}{\rho}\frac{\partial P}{\partial y} + vdiv(grad(V)) + \frac{1}{\rho}\left[\frac{\partial(-\rho\overline{u'v'})}{\partial x} + \frac{\partial(-\rho\overline{v'v'})}{\partial y} + \frac{\partial(-\rho\overline{v'w'})}{\partial z}\right]$$

Equation 3.4.3.5

$$\frac{\partial W}{\partial t} + div(W\mathbf{U}) = -\frac{1}{\rho}\frac{\partial P}{\partial z} + vdiv(grad(W)) + \frac{1}{\rho}\left[\frac{\partial(-\rho\overline{u'w'})}{\partial x} + \frac{\partial(-\rho\overline{v'w'})}{\partial y} + \frac{\partial(-\rho\overline{w'w'})}{\partial z}\right]$$

Equation 3.4.3.6

where ν is the kinematic viscosity (Massey, 1998).

$$\upsilon = \frac{\mu}{\rho}$$ **Equation 3.4.3.7**

This process results in the creation of 6 extra stress terms:

Three normal stresses:

$$\tau_{xx} = -\rho\overline{u'u'} \quad \tau_{yy} = -\rho\overline{v'v'} \quad \tau_{zz} = -\rho\overline{w'w'}$$ **Equation 3.4.3.8**

And three shear stresses:

$$\tau_{xy} = -\rho\overline{u'v'} \quad \tau_{xz} = -\rho\overline{u'w'} \quad \tau_{yz} = -\rho\overline{v'w'}$$ **Equation 3.4.3.9**

These 6 turbulent stresses are termed the Reynolds stresses.

In order to solve the RANS equations shown above, it is necessary to close the system of equations, which can be done by introducing additional transport equations or by a simplified algebraic relationship. The number of additional transport equations helps to group the methods. e.g. a system of equations that introduces two additional transport equations are known as two equation models. Generally there are 4 families of RANS based models; zero equation, one equation, two equation and 6 equation (Reynolds stress) models. As the number of additional equations increases, the computational expense of the model also increases as more equations are solved and more variables stored.

3.4.4. Eddy Viscosity

In 1877, Boussinesq proposed that the Reynolds stresses, introduced in Section 3.4.3, were proportional to mean rates of deformation (Versteeg and Malalasekera, 2007),

$$\tau_{ij} = -\rho\overline{u_i'u_j'} = \mu_t\left(\frac{\partial U_i}{\partial x_j} + \frac{\partial U_j}{\partial x_i}\right) - \frac{2}{3}\rho k\delta_{ij} \qquad \textbf{Equation 3.4.4.1}$$

where k is the turbulent kinetic energy per unit mass, given by Equation 3.4.4.2.

$$k = \frac{1}{2}\left(\overline{u'^2} + \overline{v'^2} + \overline{w'^2}\right) \qquad \textbf{Equation 3.4.4.2}$$

However to solve for the Reynolds stresses a value for the new term, turbulence eddy viscosity, μ_t must be found. The assumption made above is that the turbulence is isotropic, i.e. it is the same in all directions. Turbulence models based upon this assumption will be the main focus of this thesis.

3.4.5. Two Equation Models

To provide a solution to the system of equations, a value for eddy viscosity is required for the Bousinnesq approximation to be applied. Two equation models use two added transport equations to solve for quantities used to define μ_t. The most common of the two equation models is the $k-\varepsilon$ model (Launder and Spalding, 1974). Two equation models are used throughout this thesis.

3.4.6. The $k-\varepsilon$ Model

To close the system of equations and provide a value for eddy viscosity, the $k-\varepsilon$ model introduces two new variables k and ε. k represents the turbulent kinetic energy and ε represents the dissipation of k. These two together can specify the

eddy viscosity, μ_t as shown below in equation 3.4.6.1 (Versteeg and Malalasekera, 2007).

$$\mu_t = \rho C_\mu \frac{k^2}{\varepsilon}$$

Equation. 3.4.6.1

The transport equations for the standard $k-\varepsilon$ are given below (Launder and Spalding, 1974):

$$\frac{\partial(\rho k)}{\partial t} + div(\rho k U) = div\left[\frac{\mu_t}{\sigma_k} grad(k)\right] + 2\mu_t S_{ij}.S_{ij} - \rho\varepsilon$$

Equation 3.4.6.2

$$\frac{\partial(\rho\varepsilon)}{\partial t} + div(\rho\varepsilon U) = div\left[\frac{\mu_t}{\sigma_k} grad(\varepsilon)\right] + C_{1\varepsilon}\frac{\varepsilon}{k}2\mu_t S_{ij}.S_{ij} - C_{2\varepsilon}\rho\frac{\varepsilon^2}{k}$$

Equation 3.4.6.3

The two terms on the left of these equations relate to the rate of change of k or ε and the transport of k or ε by convection. The first term on the right hand side represents the transport of k or ε by diffusion. The middle term represents the production of k or ε and the final term is the destruction of k or ε. Within the two additional transport equations are 5 adjustable constants, with typical values shown below (Versteeg and Malalasekera, 2007):

$$C_\mu = 0.009$$
$$\sigma_k = 1.00$$
$$\sigma_\varepsilon = 1.30$$
$$C_{1\varepsilon} = 1.44$$
$$C_{2\varepsilon} = 1.92$$

The $k-\varepsilon$ model is one of the most widely used models within industry, partly due to its robust nature. The model can also be used with wall functions, described later, allowing a y^+ between 30 and 500. y^+ is the non dimensional

distance to the first cell away from a wall, and determines the level of mesh refinement adjacent to walls.

$$y^+ = \frac{y}{\nu}\sqrt{\frac{\tau_w}{\rho}} \qquad \textbf{Equation 3.4.6.4}$$

Where y is the distance to the first cell and τ_w is the wall shear stress.

The $k-\varepsilon$ model does however have limitations which are well known and documented due to its widespread use (Rumsey and Gatski, 2001; Versteeg and Malalasekera, 2007). The first of these is the isotropic nature of the model due to the Boussinesq approximation. This results in poor performance of swirling flows. The model is also renowned for over predicting the eddy viscosity in the outer regions of the boundary layer (Collie, 2005). As a result the model can lead to delayed separation in adverse pressure gradients, resulting in the over performance prediction of sails.

3.4.7. The $k-\omega$ Model

The $k-\omega$ model belongs to the same family of two equation models as the $k-\varepsilon$. The most popular $k-\omega$ model is that of Wilcox (1998). Within the $k-\omega$ model, k is combined with a new transport equation for ω. ω represents the rate of dissipation of turbulent kinetic energy. The eddy viscosity is given by equation 3.4.7.1 (Versteeg and Malalasekera, 2007):

$$\mu_t = \rho\frac{k}{\omega} \qquad \textbf{Equation 3.4.7.1}$$

The transport equations for the $k-\omega$ is given below:

$$\frac{\partial(\rho k)}{\partial t} + div(\rho k \mathbf{U}) = div\left[\left(\mu + \frac{\mu_t}{\sigma_k}\right) grad(k)\right] + P_k - \beta^* \rho k \omega \quad \textbf{Equation 3.4.7.2}$$

$$\frac{\partial(\rho \omega)}{\partial t} + div(\rho \omega \mathbf{U}) = div\left[\left(\mu + \frac{\mu_t}{\sigma_k}\right) grad(\omega)\right] + \gamma_1 \left(2\rho S_{ij}.S_{ij} - \frac{2}{3}\rho\omega \frac{\partial U_i}{\partial x_j}\delta_{ij}\right) - \beta_1 \rho \omega^2$$

Equation 3.4.7.3

Where:

$$P_k = \left(2\mu_t S_{ij}.S_{ij} - \frac{2}{3}\rho k \frac{\partial U_i}{\partial x_j}\delta_{ij}\right) \quad \textbf{Equation 3.4.7.4}$$

With typical coefficients (Versteeg and Malalasekera, 2007):

$$\sigma_k = 2.00$$
$$\sigma_\omega = 2.00$$
$$\gamma_1 = 0.553$$
$$\beta_1 = 0.075$$
$$\beta^* = 0.09$$

The main advantage of the $k-\omega$ model over the $k-\varepsilon$ model is the ability of the $k-\omega$ model to be integrated over the boundary layer. This has the advantage of providing improved accuracy in the near wall region. To utilise this advantage grid refinement is necessary to remove the dependency on wall functions. A downfall of the $k-\omega$ model is the problematic treatment of ω in the freestream. In the freestream both k and ω tend towards zero (Versteeg and Malalasekera, 2007). As shown earlier the determination of eddy viscosity is dependent upon ω. Therefore as ω tends towards zero, eddy viscosity tends towards infinity, so a non zero value of ω is specified. The dependency of the results upon the chosen value for ω is problematic (Menter, 2003).

3.4.8. The SST Model

The SST model was developed by Menter (1993) who recognised the complementary features of both the $k-\omega$ and $k-\varepsilon$ models (Versteeg and Malalasekera, 2007). Menter realised the $k-\omega$ model was far superior to the $k-\varepsilon$ model in the near wall region, whilst its free stream performance made it unreliable, despite attempts at limiting variable values. Menter therefore suggested a blending of the two models, the $k-\omega$ in the near wall region, whilst the $k-\varepsilon$ would be used in the free stream. The details of the blending functions used to move between the $k-\varepsilon$ and $k-\omega$ zones will not be detailed here but can be found in Menter *et al.*, 2003.

The SST model has now reached a level of robustness similar to that of the $k-\varepsilon$ model. The inclusion of the $k-\omega$ in the near wall regions has also vastly improved the performance of the model (Menter *et al.*, 2003). The model provides a robust and potentially suitable model for both upwind and offwind sailing applications (Collie *et al.*, 2001).

The potential improvement in accuracy in the computation of the near wall region results from the integration to the wall across the boundary layer thanks to the inclusion of the $k-\omega$ model. The laminar subregion of the boundary layer only extends between a y^+ of 0 and 5, hence the desire to place a control volume within this laminar region, resulting in a target y^+ between 2 and 3. Menter *et al.* state the impracticality of a y^+ of less than two for industrial applications (2003). Modern applications of this model now have automatic wall function switching when required, to allow for larger y^+ values if deemed absolutely necessary.

3.4.9. Wall Functions

Wall functions are used to estimate the flow in the regions adjacent to the wall. To resolve the flow right down to the laminar region can be computationally expensive as already discussed. An alternative to resolving through the boundary layer is to use wall functions. Wall functions use empirical formulas that impose suitable conditions near to the wall, alleviating the need to resolve the boundary layer, saving computational resources (ANSYS CFX, 2008).

The wall function used in ANSYS CFX is based upon the logarithmic relation defined by Launder and Spalding, 1974. This approach uses an empirical formula to bridge the viscous sublayer. A logarithmic profile is used within ANSYS CFX detailed in Equation 3.4.9.1 (ANSYS CFX, 2008).

$$u^+ = \frac{1}{\kappa}\ln(y^+) + C \qquad \textbf{Equation 3.4.9.1}$$

Where u^+ is the near wall velocity, κ is the von Karman constant, y^+ is the dimensionless distance from the wall as defined in Equation 3.4.6.4 and C is a log layer constant (C=5 for a smooth wall).

Figure 3.4.9.1 below, demonstrates the power of automatic wall functions, with the application of three different grids to the same scenario having y^+ values of approximately 0.2, 9 and 100 (Menter *et al.*, 2003). The simulations were all carried out with ANSYS CFX-5. This shows that although the strict use of the model requires very small y^+ values, the use of automatic wall functions within the model allows for significantly larger y^+ values to be used, without unduly affecting the accuracy. It should be noted that the case shown in the figure below

(Menter *et al.*, 2003) is for flow adjacent to a flat plate, which is dissimilar to flow around sails where adverse pressure gradients feature heavily. However it does show the potential for automatic wall functions to aid the modelling of cases where strict y^+ values of between 2 to 3 are unrealistic, due to meshing limits imposed by computer resources.

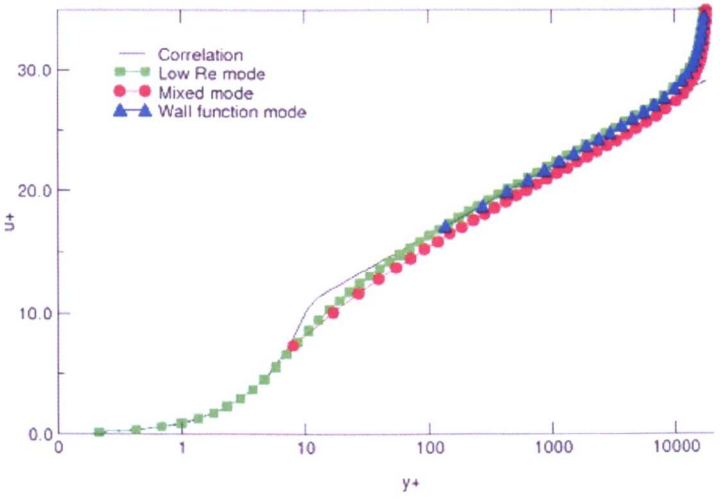

Figure 3.4.9.1. – Velocity profiles for three different near wall mesh resolutions using the automatic wall treatment of CFX-5 (Menter *et al.*, 2003) (Low Re mode y^+=0.2, Mixed mode y^+=9, Wall function mode y^+=100)

3.5. The Finite Volume Method

There are three main types of numerical discretisation techniques: Finite Volume Method, Finite Element Method and Finite Difference Method. By far the most common approach within commercially available CFD is the Finite Volume Method. The Finite Volume Method is based around the defining equations being written in a conservation law format by integration over a volume. The defining domain is split up into a series of smaller volumes, known as elements or cells.

The finite volume method ensures conservation of relevant properties (ϕ) for each cell. This states that the rate of change of ϕ is equal to the increase/decrease in ϕ due to convection, plus the rate of increase/decrease in ϕ due to diffusion and the

rate of increase or decrease of ϕ within the control volume (Versteeg and Malalasekera, 2007).

In Figure 3.5.1 elements can be seen with nodes at each corner. It is at each of these nodes that data is stored for each finite volume. Surrounding each node are a set of surfaces that define the control volume, over which the discrete variable ϕ is integrated. The control volume is shown by the shaded area in Figure 3.5.1. The node can also be seen at the control volume centre.

The conservation laws can then be applied to each finite volume. This forms the basic principles of the finite volume method. Figure 3.5.1 is shown to help clarify the process.

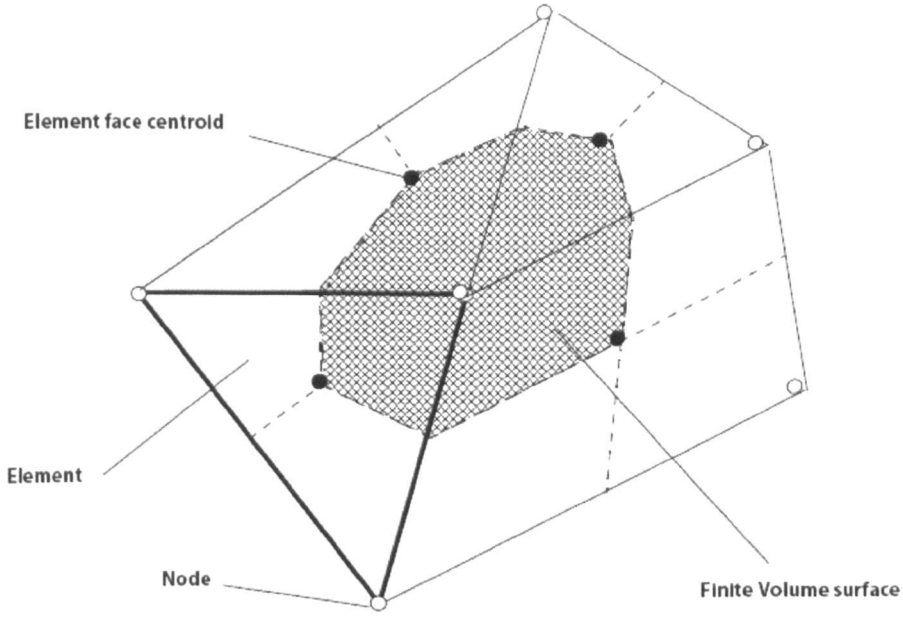

Figure 3.5.1 – Finite volume method (ANSYS CFX, 2008)

The transfer of ϕ into and out of a volume is through the volume surfaces (in 3D) and is termed flux. In addition to the transfer of flux into or out of a cell there is the creation or removal of ϕ within the volume itself. A key consideration for the

finite volume scheme is how to calculate the fluxes through the finite volume perimeters, as data is only stored at the nodes. An interpolation scheme is used to do this.

ANSYS CFX 10 was used for all computational simulations within this thesis (ANSYS CFX, 2008). ANSYS CFX 10 is an example of a three dimensional finite volume method solver. Various forms of interpolation scheme are available within ANSYS CFX, of varying complexities, robustness and accuracy.

The most basic interpolation scheme is the Upwind scheme, where the variable at the integration point is taken as the value at the upstream node,

$$\phi_{ip} = \phi_{up} \qquad \textbf{Equation 3.5.1}$$

where ϕ_{up} is the value at the upwind node and ϕ_{ip} is the value at the integration point.

ANSYS CFX also has higher order schemes which take the form of Equation 3.5.2 (ANSYS CFX, 2008),

$$\phi_{ip} = \phi_{up} + \beta \nabla \phi . \Delta r \qquad \textbf{Equation 3.5.2}$$

where ϕ_{up} is the value at the upwind node, $\nabla \phi$ is the nodal gradient of the upwind node and Δr is the vector from the upwind node to the integration point. β is a coefficient that can vary between 0 and 1, allowing for changes in the scheme to be made. A value of 0 changes it to the upwind scheme described earlier. A value of 1 changes it to a second order scheme. A blend of the two extremes can also be used. A value β can be set explicitly or computed by the software as a

function of local geometry and variable gradient. In this case, the high resolution scheme computes β, attempting to keep it as close to 1 as possible, without violating boundedness principles (ANSYS CFX, 2008). Throughout this thesis the ANSYS CFX high resolution scheme is used.

3.6. Summary

This chapter has provided an overview of viscous CFD modelling techniques available and explained the background behind the techniques used within this thesis and the rationale behind their selection for this work. The chapter has shown the fundamental principles that allow viscous solutions to potentially outperform inviscid solutions for sail flow applications.

Chapter 4

Application of Viscous CFD to Sailing Scenarios

The following chapter demonstrates the capabilities of viscous CFD and its potential performance advantages over inviscid codes. Two cases are used to demonstrate the potential of viscous CFD with comparison against experimental testing and against other computational analysis.

The final sections of the chapter use viscous CFD to analyse two dimensional rigs, providing insight into the performance of various rigs. Viscous CFD is also used to analyse the effects of masts and the potential performance gains mast rotation could yield.

4.1. Viscous CFD Methodology

The Finite Volume Method solver ANSYS CFX 10.0 (ANSYS CFX. 2008) was used for all computational simulations within this research. The meshing process was carried out using ANSYS GAMBIT. The meshing procedure is highlighted in the following section along with the typical boundary conditions used within this chapter.

The majority of runs were carried out on a multiprocessor Linux cluster. The number of processors varied from 1 to 12, depending on the size of the meshes used.

4.1.1. Meshing

Meshing domains for aerodynamic sailing applications is arguably one of the most important tasks in the model set up and can be complex when attempting to comprehensively model yacht sails. Several features of the sails make their meshing particularly complicated:

- Sail shape.
- Sail thickness.
- Masts.
- Multiple sails.
- High Reynolds numbers.

The shape of sails is an obvious complex feature of sail modelling, as sails are not regular uniform shapes, but complex curved surfaces, with varying rates of change of curvature and arc length. Their physical characteristic of being thin also creates an issue for CFD modelling, as the two sets of cells either side of the sail are adjacent, but flow cannot be allowed to transfer between them. The addition of a mast, or multiple sails, greatly increases the complexity of the meshing procedure, due to the irregular shapes and close proximity of surfaces. The final complexity is the relatively high Reynolds numbers that sails operate in. This results in the need for refined boundary layer elements in the near wall regions to maximise the potential of the turbulence model.

The accurate prediction of forces and flow around sails is strongly dependent on the quality and detail of the flow calculations in the close proximity to the sail surfaces. This results in the need for highly refined meshes in the vicinity of a sail's surface, where the velocity gradients are greatest.

All simulations within this thesis utilise boundary inflation elements or 'layers' close to the sail surfaces to ensure that the y^+ requirements of the turbulence model is met. These layers are hex based cells, which allow for careful control of the mesh quality and first cell height away from the wall. Throughout this chapter target first cell heights with a y^+ of 3 were achieved, placing the first control volume within the laminar subregion. An example mesh for a typical mainsail and mast section is shown in Figure 4.1.1.1. Within this figure quadrilateral cells are used away from all surfaces of interest. These high quality quadrilateral cells ensure the boundary layers can be suitably captured. In this example the mast and sails were meshed with boundary inflation layers away from the sail surface to capture the near wall velocity gradients.

Figure 4.1.1.2 shows a typical mesh used for the slot effect study in Section 4.5. Here the use of boundary inflation layers combined with proximity size functions are used to control the mesh away from the sail and mast surfaces. Boundary inflation elements are used to capture the boundary layer flows whilst the proximity size functions control the increase in cell size with increasing distance from the sail surfaces. This allows varying mesh sizes to blend seamlessly together, as shown in Figure 4.1.1.2.

A common problem with sail flow modelling is the desire to model geometry at varying angles of attack. One approach to solving this problem is to use a turntable approach, shown in Figure 4.1.1.3.

In this approach, the sail and mast section is placed in the central circular section, whilst outside of the central section is a fixed outer region with the central section removed. The two regions are connected with a non conformal interface within the ANSYS CFX pre processor. This set up allows the sails to be rotated to varying angles of attack within the pre-processor, representing different scenarios and allowing different simulations to be carried out without the need for remeshing. This approach is only suitable for cases that have similar flow characteristics, e.g. a small change in apparent wind angle.

For larger changes, new meshes are needed to cater for the varying flow features. When large 3D multiple sail models are created, the meshing procedure can be computationally expensive, which can be minimised with this approach (Morvan *et al.*, 2007). Care must be taken to ensure that the wake regions remain appropriate, as any wake refinement regions are rotated away from their original location.

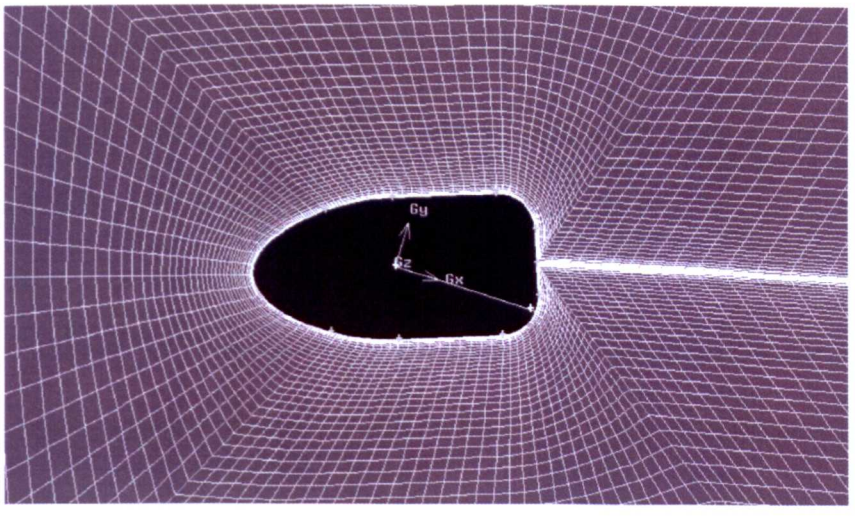

Figure 4.1.1.1 – Boundary inflation elements or 'layers' surrounding a mast.

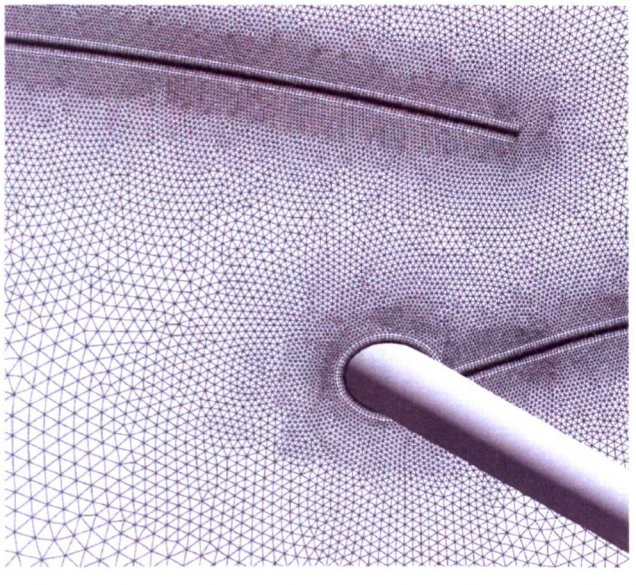

Figure 4.1.1.2 – Example mesh used around mast and sails, demonstrating the use of proximity size functions.

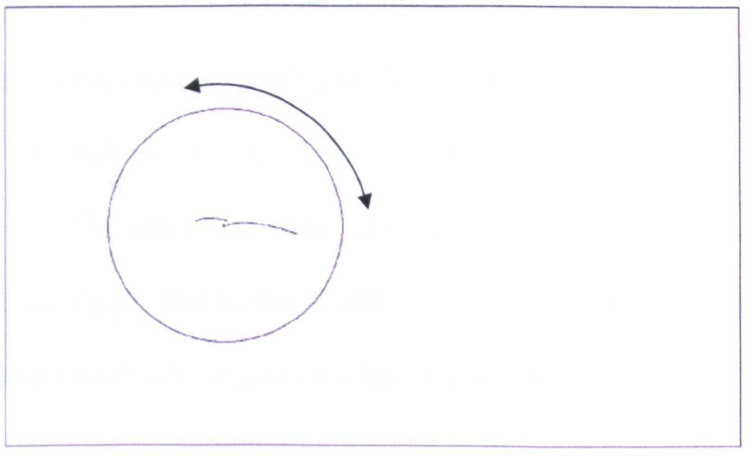

Figure 4.1.1.3 – Example domain used around mast and sails, showing central circular region used in a 'turntable' approach.

4.1.2. Boundary Conditions and Problem Set Up

The boundary conditions for all the analyses within this chapter are identical. An inlet condition is set defining the velocity vectors at the inlet face. The outlet is defined as a pressure outlet allowing flow through the face, where the flow direction is confined to the normal to the outlet surface, whilst ensuring that the face averaged pressure is equal to a set value. The majority of boundary walls are defined as free-slip walls. For wind tunnel testing, the tunnel's four walls are all modelled as free-slip smooth walls unless otherwise stated. The sail and mast surfaces were set as non-slip walls. Most simulations within this chapter were analysed using an unsteady approach. At larger angles of attack, sail flow can become time dependant, as a result unsteady simulations were used with a time averaging of coefficients for comparison. Further detailing on the time averaging of coefficients is given in Section 4.2. A high resolution second order advection scheme was used throughout this chapter.

4.1.3. Solution Convergence and Discretisation

The convergence criterion of all simulations was based upon examination of the RMS residuals, maximum residuals and the forces upon sails. A maximum RMS of 10^{-4} was obtained for all runs but in most cases considerably lower residuals were achieved. The maximum RMS was checked to ensure there were no 'hot spots' in the solutions. The forces of interest on the sails and mast, e.g. drag and lift, were also monitored to ensure they had settled and stabilised.

For all unsteady simulations, a timestep was chosen to allow convergence within a maximum of 4 iterations per timestep, well within the predetermined maximum number of iterations per timestep set at 10. Typical unsteady timesteps were in the region of 0.001s, small enough to ensure that transient effects are captured and ensuring convergence within a timestep (see Figure 4.2.6). The stabilisation of the forces was monitored over several periods to determine that an averaged ("steady") value had been reached.

4.2. Arc Validation Case

Before real sails can be modelled computationally, it is important firstly to have validated the CFD process and the choice of turbulence model. Real sailing shapes with suitable validation data are hard to come by, as there are many variables associated with flying shapes. Sail shapes in isolation are obtainable (Clauss and Heisen, 2005), as discussed in Chapter 2, as are the forces upon rigs or sheets (Hansen *et al.*, 2002). It is also possible to obtain wind and boat data sets, although these are often only at specific heights and time averaged. The sail designs and mould shapes can also be obtained. However to find data with all of the above aspects available, from a trustworthy and accurate source, is extremely difficult.

Clauss and Heissen (2002) and Hansen, Jackson and Hochkirch (2005) captured data from real sailing conditions. However, with this type of test, just about every variable can be questioned. For example, the wind is normally measured from a cup anemometer at the top of the rig, which pitches with the boat, creating induced wind. The cup also takes time to adjust to the wind speed,

curtailing the measurements and reducing the values of peaks and troughs. The sails are often also a relatively unknown entity. For these reasons, full scale results in real sail conditions will not be used for validation purposes.

In this section and Section 4.3, two simplified and idealised validation exercises are considered. Although these are simplifications of real sails and rigs, the controlled manner in which the data was collected makes them appropriate validation exercises. The first validation case is that of a simplified two dimensional arc created by Collie, 2005, Figure 4.2.1. Work done by Collie *et al.* focussed upon the two dimensional analysis of flow around downwind sails (2004). When a downwind spinnaker is cut laterally through the sail, the shape revealed is an arc. Although this may not be entirely circular in cross section it is a reasonable approximation. The major advantage of choosing a circular arc is its repeatability without the use of complex geometry files. Collie *et al.* provide both computational and experimental results for comparison (Collie *et al.*, 2005)

Collie chose a circular arc section with 24.7% camber, a radius of 200mm and a chord length of 319mm. This arc was tested both numerically and experimentally in a wind tunnel. The wind tunnel test section was 768mm x 615mm. An inlet velocity of $25ms^{-1}$ was chosen, corresponding to a Reynolds number of $5.25x10^5$. The circular arc was then rotated to varying angles of attack, between 5 and 30 degrees from the horizontal, at 2.5 or 5 degree intervals. The angle of attack was calculated as the angle between the chord line and wind tunnel upper and lower surfaces.

In Collie's numerical work, the majority of his calculations were carried out in two dimensions with the exception of 1 result for comparison. The results produced from the CFD model created in this thesis have been compared to both the numerical and experimental wind tunnel results presented by Collie (2005). Although the runs are described as two dimensional, this author's numerical runs were actually carried out on a two dimensional shape extruded 1 cell into the 3rd dimension, as ANSYS CFX is not capable of running in two dimensions. The height of the ANSYS CFX domain was increased to 1000mm to reduce blockage factors. Further discussion on blockage factors and the decision to increase the domain height is given later in this section.

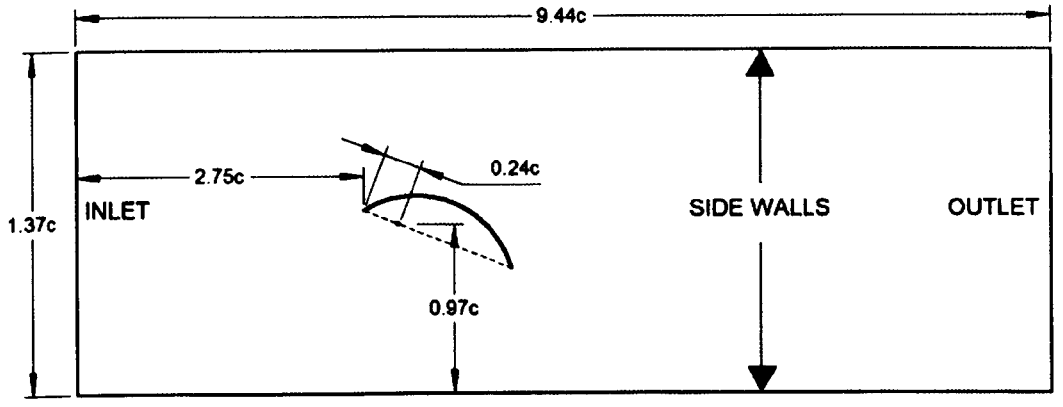

Figure 4.2.1 – Collie's validation case numerical domain (Collie, 2005)

The meshes for this family of runs were created using ANSYS GAMBIT. Although a strict mesh independency was not carried out, comparison to Collie's mesh independent solution can be made. Collie's mesh independent solution used 29,000 cells with a target surface y^+ of 1. For this study 100,000 cells were used with a maximum y^+ of 3, placing the first cell within the linear sublayer. Boundary layer elements and growth factors were used to expand the mesh away

from the arc surfaces. A suitable surface resolution was chosen to maintain cell quality and keep the surface aspect ratio acceptable, below 20.

The meshes used contained purely hexahedral cells. In order to achieve this, a complex mesh structure was created as shown in Figure 4.2.3 and 4.2.4. This was chosen to ensure that a high level of mesh quality was maintained. Another feature of the mesh used for this study, was the inclusion of a Non-Conformal Interface or General Grid Interface (GGI) and a turntable approach. Although there are added complexities associated with this type of interface, such as the often reduced stability of models, a GGI was chosen to allow easy transformation of the arc to different angles of attack.

The central mesh consisted of inflated boundary layer elements comprising 20 layers at a growth factor of 1.2. The remainder of the central mesh was broken up into the areas shown in Figure 4.2.3. Areas 1 and 2 were introduced to help expand the boundary inflation layers away from the sail.

A proximity based size function was used to expand the cells away from the arc, at a ratio of 1.05. A second proximity based size function was used to create grid refinement in the wake of the arc. This was expanded away from an imaginary line drawn along the centreline of the domain. When combined this created a mesh similar to that shown in Figure 4.2.4. A summary of the mesh used by this author and that of Collie is given in Table 4.2.1.

	Cells	y^+	Aspect ratio	Boundary layers	Cell size expansion ratio
Present author	100,000	Max 3	Max 20	20	1:1.2 Boundary layers, 1:1.05 far field
Collie	29,000	~1 (constant cell size)	2.5	/	/

Table 4.2.1 – Mesh comparison for arc validation case, Paton vs. Collie (2005).

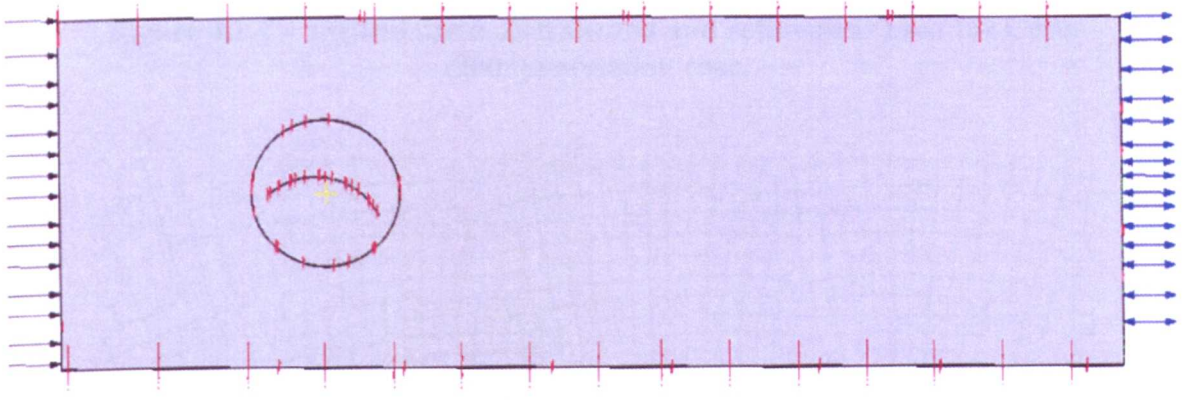

Figure 4.2.2 – Computational domain used for Collie (2005) validation case.

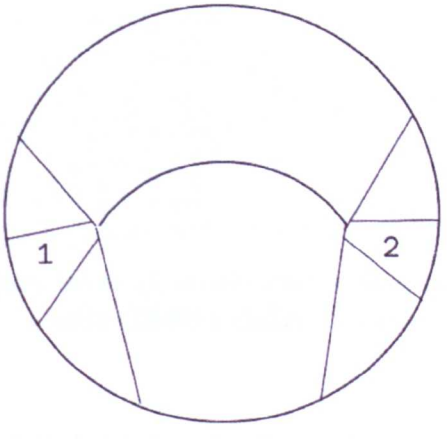

Figure 4.2.3 – Structure of central mesh region used for Collie (2005) validation case.

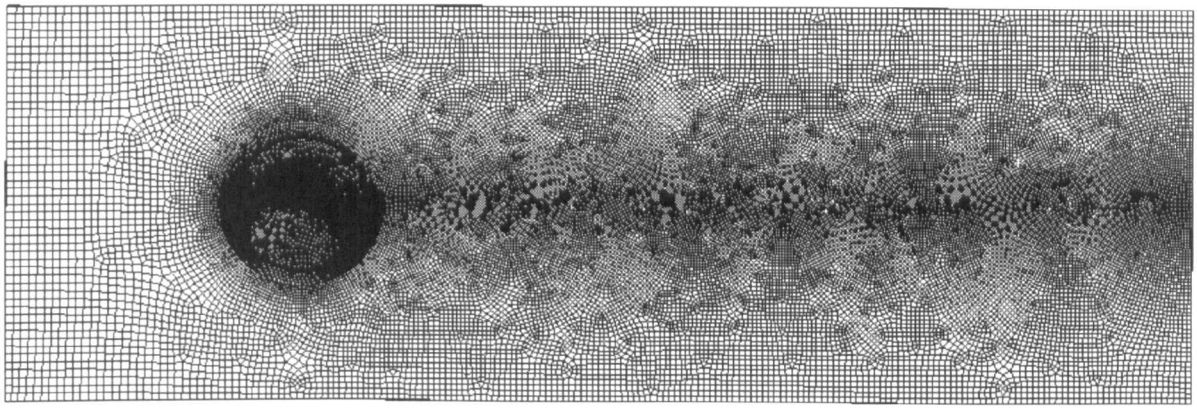

Figure 4.2.4 – Typical mesh distribution and refinement used for Collie (2005) validation case.

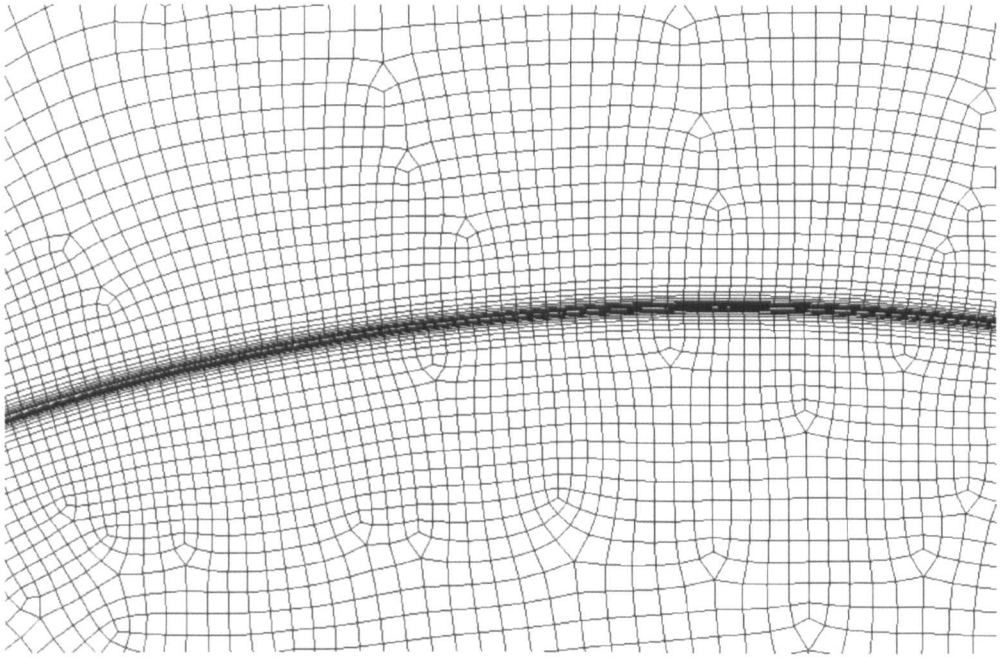

Figure 4.2.5 – Boundary layer elements and near wall mesh detail used for Collie (2005) validation case.

The sail was considered to be infinitely thin and was constructed using 2 non connected faces. The SST model was used throughout the study. Various turbulence models were investigated, including the $k-\varepsilon$, $k-\omega$ and SST model. However, Collie *et al.*, stated in their review of turbulence models for sailing applications (2001) that the SST model was the best suited and has been

used for all documented results within this thesis. The newly available SAS model (Menter and Egerov, 2005) was also investigated, but problems with robustness negated any possible advantages.

The left face, as seen in Figure 4.2.4, was set as a velocity inlet with 5% turbulence intensity. The inlet velocity was set at $25ms^{-1}$ which corresponds to a Reynolds number of 5.25×10^5. The downstream face was set as a pressure opening. The arc surfaces were set as non-slip walls, whilst the containing box was created from free slip walls. As described earlier, the interface between the two meshes was set up as a GGI. The simulations were run unsteady, with a reduced timestep compared to that of Collie (a timestep of 0.001s was with a Second order backward Euler transient scheme). The reduction in timestep over Collie is to be expected and necessary due to the reduction in average cell size. For force comparisons an average was taken over 10 periods of oscillation. A typical force convergence plot is shown in Figure 4.2.6. Here the drag force can be seen to converge to a regular oscillating pattern (17.5 degree case).

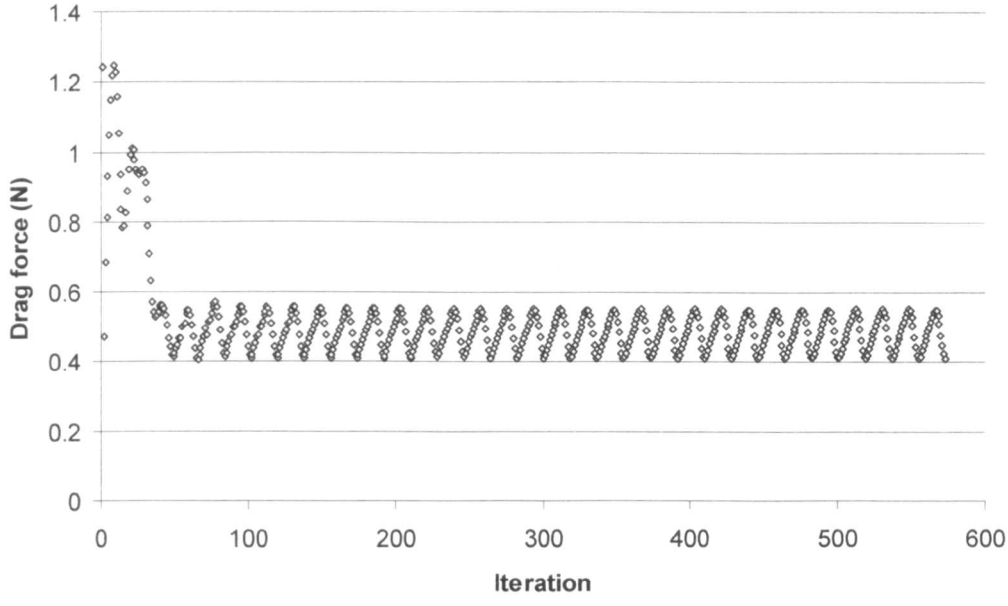

Figure 4.2.6 – Drag convergence plot for 17.5 degrees angle of attack arc validation case.

A summary of the differences in boundary conditions and solution control used by this author and Collie (2005) are shown in Table 4.2.2.

	Inlet turbulence intensity	**Timestep**	**Domain Size**
Paton	5%	0.001s	1000x2500mm
Collie	1%	0.0125s	435x3011mm

Table 4.2.2 – Boundary condition/solution control comparison for arc validation case, Paton vs. Collie (2005).

Figure 4.2.7 displays both Collie's experimental and numerical results (2005). One of the main features of the experimental lift coefficient data is that of the 'S' curve, with 2 points of inflexion. Another feature of note is the continuing rise in lift coefficient with angle of attack. The arc continues to create an increase in lift with increasing angle of attack, where perhaps the lift would be expected to

plateau or perhaps drop off once separation/stall has occurred. Collie's numerical results failed to predict either of the inflexion points from the lift curve shown in the left side of Figure 4.2.7

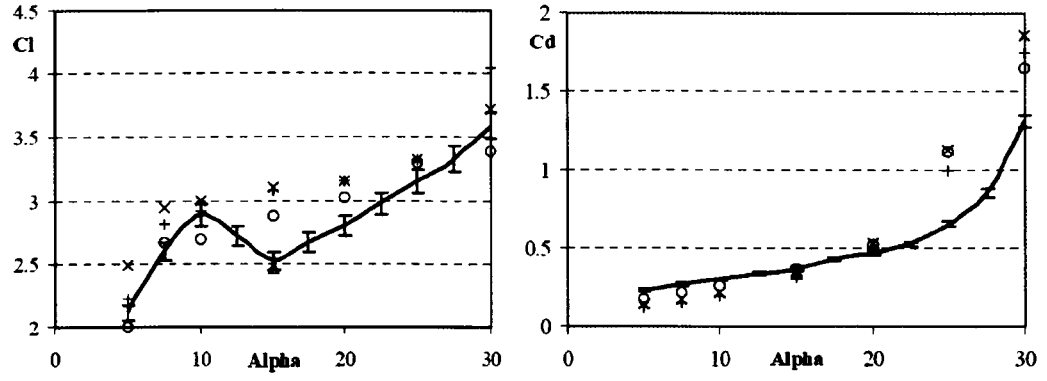

o SST, + $k-\omega$, x $k-\varepsilon$, Δ 3D solution (SST), - experimental.

Figure 4.2.7 – Collie's experimental and numerical results (Collie, 2005).

The numerical results produced by the method developed in this thesis are shown in Figure 4.2.8 and Figure 4.2.9. It can clearly be seen that the results have correctly predicted the angle of attack for both the peak and trough in the lift curve. However there is an offset between the numerical results of this author and experimental results of Collie (2005). It is expected that much of this offset is due to the increased domain size used within the numerical model of this thesis. The differences between the domain and boundary conditions used by this author and during Collie's experimental testing are summarised in Table 4.2.3.

	Domain Size	Blockage Ratio (% frontal area)	Inlet turbulence
Experimental (Collie, 2005)	435x3011mm	22-38%	1%
Present Author	1000x2500mm	9-17%	5%

Table 4.2.3 – Summary of geometry and boundary condition differences between experimental and numerical results.

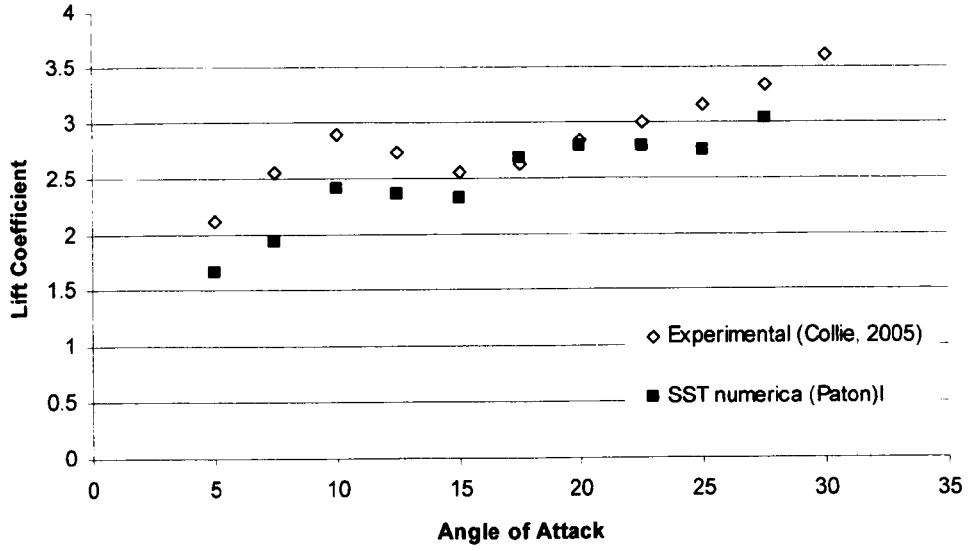

Figure 4.2.8 – Comparison of numerical results to Collie's experimental data (2005) - lift coefficient vs. angle of attack

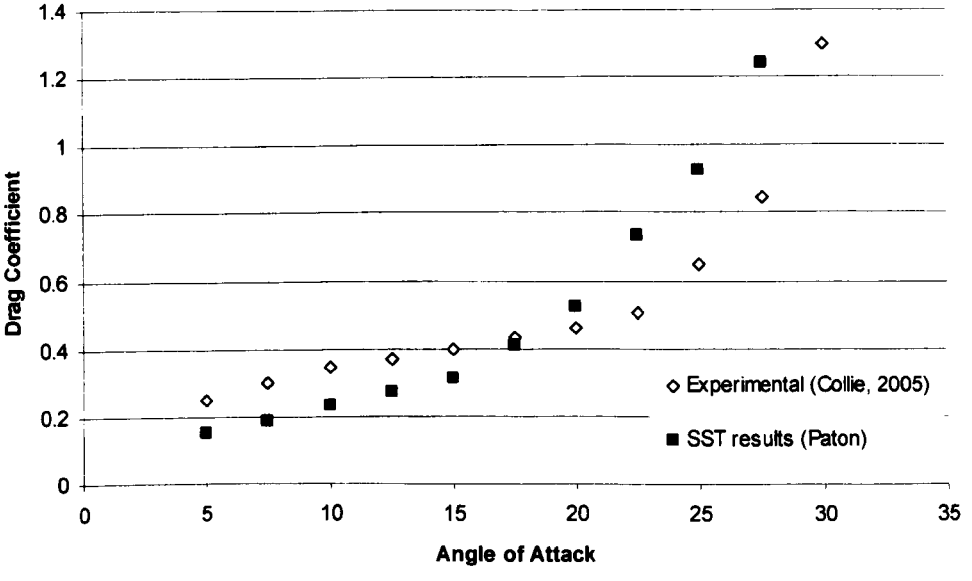

Figure 4.2.9 – Comparison of numerical results to Collie's experimental data (2005) - drag coefficient vs. angle of attack

The increase in domain size was intended to help reduce any blockage effects. In hindsight it would have been better to replicate the experimental domain, with blockage effects playing a major role in the flow patterns at the higher angles of attack. If the exercise were to be repeated, replication of the experimental domain would be recommended. The increased domain could explain the errors at higher wind angles. With the experimental domain being smaller, the blockage ratio would have been increased, thus increasing drag. Further discussion on the three dimensional effects and blockage factors is given later. The large blockage effects would also explain the apparent continuing increase in lift at large angles of attack. One would expect the lift coefficient to plateau or drop once the leading edge has separated. Due to the large blockage effects the increase in pressure on the windward side overcomes the drop in performance from the separated leeward side.

Post processing of the simulations at and around the inflexion point gives a clear explanation to the drop in lift that occurs at around 10 degrees. This is shown in Figure 4.2.10. The post processing images show contours of both turbulence kinetic energy and velocity contours with vectors. These plots detail the flow at the leading edge, in particular showing the onset of leading edge separation. The onset of the leading edge separation bubble created on the leeward side can clearly be seen as the angle of attack increases from 10 degrees.

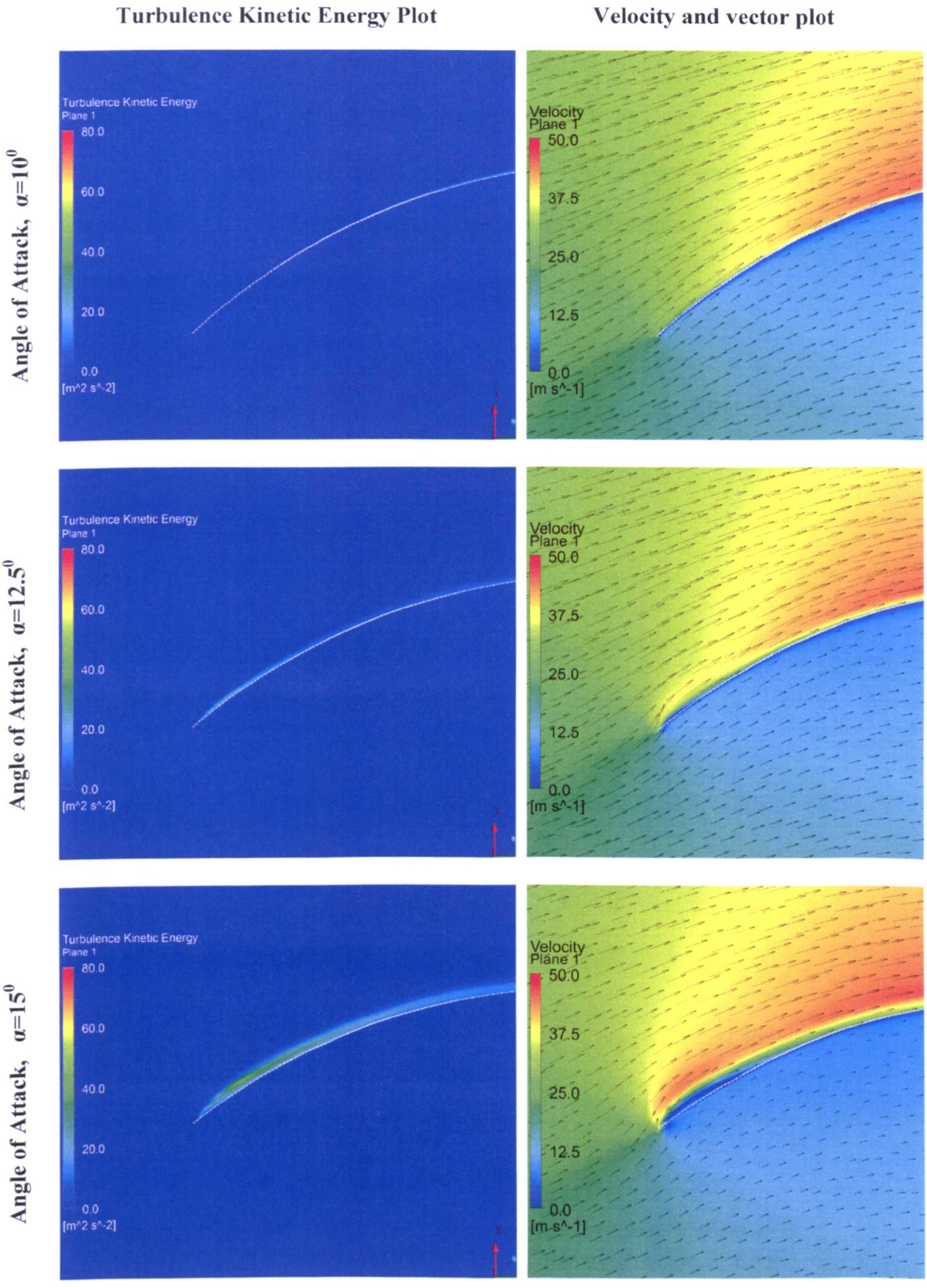

Figure 4.2.10 – Changes in flow at the leading edge for the Collie Validation case (left = turbulence kinetic energy, right = velocity)

To correct the differences present due to the changes in domain size and the variation in blockage ratio between the experimental and numerical results, Figures 4.2.11 and 4.2.12 show drag and lift coefficients with blockage corrections. An area based correction factor was used (Barlow *et al.*, 1999) shown below in Equation 4.2.1.

$$F_{Corrected} = \frac{F}{(1+0.25\left(\frac{Area_{Blockage}}{Area_{Tunnel}}\right))^2} \qquad \textbf{Equation 4.2.1}$$

Where $F_{Corrected}$ is the corrected force, F is the uncorrected force, $Area_{Blockage}$ is the cross sectional area of the blockage and $Area_{Tunnel}$ is the cross sectional area of the wind tunnel without the blockage.

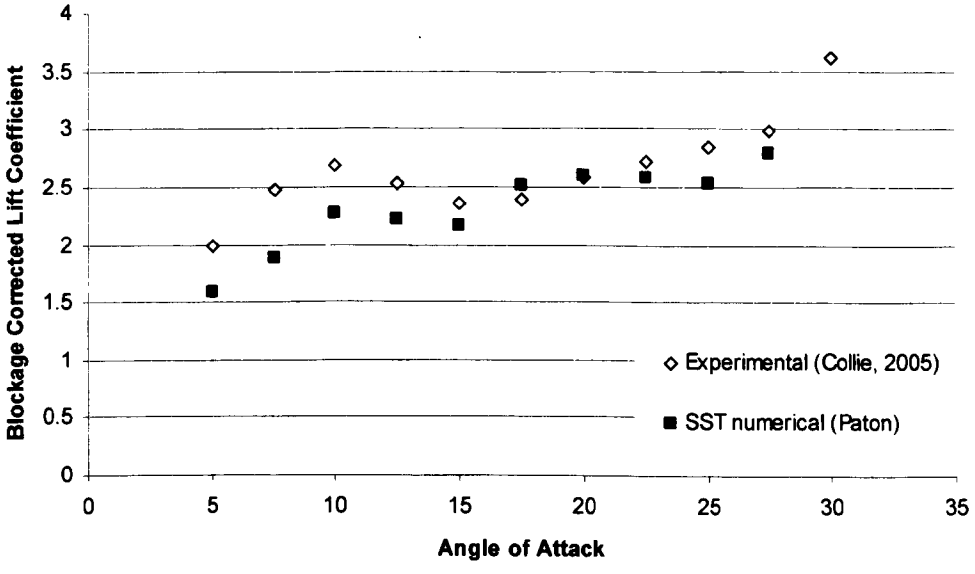

Figure 4.2.11 – Blockage corrected comparison of numerical result to Collie's experimental data (2005) - lift coefficient vs. angle of attack

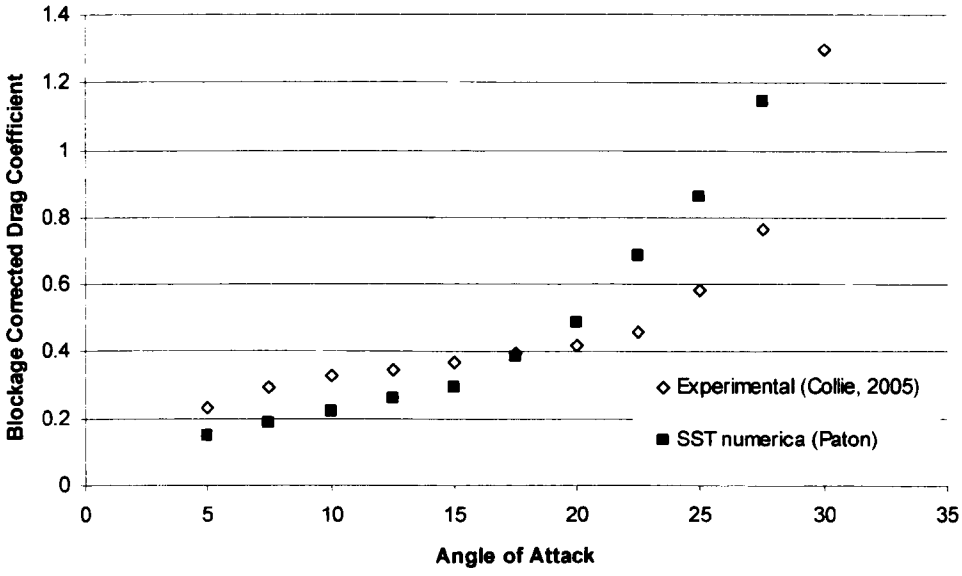

Figure 4.2.12 – Blockage corrected comparison of numerical result to Collie's experimental data (2005) - drag coefficient vs. angle of attack

The blockage corrected results give a slight improvement in correlation to the numerical results, in particular the lift coefficients. Quantitatively this reduced the average error in lift coefficient from 10.7% to 8.6%, a 24.6% reduction in error. It shows the importance of accurately recreating the experimental results. In hindsight the attempt by this author to reduce the effects of the blockage within his numerical results was perhaps erroneous.

Collie himself highlighted some of the errors present in his wind tunnel validation case and suggested that validation of CFD could not be determined purely on this test case. He suggested three main problems with his data set. He believed that there were 3 dimensional effects present in the wind tunnel test. He also suggested that the blockage ratio created due to the limited size of the wind tunnel would affect the results which this author has also determined. His final point of note was the lack of pressure and velocity data for the study. The first

two points raised would undoubtedly have affected the results, but it is this author's opinion that despite the less than ideal testing circumstances, useful comparisons can be made. The final point of note with regards to the pressure and velocity comparison will be dealt with in the following section, with the use of Wilkinson's validation case (1990).

The validation data case presented here is not without inaccuracies from both the experimental errors and differences with the domain replication in the CFD study. However, despite these factors, the CFD model did correctly predict the general trends of the experimental results, in particular the onset of leading edge separation, which inviscid codes could not predict.

4.3. Wilkinson's Validation Case

The validation case covered in the previous section highlights the potential of RANS based CFD to accurately model thin aerofoil and sail type applications. However, the advantages of viscous codes over inviscid codes can be seen further as the models are made more realistic and physical objects such as masts are included. Validation data sets of pressure profiles are difficult to obtain, but one such data set is that of Wilkinson (1990). Wilkinson provides wind tunnel data for a mast and sail combination, providing an obvious extension to the validation exercise in the previous section. The research was carried out during Wilkinson's PhD at the University of Southampton in 1984. His experimental data involved the modelling of a rigid sail and mast, in a wind tunnel in conditions representing upwind sailing.

Wilkinson's simulation was intended to represent a section through a typical yacht mainsail under close hauled (upwind) conditions, one third up from the foot (Wilkinson, 1990). The ratio of mast diameter to sail chord was 4.03% with a camber to chord ratio of 12.5%. The angle of incidence of the sail was 5 degrees at a Reynolds number of 709,000. The camber distribution represents that of a NACA a=0.8. The sail was constructed from a 5mm thick aerofoil of 2.11m span and 0.7m chord, fitted horizontally across the wind tunnel. The sail was fitted with pressure tappings at mid span (Wilkinson, 1990).

The RANS model geometry was constructed from the details given by Wilkinson, with the exception of the aerofoil thickness (Wilkinson, 1990). For the CFD simulations, the sail was created as an infinitely thin aerofoil, i.e. it has no thickness. This was chosen to be consistent with the meshing strategies used throughout this thesis. This was considered to be an acceptable assumption, given that the leading edge was not present, due to the inclusion of the mast.

The mesh used had approximately 160,000 cells in two dimensions. The model was extruded one cell into the third dimension, due to the prerequisite of a 3 dimensional mesh for ANSYS CFX. The domain and mesh are shown in Figures 4.3.1-3. A triangle based mesh extruded into three dimensions, was used with inflation layer elements away from the mast and sail surfaces. The simulation was run in a steady state scenario with the SST turbulence model within ANSYS CFX. A high resolution advection scheme was used. RMS residuals of 10^{-4} were achieved. The upper and lower surfaces were set as non-slip walls. The domain walls were set as free-slip walls

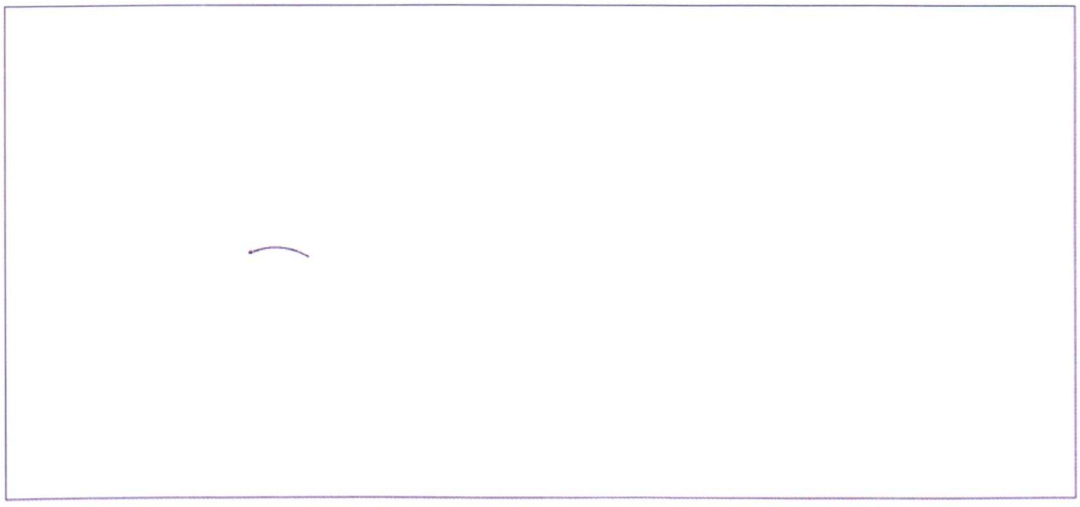

Figure 4.3.1 – Wilkinson case (1983) computational domain.

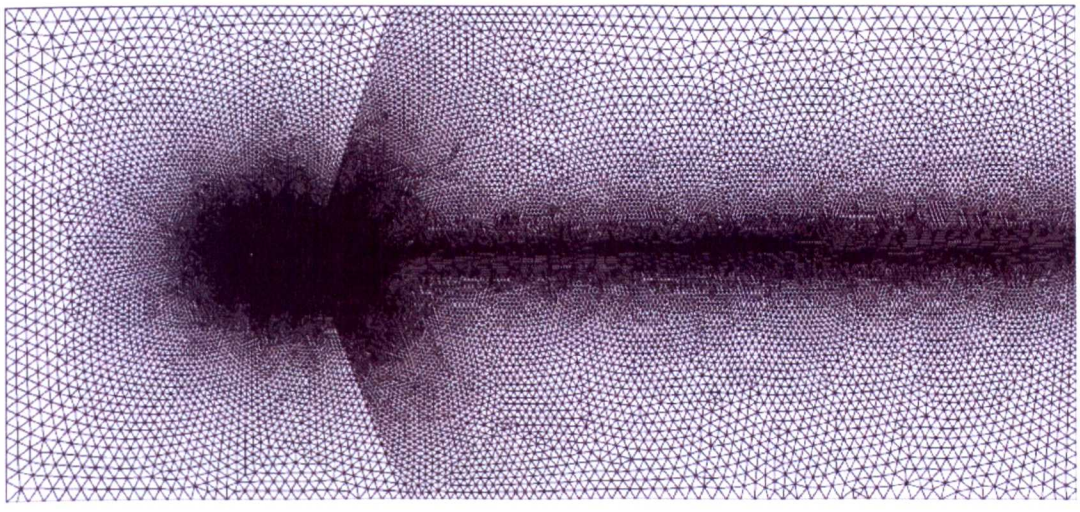

Figure 4.3.2 – Wilkinson case (1983) mesh wake and proximity mesh refinement.

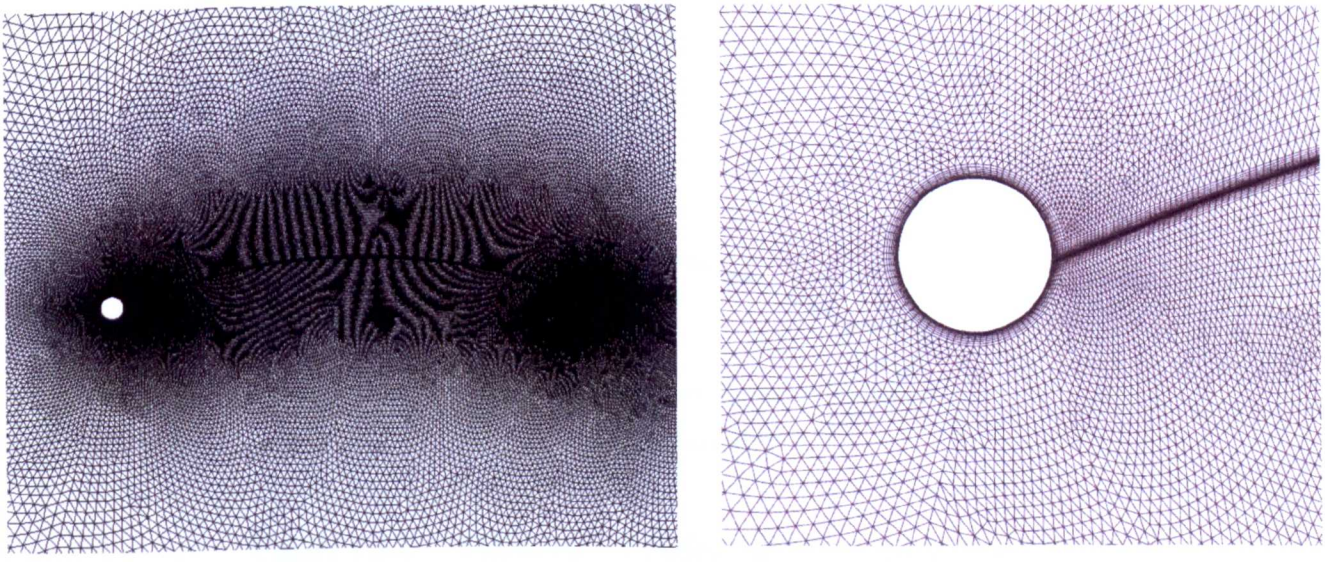

Figure 4.3.3 – Wilkinson case (1983) mesh refinement and inflation elements used close to sail and mast surfaces (Right – Close up of mesh around mast).

As reported in Chapter 2, Wilkinson highlighted the 9 regions of flow around a mast and sail combination (1990). These regions are detailed again in Figure 4.3.4, shown with the results from the corresponding RANS simulation, Figure 4.3.5. Figure 4.3.5 shows velocity contours.

Qualitatively the RANS results shown in Figure 4.3.5, give very similar regions of interest. The upper separation bubble, attached region and trailing edge separation are clear to see on the upper side of the sail. Equally on the lower side, the lower separation bubble and attached region are clearly identifiable.

The upper separation bubble (a-c) is one of the challenges that the mast and sail combination poses to both the sail designer and computational modelling process. Separation and reattachment points are well studied but still remain a region of inaccuracy and a potential area of improvement for RANS modelling.

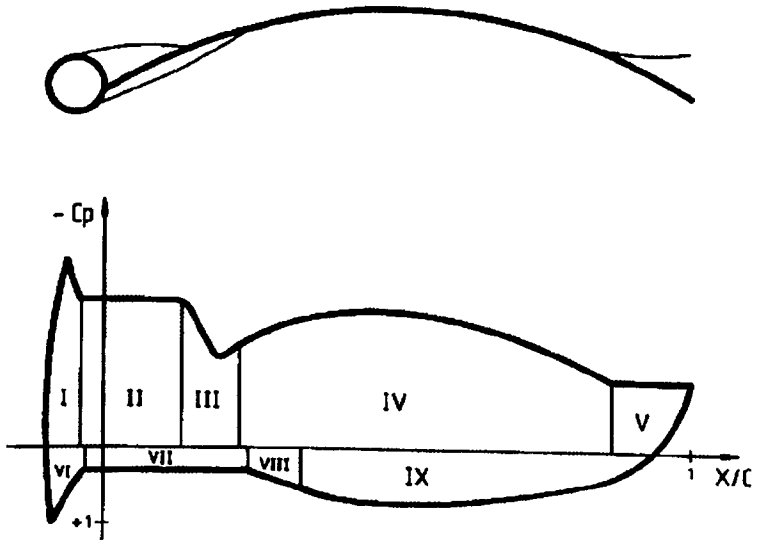

Figure 4.3.4 – Wilkinson's 9 regions of flow around a mast and sail (Wilkinson, 1983).

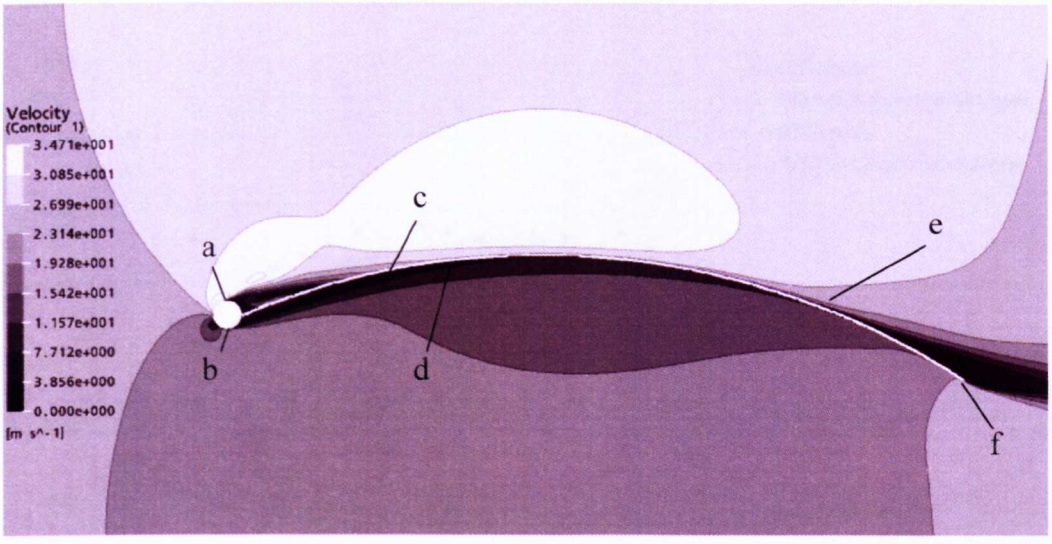

Figure 4.3.5 – Velocity contours for RANS based solution of Wilkinson's validation case (1983).
(a,b,e,f = separation points, c,d = reattachment points)

Common validation cases for separation bubbles include that of the backward facing step (Williams and Baker, 1997). It is recognised that RANS based turbulence models have difficulty in modelling separation bubbles and adverse pressure gradients (Collie *et al.*, 2001).

Quantitatively Wilkinson provided a pressure profile along the length of the sail arc for comparison. These experimental results are shown in Figure 4.3.6 compared to that of the RANS simulation.

Importantly the general trends are very well predicted; however, the under prediction of the upper separation bubble is apparent. The trailing edge separation bubble is another region of error. A mean error in pressure coefficient of 0.161 or 16.5% was achieved. This was based upon values extracted from the numerical data at chord locations matching the data from Wilkinson.

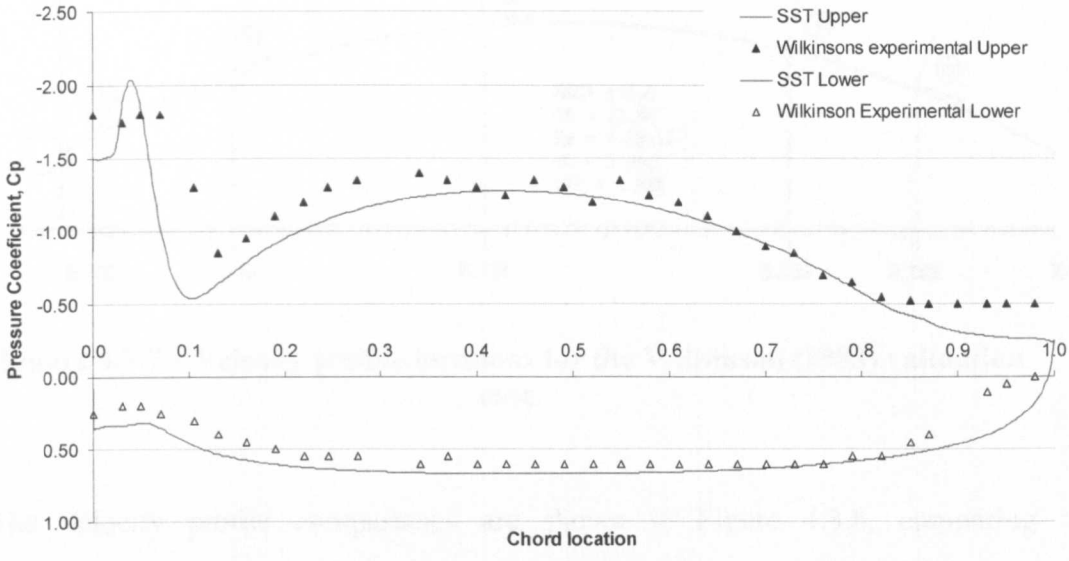

Figure 4.3.6 – Pressure coefficient distribution along sail arc for the Wilkinson (1983) validation case, comparing experimental and numerical data.

The final sets of data to compare to that of Wilkinson (1983) are velocity profiles at 5 different locations along the sail's upper surface. These were positioned to coincide with the 5 regions on the upper surface shown in Figure 4.3.4.

The 5 regions introduced in Chapter 2 initially identified by Wilkinson are:

- Upper separation bubble.
- Upper separation reattachment location.
- Upper lifting section.
- Trailing edge separation location.
- Trailing edge separation zone.

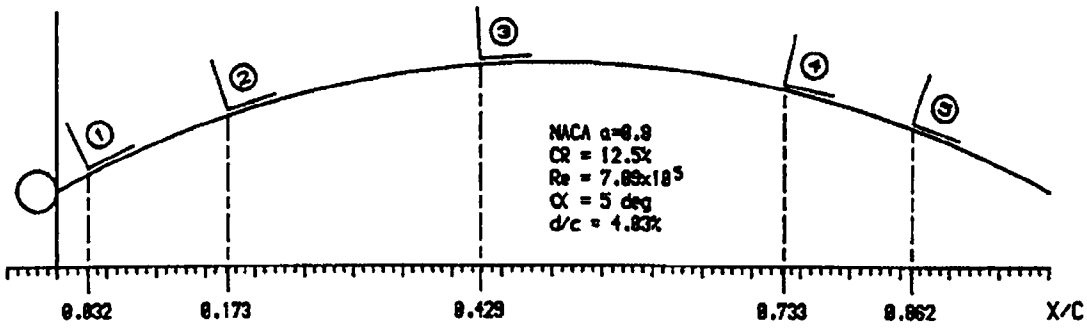

Figure 4.3.7 – Velocity profile locations for the Wilkinson (1983) validation case.

The velocity profile comparisons are shown in Figure 4.3.8, comparing Wilkinson's experimental profiles to those created by the SST model in ANSYS CFX 10.0. For a correctly trimmed sail the 'upper lifting section' is dominant and covers the majority of the upper surface. This coincides with the regions between locations 2 and 4, represented by profile 3. The velocity profiles at this location compare well, with an average error in u/U of 0.128 or 11%, where u is the local velocity and U is the freestream velocity.

At either end of the sail the regions of separation have caused some discrepancies between the two sets of results. However, the underlying trends are well represented. Wilkinson's experimental results were not capable of capturing the profiles in reversed flow and this is shown by the lack of data at location 1.

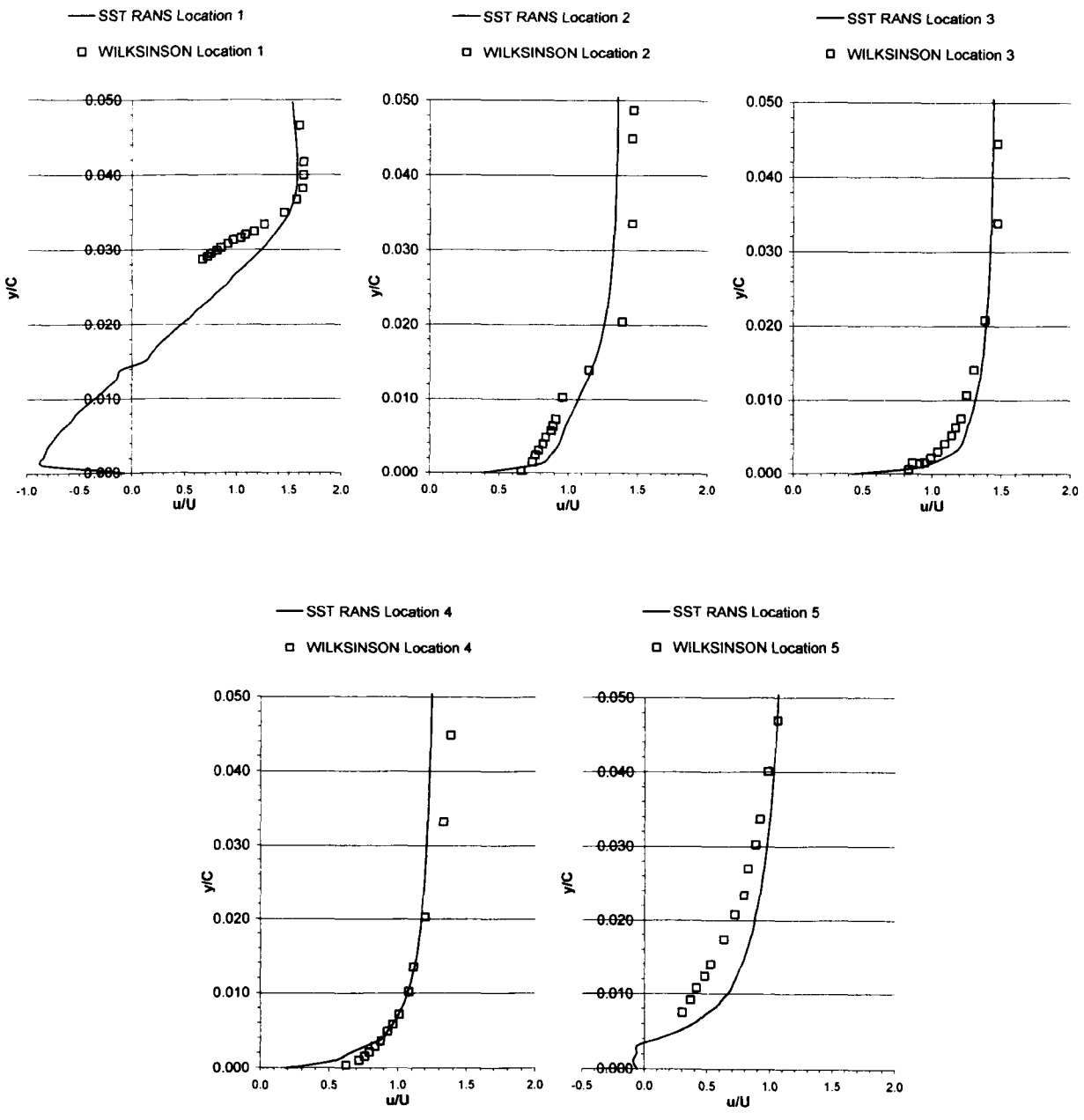

Figure 4.3.8 – Velocity profile comparison for RANS (Paton) and experimental data for the Wilkinson (1983) validation case.

Wilkinson concluded that although reversed flow was present, as seen by the tuft movements, it was not detected by the probe (Wilkinson, 1984). This highlights some of the inherent inaccuracies and difficulties associated with wind tunnel testing. Unsteady data at the separation and reattachment points would also provide valuable information for validation purposes. This gives another

advantage of viscous CFD, when compared to both inviscid and experimental methods.

The development of the boundary layer between locations 2 and location 4 can also be seen. As the boundary layer travels along the sail, the profile becomes steeper as the turbulent mixing in the boundary layer increases. The thickening of the boundary layer can also be seen by the distance taken for the velocity to reach free stream.

The SST RANS turbulence model has performed well when comparing pressure profiles and boundary layer profiles to the wind tunnel data. Qualitatively the model predicts very well the experimental results and quantitatively it has also faired well. Most importantly the numerical results have correctly predicted the trends of the experimental data, even though some errors in quantitative values have been observed. For the upper lifting section an error in the boundary layer profile of 11% was seen.

4.3.1. Comparison with other Computational Methods

The work of Chapin *et al.* (2005a), also used the Wilkinson case for validation of their viscous CFD solution. Although Chapin *et al.* use viscous CFD their method does differ to this author's, with variation in meshing strategy, turbulence model and solver. A summary of the differences between Chapin *et al.* and this author's method is given in Table 4.3.1.1. Further details of Chapin *et al.'s* approach can be found in Chapin *et al.*, 2005a.

	Meshing Software	Solver	Turbulence Model
Present author	GAMBIT	ANSYS CFX	SST
Chapin *et al.* (2005)	ICEM-CFD	FLUENT	SPALLART-ALLMARAS

Table 4.3.1.1. – Comparison of Chapin *et al.* (2005a) and this authors computational methods.

Shown in Figure 4.3.1.1 is a comparison of the results for the Wilkinson validation case, with data from Chapin *et al.* and this author. The results were extracted from Chapin *et al.*, 2005a. Here it can be seen that both RANS based models struggle in similar areas. Chapin *et al.* under predict the separation bubble by more than this author. Both approaches give good predictions for the main lifting section, from chord 0.3-0.7. Both approaches struggle to determine the pressures at the trailing edge.

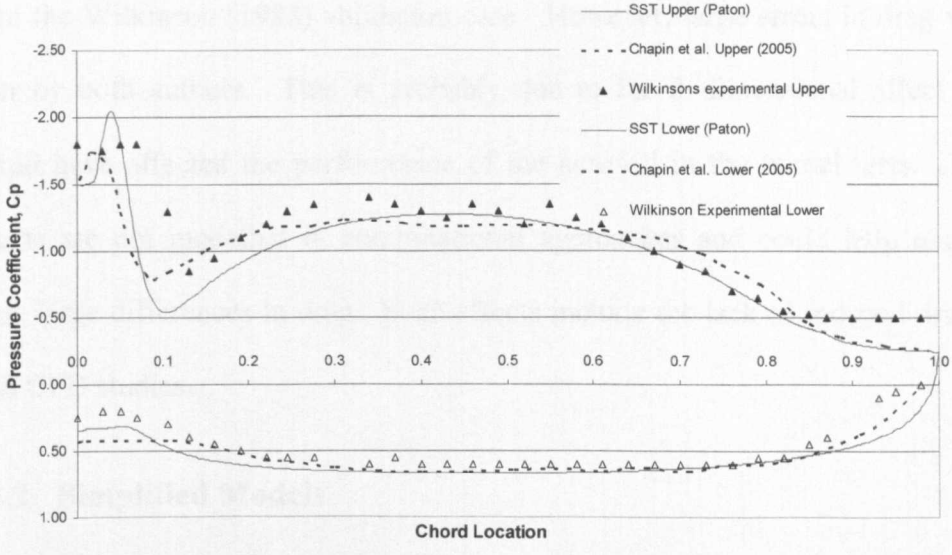

Figure 4.3.1.1 – Comparison of viscous RANS based results for Wilkinson (1983) validation case (Results taken from Chapin *et al.*, 2005a)

The total drag and lift coefficients and errors, as a percentage of the Wilkinson values, are given in Table 4.3.1.2. Both Chapin *et al.* and this author have more

accurate predictions for lift than for drag. This author has more accurate drag predictions with a 23% error in drag compared to a 36% error reported by Chapin *et al.* For lift, both numerical approaches perform better with Chapin *et al.* Reporting accuracies of 3.8% compared to 8.7% from this author.

	C_d	C_d Error as % of Wilkinson	C_l	C_l Error as % of Wilkinson
Present author	0.050	23.61%	1.433	8.71%
Chapin *et al.* (2005)	0.042	36.61%	1.63	3.82%
Wilkinson	0.066	-	1.57	

Table 4.3.1.2 – Coefficient comparison for the Wilkinson validation case, Paton vs Chapin *et al*, 2005a.

Both approaches have shown that they are capable of predicting the flow features from the Wilkinson (1983) validation case. However, large errors in drag were seen by both authors. This is probably due to the 3 dimensional affect that would have affected the performance of the aerofoil in the tunnel tests. These affects are not modelled in computational approaches and could help explain these large differences in drag. Such effects include the lack of induced drag in both CFD studies.

4.3.2. Simplified Models

The desire for faster CFD turnaround times is nearly always a key requirement for designers. With the added complexity the mast poses to the meshing procedure, it is tempting to simplify the model and not include the mast.

Removing the mast from the model would significantly reduce meshing times and usually the solving times (assuming reduced cell count).

The question that has to be answered is to what extent are results affected by the simplification of not including a mast? Masuyame *et al.* (2007) suggested that the inclusion of the mast increased the drag coefficient by 11%, a significant amount.

To investigate this further, the Wilkinson case is revisited. The model is recreated in ANSYS CFX 10.0 without the mast. All other conditions remain the same as in Section 4.3. A similar meshing strategy is used as that in Section 4.3. The results are shown in Figures 4.3.2.1-2 with comparison of velocity and pressure profiles. A surprising similarity is present for the results of the sails after maximum curvature. This is because the flow reattaches in both cases by mid chord and velocity and pressure contours become similar from that point onwards. The significant differences are at the leading edge where clearly the upper and lower separation bubbles are not recreated.

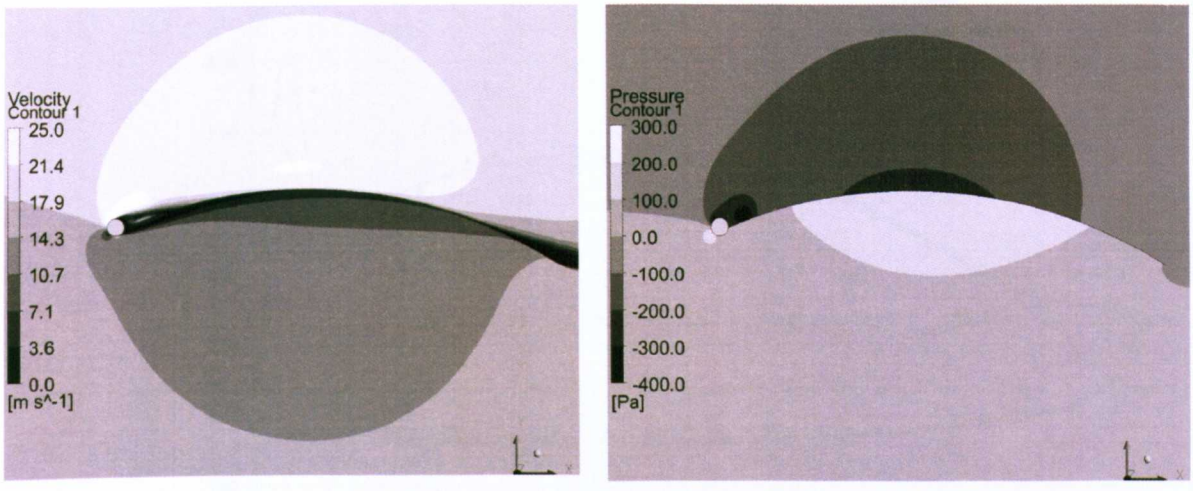

Figure 4.3.2.1 – Velocity and pressure contours for Wilkinson (1983) test case.

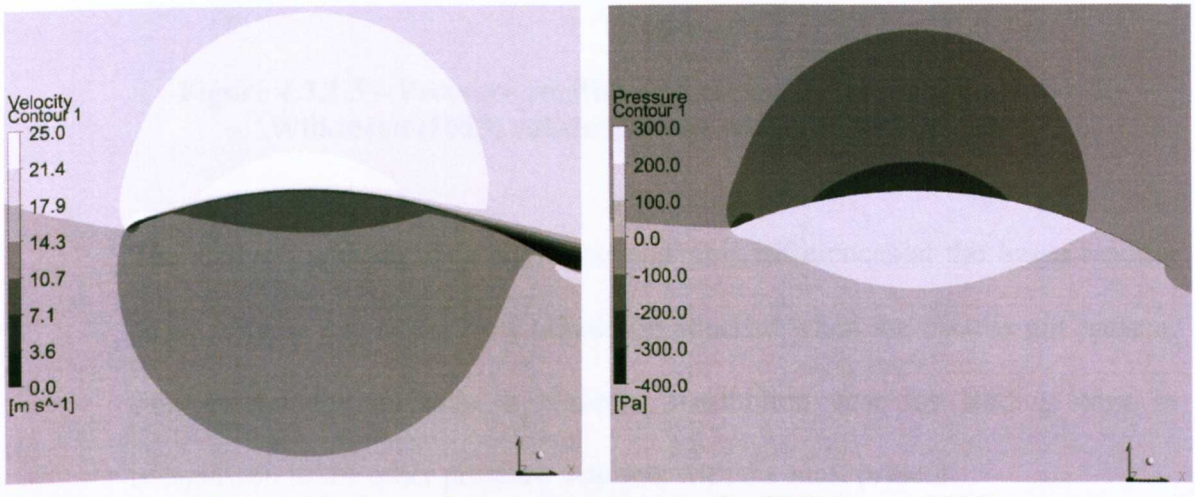

Figure 4.3.2.2 – Velocity and pressure contours for Wilkinson (1983) test case without mast.

The pressure plot shown in Figure 4.3.2.3 shows a comparison of the pressure distribution. For comparison the figure shows Wilkinson's experimental data and the RANS SST data for the simulation with a mast from the previous section. This plot shows the similarity in the pressure distribution for the second half of the sail arc, from chord location 0.5 to 1.0.

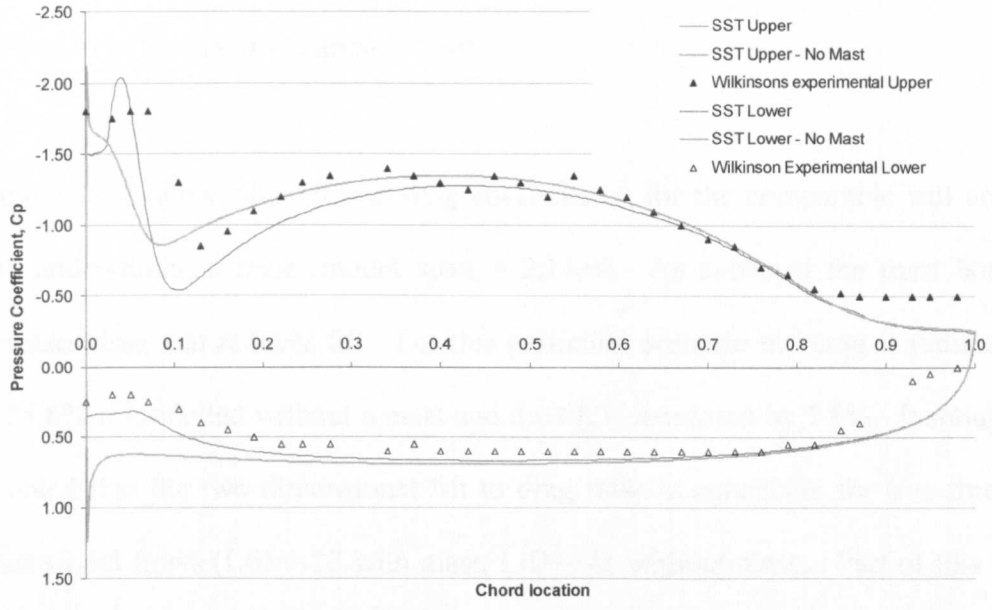

Figure 4.3.2.3 – Pressure coefficient distribution along sail arc for the Wilkinson (1983) validation case with and without mast.

The analysis without mast shows considerable differences at the lower leading edge. This is due to the flow remaining attached when the mast is not present. This creates the increase in pressure distribution near the leading edge in comparison to the other pressure data sets with the mast present.

On the upper surface, the flow initially appears to have similar trends for all three data sets, including the trough seen at approximately X/C=0.1. This is due to the flow separation seen in all 3 cases. Although the bubble is significantly smaller without the mast, the flow does follow a similar trend. However, for other sails with different cambers and angles of attack, the results could vary much more significantly. If the arc was at a lower angle of attack the flow on the upper surface could remain attached. As a result, one would fail to see this increase in pressure, as shown in Figure 4.3.2.3, which is created at the location where the flow reattaches. This phenomenon was first detailed independently by

Korst (Korst *et al.*, 1955) and Chapman (Chapman *et al.*, 1957) and is now often referred to as the Korst-Chapman theory.

Table 4.3.2.1 shows the lift and drag coefficients[1] for the comparable sail arc, with and without a mast (model span = 2.11m). As expected the mast both increases drag and reduces lift. For this particular scenario the drag is reduced by 25.6% if modelled without a mast and the lift is increased by 7.8%. It should be noted that the two dimensional lift to drag ratio is unrealistic for true three dimensional flows (L/D=~28 with mast, L/D=~41 without mast). Part of this is due to the inherent inaccuracy of modelling drag in two dimensions. The exact values of lift and drag coefficients would not be carried through to true three dimensional analysis. With two dimensional analysis, only pressure drag can be accounted for resulting in unrealistic lift to drag ratios.

	With mast	**Without mast**	**Difference as a % of 'With Mast'**
Drag Coefficient, C_d	0.0505	0.0375	25.6%
Lift Coefficient, C_l	1.4333	1.5455	7.8%

Table 4.3.2.1 – Lift and drag coefficients for the Wilkinson geometry, with and without masts

It is clear from this analysis that the inclusion of a mast in sail pressure analysis is very important when trying to recreate realistic pressure profiles. A 5% improvement in the prediction of the pressure coefficient was observed when the

[1] The arc surface area was used for the drag and lift coefficients

mast was included. The inclusion of the mast is therefore important when trying to estimate a rig's performance. The mast significantly influences the drag and lift coefficients, 25.6% and 7.8% respectively. This is a direct consequence of reducing the separation at the leading edge, as seen in the pressure profile comparison, Figure 4.3.2.3. In conclusion to accurately predict sail flows and pressure distributions, it is essential to include the mast in the analysis.

4.4. Masts and Mast Rotation[2]

The previous sections have shown the ability of the SST turbulence model and the CFD method outlined in this chapter to predict: leading edge separation, reattachment locations and velocity boundary layer profiles. The method has also shown to be capable of modelling flow around masts and around arcs with high curvature, similar to that of offwind sail sections. The modelling of similar scenarios would be impossible with inviscid methods. The next two sections use the tools detailed in this chapter to further investigate situations that would not be within the capabilities of inviscid method. These include investigations into mast shapes, mast rotation and sail interaction. Both applications involve the modelling of separation zones around masts.

As seen in the previous section, the impact of the mast on the performance of a sail section can be considerable. This section looks at the important influence of

---

[2] The work within this section has been published as a journal paper 'The effects of mast rotation on the performance of sails' within the International journal of marine engineering (Paton and Morvan, 2007)

the mast on the performance of sails and also how masts can become beneficial to boat performance. This subject has become prominent following the 'BMW Oracle Wing' utilised so effectively in the 33rd America's Cup in 2010.

From an initial look at the mast in the previous section, it would appear it has a purely negative impact upon the flow, with the mast's sole purpose to hold the sail and rigging in place. Within this chapter rotating masts are investigated and their performance explained with the help of flow visualisation and quantitative analysis.

One of the detrimental effects of the mast is the upper separation bubble discussed in detail in the previous section with the Wilkinson validation case. The pressure differential acts locally at a normal to the sail. Close to the mast, during upwind sailing, the net pressure force projected on the boat's longitudinal axis is at its largest and acts in the direction of travel. It is therefore advantageous to minimise this separation bubble to maximise performance.

The choice of mast shape is an obvious area for optimisation, although for many classes of yacht there are restraints placed upon both size and shape. There is a temptation to try and utilise the mast in an attempt to help generate driving force, rather than its presence being detrimental. This can be done with such techniques as mast rotation. The rotation of the mast to windward can help in reducing the effects of the upper separation bubble significantly, with the mast effectively forming the leading edge of the foil. A similar process is used by aircraft wings with the use of slats to alter their lift and drag coefficients.

A mainsail section 8.75m in arc length and 4m in height was chosen with varying mast geometries. These masts were then rotated to investigate the effects of mast rotation. Throughout the analysis the wind direction and speed remains constant for comparison at $5ms^{-1}$. A velocity inlet with a 5% turbulence intensity and a pressure outlet were used. The overall domain was 150m in length and 100m tall. The models were set at an angle of 7.5 degrees to the free stream wind.

The meshes created contain hexahedral based cells and in very rare occasions, where the cells created had high skew values, prism based cells were used, for example, in the region between the mast and the sails. Boundary inflation layer cells were used around the surfaces to resolve the flow in the boundary layer. y^+ values on the sail and mast surfaces were approximately 3. All simulations were carried out in two dimensions to erase any complex three dimensional phenomena. Significant mesh refinement was used at and around the mast location, as this was the focus of the study. An example of the mesh refinement and the boundary inflation layers used around the masts is shown in Figure 4.4.1.

The commercial CFD code ANSYS CFX 10 and the SST RANS turbulence model have been used for all the simulations within this section. The convergence of runs was based upon RMS and maximum residuals. A maximum RMS of 10^{-4} was obtained for all runs but in the vast majority considerably lower residuals were achieved. The maximum residuals were checked to ensure they were satisfactory and not in an area of importance. The

forces of interest on the sails and mast, e.g. drag and lift, were also monitored to ensure stability.

A physical timestep of 0.001s was chosen to ensure convergence within a maximum of 4 iterations per timestep. In a similar way to that detailed in Section 4.2, the time averaging of forces was used to create single force coefficients.

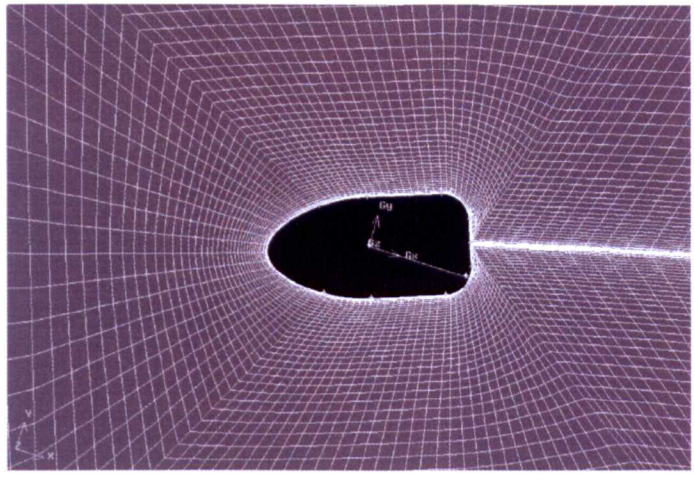

Figure 4.4.1 – Example mesh refinement around rotating mast

4.4.1. Mast Shapes

Masts can typically take any geometrical shape the designer wishes within certain limitations. Traditional sections are round, which are both easy to manufacture and tune, as their sectional properties are constant irrespective of rotation. A close adaptation of this is the circular section with fairings at the trailing edge. These are easy to manufacture, as they tend to be adapted circular sections with cosmetic rather than structural sections making up the fairings at the trailing edge. Classic America's Cup rigs (AC32 regulations) tend to use a double rounded section, with both the leading and trailing sections being rounded but slightly elongated. They also tend to have the maximum section

width towards the rear. The final mast shape used in this analysis is the flat backed section or bullet mast. This has become a popular choice with mast designers. The advantages and disadvantages of all the designs will be highlighted in the following analysis. The three mast sections used within this study are shown in Figure 4.4.1.1.

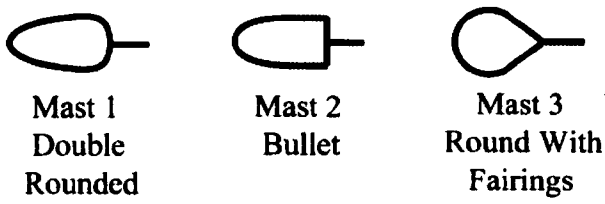

Figure 4.4.1.1 – Comparison of different mast shape profiles used within the mast rotation study.

The analysis contained within this section represents a non specific class of yacht. The aim of this work is to not provide a direct application but demonstrate the potential advantages of mast rotation. The mast dimensions chosen represent a realistic mast size and diameter for the chosen chord length.

4.4.2. Mast Shape 1 - Double Rounded

The majority of racing yachts use some form of the double rounded section so this is the focus of the first section. Figures 4.4.2.1-3 show the double rounded section attached to a mainsail section, with the mast at different rotations.

The three different mast rotations used within this study were:

- Aligned with the sail chord
- Aligned with the sail tangent
- Fully rotated

Figure 4.4.2.1 shows plots of velocity and pressure contours for the double rounded section aligned to the sail chord. The free stream flow direction is horizontal from left to right. The separation that occurs in the flow can clearly be seen as the dark contours shown in the velocity plot. The separated region is along the entire length of the sail as the flow fails to reattach. Figure 4.4.2.2 shows the tangent rotated scenario. This dramatically improves the flow over the sail as the flow reattaches to the sail, shown by the vastly reduced dark areas on the velocity plot. This improved flow leads to greatly improved pressure distributions over the sails, shown later. Figure 4.4.2.3 shows the CFD results for the positively rotated mast. This setup improves the flow further with reduced separation on the suction side, increased velocities around the mast section and higher pressure forces on the windward side. Another advantage is that the pressure differential across the mast is now in a more favourable direction, being rotated further towards the wind.

The plots throughout Figures 4.4.2.1-3 have the same contour scales and one can clearly visualise how the suction forces near to the mast have increased significantly with mast rotation, shown by the darker contours in Figure 4.4.2.3. It has also acted to increase the pressures on the windward side. Another advantage is that the pressure differential across the mast is now in a more favourable direction, being rotated further towards the wind.

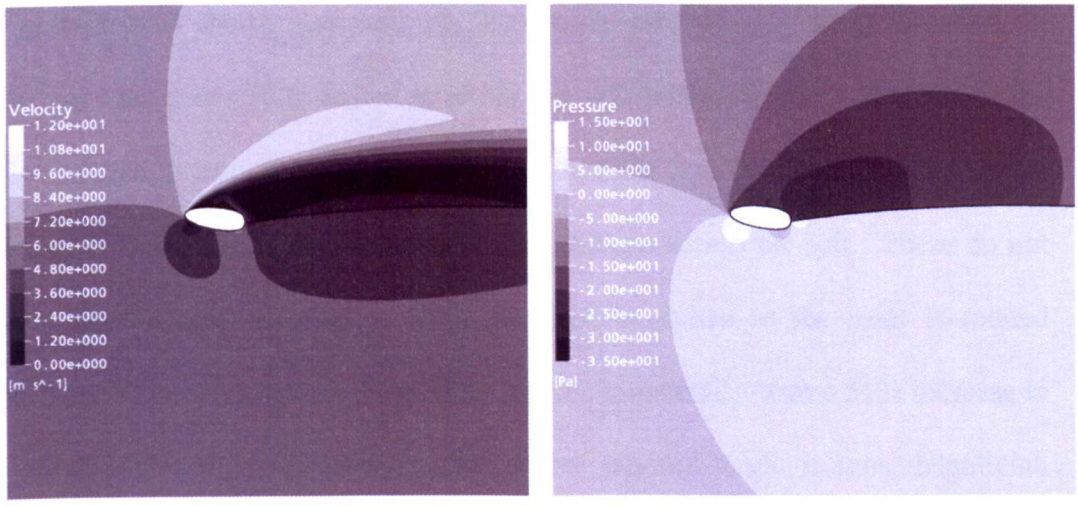

Figure 4.4.2.1 - Velocity and pressure contours for the chord aligned double rounded mast.

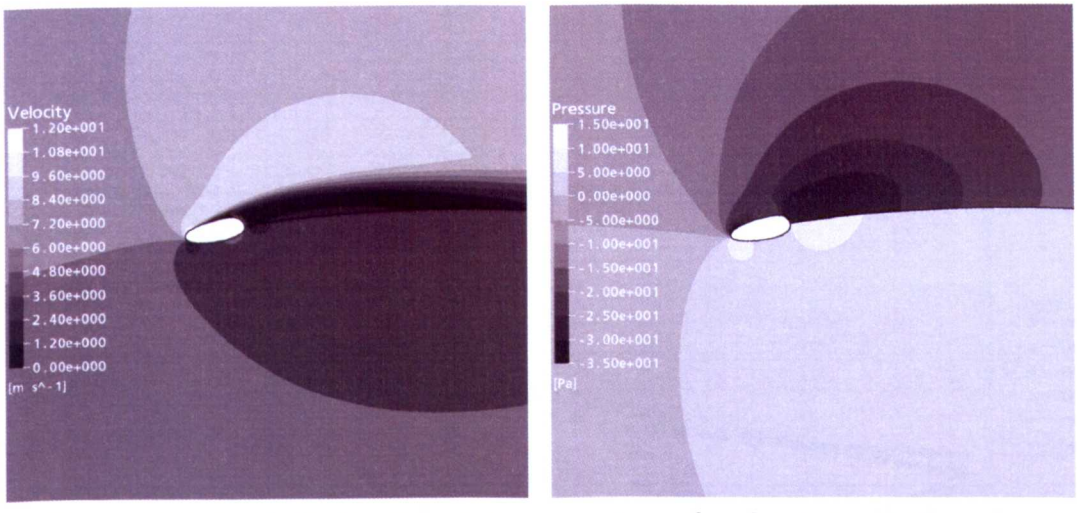

Figure 4.4.2.2 - Velocity and pressure contours for the tangent aligned double rounded mast.

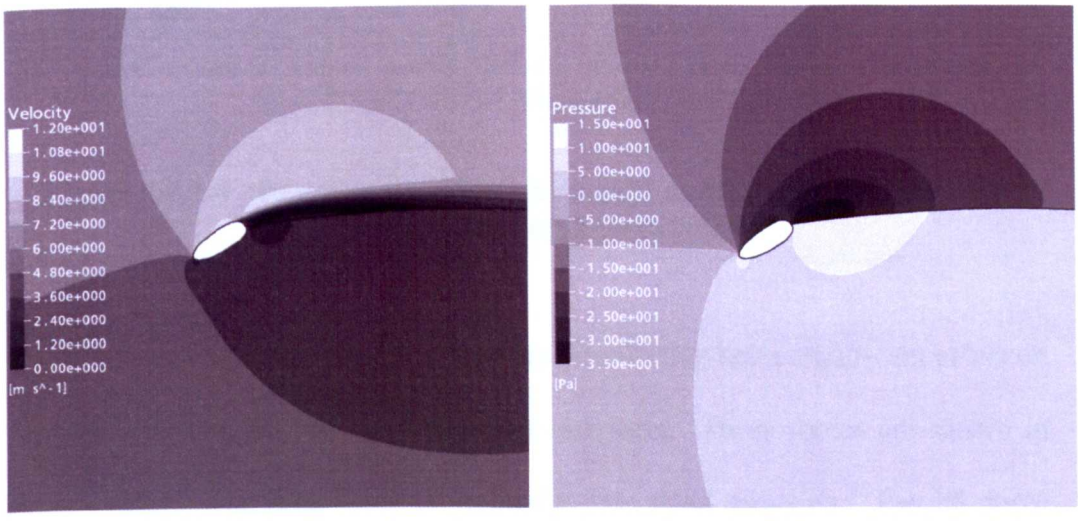

Figure 4.4.2.3 - Velocity and pressure contours for the fully rotated double rounded mast.

Figure 4.4.2.4 shows quantitatively the results that have just been discussed. It displays the pressure distribution along the sail, where X is the distance in the flow direction from the mast, in metres. The three lines in the bottom section of the plot show the windward pressure distributions across the sail. These do not vary dramatically although a slight increase is shown as the mast is rotated further. The leeward plots, however, change dramatically with a 51% increase in suction pressure at the leading edge where the sail angle is most beneficial. These leeward pressures are shown in the top section of Figure 4.4.2.4.

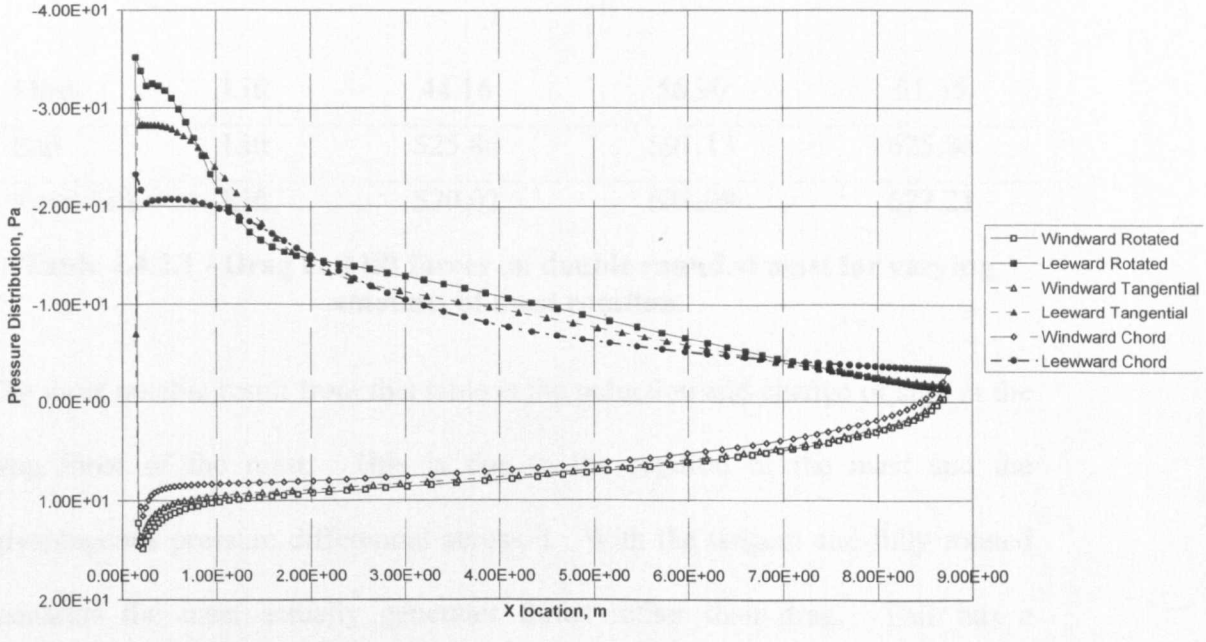

Figure 4.4.2.4 - Pressure distribution around double rounded mast for varying amounts of mast rotation.

This dramatic improvement in the pressure distribution has a significant effect on the total drag and lift forces on the mast and sails. These forces are shown in Table 4.4.2.1. The drag force is parallel to the wind direction. The lift force represents the force perpendicular to the freestream wind.

The drag and lift forces created on the rig are a combination of the mast and the sail forces. It is clear from the pressure plots that with the mast rotation the increased contribution towards driving forces from both the mast and the sail is significant. This is demonstrated quantitatively in Table 4.4.2.1.

Locator	Force	Chord Oriented (N)	Tangent Oriented (N)	Fully Rotated (N)
Mast	Drag	7.86	-14.92	-27.77
Sail	Drag	42.86	45.74	49.30
Total Drag	Drag	50.72	30.82	21.53
Mast	Lift	44.16	56.96	51.35
Sail	Lift	525.86	591.13	625.86
Total Lift	Lift	570.02	648.09	677.21

Table 4.4.2.1 - Drag and lift forces on double rounded mast for varying amounts of mast rotation.

The most notable result from this table is the reduction and change of sign in the drag force of the mast. This is due to the rotation of the mast and the advantageous pressure differential across it. With the tangent and fully rotated scenarios the mast actually generates thrust rather than drag. This has a significant effect upon the total drag of the sail and mast combination with a reduction of 60% between the fully rotated and chord orientated masts. This is not to say that with fine tuning further reductions couldn't be found.

Equally as important to the drag forces are the lift forces. An increase of 20% is found between the fully rotated and chord orientated masts. It has been assumed for this study that the goal is to minimise drag and maximise lift. It is

understood that this is not always the design objective, but this will be used throughout this section.

4.4.3. Mast Shape 2 - Bullet

Mast shape 2, bullet shaped, is similar in size to mast shape 1, the double rounded mast. It has the same maximum width and the same length although the profile is different. This mast has a flat back and is often described as bullet shaped. Although it appears to be a less streamlined shape its performance is quite surprising. To a non aerodynamicist a teardrop type shape would appear to be an obvious choice as it would appear to reduce sharp edges and hopefully allow smooth attached flow to establish (Speer, 2007). However, in contrast, the performance of the bullet mast is impressive, despite its aggressive trailing edge, as shown in this section.

Figures 4.4.3.1-3 show the flow around the bullet mast throughout the different angles of rotation. Again the plots focus upon the leading edge separation. In a similar way to that of the double rounded mast, the bullet mast has to be rotated for its advantages to be seen. Before the mast is rotated the leeward separation is extensive, which is gradually reduced as it is rotated, until the fully rotated state where the separation is minimised.

It is clear to see from these plots that, for the fully rotated case, Figure 4.4.3.3, the flow remains attached across the flat section of the mast and does not separate until the trailing edge of the mast. This has a positive effect upon the lift contribution from the mast itself. Note that the separation bubble it creates is

significantly smaller than the bubble with the double-rounded mast at the same rotation.

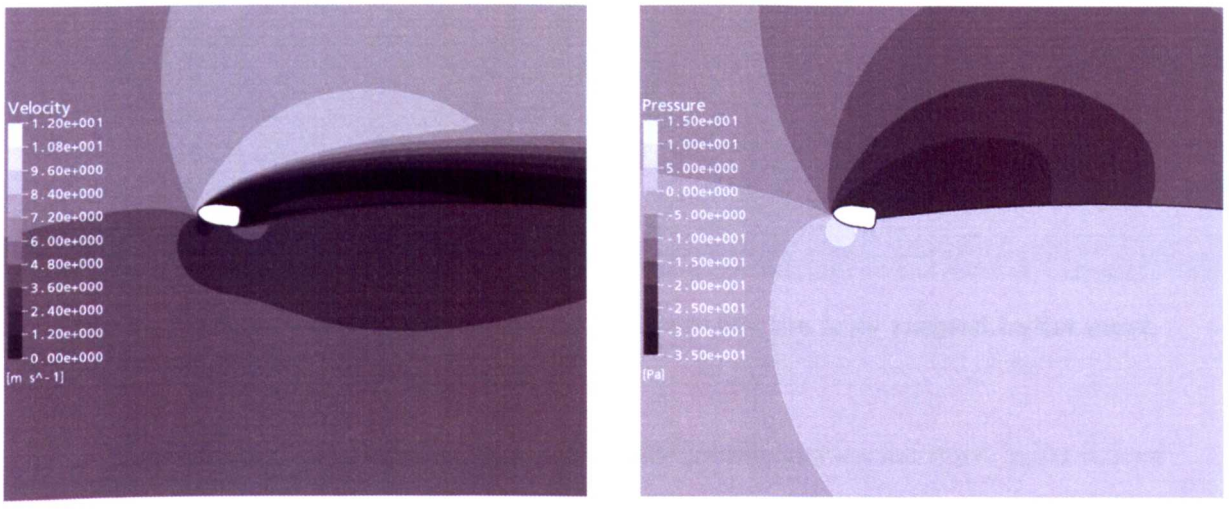

Figure 4.4.3.1 - Velocity and pressure contours for chord aligned bullet mast.

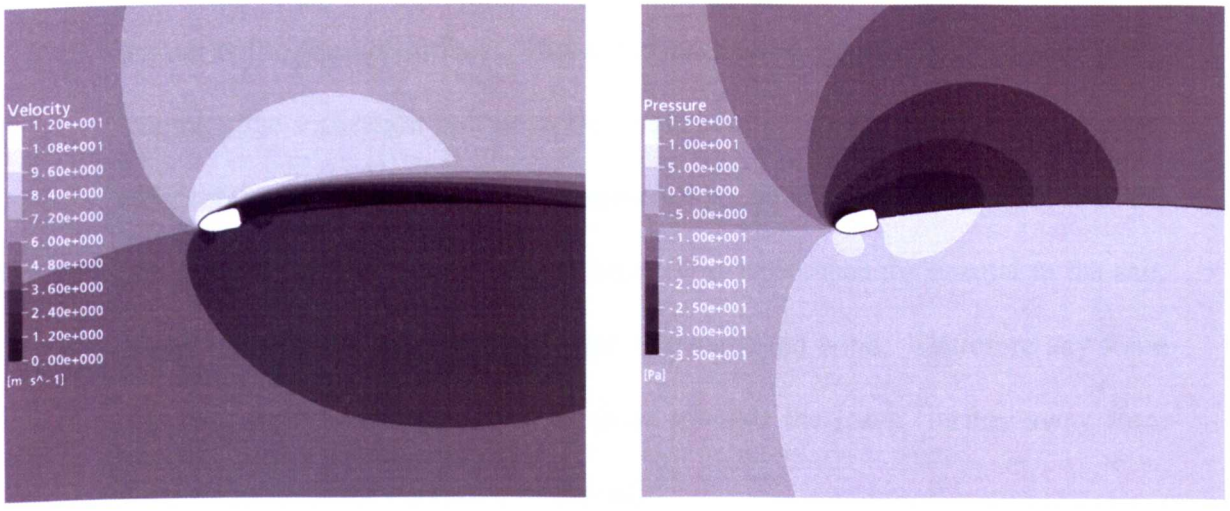

Figure 4.4.3.2 - Velocity and pressure contours for the tangent aligned bullet mast.

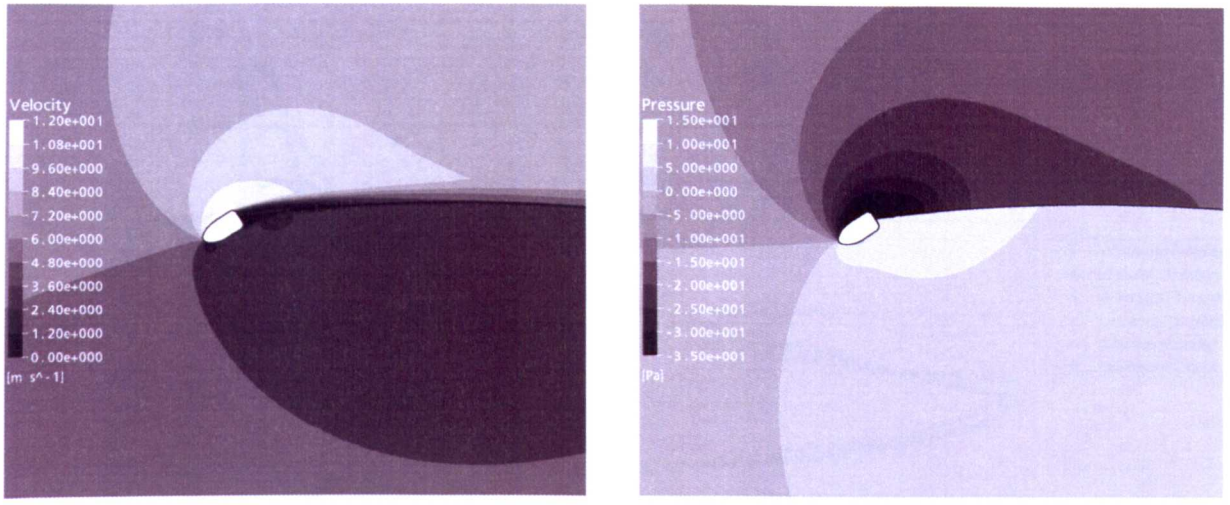

Figure 4.4.3.3 - Velocity and pressure contours for the fully rotated bullet mast.

Additionally, the angle of the pressure differential across the mast helps reduce the drag. When the mast is rotated, the forces from the mast actually oppose that of drag and help to drive the boat into the wind. The pressure differences act at the normal to the sail surface. This is the motivation behind trying to reduce this leading edge separation bubble as the angle here is more advantageous. The sail adjacent to the mast is usually considered to be the most important and the pressure differential is most critical here. This is because the normal to the sail, nearer to the mast, actually points closer towards the wind. Therefore any force acts in a more beneficial way than those towards the leech (further away from the mast), due to the curvature of the sail.

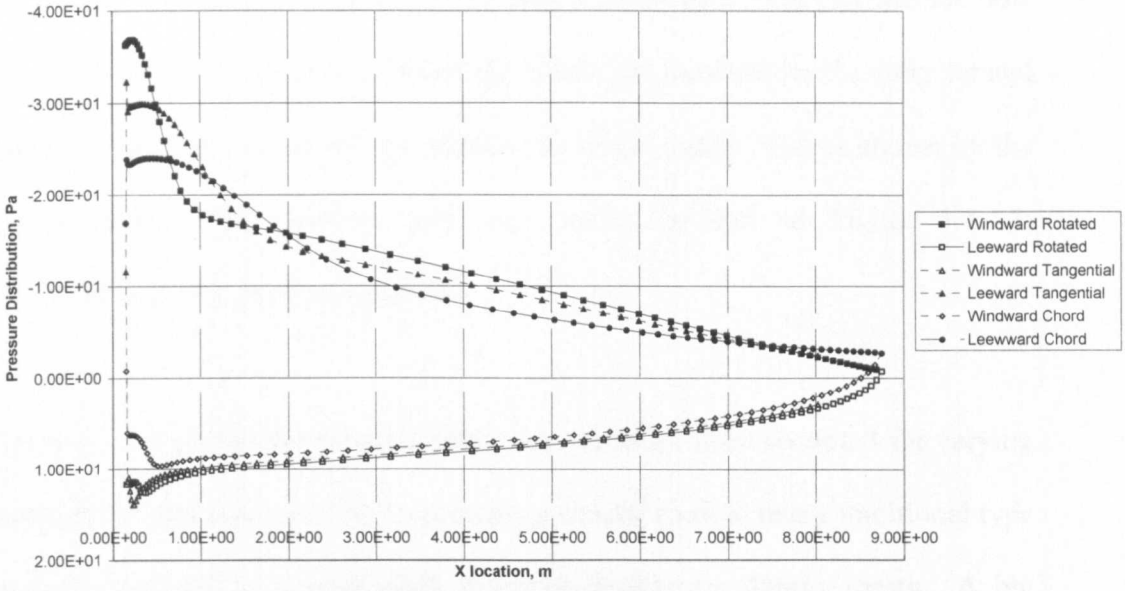

Figure 4.4.3.4- Pressure distribution for bullet mast for varying amounts of mast rotation.

4.4.4. Mast Shape 3 - Round with Fairings

Mast section 3 represents a round mast with fairings. This mast attempts to reduce the disruption to the flow as it leaves the mast. This mast section is very popular as it is a simple shape to create. A simple round mast with a slightly exaggerated mast groove easily creates this type of section, although a little less pronounced than the section shown. Figures 4.4.4.1-3 show the velocity and pressure plots around the round mast with fairings at the different angles of rotation.

Mast 3 provides the smoothest geometric transition on the leeward side of all the sails when fully rotated. Despite this the flow actually separates before the transition, creating a significant separation bubble on the leeward side. Qualitatively this mast section has larger separation bubbles than the previous two masts. Another feature, not seen in the previous two mast sections, is the

windward separation that appears in the fully rotated state. One can also see how the windward separation has reduced the windward pressure for the fully rotated mast. As the flow reattaches the pressure increases again. This is shown by the lighter contour that appears part way down the sail in Figure 4.4.4.3, representing a high pressure contour.

Figure 4.4.4.4 shows the pressure plot comparison for mast section 3 for varying amounts of mast rotation. This represents a similar mast to many traditional type mast sections and is a particularly common profile for dinghy masts. A big advantage for this type of section is that the mast structural properties are relatively similar at different angles of rotation.

A key feature for the flow around mast 3 is the separation bubble that forms on the windward side of the sail, shown by the reduction in pressure between X location 0 and 0.6m. The windward pressures could perhaps be improved with a reduction in the rotation angle. This under rotation might be at the expense of some of the leeward benefits. This demonstrates the effect caused by over rotation of mast sections.

Further work would need to be done to establish the optimum angle of mast rotation. If the mast were rotated further, the windward separation bubble would propagate further down the sail. This would have an effect upon the windward pressure, extending the region of lower pressure on the windward side. Discussion on the forces and their breakdown will be given in Section 4.4.6.

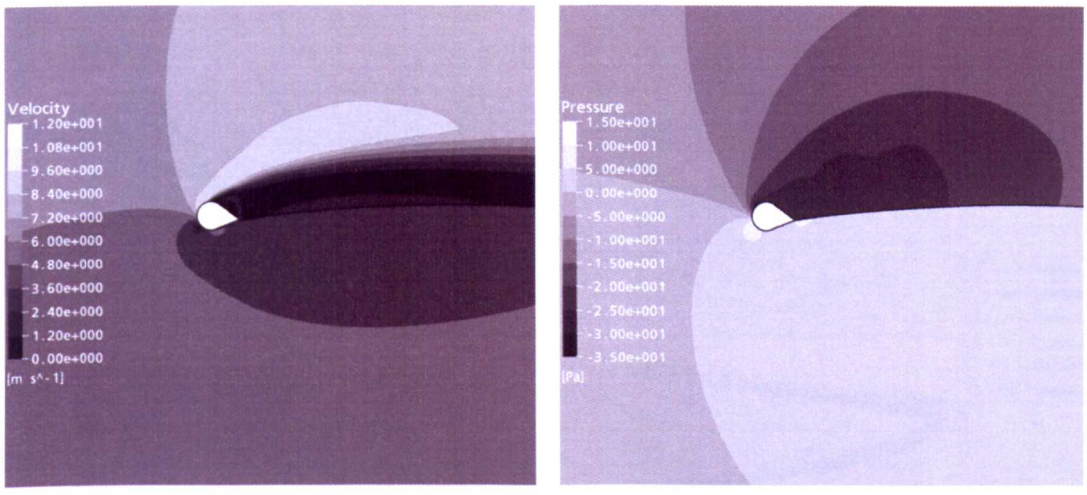

Figure 4.4.4.1 - Velocity and pressure contours for the chord aligned round mast with fairings.

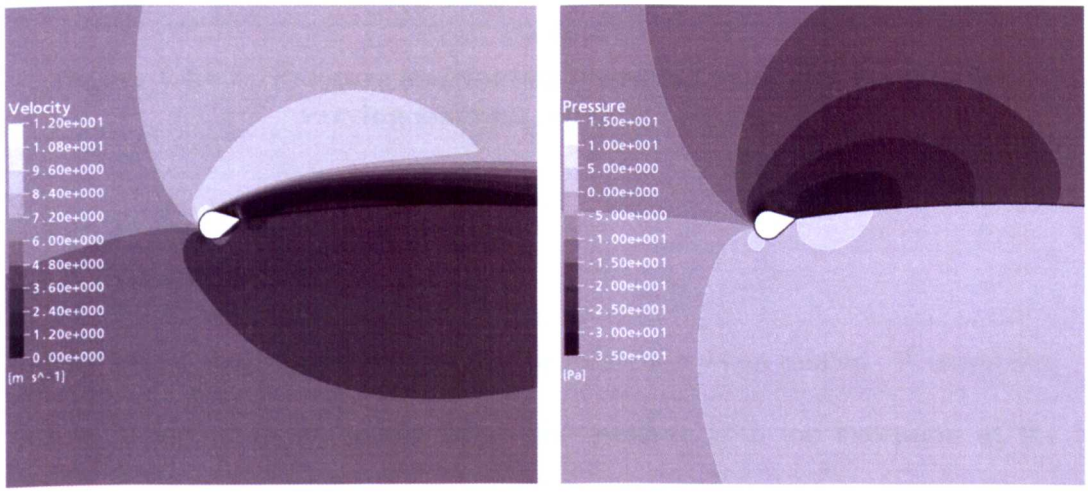

Figure 4.4.4.2 - Velocity and pressure contours for the tangent aligned round mast with fairings.

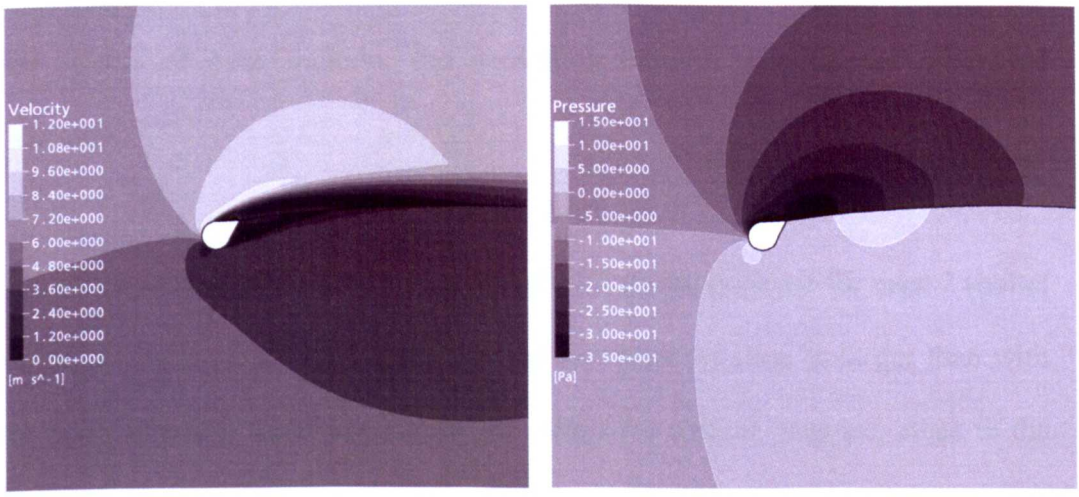

Figure 4.4.4.3 - Velocity and pressure contours for the fully rotated round mast with fairings.

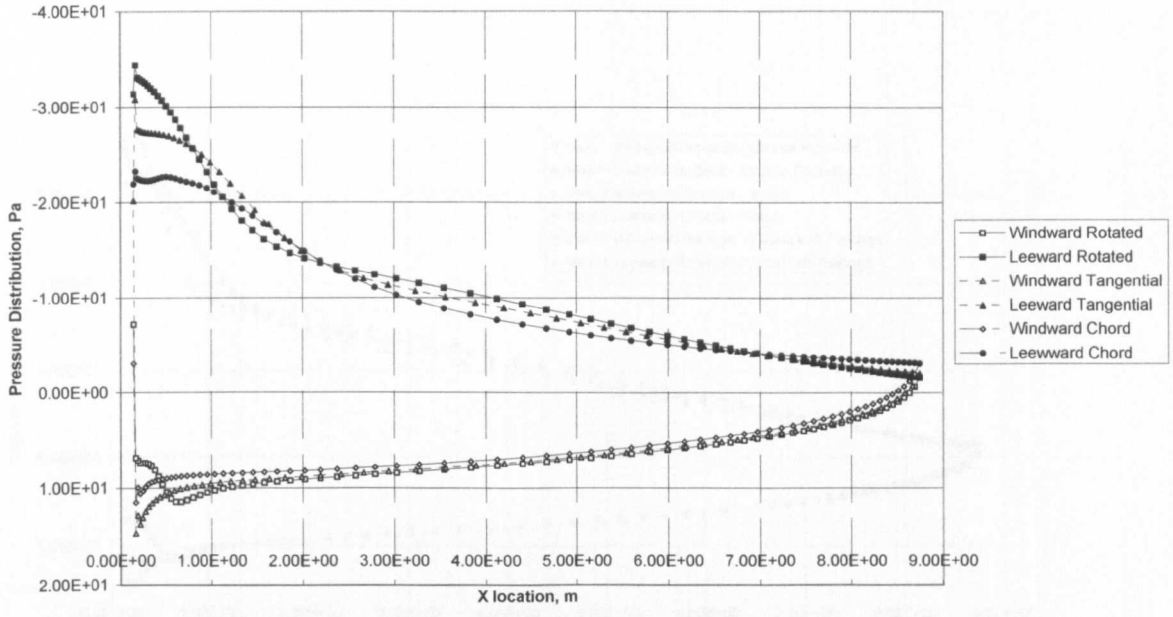

Figure 4.4.4.4 - Pressure distribution for round mast with fairings for varying amounts of mast rotation.

4.4.5. Mast Comparison

Figure 4.4.5.1 shows pressure profiles for masts 1-3 when rotated. A surprising feature is the similarity of the windward pressure with the exception of the leading edge. It is evident that the bubble that occurred with mast 3 (round with fairings) reduced the windward pressure at this location. This is an early sign of the effects of over rotation, the separation bubble reducing the windward pressures.

The other point to note is the high peak of the leeward pressure for mast 2 (bullet shape) at the leading edge. Although the low pressure peak is larger than with the other masts, it does drop below the others for a short distance, close to the mast, before increasing above the other mast sections as the distance from the

mast is increased. As discussed in Section 4.3 this is due to the earlier reattachment location for mast 2.

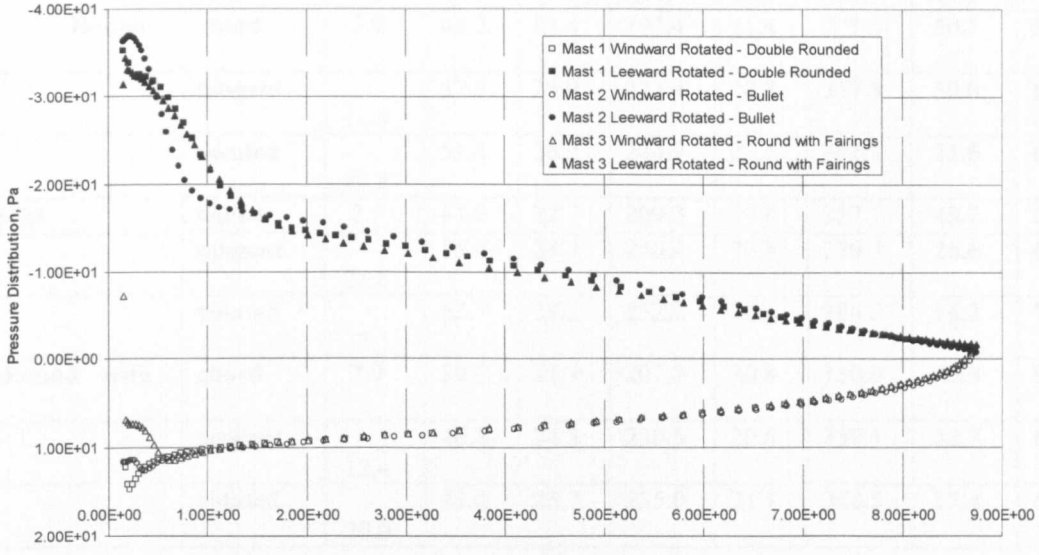

Figure 4.4.5.1 - Pressure comparison of rotated masts.

Figures 4.4.5.2 and 4.4.5.3 show the total forces on the mast-sail combinations at the different rotation angles. These plots show clearly that performance gains are seen by all of the masts, irrespective of their shape; they all give improved results as they are rotated. These improvements can be as significant as a 65% reduction in drag and a 25% increase in lift. Figures 4.4.5.2 and 4.4.5.3 also highlight the importance of mast profile shape especially when rotated. The difference in drag between masts 2 and 3, when rotated, is over 40%, Table 4.4.5.1. There are significant gains to be obtained from careful analysis and choice of mast section, whether rotated or fixed.

		Mast		Windward Sail Surface		Leeward Sail Surface		Total Drag	Total Lift
		X	Y	X	Y	X	Y	X	Y
	Rotation	(N)	(N)	(N)	(N)	(N)	(N)	(N)	(N)
Mast 1 - Double Rounded	**chord**	7.9	44.2	21.4	202.4	21.4	323.5	**50.7**	**570.0**
	tangent	-14.9	57.0	24.9	233.4	20.8	357.8	**30.8**	**648.1**
	rotated	-27.8	51.4	26.2	244.7	23.1	381.1	**21.5**	**677.2**
Mast 2 - Bullet	**chord**	2.7	41.0	22.7	209.3	19.8	337.1	**45.2**	**587.4**
	tangent	-21.6	55.4	25.7	240.4	22.5	370.3	**26.6**	**666.1**
	rotated	-37.5	62.7	27.3	252.2	26.4	386.2	**16.2**	**701.1**
Mast3 - Round with Fairings	**chord**	2.9	39.0	21.9	207.7	20.8	330.0	**45.5**	**576.7**
	tangent	-12.4	46.8	24.3	230.5	20.8	359.1	**32.7**	**636.4**
	rotated	-20.0	47.0	25.7	235.0	21.7	368.5	**27.4**	**650.5**

Table 4.4.5.1 – Mast rotation force breakdown

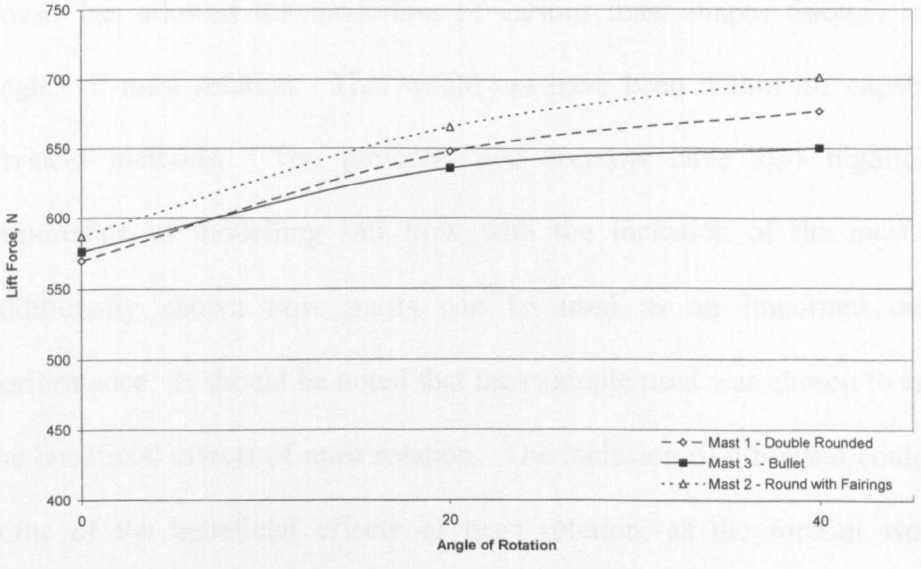

Figure 4.4.5.2 - Lift force comparison for different mast shapes through a range of mast rotations.

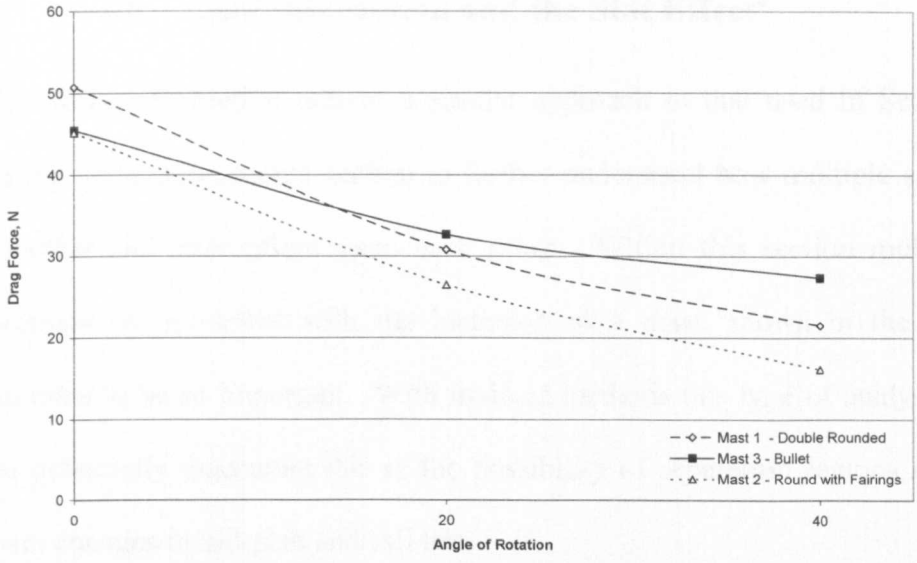

Figure 4.4.5.3 -Drag force comparison for different mast shapes through a range of mast rotations.

4.4.6. Mast Effect Summary

The capabilities of viscous CFD to predict separation zones and reattachment points has allowed the modelling of various mast shapes through increasing angles of mast rotation. This would not have been within the capabilities of inviscid methods. The previous two sections have also highlighted the importance of modelling sail flow with the inclusion of the mast. It has additionally shown how masts can be used as an important aid to rig performance. It should be noted that the example used was chosen to emphasise the beneficial effects of mast rotation. The inclusion of a foresail could remove some of the beneficial effects of mast rotation, as the foresail would help maintain attached flow along the mainsail. Despite this caveat, the potential of mast rotation to improve performance is significant, with drag savings of up to 65%.

4.5. Sail Interaction and the Slot Effect[3]

The following section utilises a similar approach to that used in Section 4.4, using a two dimensional section to further understand how multiple sails work together and their effect upon each other. Within this section multiple sail sections are modelled with the inclusion of a mast, shown in the previous sections to be so important. With inviscid methods this type of analysis would be potentially inaccurate due to the possibility of separation regions appearing with changes in sail plan and sail trim.

Initially the foresail's effect upon performance is investigated and how the two sails of a standard sloop interact, Section 4.5.2. Following this initial study into the interaction between sails, a brief study into the effect of foresail trim is investigated, Section 4.5.3. This details how relatively small changes in trim can affect the performance of the rig.

4.5.1. Mesh and Case Setup

A similar computational approach to that used and detailed in the previous sections (Section 4.1 to Section 4.4) has been utilised within this section. The commercial CFD code ANSYS CFX 10 and the SST RANS turbulence model have been used for all the simulations presented in this section. The meshes created contained a mixture of hexahedral and triangular prism based cells.

---

[3] The work within this section has been published as a journal paper *'Using computational fluid dynamics to model sail interaction - the 'slot effect' revisited'* in the Journal of wind engineering and industrial aerodynamics (Paton and Morvan, 2007c)

Boundary inflation layer cells were used around the surfaces to resolve the flow within the boundary layer, Figure 4.5.1.1. y^+ values on the sail and mast surfaces of approximately 3 were obtained.

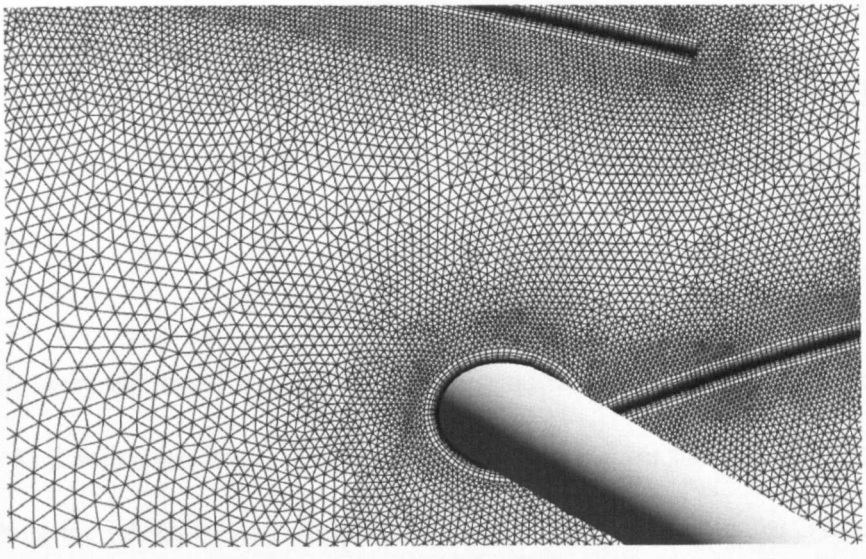

Figure 4.5.1.1 - Typical mesh refinement used throughout the sail interaction section.

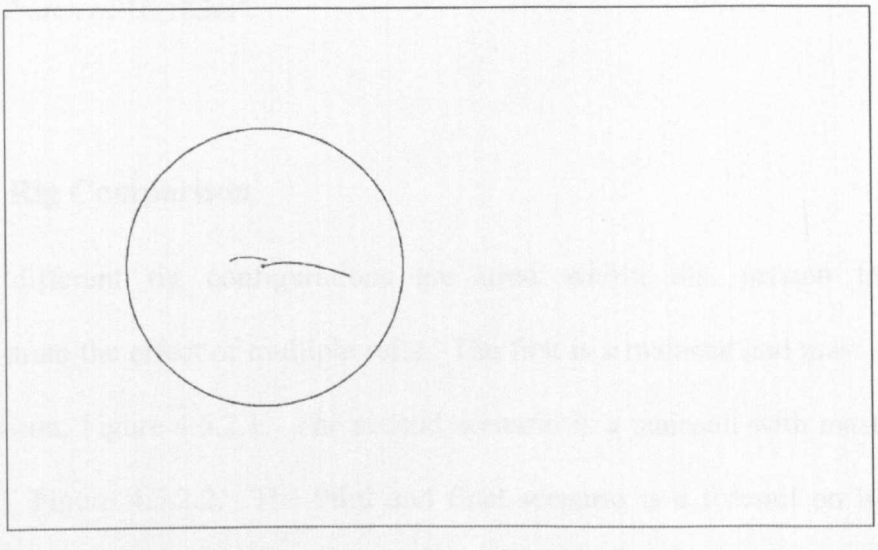

Figure 4.5.1.2 – Central rotating region and fixed outer region used throughout the sail interaction study.

The meshes used the turntable approach, with a central circular rotating sector, enclosing the sail and the mast, and an outer fixed sector, Figure 4.5.1.2. This is a similar approach to that detailed in Section 4.2. The convergence criteria

detailed in Section 4.2 has also been used throughout this section. The domain was 30m high and 50m long.

Physical timesteps were chosen of 0.001s to ensure convergence within a maximum of 4 iterations per timestep. A time averaging of coefficients was used as detailed previously in Section 4.2. A high resolution advection scheme was used.

The sails were all tested in upwind sailing conditions in a moderate breeze of 5 ms^{-1} or 11.2 miles per hour. This equates to a force 3 on the Beaufort scale. A 5% turbulence intensity was set at the inlet. The sail sections were created from extruded two dimensional curves, resulting in a foresail area of 4.245m^2 and mainsail area of 10.183m^2.

4.5.2. Rig Comparison

Three different rig configurations are used within this section to help demonstrate the effect of multiple sails. The first is a mainsail and mast section in isolation, Figure 4.5.2.1. The second scenario is a mainsail with mast and a foresail, Figure 4.5.2.2. The third and final scenario is a foresail on its own, Figure 4.5.2.3. The aim of this section is to determine the influence that a foresail, which is correctly trimmed, can have upon a mainsail. It should be noted that all sail sections were kept at a constant angle to the wind for comparison.

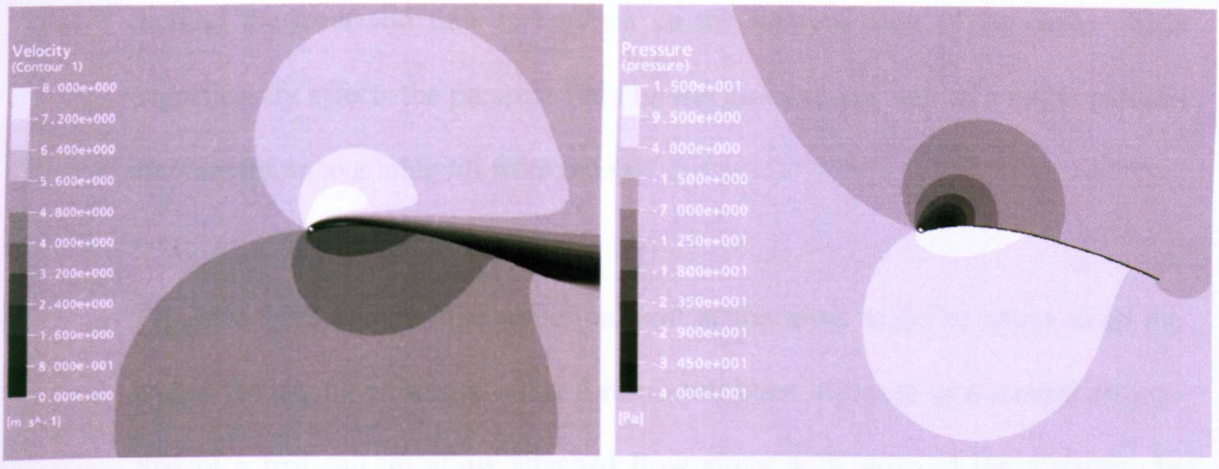

Figure 4.5.2.1 - Velocity and pressure plots over a mainsail in isolation.

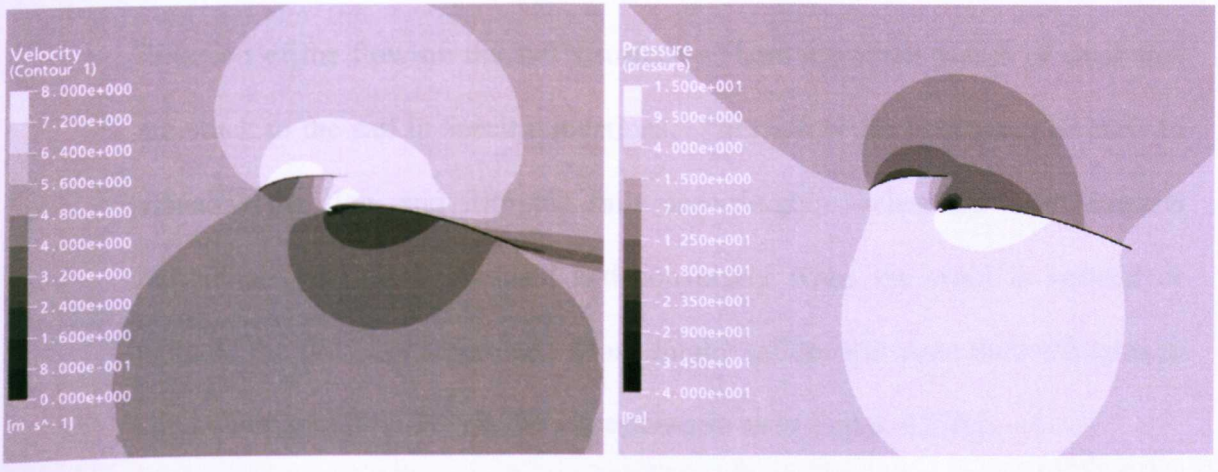

Figure 4.5.2.2 - Velocity and pressure plots over a mainsail and foresail combination.

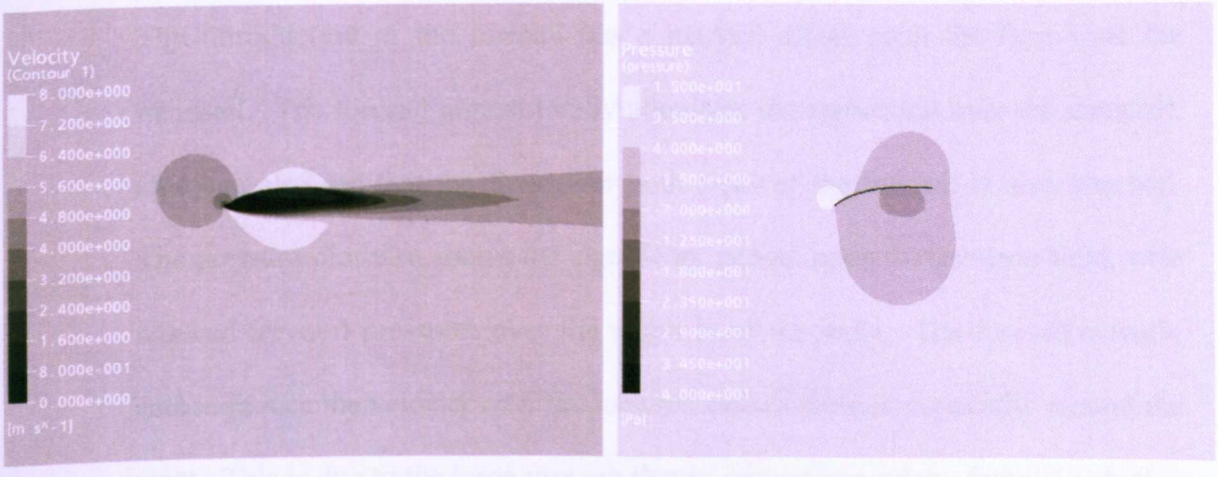

Figure 4.5.2.3 - Velocity and pressure plots over a foresail in isolation.

Figure 4.5.2.1 shows velocity and pressure contours past a mast with a mainsail. The most notable feature of the flow is the large area of separation that forms

behind the mast and fails to reattach on the leeward face of the main. This significantly affects the pressure field on the leeward side and as a result reduces the maximum available lift from the sail.

Figure 4.5.2.2 features the same mainsail at the same angle of attack with the added feature of a foresail. The foresail has been trimmed in a similar way to that of a real sail, to allow attached flow along both sides of the foresail. In smaller sailing vessels such as racing dinghies, 'tell tales' are used to show the direction of the flow on the sail's surface. These are small pieces of wool that are stuck to the sail in specific locations. They allow the helmsman or crew to visualise the flow and trim the sails accordingly. When the wool streams horizontally the air is attached and conversely when the wool is vertical or agitated the flow has separated. Most dinghy sailors will want their tell tales to stream horizontally. This is the same scenario as in Figure 4.5.2.2.

The introduction of the foresail has a marked effect upon the flow over the mainsail. The foresail almost totally alleviates the separation over the mainsail. One can also see that the flow over both sides of the foresail is also attached. The pressure plot also shows the significant impact upon the pressure field, with reduced leeward pressures over the majority of the main. The foresail actually acts to reduce the velocity over the leeward side of the sail, especially around the mast. This is due to the large upwash that is created around the foresail reducing the flow and velocity of the air in the slot. Some of the air that would have flowed along the leeward side of the mainsail and mast is now taken around the foresail.

Figure 4.5.2.5 also demonstrates the changing velocity of the air within the slot. From this figure it is easy to visualise how the foresail could be described as creating a Venturi, as the flow does accelerate as it travels through the slot. This is visible from both the vector plots and the converging streamlines shown in Figure 4.5.2.5. The flow is accelerated through the slot which helps to maximise lift over the mainsail. Despite the slight Venturi type effect seen from the foresail, the main benefit of the foresail on the mainsail is the reduction in the separation around the mast. The comparison of the velocity plots in Figure 4.5.2.1 and Figure 4.5.2.2, demonstrates the reduction in mainsail separation. Separation is also minimised behind the mast, maintaining attached flow across both sails.

Figure 4.5.2.3 is a plot of the foresail in isolation. The lack of the mainsail has a significant effect and allows the flow to separate on the windward side of the foresail. As mentioned earlier, this is due to the lack of upwash from the mainsail that would help keep the windward flow attached. The flow separates at the leading edge of the foresail with a large turbulent region in the sail's wake. This separation clearly dramatically affects the lift, with reduced pressures on the windward side. In reality the sail would collapse as there is not a significant pressure differential across the sail. This could be overcome by turning the boat away from the wind, thus increasing the angle of attack of the foresail and the pressure differential across it.

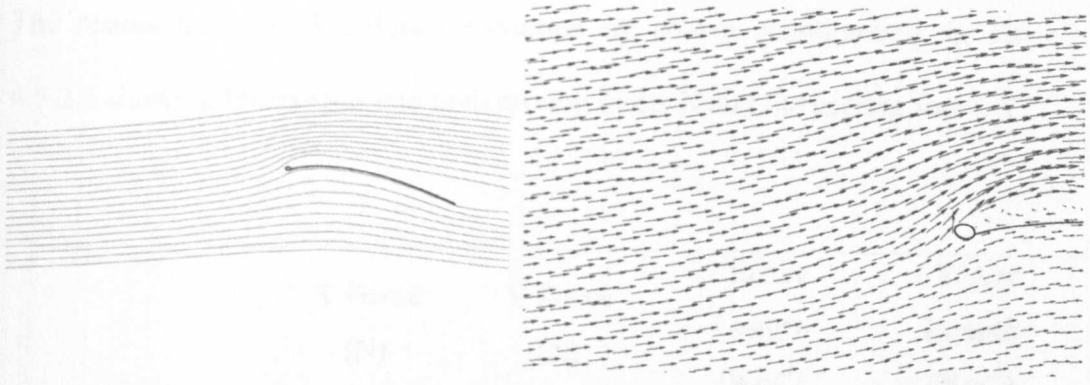

Figure 4.5.2.4. Streamlines and vector plots for the mast and mainsail.

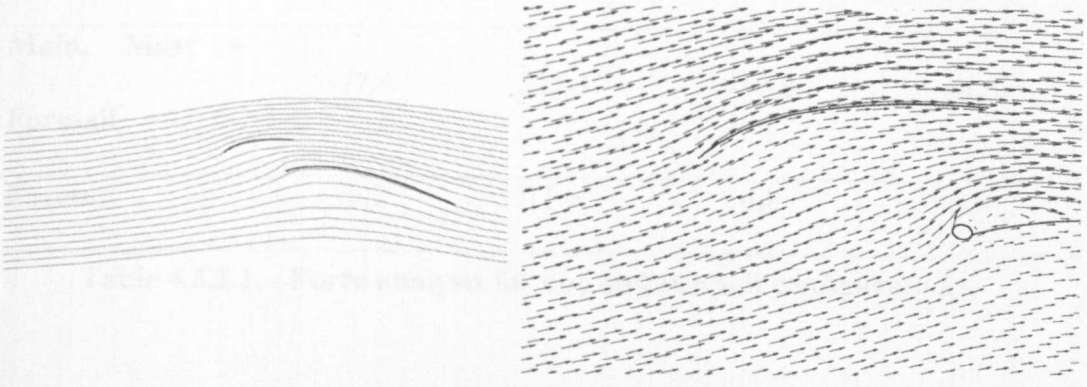

Figure 4.5.2.5 - Streamlines and vector plots for the mast, mainsail and foresail.

The streamlines in Figure 4.5.2.4-5 graphically illustrate the upwash created around the sails. The amount of upwash is greater for the two sail configuration than for the single mainsail. However, despite the increase in upwash there is less separation around the mast and mainsail. This is caused by the reduced peak in the leeward pressures and the gentle approach of the stagnation streamlines, Figure 4.5.2.5. The flow through the slot also acts to re-energise the boundary layer, delaying separation, when compared to a single aerofoil with similar chord length and curvature. The velocity vectors show how the foresail acts to initiate the upwash at an earlier stage than that of the mainsail only, with a gentler approach angle.

The results from the 3 different scenarios are shown quantitatively in Table 4.5.2.1 showing forces split into both driving force, X and the heeling force, Y.

	X Force (N)	Y Force (N)	X/Arc Length (Nm^{-1})	Y/Arc Length (Nm^{-1})
Main + Mast	-32.6	211.7	-6.4	41.6
Main, Mast + Foresail	-77.4	321.3	-10.7	44.6
Foresail	10.2	11.6	4.8	5.5

Table 4.5.2.1. - Force analysis for one and two sail configurations.

For a sailor or designer the most important factor in increasing boat speed is maximising the driving force whilst keeping the healing force within acceptable limits. The X forces in Table 4.5.2.1 are aligned with the vessel and thus represent the driving force. The Y Force is the force perpendicular to the X force and would represent the force creating a healing moment. The combined sail configuration clearly creates significantly more driving force; however there is an increase in sail area which would account for some of this. Also included in Table 4.5.2.1 are the forces divided through by the area of the sail, to provide an indication of the efficiency of the sails. This shows how much more efficient the combined sail rig is than the mainsail alone.

The X force for the foresail on its own is positive. This would represent a negative driving force and the vessel would actually fail to make positive progress at this angle to the wind. With regard to the two sail configuration, an

interesting feature is that the total force is drastically different to that of the two individual sails added together. The combined sail created a total driving force of 77.4N, compared to the sum of the individual sails creating a total driving force of 22.4N

It is worth noting at this point that the sail geometries have not been optimised. The angle of attack for a two sail configuration is not necessarily suitable for a single sail. However a constant angle of attack was chosen to show the effect of the interaction with more clarity.

In Table 4.5.2.2 the forces for the two sail configuration are broken down into their individual components and compared to the individual sails seen in Table 4.5.2.1. This helps illustrate the effect the foresail has upon the mainsail.

	Combined Sail Breakdown		**Individual Sails**	
	X Force (N)	**Y Force (N)**	**X Force (N)**	**Y Force (N)**
Main + Mast	-24.3	204.8	-32.6	211.7
Genoa	-53.1	116.5	10.2	11.6
Total (mainsail, mast +foresail)	-77.4	321.3	-22.4	223.3

Table 4.5.2.2. – Force comparison for sails when used in a 2 sail rig and in isolation.

The introduction of the foresail causes a 30% reduction in the driving force of the mainsail in the isolated scenario. Despite this the total force increases from

-22.4.6N to -77.4N. This large increase is down to the contribution from the foresail which has a significant impact on the lift of the combined rig. As mentioned earlier the foresail is much more efficient than the mainsail. The two sails complement one another and help improve the flow and reduce separation.

In Summary, the foresail affects the mainsail by:

- Reducing the velocity of the flow around the mast.
- Reducing the pressure gradient around the mast
- Reducing rapid 'upwash' around the mast.
- Reducing separation around the mast.
- Maintaining attached flow along the leeward side of the mainsail.

The mainsail affects the foresail by:

- Reducing windward separation.
- Increasing 'upwash' around the foresail.
- Reducing the angle to which the foresail can sail to the wind.

4.5.3. Foresail Trim Comparison

In the previous section the foresail was set to a realistic trim, where the flow remains attached over both faces of the foresail, Figure 4.5.2.2. The sheeting angle of the foresail can simply be changed by altering the foresail sheet length. If this sheet is pulled in further the angle of attack is increased, often termed 'closing the slot'. This has the effect of reducing the size of gap between the foresail and mainsail, which increases the velocity of the air in the slot. The

oversheeting of the foresail is demonstrated in Figure 4.5.3.1 and Figure 4.5.3.2. The oversheeting of the foresail has some beneficial effects. The most obvious of this is the increased velocity of the air flow over the leeward side of the mainsail reducing the separation around the mast. However despite this reduction in separation the lift created from the mainsail alone actually reduces. When oversheeting of the foresail has an adverse effect on the sails performance, it is known as 'choking the slot'.

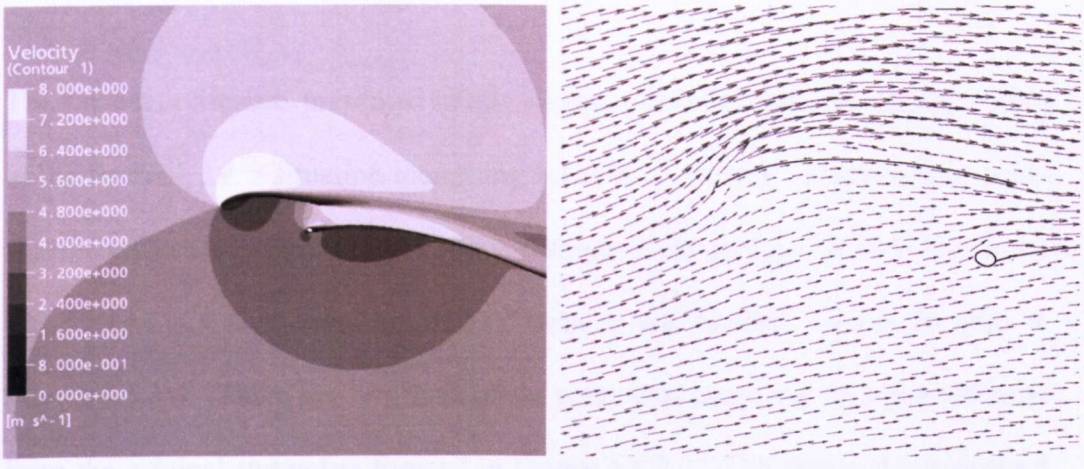

Figure 4.5.3.1 - Velocity and vector plots for a slightly oversheeted mainsail.

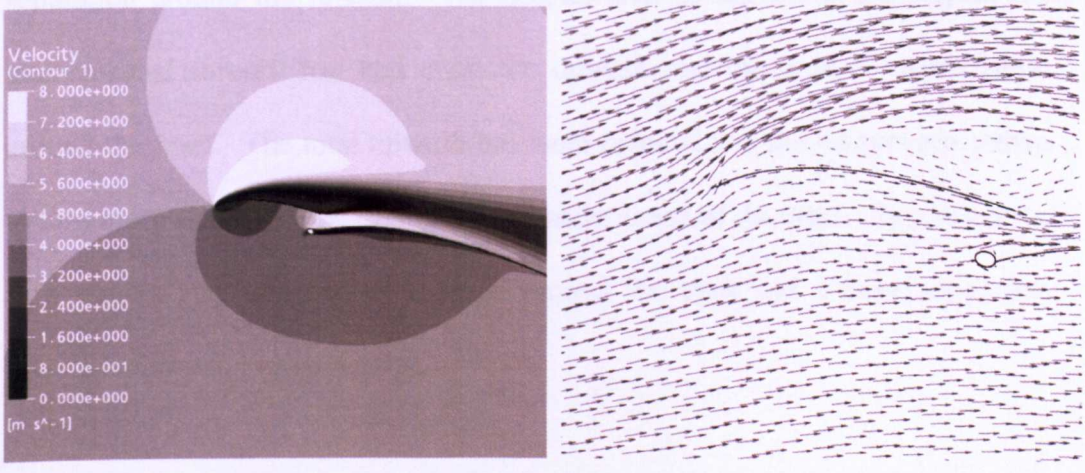

Figure 4.5.3.2 - Velocity and vector plots for a heavily oversheeted mainsail – the choked slot.

Figure 4.5.3.2 shows the choking of the slot to the extreme. In this scenario the foresail is sheeted in significantly towards the mainsail, funnelling the flow over the mainsail, commonly described as a Venturi type situation (Gentry, 1981). This still fails to increase the lift of the mainsail and significantly affects the flow over the foresail, creating a large separation bubble on t

he leeward side of the foresail. This dramatically reduces the lift force created from the foresail and as a result the overall rig's driving force.

The final set of results presented in this section is created from the undersheeting of the foresail, i.e. a situation increasing the size of the slot. This scenario could also be termed an open slot. It can occur when the foresail sheet is let out or when there is a significant amount of twist in the foresail. It can be seen in Figure 4.5.3.4. There are two immediate areas that stand out as being different from the original streaming foresail in Figure 4.5.2.2. The first is the windward separation around the foresail. The second area of interest is the impact the undersheeted foresail has had upon the upwash and the area of recirculation around the mast. The total upwash has been reduced and the vectors are shown to turn more sharply in the region immediately ahead of the mast. As a result the flow cannot stay attached as it flows around the mast and a large separation bubble is formed, Figure 4.5.3.4.

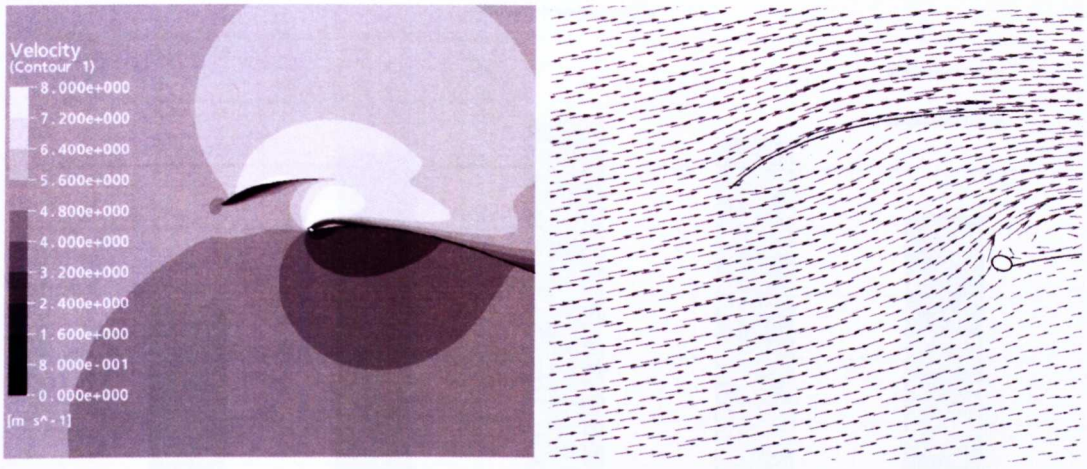

Figure 4.5.3.4. - Velocity and vector plots for an undersheeted foresail.

Figure 4.5.3.5 shows a comparison and breakdown of the driving forces for the different foresail sheeting angles, including an extra case for a foresail undersheeted yet further than that shown in Figure 4.5.3.4. The plot breaks down each sail into its components, the foresail and the mainsail. From the total forces it is clear to see that the optimum sheeting angle was the original, with attached flow on both sides of the foresail. Figure 4.5.3.5 also highlights the trend of the mainsail contribution, which continues to increase as the foresail is let out. This is due to the foresail having a reducing impact upon the mainsail leeward flow field.

An interesting feature of Figure 4.5.3.5 is the relatively flat top to the total driving forces. The driving forces for the over sheeted and under sheeted foresails are not significantly different from the maximum value, with a maximum deviation of 7%. To get a small increase in driving force the sails have to be constantly 'played' to adjust the sails to the constantly changing environment of the wind in the real world. This can be further complicated by the effect of waves, wind twist and gusts.

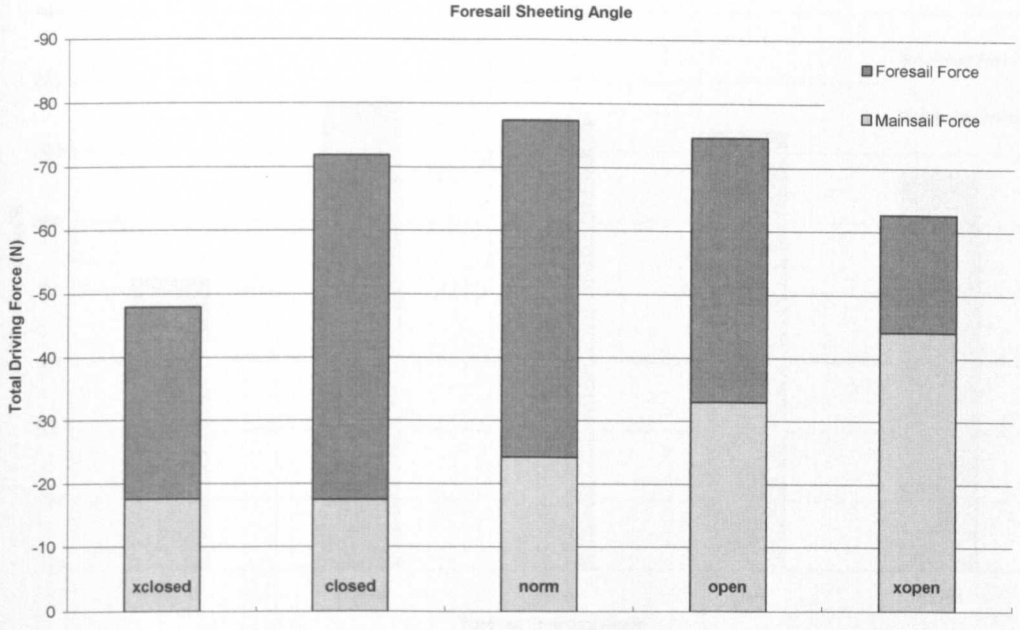

Figure 4.5.3.5 – Comparison of driving forces at different foresail sheeting angles.

The other force component analysed in this section is the healing force. This is the force perpendicular to the driving force and is the lateral force on the sail and boat, causing the boat to heal. Figure 4.5.3.6 shows the total healing forces for the various foresail sheeting angles, with its components from mainsail and foresail. The largest healing force is created when the sheet is slightly over sheeted. It is perhaps surprising that the healing force for the extra closed slot is considerably reduced. This is due to the stalled foresail.

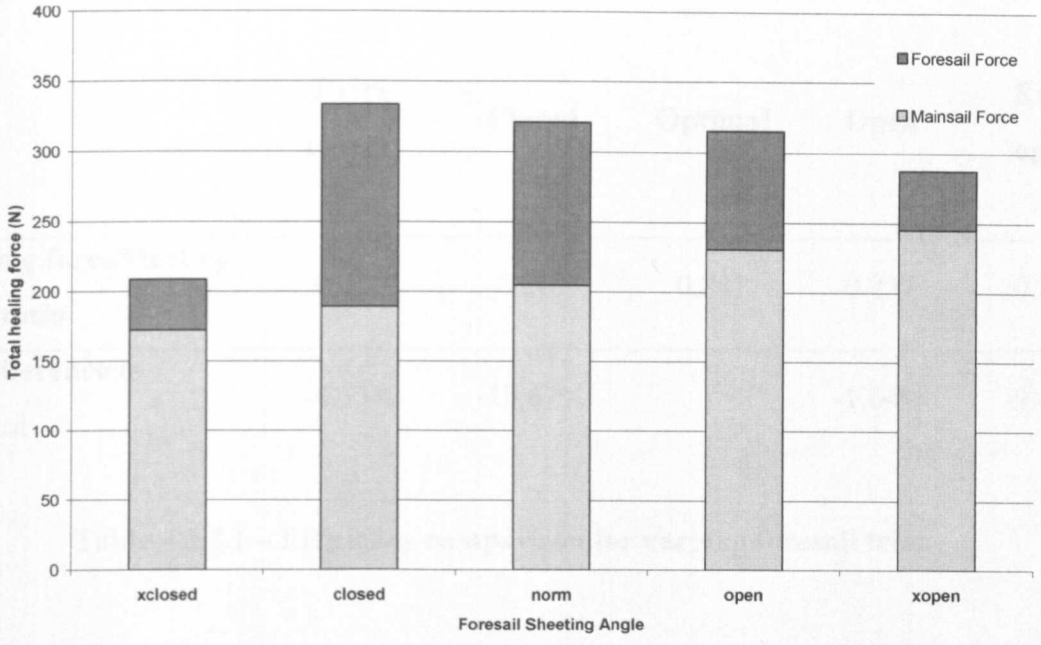

Figure 4.5.3.6 – Comparison of healing forces at different sheeting angles.

A measure of efficiency for airofoils often used is the lift/drag ratio. For this scenario the ratio has been adapted for driving force/healing force. These are shown in Table 4.5.3.1. Here it can be seen that unsurprisingly the streaming case is the most efficient. The case with a slightly closed slot has a significant drop in efficiency with a 10% reduction relative to the optimal case. The slightly open case has a less significant reduction in efficiency with a 1.64% reduction in efficiency relative to the optimal case. In real life this is a useful coincidence as it allows the foresail trimmer to slightly undersheet the sail until it blows back or 'luffs' and then sheet in a little, a common practice for genoa and spinnaker trimmers.

	Extra closed	Closed	Optimal	Open	Extra open
Driving force/Healing force ratio	0.230	0.215	0.241	0.237	0.218
% difference to optimal	-4.55%	-10.67%	/	-1.64%	-9.45%

Table 4.5.3.1 – Efficiency comparison for varying foresail trim.

4.5.4. Sail Interaction Summary

The closed slot creates a reduction in the mast separation, but despite this a reduction in driving force is achieved. The converging streamlines in the slot and the accelerating flow, similar to that of the Venturi theory, was also observed. These results show clearly that although a Venturi type scenario exists, with converging streamlines and increasing velocities, exaggerating this effect is not beneficial and fails to increase the driving force in such flow conditions.

This section underlines the need to model multiple sails as an integral system rather than in isolation. It also highlights the need to capture separation, again highlighting the potential benefits of RANS based methods over inviscid methods. The work highlights the complexity of sail flow and how sail design must be taken as a whole rather than as individual parts. The interaction of sails with each other and the mast is fundamental in designing a fast vessel. As in a Formula 1 car, the rear wing should not be designed without knowing how the

rest of the car impacts the onset flow, similarly a holistic philosophy should be applied to sailing rigs and modelling their performance.

4.6. Summary

Within this chapter the use of RANS based CFD has been proposed for the study of sail performance and validated against existing numerical and experimental cases. The SST turbulence model has shown to perform well and to be a suitable choice for the work. Its accuracy level, strengths and flaws have been ascertained for the application considered.

The method correctly modelled the trends of a circular arc section through a range of wind angles, replicating Collie's study (2005). The study predicted the lift coefficient to within an average percentage error of 8.6%. Post processing of these results also gave added insight into the fundamental causes of the trends, in particular the onset of leading edge separation.

Additionally the method correctly replicated the velocity and pressure profiles of Wilkinson's validation case (1990). The regions of sail flow identified by Wilkinson were also easily identifiable by post processing, which would not all have been captured by inviscid methods.

The influence of the mast upon the sail flow was investigated, to determine the extent to which the flow and forces were affected by it. A mainsail was modelled with and without a mast, with the reduction in drag force of 25.6% and increase in lift of 7.8% when the mast was omitted. This highlighted the importance of including a mast within rig performance analysis. This was

further backed up by the modelling of a rotated mast section, with significant benefits to the rig's performance and potential drag savings of 65% when the mast was rotated.

The final section investigated the influence of sails upon each other. The section highlighted the importance of modelling sails in combination, significantly changing the individual performance of sails at similar angles of attack.

This chapter has shown how complex sail flow can be. The chapter has shown that regions of separation are present for both upwind and offwind sailing conditions and show the important of modelling sailing flows using viscous CFD.

Chapter 5

Fluid Structure Interaction

5.1. Introduction

The simulation of a flexible membrane in fluid flow is complex, requiring the modelling of the complicated interaction between both structural and fluid mechanics. Changes in the flow field affect the shape of the membrane, which in turn affects the resulting fluid response. As described in Chapter 2 there are several different types and approaches to Fluid Structure Interaction. During upwind and certain offwind sailing conditions, the sail shapes created can form steady state geometries. These operating conditions will be the target of the analysis within this thesis.

This steady state simplification of the target use for the FSI simulation, makes an iterative partitioned approach appropriate. This has advantages and disadvantages over a monolithic coupled approach as discussed in Section 2.5. The partitioned approach allows for bespoke software to be used for both the fluid and structural aspects of the analysis. If a monolithic approach were to be used, sacrifices and simplifications would have to be made to make the analysis computationally affordable. The decision was made within this research to develop a partitioned iterative method, suitable for applications where sails form steady flying shapes.

In this chapter, the design and operation of a partitioned coupling procedure between fluid mechanics and structural analysis software is explained. The FSI

loop is covered in detail, including the mesh deformation solution and data transfer utilities used within the partitioned approach. This chapter also includes a discussion about FSI iteration convergence and a validation case for the FSI solution is presented. The validation case comprises of a bespoke wind tunnel test to allow the comparison of the computed flying shapes created from the FSI solution against the sail shapes measured in the wind tunnel. The experimental trials were undertaken in the School of Mechanical, Materials and Manufacturing Engineering climatic wind tunnel, at The University of Nottingham.

5.2. The FSI Loop

Within this section the FSI loop is detailed, documenting the partitioned iterative method. As detailed in Chapter 2, iterative methods are currently already being used in the marine industry, commonly with inviscid codes (Jeremy Elliot, 2008, *personal correspondence*; Peter Heppel, 2008, *personal correspondence*). This type of scheme involves the sequential running of the fluid solver and the structural solver, with the passing of information between the two codes. With the methods currently being used by researchers and sail designers, simplifications are being made in one form another, whether it be the use of an inviscid solver (Shankaran, 2005) or simplified structural solvers (Renzsch *et al.*, 2008).

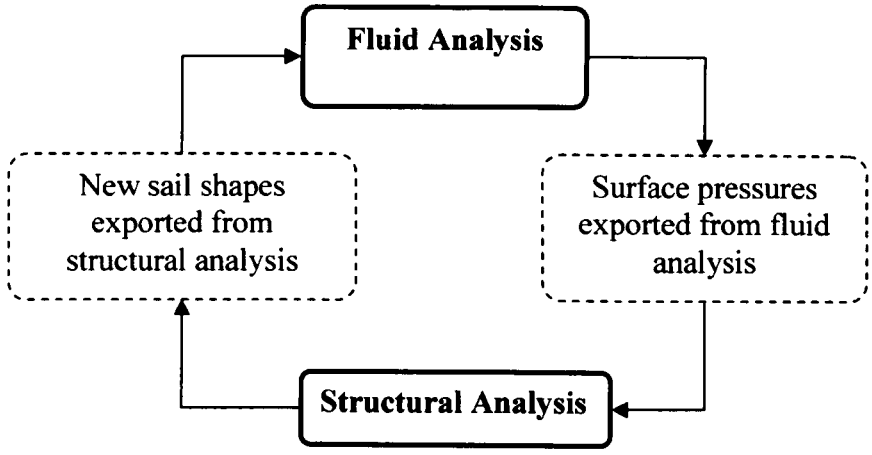

Figure 5.2.1 – Basic FSI loop

Figure 5.2.1 shows the FSI loop for a partitioned FSI solution in its most simplified form, showing the two solvers and the transfer of data between them. For the structural solver to run, it requires the pressure differential across the sail surfaces. The fluid solver requires the deformed sail shape geometry which is taken from the structural solver. Once the loop is started it becomes self perpetuating. Ways of initiating the loop are discussed in Section 5.2.3. This loop is then repeated until a converged solution is achieved and the sail shape converges to a steady state. This is based on initial input parameters that define the wind conditions and details of the rig and trim. Additional measures of convergence include the monitoring of pressures or the primary forces on the sail.

5.2.1. FSI Loop Considerations

Although the FSI loop shown in Figure 5.2.1 appears straightforward, in reality it is not quite so simple. The following considerations need to be taken into account:

- The desire to minimise total computation times whilst maintaining accuracy.

- The difficulty in initiating the FSI loop.
- How to transfer data between the fluid and structural solvers.

The components of the total computation time for a partitioned iterative FSI simulation are summarised in Figure 5.2.1.1 for a single iteration.

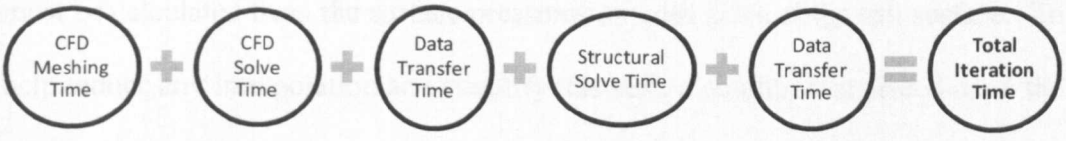

Figure 5.2.1.1 – FSI total iteration time breakdown

To maximise the efficiency of the simulation and minimise computation times, either the total iteration time has to be reduced or a reduction in the number of FSI loop iterations must be achieved. As the CFD solve time and the structural solve time remain relatively fixed, the potential for reduced iteration times must be achieved by improving the meshing time or the data transfer times. Further details on how this has been achieved with this FSI system will be given later, Section 5.3. The data transfer issue is detailed in Section 5.2.2 followed by the FSI loop initiation discussion in Section 5.2.3.

5.2.2. FSI Loop in Detail and Data Transfer

For the FSI loop to be completed, data needs to be transferred between the two solvers. One option is to introduce a third piece of software to host the FSI loop and transfer the data between the solvers. An example of this is MPCCI which is sold as a coupling piece of software (MPCCI, 2009). The disadvantage of such an approach is that it can introduce yet more unnecessary data transfer, with the potential to render the process less efficient and computationally more costly. For

the solution developed in this research, bespoke code was written to link the two pieces of software.

For the structural software to calculate the new deformed sail shapes it is necessary to provide it with a pressure differential across the sail surface. This must be calculated from the surface pressures on both sides of the sail surface. To help reduce any interpolation and simplify this task, a condition is placed upon the sail surface meshing that the surface meshes on both sides of the sail must be identical, i.e. same node locations but on separate sides of the sail. This helps reduce any interpolation errors when calculating the pressure differential file. This pressure differential must also be converted into a specific co-ordinate system and format suitable for the structural code.

Within this research the structural code utilised a (U,V) coordinate system on the sail surface, U being the luff to leach and V along lines from the foot converging to the head. The values of U and V can vary between 0 and 1, with V being 0 at the foot of the sail and 1 at the head, whilst U is 0 at the luff and 1 at the leech. Put in an alternative way, the structural code uses a 2D coordinate system mapped onto the sail surface. This type of coordinate system has the advantage of data always lying on the sail surface. It also allows easier mapping of the old CFD node locations from the previous iteration onto a new sail surface. Following this data transfer the structural code can then solve.

Once the structural solver has completed, data must now be transferred to the fluid solver. The fluid solver requires the new geometry of the deformed sail shape

from the structural solver. In this process a geometric representation of the deformed sail shape is exported from the structural solver as a Non-Uniform Rational Basis Spline (NURBS) surface. Following the export of the new geometry, one option would be to remesh the CFD domain with the new geometry. However, a more computationally efficient option is to deform the node locations of the existing cells, thus manipulating the existing mesh to recreate the new geometry. This technique is called mesh deformation and will be detailed in Section 5.3.

For the deformation of the sail surfaces to occur within the fluid solver, details of the new node locations must be calculated and manipulated into a format for the fluid solver. The fluid solver then updates the node locations before solving. Following this the sail surface pressure differences need to be extracted and the structural solver and FSI loop can start again.

5.2.3. FSI Loop Initiation

Before the FSI loop can be self perpetuating, the structural and fluid models must first be setup. This results in the first FSI loop being slightly different from the subsequent iterations. For the fluid model to be created, a geometry of an initial flying shape must be determined. From this the sail surfaces and domain can be meshed and suitable boundary conditions applied. For the structural code to be able solve it needs a pressure differential across the sail. In consequence, there is no obvious way to start the loop as both require information from the other. One of the most efficient ways of starting the loop is to 'inflate' the sails with a constant pressure differential. This then creates an initial sail geometry which can

be used in the meshing process to start the FSI loop. The initial FSI loop is shown in Figure 5.2.3.1.

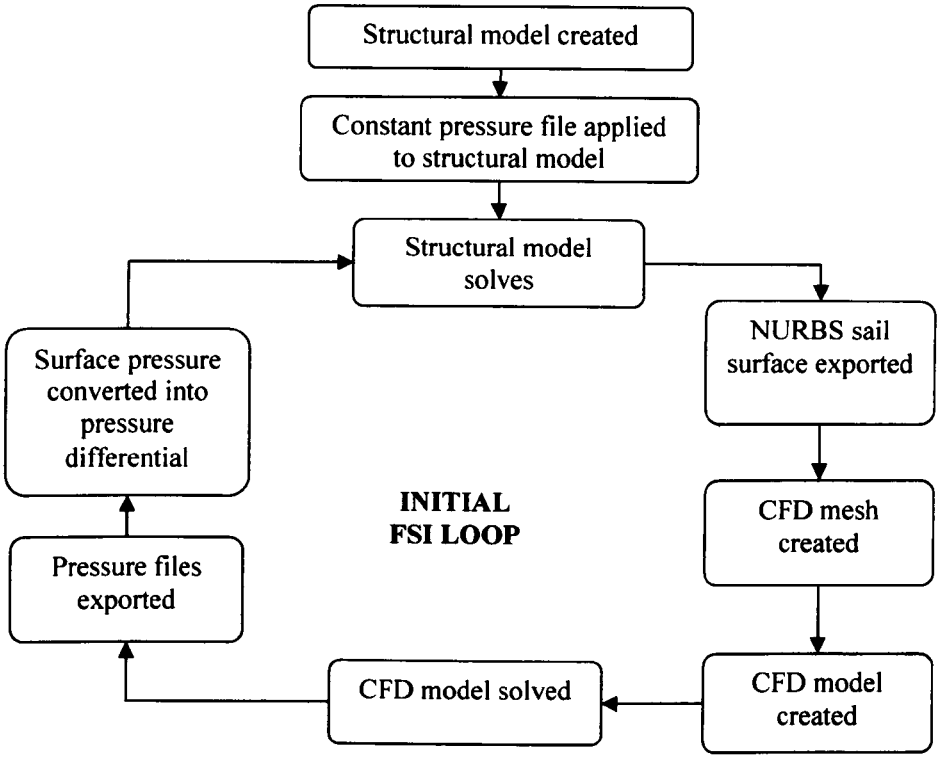

Figure 5.2.3.1 – Initial FSI loop flow chart

5.2.4. Software Execution and Loop Hosting

Another consideration when designing a partitioned iterative FSI simulation is how the FSI simulation is controlled and hosted. Code executions have to be made to launch the relevant data transfer utilities, structural or fluid solvers. Decisions also have to be made as to when to stop the FSI loop. There are various options available including introducing a hosting piece of code such as MPCCI (MPCCI, 2008) which controls the FSI simulation and executes programs or utilities when needed. An alternative is to host the FSI simulation by either the fluid or structural solver. The structural code used in this thesis is RELAX, a bespoke sail modelling code described in Section 5.4 (PHA, 2009). RELAX has

the capabilities to execute commands when required, reducing the need for a third party coupling code. As a result the FSI loop within this thesis is controlled from within the structural solver, in addition to all structural modelling controls. As a consequence, the structural solver remains open throughout the FSI simulation, and when required executes the data transfer and fluid codes. When the structural solver requires a new pressure field it launches the necessary data transfer routines followed by the fluid solver. Finally the second set of data transfer routines are run to complete the loop.

As shown in Figure 5.2.1, in addition to the structural analysis, there are 3 other processes in the FSI loop.

The 3 groups of commands are listed below:

- **Data transfer prior to fluid solver**

  Extracting data from the structural solver and preparing it for the fluid solver.

- **Fluid solver**

  Executing commands to launch the fluid solver.

- **Data transfer prior to structural solver**

  Extracting data from the fluid solver and preparing it for the structural solver.

5.2.5. Process Summary

Following the successful completion of the structural analysis the commands for data transfer prior to executing the fluid solver are called, extracting the sail shape as a NURBS surface and extracting the node coordinates for the fluid solver in the correct format. The fluid solver is then called and launches without any user

interface, updates the sail surface and solves on specified computational resources. The final set of commands are for the data transfer prior to structural solver. These include extracting the pressures from the sail surfaces and creating the pressure differential, before converting them into a format for the structural solver. A linear scheme is used to interpolate the surface pressure from the CFD code onto the structural mesh. Control then returns to the structural solver where the structural analysis is performed. The structural solver then has to decide whether convergence has been achieved and determines the next course of action, whether it be to carry out another FSI loop or stop the analysis. A schematic of the processes involved is shown in Figure 5.2.5.1.

For the FSI solution developed within this research, the fluid and the structural codes were both commercially available. The structural code had also previously been coupled to an inviscid code and so was capable of hosting the FSI solution and capable of reading pressure differential files. This author developed the code coupling routines and the FORTRAN routines called within the fluid solver to update the node locations on the sail surfaces.

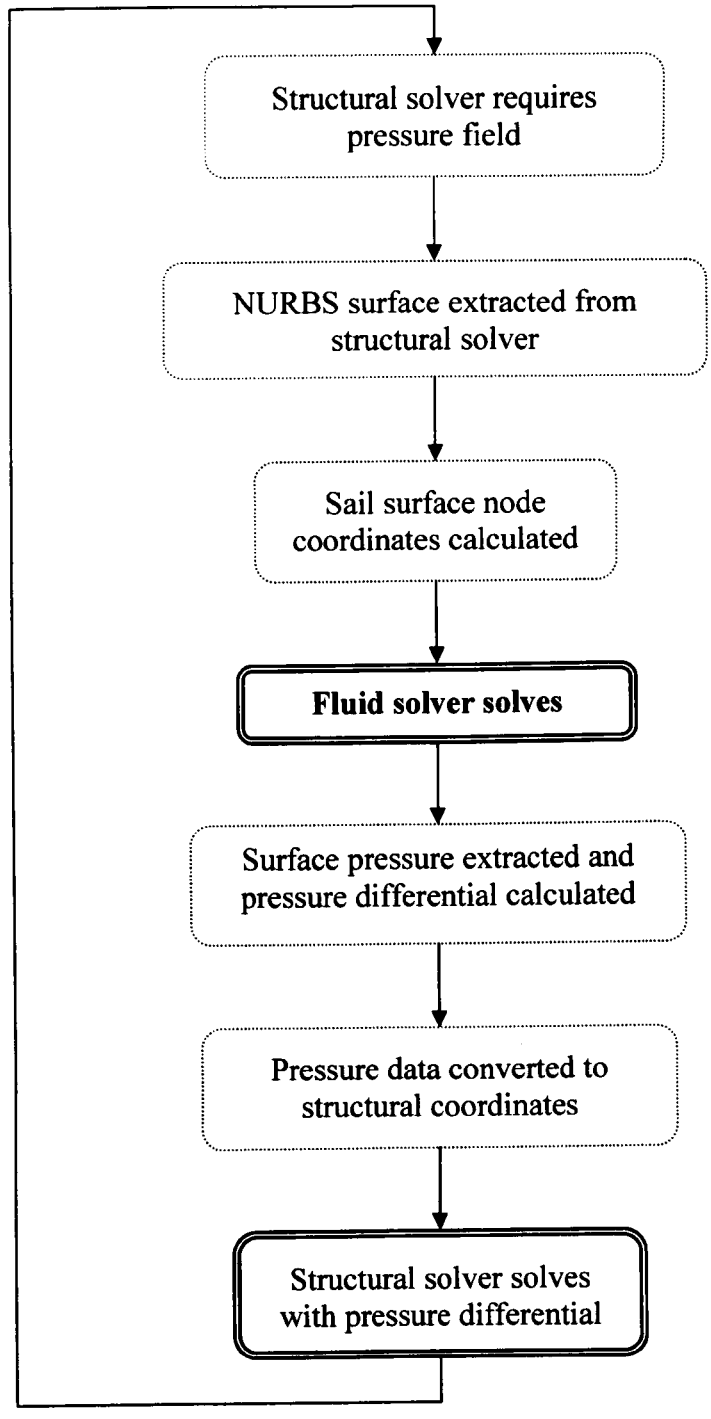

Figure 5.2.5.1 – FSI loop control

5.2.6. Verification of the Code Coupling

To determine the errors introduced from the coupling code, a brief verification exercise was carried out. For this case a set of pressure files from RELAX were exported with a corresponding NURBS surface. These were then converted into the fluid solver coordinates and run through the fluid solver without the mesh deformation routines present. Pressure files were then exported and converted into a single pressure differential file. These were then converted to the (U,V) co-ordinate system ready for the structural solver. The final phase was to convert the files back to (X,Y,Z) fluid solver mesh coordinates for comparison. This is done with the same NURBS surface as the previous loop. This should convert the coordinates back to their starting point, providing errors are not introduced by the coupling code. The verification exercise resulted in maximum coordinate errors below 10^{-6} m, which is acceptable for the purpose of this FSI scheme.

5.3. Mesh Deformation

To allow the sails to deform, the mesh within the fluid solver has to change to match the shapes computed in the structural solver. This could be done with a remeshing process (e.g. Richter and Horrigan, 2003) which takes the new shape from the structural code and remeshes the entire domain with an external meshing piece of software. Such an approach is computationally expensive as the meshes used in these domains are of considerable size. To overcome this, the sail shape is changed using 'mesh deformation', a feature within ANSYS CFX that allows specific locations within the domain to be updated to a new specified location. Figure 5.3.1 shows a basic demonstration of the principle behind mesh

deformation. The figure on the left shows the original mesh and the vertical line in the centre represents part of the sail. In the second figure the sail has rotated. The nodes around it have moved but the connectivity has remained constant. Although the figure shown shows a highly structured mesh, this does not have to be the case.

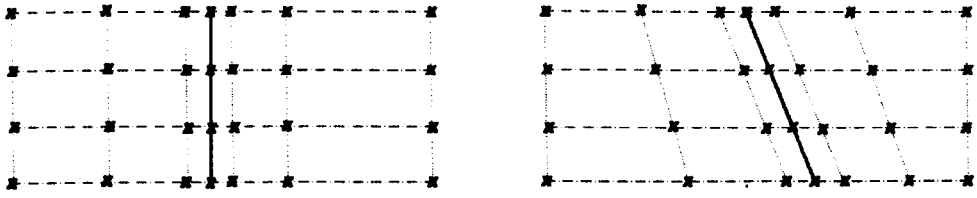

Figure 5.3.1: Mesh deformation within ANSYS CFX

The method behind the mesh deformation used within ANSYS CFX is the displacement diffusion mesh motion model. This theory is used to locate all nodes within the domain which are not explicitly set, either by restrictions placed upon them or because they have been explicitly specified in the mesh deformation process. The displacements are diffused to other mesh points by solving equation 5.3.1 (ANSYS CFX, 2008).

$$\nabla.(\Gamma_{disp}\nabla\delta) = 0 \qquad \textbf{Equation 5.3.1}$$

Where δ is the displacement relative to the previous mesh locations and Γ_{disp} is the mesh stiffness, which determines the degree to which regions of nodes move together. This type of approach is designed to preserve relative mesh distributions e.g. regions of high mesh resolution will remain with high mesh resolution following the redistribution of nodes. Throughout this work mesh stiffness was

specified as being inversely proportional to the element volume. This allows cells with larger volumes to absorb more of the deformation, as their size permits this without unduly affecting cell quality. In contrast the smaller cells, closer to the regions of interest, have smaller deformations and can maintain cell quality.

The mesh deformation process is controlled within ANSYS CFX by calling a 'Junction Box' routine; this in turn calls a FORTRAN routine. A Junction Box routine allows arguments to be transferred from within ANSYS CFX to the FORTRAN code. In this instance the coordinates of the nodes on the sail's surface are transferred.

These coordinates can then be updated to their new locations and returned to the solver. A specific feature of Junction Box routines within ANSYS CFX is their limitation to the return of just a single variable to the solver. This results in the need to run three Junction Box routines, a FORTRAN routine to update each of the X, Y and Z coordinates. Although this is not as efficient as a single routine would be, the mesh deformation expense is relatively insignificant in comparison to the structural and fluid solver times.

As mentioned in Section 5.2.2, to simplify the procedure and reduce the computational expense, the nodes on both sides of the sail's surfaces are stipulated to be coincident. This requirement is specified when creating the original mesh. This helps for two main reasons; the first is that it reduces the time taken during data transfer, which is important when iterative coupling schemes are implemented, by halving the number of nodes to move and the size of the new

node look up matrix. It also helps reduce the time taken during the mesh deformation process itself. This gain is further amplified because of the three routines necessary to update the surface nodes.

When the mesh deformation process is initiated, (X,Y,Z) coordinates of the nodes on the surfaces are transferred to the FORTRAN routine and stored within an array. A search routine is used to find the corresponding (X,Y,Z) location in a 'lookup file' created earlier by the data transfer utilities. This file contains data of the coordinates on the sails surfaces, with both the old and new locations, Figure 5.3.1. The old coordinates are searched for and upon a successful match, the new coordinates are retrieved. A tolerance is specified to allow for slight differences in the coordinate locations due to rounding errors during the transfer process. An example of the lookup table is given below. Once the surface nodes are updated, the remaining nodes in the domain are then deformed using the displacement diffusion mesh deformation model described earlier.

X_{old} (1)	Y_{old} (1)	Z_{old} (1)	X_{new} (1)	Y_{new} (1)	Z_{new} (1)
...					
X_{old} (i)	Y_{old} (i)	Z_{old} (i)	X_{new} (i)	Y_{new} (i)	Z_{new} (i)
X_{old} (i+1)	Y_{old} (i+1)	Z_{old} (i+1)	X_{new} (i+1)	Y_{new} (i+1)	Z_{new} (i+1)
...					
X_{old} (Nloc)	Y_{old} (Nloc)	Z_{old} (Nloc)	X_{new} (Nloc)	Y_{new} (Nloc)	Z_{new} (Nloc)

Table 5.3.1 – Lookup example: 1 < i< Nloc, where i is the node number and Nloc the maximum number of surface nodes

A flow chart summarising the stages involved in the sail/mesh deformation process within this FSI solution is given in Figure 5.3.2.

Care must be taken to ensure the quality of the mesh is maintained, otherwise the cells can degrade when the deformation process occurs. Degradation can be caused by the movement of the cell nodes, causing changes in cell size, skew and aspect ratio. Measures such as the varying mesh stiffness are an attempt to solve these local issues. Other approaches to mesh deformation, such as fixing a region of mesh around the key areas of interest, help maintain cell quality in important areas. However, this alternative type of approach is not applicable due to the flexible nature of the sail surfaces.

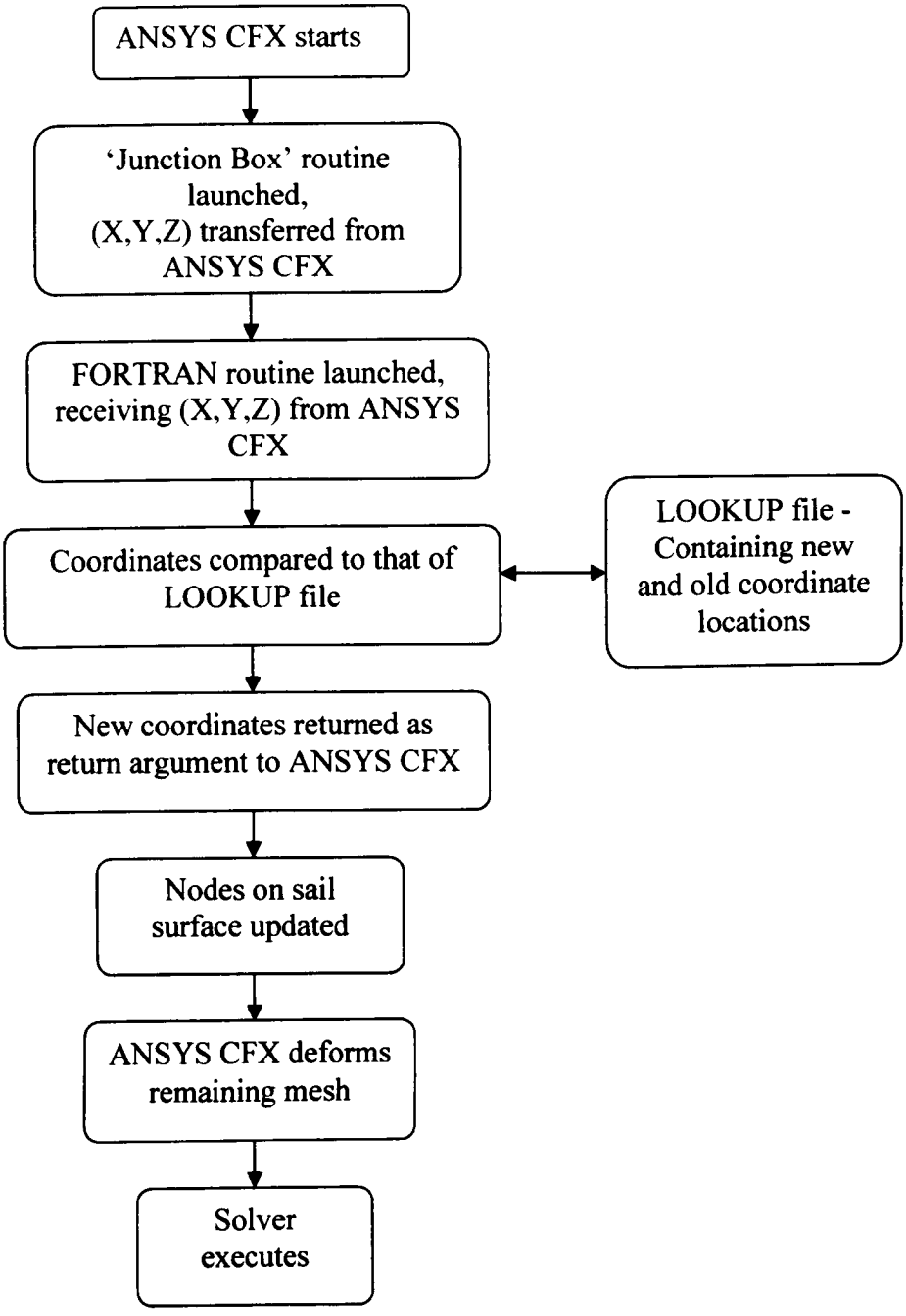

Figure 5.3.2 – Mesh deformation process used to update the sail geometry

5.4. Structural Analysis

As discussed in Chapter 3, the most common form of numerical structural modelling is that of Finite Element Analysis (FEA). Within this FSI solution the Finite Element (FE) code RELAX is used (PHA, 2009), a non-linear Finite Element code, purpose built for the modelling of yacht sails.

The solver is based upon Barnes' studies (Barnes, 1977; Barnes 1994; Barnes, 1999) of dynamic relaxation and kinematic damping. The fundamental principle behind dynamic relaxation is to trace the movement of each node with small time increments, until due to artificial damping the structure comes to static equilibrium. The approach used within RELAX is based upon kinematic damping (Day, 1966; Day 1969). The kinematic damping procedure tracks the total kinematic energy of the system. When a peak in the total kinematic energy is found, all velocities are reset to zero. The process is then restarted until the total kinematic energy tends to zero and the model has reached static equilibrium. Further details of the iterative stages of dynamic relaxation and kinematic damping can be found in Barnes, 1999. During the iterative process, restraints and partial restraints can be placed upon nodes to limit their motion. Restraints are placed upon elements within the mast groove to allow movement only along the mast. Other nodes are fixed such as the tack of the foresail or the head of the mainsail.

The modelling of sailing rigs can be done with membrane elements to model the sail and beam elements to model the battens and mast. A membrane is the limiting case of a shell, where thickness tends to zero. Consequently, it does not

resist bending moments. Sail materials are actually complex composite materials, with modern racing sails consisting of filaments, laid between two films to hold them in place. As a result the material properties of the sails are highly anisotropic (vary with orientation). It is important that these anisotropic material properties can be modelled by the structural solver to allow an accurate representation of the sail.

Prior to meshing of the surfaces, first the sail shape must be created within RELAX, including the thread layout, batten locations and any additional detail required in the model. Within RELAX, physical attributes are then applied to each of these features. The mould surface can then be meshed to create a set of triangular membrane elements, with a suitable mesh density and localised refinement i.e. near the clew. The meshing of the sail surfaces in RELAX is carried out using an automated triangle based mesher. The process of triangulation is based upon Delaunay triangulation, where the grid is refined to panel edges and regions of curvature. During the iterative process the surface mesh remains constant. Each triangular element then interrogates the property field to determine the mechanical properties to be stored at the triangle centroid. Fully orthotropic (material properties are independent of direction) values can be interrogated and stored. The solver can then solve and store data for later use or post processing.

5.5. Convergence

As the FSI loop iterates, the sail shapes should converge towards a steady state solution. The less FSI loops needed to converge, the faster the simulation. Perhaps as important to the speed of convergence is the stability of the FSI solution. Large changes in trim provide a good test case for the stability and rate of convergence of an FSI scheme.

Shown below in Figures 5.5.1-3 is the iterative convergence of a generic mainsail. The three plots represent sections through the sail at three different heights up the mast, 10, 20 and 30m from sea level (approximately ¼, ½ and ¾ of mast height). The convergence example shows slices at each iteration for a significant re-trim of a poorly trimmed mainsail (the different scales on each axis should be noted).

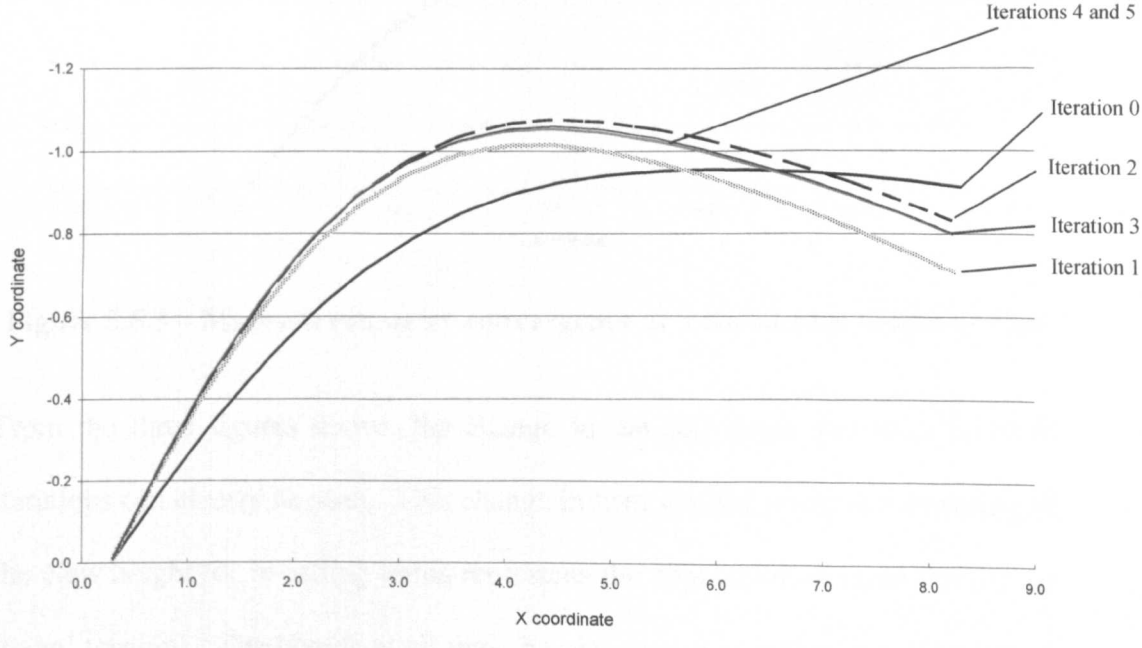

Figure 5.5.1 – Mainsail geometry convergence at a chord slice height of 10m

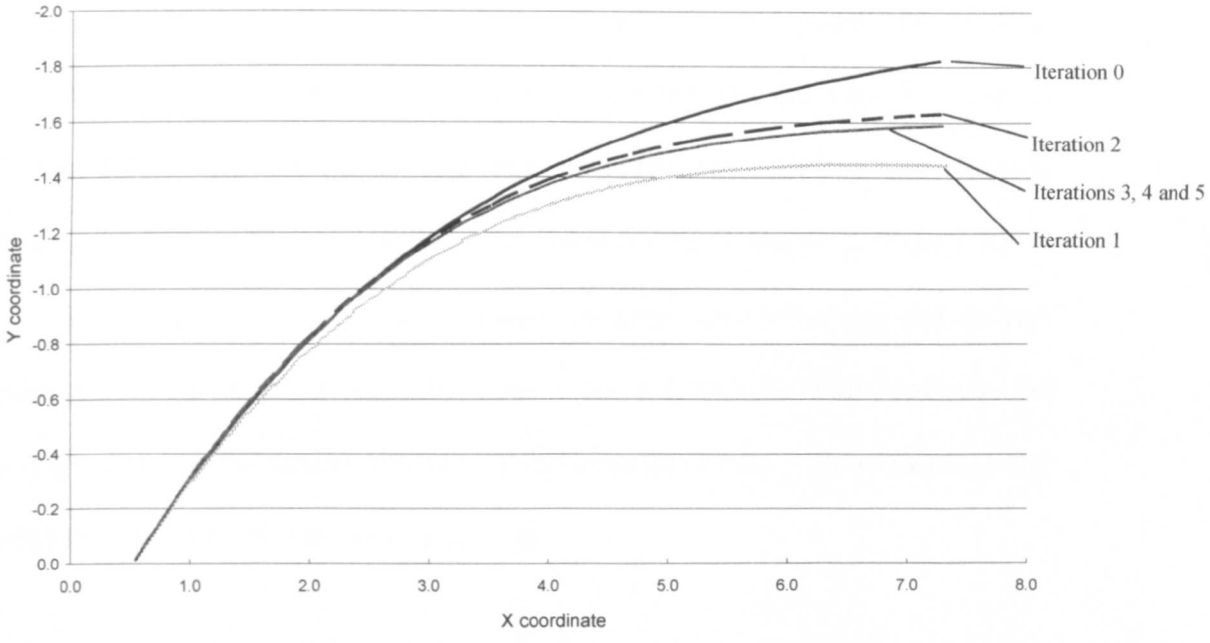

Figure 5.5.2 – Mainsail geometry convergence at a chord slice height of 20m

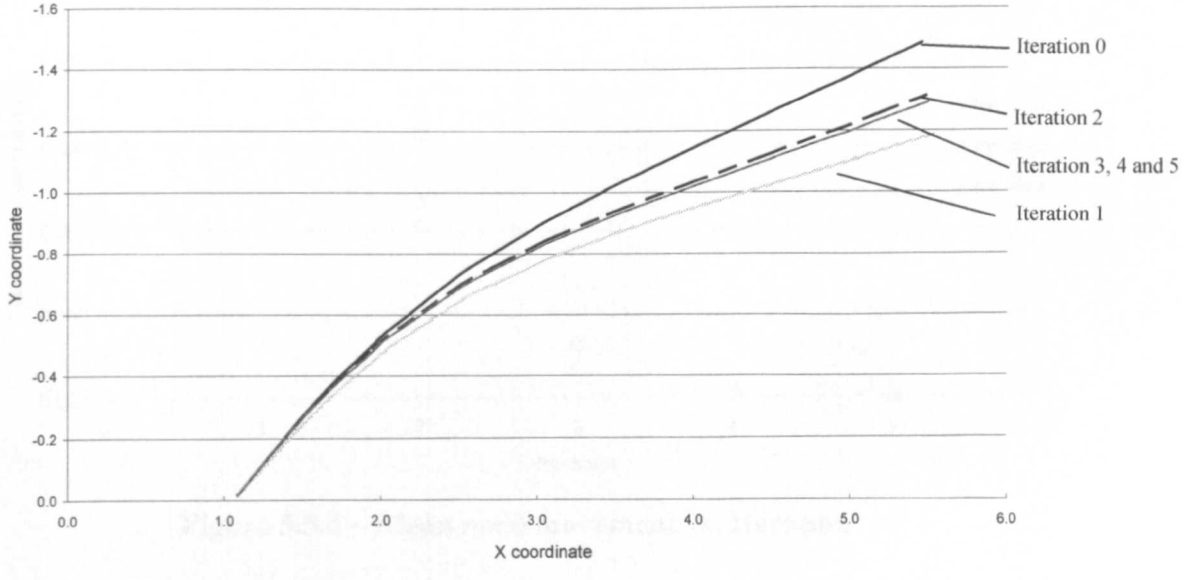

Figure 5.5.3 – Mainsail geometry convergence at a chord slice height of 30m

From the three figures above, the change in the sail shape and twist between iterations can clearly be seen. This change in trim was the result of a lowering of the clew height (or in sailing terms represents the application of more 'kicker' or 'vang' tension). The chords at all three heights converge within approximately 4 iterations and the sail shape does not change significantly from this point onwards, indicating that convergence has been achieved. This is representative of

both main and foresails during upwind and offwind solutions modelled throughout this thesis. Further discussion on convergence for offwind sails is given in Section 5.7.3. The oscillatory convergence pattern, towards the end shape is evident. A quantitative approach to the convergence is shown in Figure 5.5.4. This figure shows clearly that the solution has converged to an acceptable level (node movement less than one millimetre) within 5 iterations. This illustrates the average distance the nodes are moving between iterations. By iteration 5 the mean node movement was below $2x10^{-5}$ m.

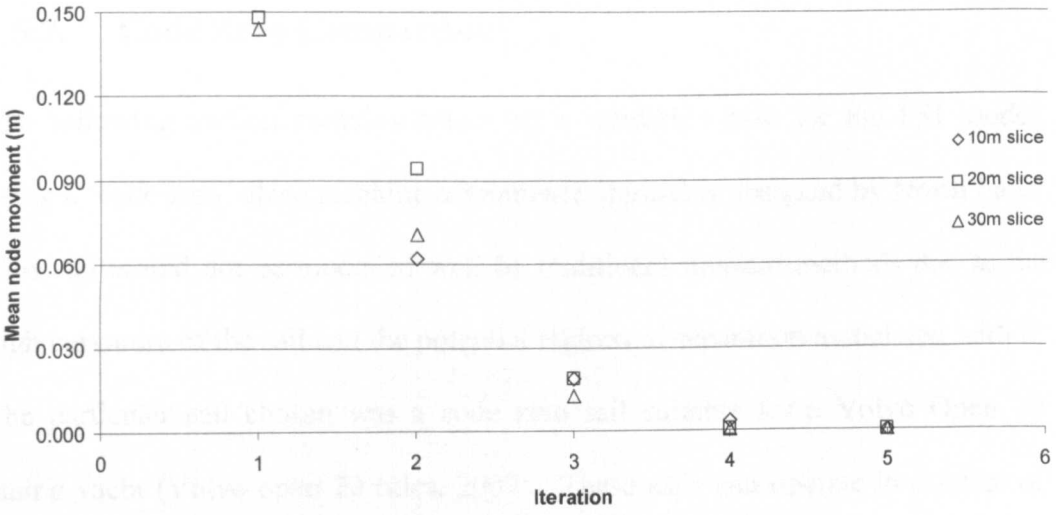

Figure 5.5.4 – Mean node movement vs. Iteration

5.6. Multiple Sails

In reality racing yachts use a combination of sails, usually a main sail with genoa or jib during upwind sailing, or a mainsail and spinnaker during downwind sailing. This introduces added complexity into the simulation, as effectively each sail needs to be modelled, including their interaction. RELAX is capable of managing more than one sail as it is designed for bespoke sail modelling. This

highlights again the advantages of using this type of structural modelling solver, rather than a generic FE package, where this would be more difficult to achieve. ANSYS CFX is also capable of modelling flow past interacting sails, as the author has shown in Section 4.5 (Paton and Morvan, 2007C). However, the utilities that transform the data between the solvers need adapting. The transfer utilities deal with multiple sails by running each operation twice, once for each sail. RELAX has two pressure files to read, one for each sail with appropriate file name conventions. In a similar manner ANSYS CFX has two 'lookup' files, to update the main and foresail nodes as appropriate

5.7. Code Zero Comparison

The following section contains details of a validation case for the FSI model, using a 'code zero' close reaching asymmetric spinnaker designed by North Sails. This sail would not be modelled well by traditional inviscid methods due to the high curvature of the sail and the potential regions of separation associated with it. The particular sail chosen was a code zero sail suitable for a Volvo Open 70 racing yacht (Volvo open 70 rules, 2007). These sails can operate in a range of wind angles between 30 and 60 degrees AWA (Jeremy Elliot, 2008, *personal correspondence*).

Details of the experimental and numerical modelling of the code zero sail are included in this section. Included with the experimental description is the method used for the sail shape capture. A comparison and validation of the numerical model (computed FSI shapes compared with measured experimental sail shapes) is then performed before conclusions on the performance of the solution drawn.

5.7.1. Experimental Set Up

The purpose of the experimental testing was to provide a validation case for the FSI system. The experimental results involve the testing of a code zero close reaching asymmetric spinnaker in a wind tunnel. From this model, flying shapes were captured to allow a detailed analysis and comparison of the flying shape predictions.

There are two main types of wind tunnel: Closed and open loop tunnels. The two variants depend upon how the wind enters the tunnel, and whether the flow is returned from the working section to the fan. With open loop tunnels the flow enters the fan from the surroundings or the room it is placed in, and is free to exit after the working section. Closed loop tunnels have a pre-determined route for the flow exiting the working section to return to the upstream section. There are various pros and cons for both approaches. The open tunnel has the advantages of having lower construction costs and no accumulation of exhaust gases within the working section. The closed loop tunnel has the advantage of lower operating costs as the fans do not have to continuously accelerate the flow. Both approaches can deliver controlled flow conditions to the working section if designed properly.

The wind tunnel used for this evaluation is the 'Climatic Wind Tunnel' at The University of Nottingham. The wind tunnel is predominantly used for the modelling of full scale automotive vehicles but was used in this instance for the modelling of the scale sail. The climatic wind tunnel is a closed loop full scale automotive wind tunnel. Its primary use and initial design specification was to

simulate wind and rain around a vehicle, with various wind, rain and temperature configurations, up to 50kph. It was not however designed for aerodynamic modelling and as a consequence it is not ideal for the modelling of offwind sails. However, due to the limitations in available resources, this was the only viable option for FSI validation, considering the lack of existing detailed research in this field and the facilities available.

The tunnel layout is shown in Figure 5.7.1.1. The closed nature of the tunnel can be seen, with the vertical return and single fan located above the working section. The upper and lower guiding vanes can be seen. It should be noted that the honeycomb screen was not used for this experimental testing. A potential limitation of the tunnel is the short length of the working section and the geometry of the tunnel, making the boundary layer questionable. An attempt to improve the boundary layer has been made with the combination of the lower guiding vanes and a slatted screen. This consists of constant diameter tubes at varying vertical spacing as shown in Figure 5.7.1.2. This variation in bar spacing is used to produce resistance in the flow and control the boundary layer. It is acknowledged that the specification of the tunnel reduces confidence in the accuracy of the results and the subsequent validation work. During the experimental testing, changes in the free stream velocity with height could not be detected with the use of a hand held anemometer. The added turbulence to the free stream due to the slatted screen is also noted and no attempt to estimate the free stream turbulence was made. The lack of tunnel contraction is also a notable feature of the climatic wind tunnel design.

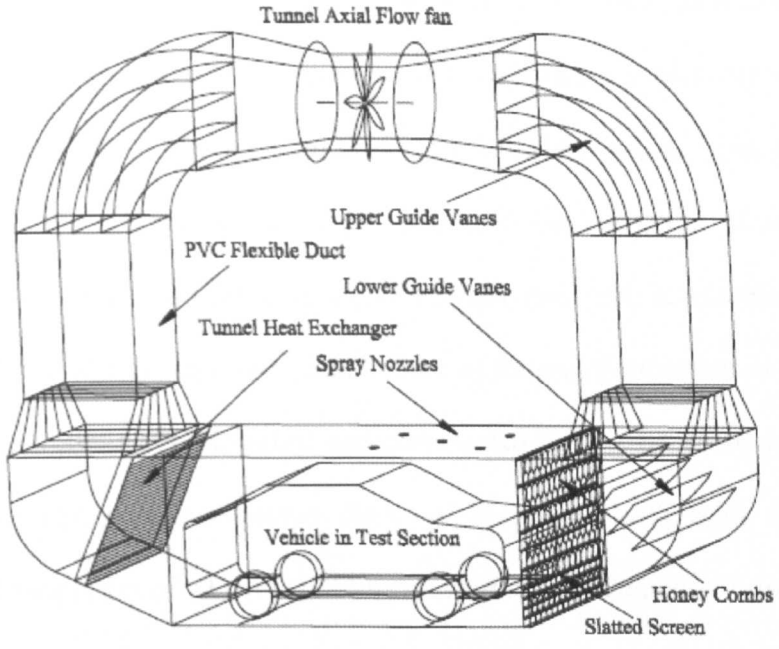

Figure 5.7.1.1 – Nottingham climatic wind tunnel schematic (Ghani *et al.*, 2001).

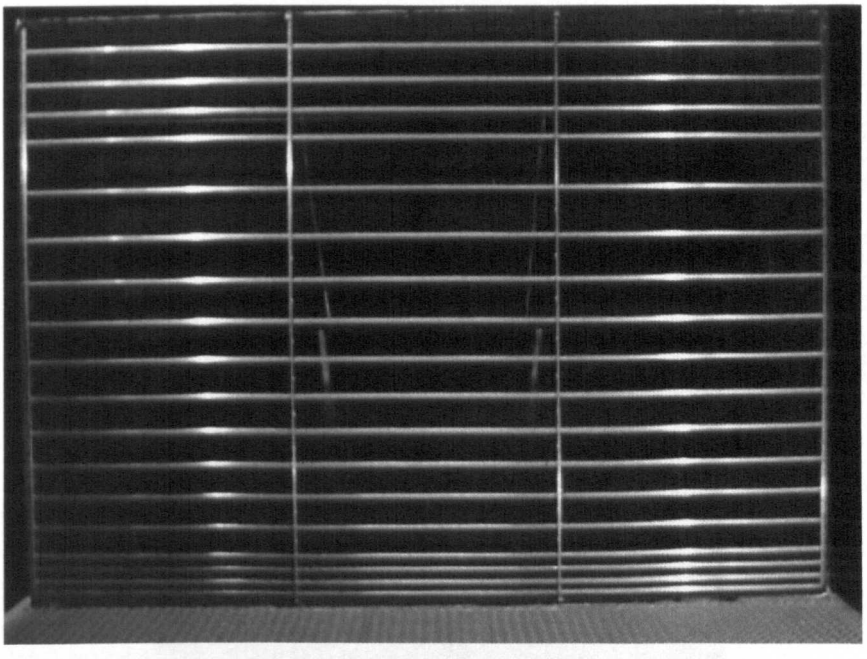

Figure 5.7.1.2 – Nottingham climatic wind tunnel slatted screen (Ghani *et al.*, 2001).

The wind tunnel dimensions restricted the scale of sail that could be placed in the wind tunnel. With a working section height of 2.1m, a maximum sail height of 1.5m was chosen. This was based upon advice from sailing wind tunnel expert Peter Richards (Richards, 2007, *personal correspondence*). This dimension restriction resulted in a 1/20 scale Volvo 70 code zero sail. A suitable rig was then built to fit the 1/20th scale sail. A summary of the sail dimensions is given below. The sail was generously designed and constructed by Jeremy Elliot at North Sails, UK. The sail was constructed from an in-house North Sails laminate, the structural properties of which cannot be given due to commercial sensitivity.

Sail - 1:20 scale Volvo 70 code zero;

Luff – 1.548m **Leech** – 1.43m **Foot** – 0.98m

Material – North Sails laminate

Figure 5.7.1.3 – Test rig and 1/20 scale code zero sail

The primary aim of the wind tunnel testing was to create a data set to provide flying shape validation for the FSI solution detailed earlier in this chapter. Ideally sail forces would also have been captured but due to the lack of a suitable measurement device/tunnel balance or funding, this was not possible. The code zero sail was tested at 40 and 60 degrees AWA at a free stream velocity of 11mph or 4.914ms^{-1}. The sails were trimmed by North Sails' Jeremy Elliot. For each angle of attack the flying shapes were captured using close range photogrammetry, described in the following section.

5.7.2. Close Range Photogrammetry

Previous attempts at sail shape capture have proved problematic with accuracies in the region of a half inch predicted (Mairs, 2003). The problems encountered with sail shape capture include the unsteady nature of wind tunnel models and the inherent instability of sails. Other issues include problems associated with the influence of the measuring equipment on the capture of the sail shapes. In his PhD, Mairs (2003) utilised a physical 'Romer' device, Figure 5.7.2.1, which in this writer's opinion would severely influence the shapes of the sails. The Romer is a device that measures spatial location by physical contact of a pointer onto the surface of the sail.

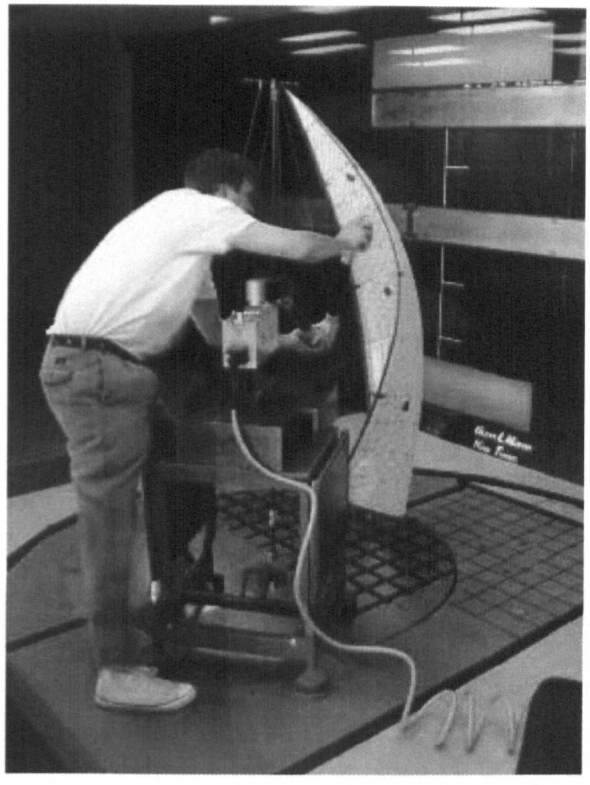

Figure 5.7.2.1 – Mairs' 'Romer' device (Mairs, 2003)

The Romer would have significantly affected the flow both up and down stream. This is likely to be the cause of the relative inaccuracy of the shape capture detailed by Mairs, 2003. Other solutions include the use of laser scanners (e.g. Coiro *et al.,* 2002), but these scanners can take several minutes to capture the entire shape, which can result in capturing the various instabilities of the sail. Ideally the sail shape has to be captured 'instantaneously', without influencing the shape of the sail and to accuracies within a millimetre for the scale sail. This can be achieved with close range photogrammetry (Luhmann *et al.*, 2006), which was used in the present work and is detailed in the followed sub section.

Close range photogrammetry involves the taking of photographs from various locations around the subject. Common points are identified on each photographic

image. By means of triangulation these points can then be located in 3D space. For this application, cameras were triggered simultaneously to capture the shape at a single moment in time. This is achieved with the use of remote triggers.

Calibration coefficients can also be calculated to reduce effects such as barrel effects, where images are distorted radially away from the centre of the lens. This was carried out using the calibration frame in the photogrammetry laboratory at The University of Nottingham. The experience and guidance of Martin Smith and Nicholas Kokkas of the Institute of Engineering Surveying and Space Geodesy (IESSG) at The University of Nottingham were paramount to obtaining an accurate photogrammetric solution for the capture of sail shapes. To allow for recognisable and repeatable points to be located on the sails, a series of retro-reflective targets were placed on the sail surface. These are highly reflective circles surrounded by a black surface, Figure 5.7.2.5. When a camera with flash takes photographs, the retro targets reflect the light and create very high contrast dots over the sail's surface.

As the sail is in a 'steady' but dynamic state, it was necessary to capture all the images at a single instance. This was achieved using a pair of Nikon D200 cameras as shown in Figure 5.7.2.2. The specification of the cameras includes: Sensor of 10.2 m pixels (3872x2592), pixel size of 0.0061mm and a nominal focal length of 28mm. They were both fired together by the use of remote control from outside the wind tunnel within the control office. Figure 5.7.2.2 shows the bars where the air enters the tunnel on the left and an observation window behind the cameras, which were used with the integral flash.

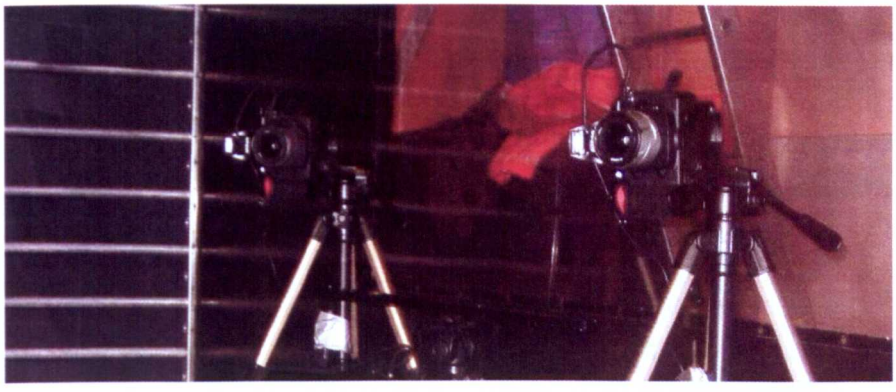

Figure 5.7.2.2 – Sample 'stereo pair' of photogrammetry images

After the trials were completed, the images were processed using Australis 7 (Photometrix, 2009). An example of the output from the measurement processing is shown in figure 5.7.2.3. As the object, the sail, to be measured is relatively planar; it was decided not to use an in-situ calibration. Instead, the cameras were calibrated using the laboratory frame and Australis 7 software. Figure 5.7.2.4 shows the calibration frame.

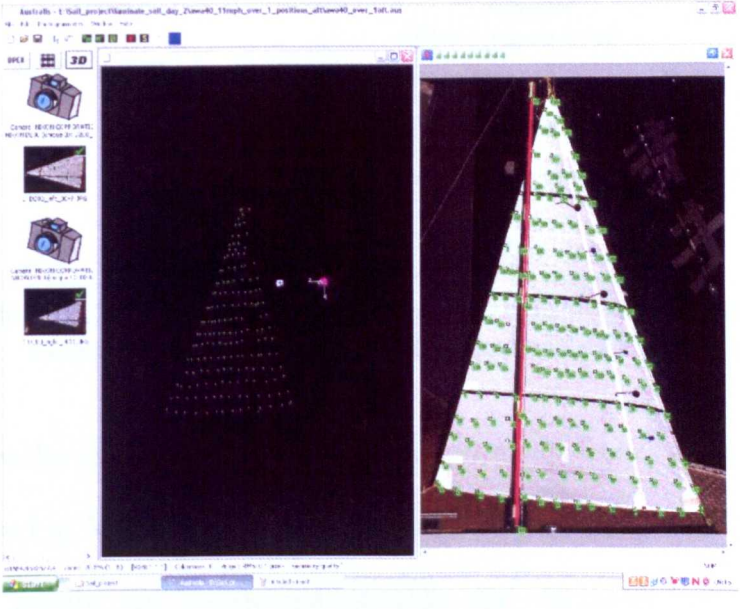

Figure 5.7.2.3 - Example of Australis 7 measurements

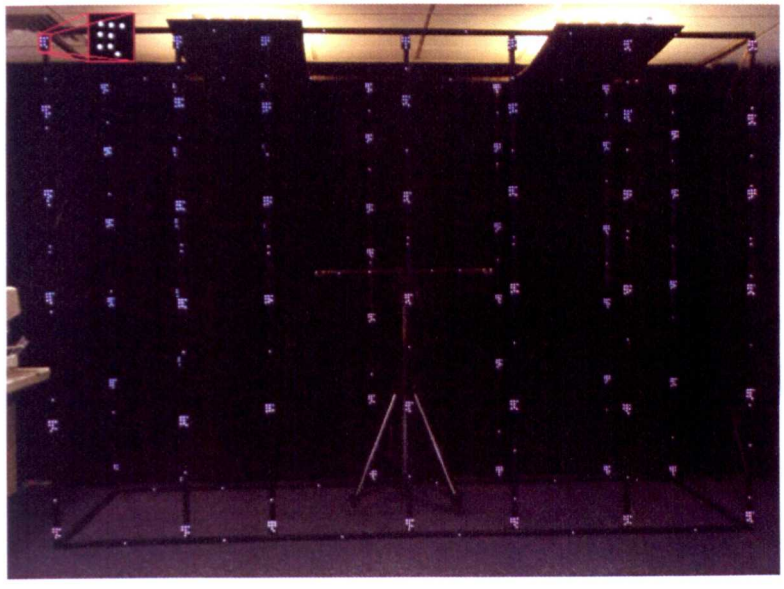

Figure 5.7.2.4 - The University of Nottingham camera calibration frame (Smith and Taha, 2009)

Table 5.7.2.1 gives the summary of statistical accuracy estimates, with X and Z axes approximately parallel to the plane of the sail.

AWA	*Sail Adjustment*		*Estimated accuracy of 3D point coordinates (RMS 1-sigma level)*			*Estimated accuracy of image referencing (RMS 1-sigma level) (pixels)*
			X (mm)	*Y (mm)*	*Z (mm)*	
40	stream	central	0.398	1.738	0.359	0.36
60	stream	central	0.088	0.463	0.085	0.05
Mean			0.243	1.099	0.222	0.205

Table 5.7.2.1 – Statistical accuracy of the photogrammetry results for all cases carried out in the wind tunnel code zero validation case.

The results show, as expected from the geometry, better accuracy estimates were achieved in X and Z than in Y (the approximate out of sail component). All of these results are considered suitable for validation of the computational modelling. The camera locations were restricted to minimise their impact on the airflow and practical limitations of mounting the cameras. Ideally additional cameras would have been located both above and directly downstream of the sails

to help reduce errors in the Y direction but this would have adversely affected the flow within the tunnel. To minimise the impact on the flow the cameras were kept close to the tunnel walls near the tunnel control room.

The final output from Australis 7 is a cloud of points representing the surface of the sail, an example is shown in Figure 5.7.2.6. This was input into Rhino (Rhino, 2009), a CAD package where surface fitting was performed using Non-Uniform Rational B-Spline (NURBS) surface functions with stiffness/relaxation parameters. Due to the high quality of the photogrammetric measurement no 'smoothing' was performed or necessary (all points lie on the surface). Although the software has the potential to perform surface smoothing this was not carried out. These surfaces could then be used for comparison to the surfaces created by the FSI analysis.

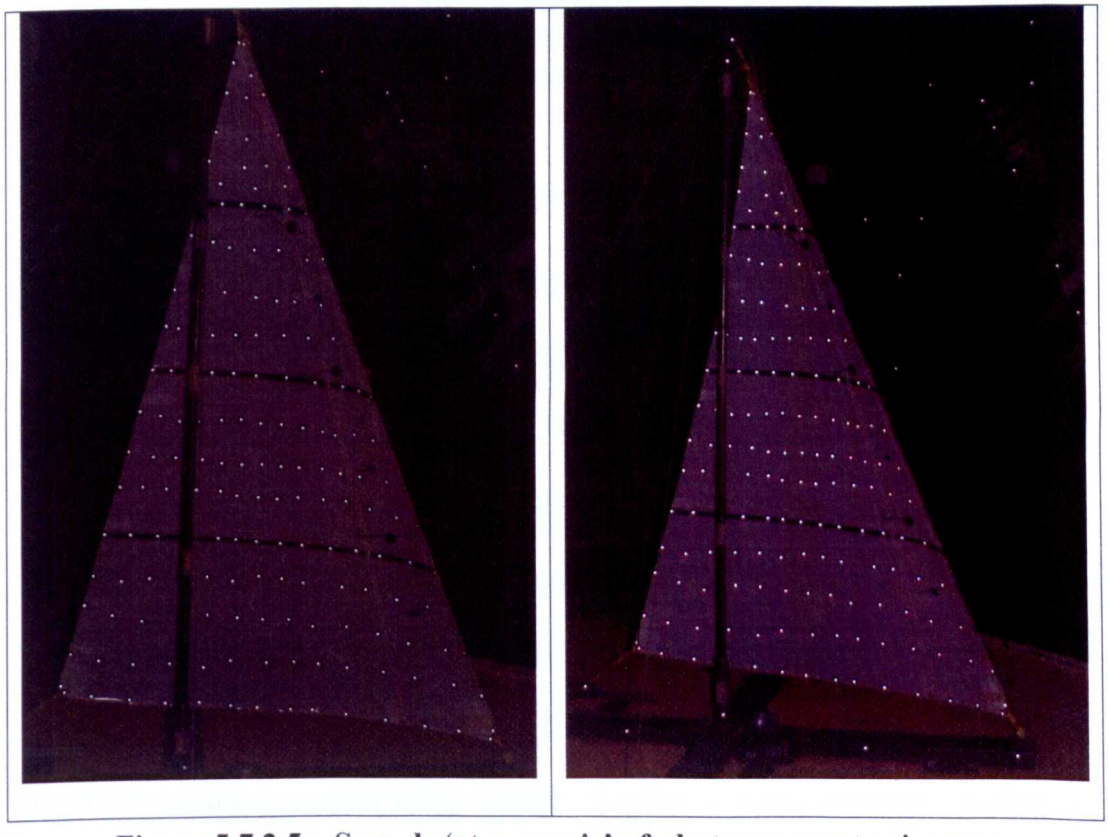

Figure 5.7.2.5 – Sample 'stereo pair' of photogrammetry images

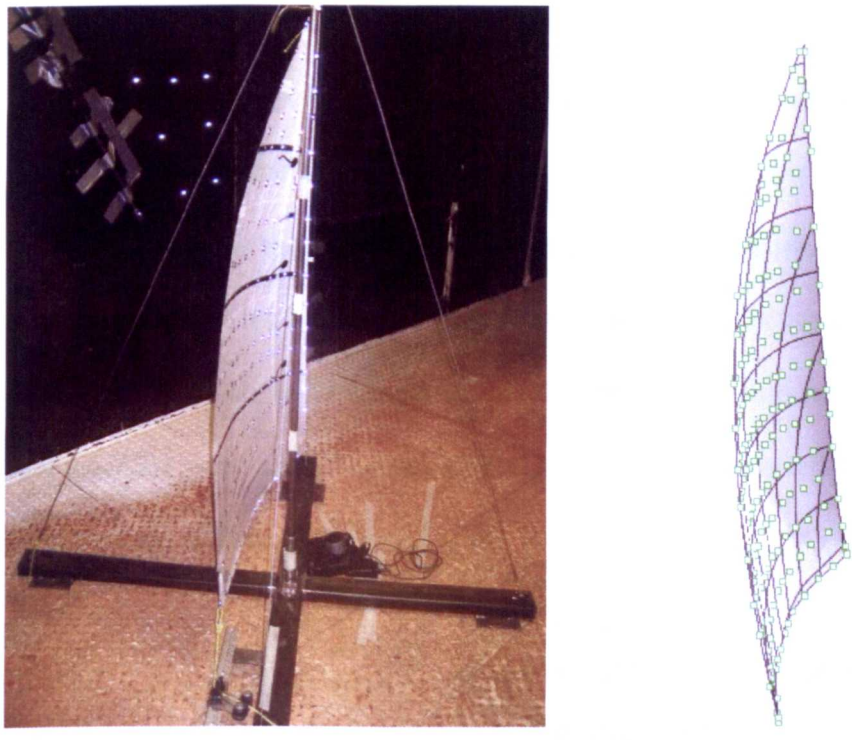

(a) (b)

Figure 5.7.2.6 - Point cloud and corresponding surface: (a) picture from the wind tunnel, (b) corresponding data set with a surface fitted through the points (shown in green)

5.7.3. Computational Set Up

The FSI set up began with the creation of the design shape of the sail within a CAD program. Details of the sails, including seam locations and orientation are included at this stage. The CAD model was then imported into the structural code where structural properties for the rig are applied. The triangle based meshing of the sail surface was also carried out. An arbitrary low constant pressure field of 5 Pa was used to 'inflate the sail'. This creates a first guess at the sail shape, resulting in less movement within the mesh deformation phase.

The CFD mesh was created using Gambit. A predominantly tetrahedral and prism based mesh was used with boundary layers elements, proximity refinement and

wake blocks to control the mesh sizes. Further details of the mesh can be found in Table 5.7.3.2. A constraint is also placed upon the CFD mesh; the CFD and the structural orientation of the sails must match. Therefore it was necessary to align the X direction of the CFD model to the centre line of the boat. The domain was created to replicate the wind tunnel working section. The domain was 2.1m high, 3m wide and 6m long. Boundary conditions for the CFD model also have to be allocated. For the wind tunnel model, boundary conditions as summarised in Table 5.7.3.1 were used. The velocity at the inlet and initial conditions of the flow were defined as normal to the inlet face.

INLET	Constant velocity Normal velocity vectors to inlet surface
OUTLET	Pressure outlet
WALLS	Free slip walls Smooth
SAIL SURFACES	Non slip Infinitely thin Matched meshes on both sides of the sail

Table 5.7.3.1 – Numerical boundary conditions for code zero validation case

Mesh Size	~5.5 million cells
Boundary Inflation Layers	10 layers, 1:1.2 expansion ratio
Y^+	~3
Sail Face Element Length	10mm
General Expansion Ratio	1:1.05

Table 5.7.3.2 – Mesh Details for code zero validation case

The simulation was run utilising the Shear Stress Transport model described and validated in the previous chapter. The simulation was carried out in a time dependent scenario until a steady solution was obtained. Timesteps of 0.02s were used, to ensure convergence within each iteration. Drag and lift coefficients were monitored to ensure convergence to a steady solution had been achieved. RMS residuals of the solution equations were also set to a non-dimensionalised convergence criterion of 10^{-4}. Convergence within each timestep of the transient loop was achieved within 4 iterations.

The FSI solution generally took 4 loops before converging to a steady flying shape (node movement <1mm). The convergence was found to be robust, with only a rare number of cases failing. The majority of these failed cases were due to negative elements during the mesh deformation phase. Only approximately 1% of simulations carried out within this research failed and required remeshing.

5.7.4. Mesh Independence

To ensure that the validation study was not affected by discretisation errors, a CFD mesh independence study was carried out. This involves the running of the same scenario with different mesh sizes and the calculation of the relative error in both forces and pressures. For this investigation the number of sail face cells was adjusted, by changing the cell edge length on the sail surfaces. The first cell height was kept constant. As an example Mesh 4 (~2500 face cells) had a face cell length of 10mm, a Y^{+} of approximately 3 and a total mesh size of 5.5 million cells.

For this study a code zero spinnaker, not perfectly trimmed, was chosen. The results are compared based upon the number of faces/the node spacing on the sail surface. At all times a suitable y+ of 3 was maintained. However, this did result in the coarser meshes having worse quality cells, in terms of cell aspect ratio. For boundary inflation layers, the aspect ratio is defined as the surface edge length to first cell height ratio.

The results are shown in Figure 5.7.4.1 and 5.7.4.2. The figures represent the error in forces when compared to the most detailed model with approximately 5500 surface faces. The forces are seen to plateau in Figures 5.7.4.1 and 5.7.4.2, with an error of approximately 1% for meshes 3 and 4, with approximately 1600 and 2500 surface faces. This is deemed acceptable given the complex flow features in addition the evidence given in Figures 5.7.4.3 and 5.7.4.4.

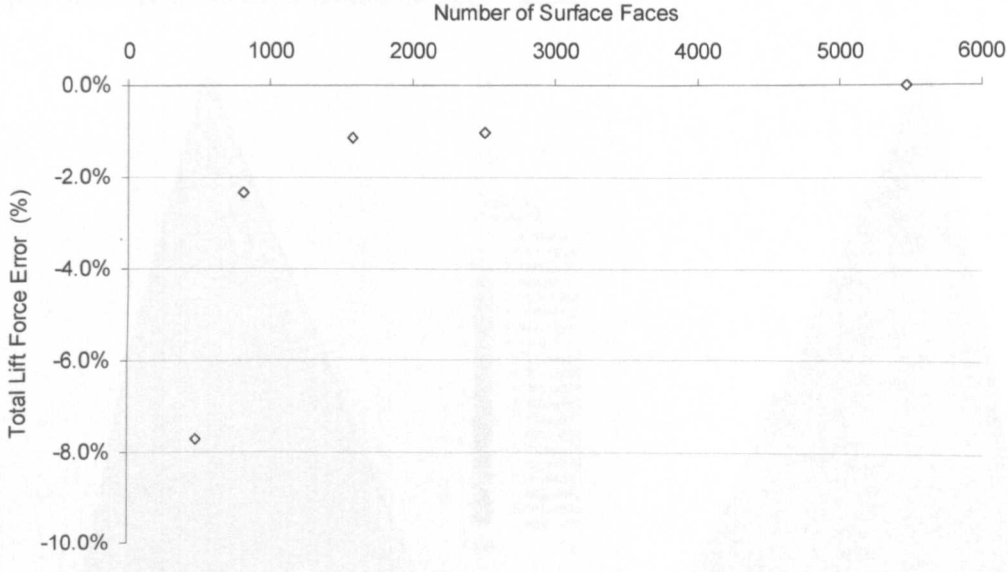

Figure 5.7.4.1 - Error in total lift force for varying mesh densities

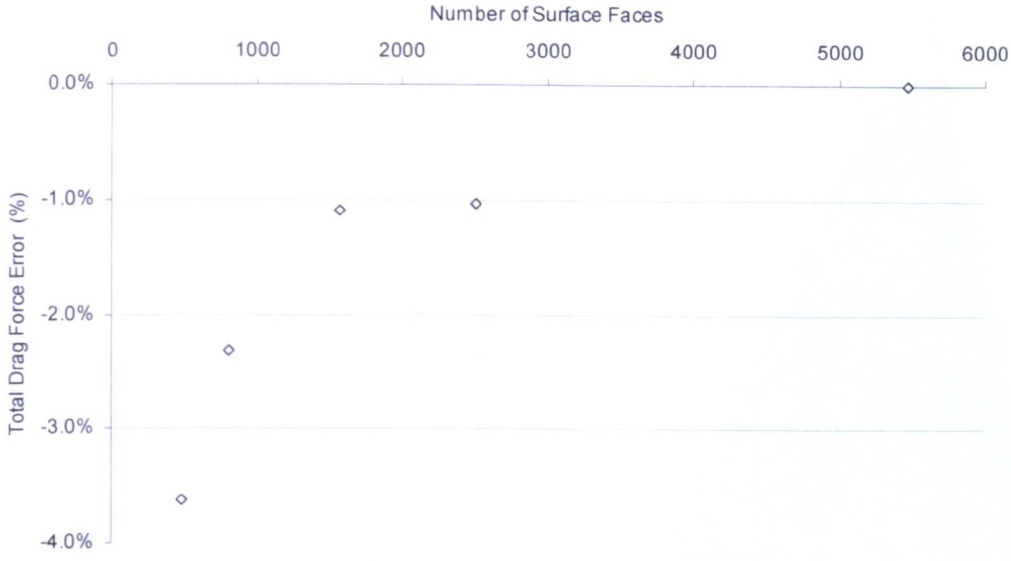

Figure 5.7.4.2 - Error in total drag force for varying mesh densities

Figure 5.7.4.3 and 5.7.4.4 show a comparison of the pressure profiles from the solution with approximately 1600 face nodes to that of the solution with that of 5500 nodes. This shows the surface pressures are similar with little variation between them. From this analysis it was decided a surface mesh resolution of approximately 2500 cells would be appropriate.

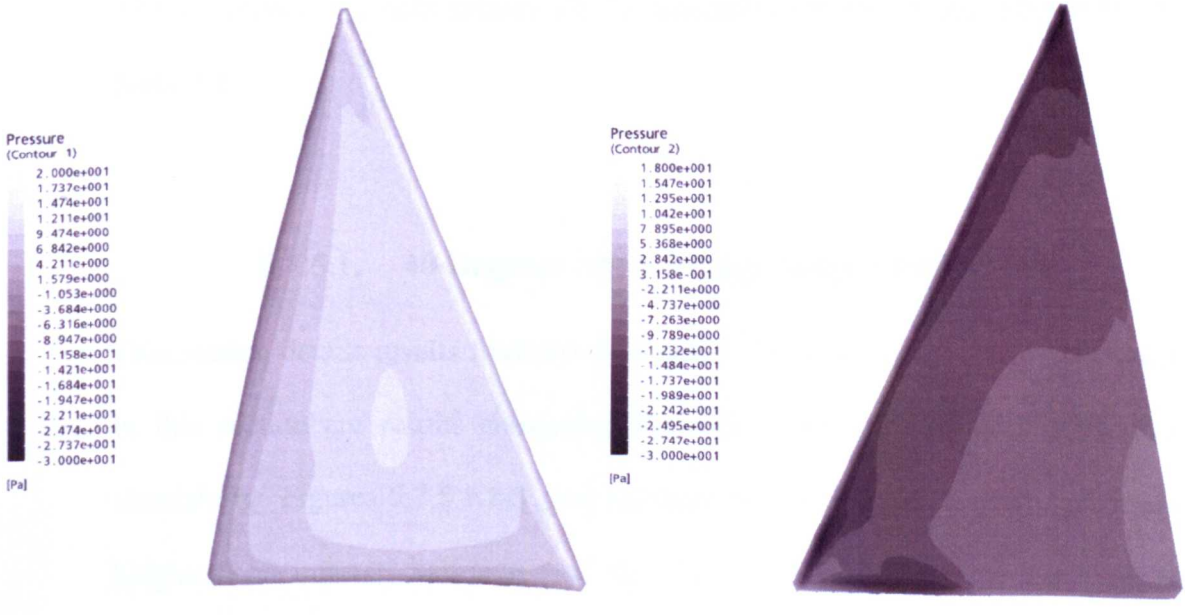

Figure 5.7.4.3 – Foresail surface pressure contours for case with ~1600 surface faces

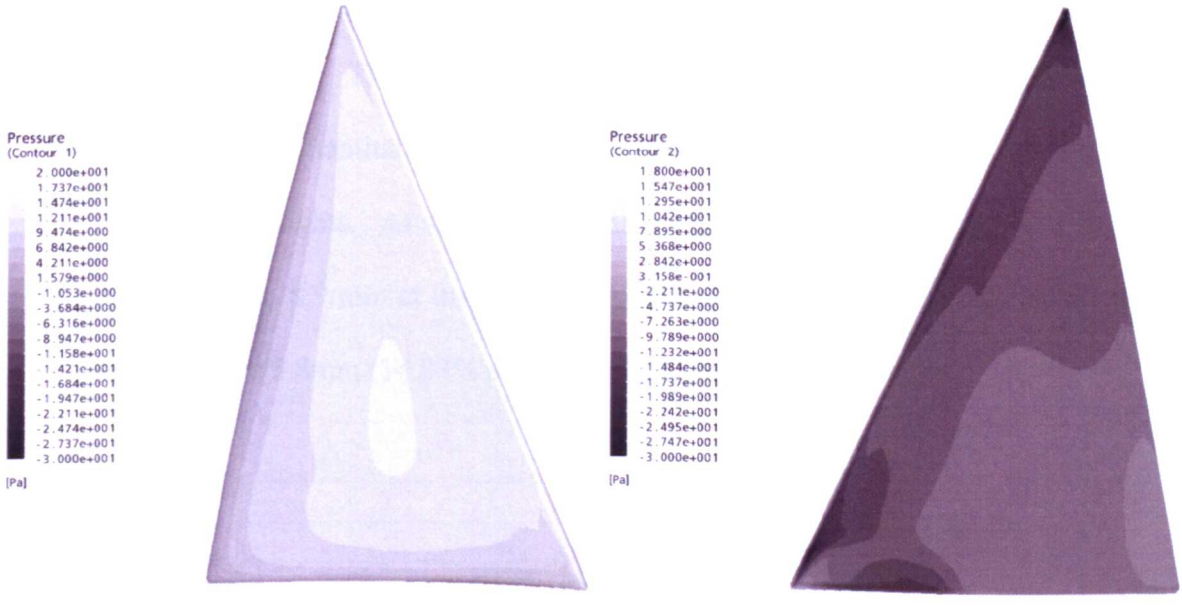

Figure 5.7.4.4 – Foresail surface pressure contours for case with ~5500 surface faces

5.7.5. Wind Tunnel Comparison

Two cases were run numerically, representing sailing conditions at 40 and 60 degrees AWA at a wind speed of 4.914 ms^{-1} to replicate the experimental data. The trimming of the sails at both AWAs was carried out by Jeremy Elliot of North Sails, UK.

5.7.5.1. 40 Degrees AWA Flying Shape Comparison

This section details results from the 40 degrees AWA wind tunnel test. Included in this section are results comparing the wind tunnel and corresponding FSI simulation. Figures 5.7.5.1.1-3 give sections through the sail, at three different heights; one quarter, half way and three quarters up the sail in the vertical direction.

The three figures demonstrate the ability of the FSI solution to accurately model the sail shapes. The slices were divided into 40 equal length sections. Table 5.7.5.1 gives quantitative details of the mean differences in node location at the three slice heights. At a quarter height the average node difference was 2.8mm, increasing to 8.9 mm at three quarter height. The average difference of the three heights was 5.8mm (14.83% as a % of the experimental camber).

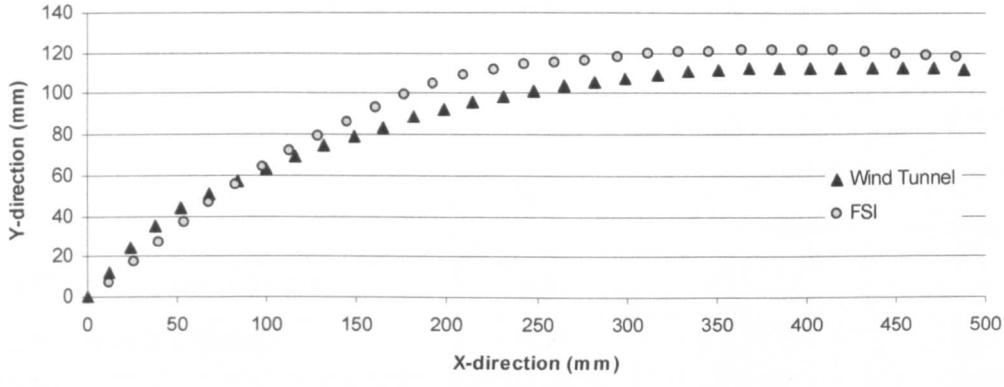

Figure 5.7.5.1.1 – Quarter height slice (40 degrees AWA)

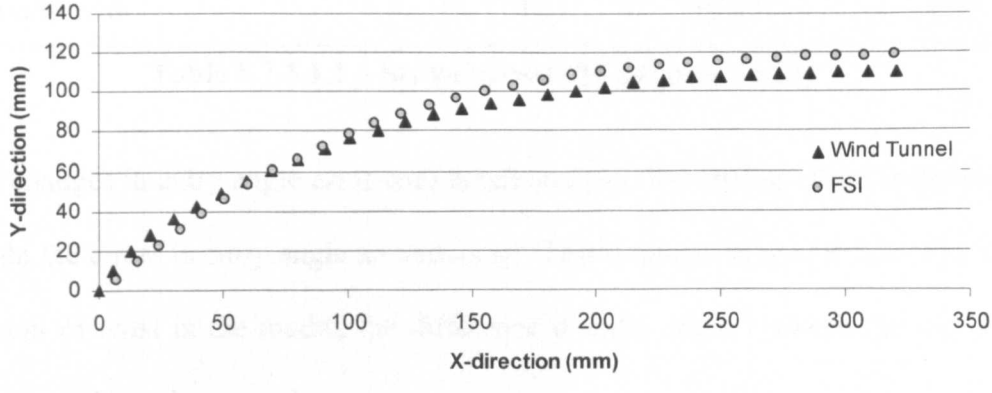

Figure 5.7.5.1.2 – Half height slice (40 degrees AWA)

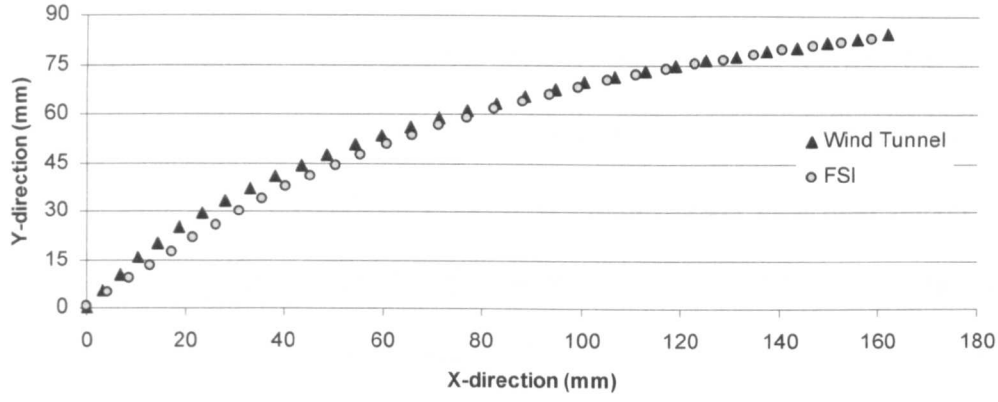

Figure 5.7.5.1.3 – Three quarter height slice (40 degrees AWA)

	Error (mm)	Error as a % of experimental slice camber	Error in entry angle (degrees)
Node difference quarter height	8.87	15.10%	0.55
Node difference half height	5.75	12.87%	0.71
Node difference three quarter height	2.82	16.52%	0.04
Average difference of all three heights	5.81	14.83%	0.43
Maximum error	14.57	16.52%	0.71

Table 5.7.5.1.1 – Stripe errors (40 degrees AWA)

The changes in entry angle error with height are also interesting. With increasing height the errors in entry angle are reducing. This is due to an over estimate in the amount of twist in the model, the difference in entry angle between the top and bottom of the sail.

5.7.5.2. 60 Degrees AWA Flying Shape Comparison

The 60 degrees AWA case is reported within this section. The rig setup and tension were kept constant from the 40 degrees AWA case. The sail shape comparison is displayed in the same format as the 40 degrees AWA case. Figures 5.7.5.2.1 to 5.7.5.2.3 show slices through the sail at a quarter, half way and three

quarters up the sail, measured vertically. It can be seen from these images that the sail shapes are reasonably well predicted however there are differences. The main cause for error is due to the lack of luff sag within the structural model. This is evident in Figure 5.7.5.2.4 and has a more prominent effect here than for the 40 degrees AWA case, as the deformation is away from the boat centreline and forces on the sail of a higher magnitude.

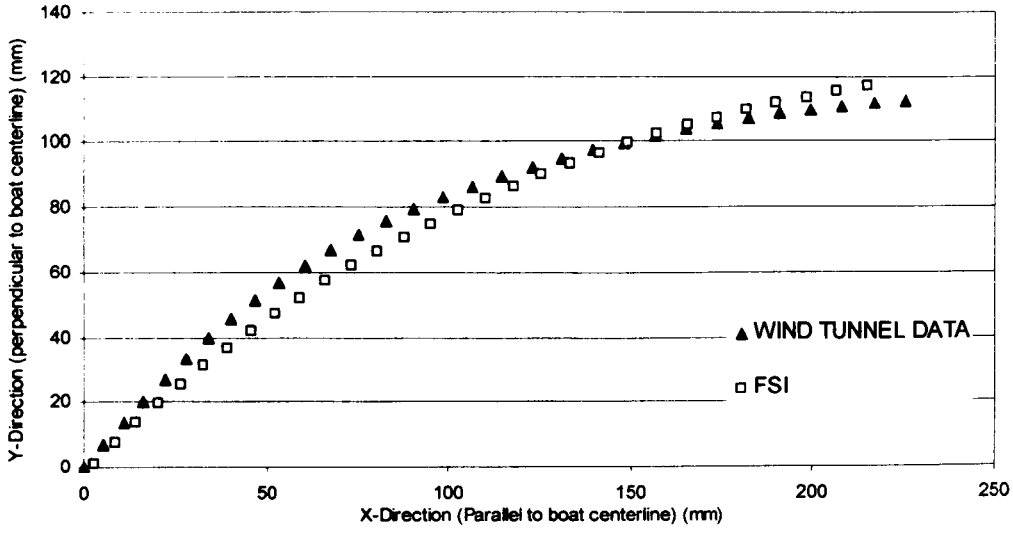

Figure 5.7.5.2.1 – Quarter height slice comparison (60 degrees AWA)

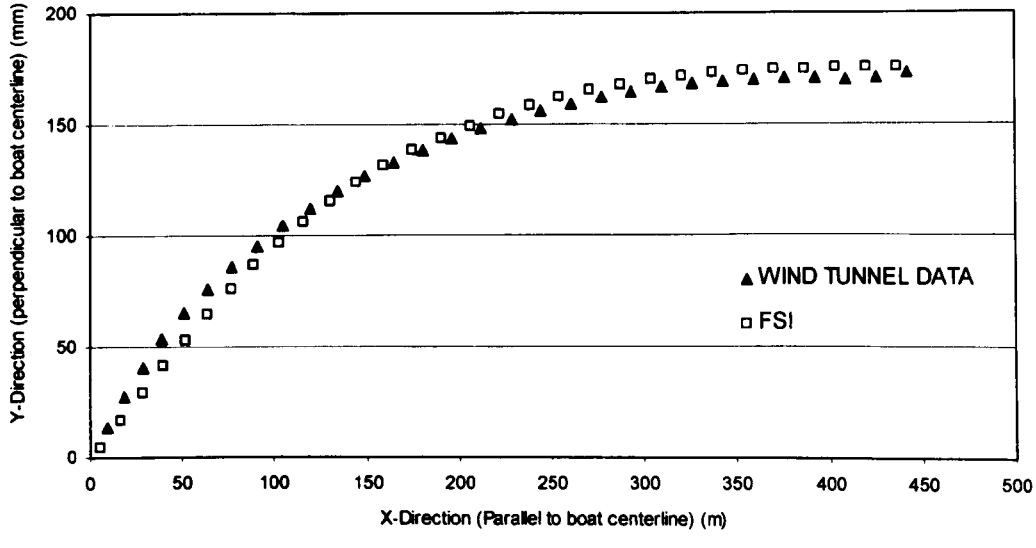

Figure 5.7.5.2.2 – Half height slice comparison (60 degrees AWA)

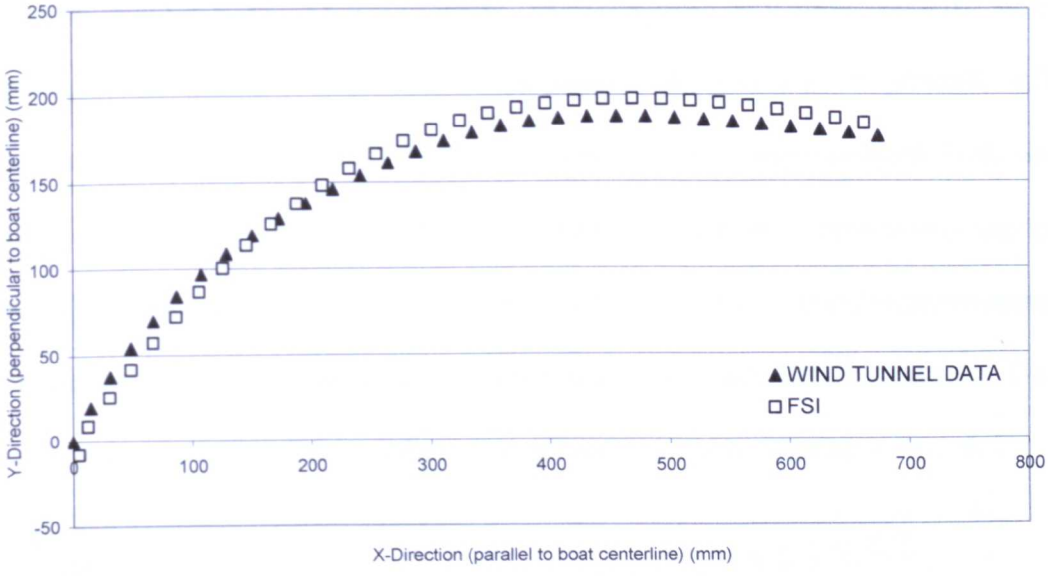

Figure 5.7.5.2.3 – Three quarter height slice comparison (60 degrees AWA)

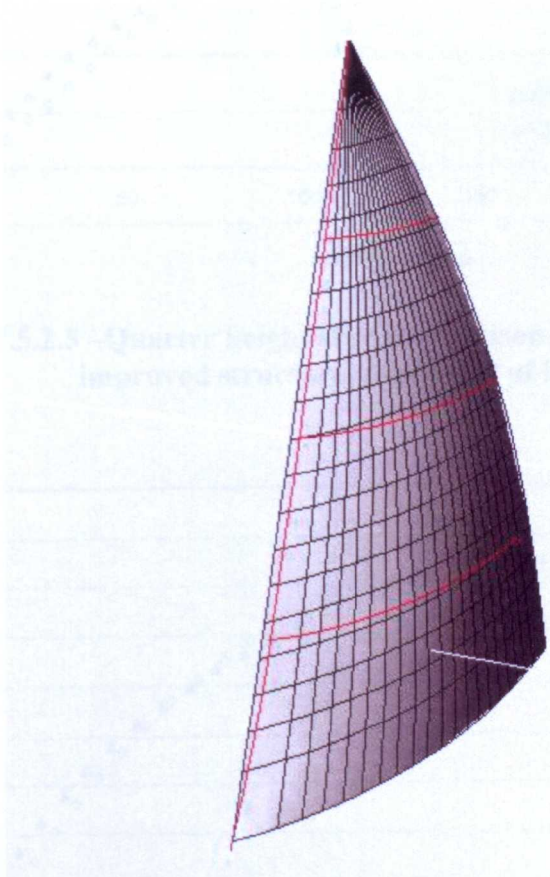

Figure 5.7.5.2.4 –Luff sag comparison (60 degrees AWA)

(Red outline – wind tunnel, Grey shaded – FSI)

Figures 5.7.5.2.5 to 5.7.5.2.7 show an improved structural model, with approximated structural characteristics applied to the forestay, to generate luff sag. In the initial structural model the forestay was approximated with an unrealistically high Young's modulus to remove any added complications due to the luff tension. In the improved structural model a Young's modulus appropriate for the stainless steel wire used as the forestay was used, $E=107Kn/mm^2$. The improved correlation of the results is immediately obvious, Figures 5.7.5.2.5-7.

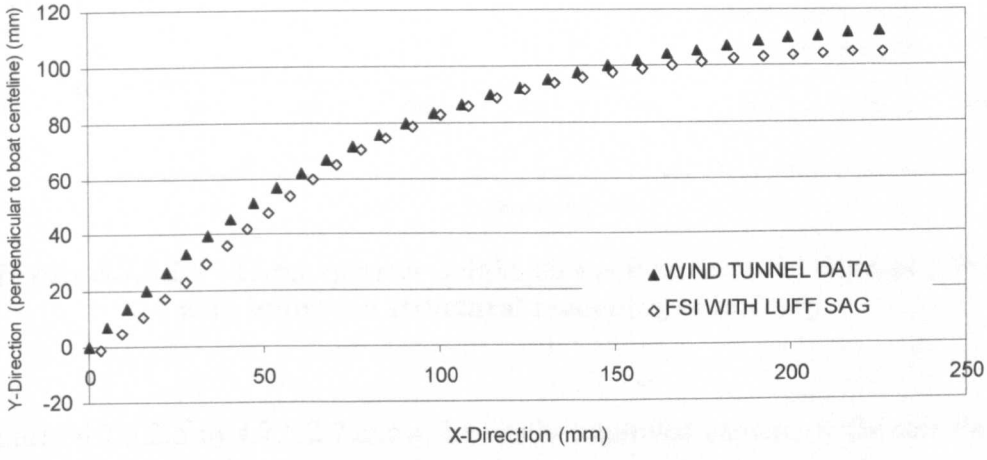

Figure 5.7.5.2.5 –Quarter height slice comparison (60 degrees AWA with improved structural modelling of luff sag)

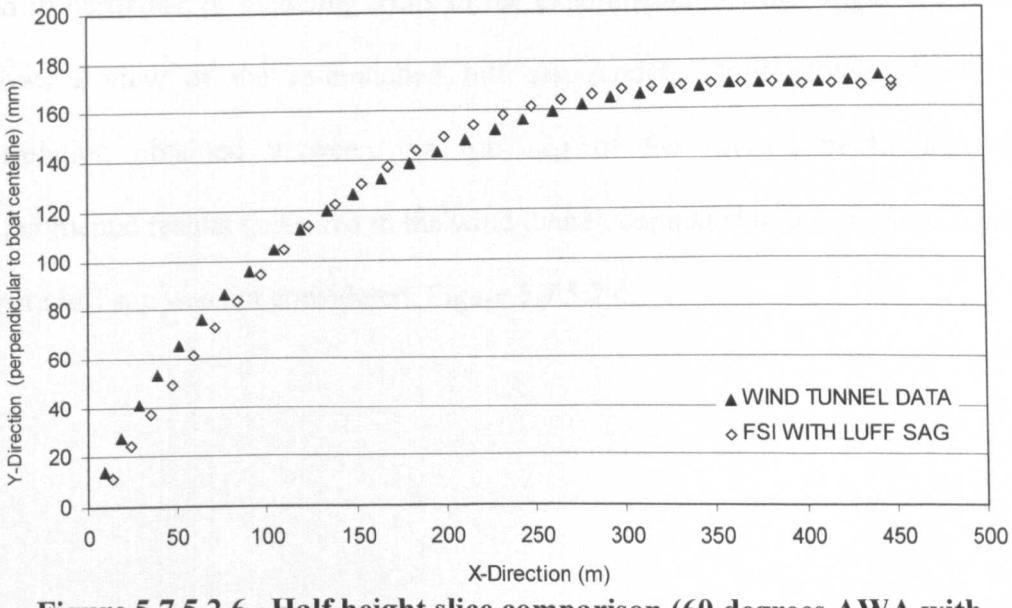

Figure 5.7.5.2.6 –Half height slice comparison (60 degrees AWA with improved structural modelling of luff sag)

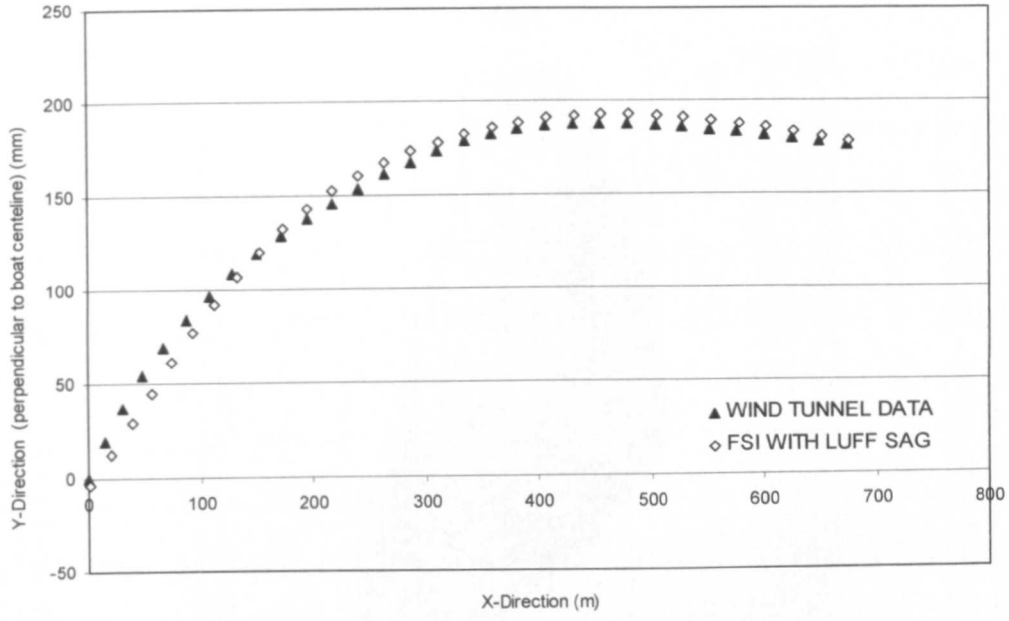

Figure 5.7.5.2.7 –Three quarter height slice comparison (60 degrees AWA with improved structural modelling of luff sag)

Figures 4.7.5.2.5 to 4.7.5.2.7 show the vastly improved capture of the sail shape, as a consequence of the minor change to the structural model, where luff sag was permitted. This clearly highlights the importance of correctly modelling the rig and in particular of matching trims to the experimental set-up. Figure 5.7.5.2.8 shows a view of the re-modelled luff sag model. It illustrates the closer correlation obtained between the luff sag of the revised model and the experimental results measured in the wind tunnel, compared to the previous model where luff sag was not considered, Figure 5.7.5.2.4.

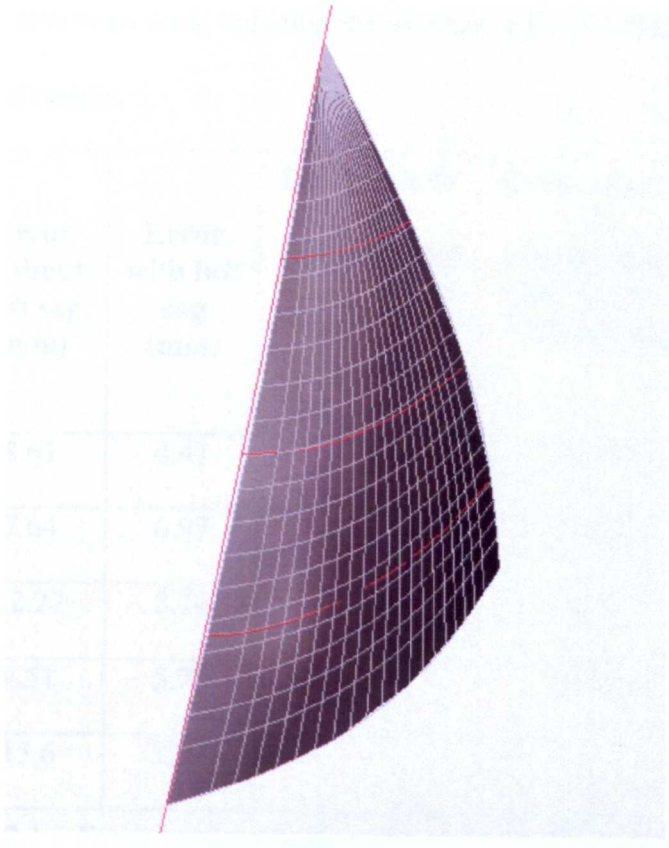

Figure 5.7.5.2.8 –Luff sag comparison (60 degrees AWA with improved structural modelling of luff sag)

(Red outline – wind tunnel, Grey shaded – FSI with luff sag)

To render the results presented above in a quantitative form, Table 5.7.5.2.1 gives the errors of the FSI models in comparison to the wind tunnel shapes. The slices were divided into 40 equal length sections with a similar method to that used with the 40 degrees AWA model. The errors stated below are average differences between the slices obtained from the FSI model and those obtained experimentally from the wind tunnel. Without the luff sag an error of 9.51mm was achieved. With the improved modelling of the luff sag an average displacement over the 3 slices of 5.7mm (10.7% as a percentage of slice camber) was achieved; a reduction in error of 40%. The maximum error has also been reduced from 15.6mm to 12.2 mm; a reduction of 22%. An improvement in the

entry angle has also been seen, reducing the average error to within 0.6 degrees of the experimental results.

	Error without luff sag (mm)	Error with luff sag (mm)	Error as a % of experimental slice camber without luff sag	Error as a % of experimental slice camber with luff sag	Error in entry angle without luff sag (degrees)	Error in entry angle with luff sag (degrees)
Quarter Stripe	8.61	4.47	27.9%	14.5%	1.01	0.84
Half Stripe	7.64	6.97	12.1%	11.1%	0.22	0.34
Three Quarter Stripe	12.27	5.74	13.7%	6.4	0.99	0.63
Average error	9.51	5.73	17.9%	10.7%	0.74	0.60
Maximum error	15.6	12.2	-	-	-	-

Table 5.7.5.2.1 – Error comparisons with and without corrected luff sag model

5.7.6. Conclusions

The FSI scheme developed within this section has been validated with the use of wind tunnel data, for scale offwind code zero sails. Close range photogrammetry has been used to capture sail shapes to an acceptable level (~1mm) with no impact upon the sail's performance or shape. The FSI solution has reproduced the wind tunnel data to within a maximum average difference in slice node location of 5.8mm. The validation process has also highlighted the importance of matching the structural model to that used in the wind tunnel, in particular the structural properties of the forestay.

One of the (few) other authors who has tried to validate a FSI solution for offwind sails is Mairs. Figure 5.7.6.1 is taken from Mairs's PhD, 2003, showing his

modelling of a code zero. Within his thesis he states that his tunnel shapes were captured to within ±1/2 inch (12.7mm) for a similar scale model sail. He also states 'the bulk of the computational flying shape within a plus or minus 0.75inch window of the experimental flying shape' (19mm), for a similar code zero sail at 45 degrees. Trials undertaken at The University of Nottingham show maximum error with the FSI model for a code zero at 40 degrees was 14.6mm with an average of 5.8mm. In addition, the accuracy of the sail shape measurement was to within a statistical accuracy of 1mm. This represents a significant improvement on the accuracy achieved by Mairs, both experimentally and computationally. These results are summarised in Table 5.7.6.1

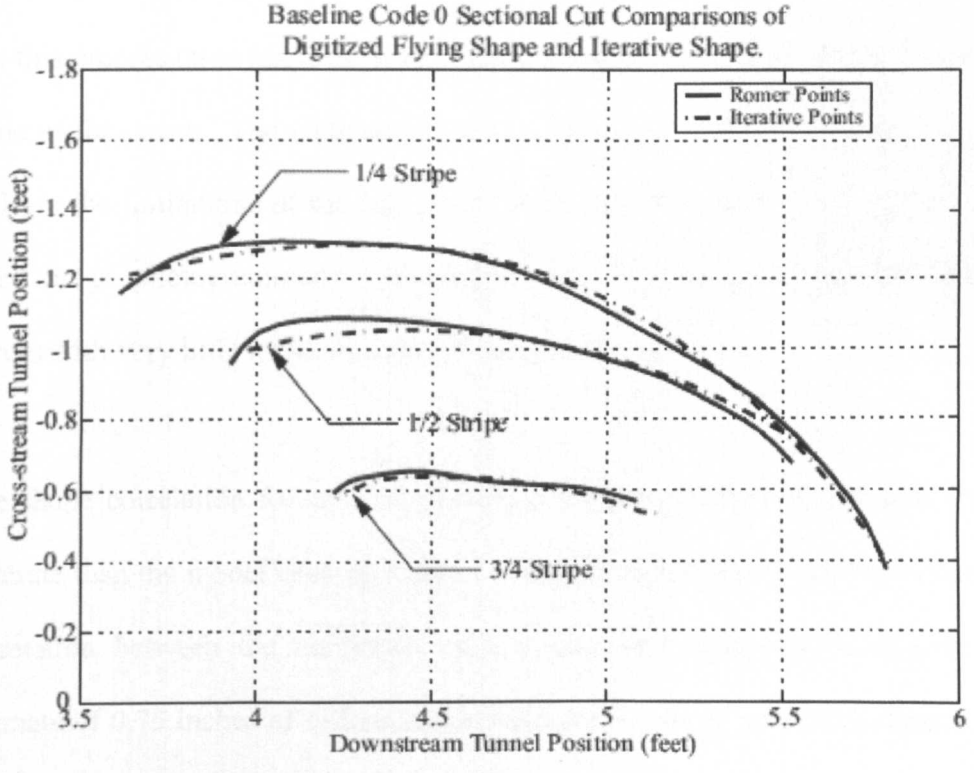

Figure 5.7.6.1 – Mairs' code zero 45 degrees (Source: Mairs, 2003)

Author	Sail	AWA	Shape Capture Accuracy	FSI correlation
Present	**Code Zero**	40	1mm	5.8mm
Mairs (2003)	**Code Zero**	45	12.7mm	~19mm

Table 5.7.6.1 – Summary of improvements in FSI correlation compared to Mairs, 2003.

The main advantages of the photogrammetry are the instantaneous capture of the sail shapes and its non intrusive nature. In contrast the 'Romer' is both intrusive to the flow and takes much longer to capture. Although no estimate of the time taken to physically capture the different points of the sail was given, it is assumed that this process takes minutes rather than seconds and therefore could account for some of the errors. The undulating nature of the results shown in Figure 5.7.6.1 indicate the limitations of the sail shape capture used by Mairs. In contrast, the close range photogrammetry measurements have produced relatively smooth curves with very little noise, as reported in Section 5.7.2.

The shape correlation for the FSI numerical model was also significantly more accurate than the model used by Mairs. Although Mairs fails to do any statistical correlation between the computed and experimental shapes he does give an estimate of 0.75 inches of difference between them. Some notable differences in approach that may account for the improvement in FSI correlation are to be found in both the structural and fluid analysis. Within Mairs' research he made no attempt to model the material properties of the sail as he concluded the material strains would be small. Improvements to the structural model of Mair's work

would inevitably help improve the correlation to the experimental results. Within the Nottingham study the material properties of the sail were approximated. As shown in 5.7.5, the structural properties of the forestay were shown to be sensitive to the converged sail shapes. Finally, Mairs utilised the $k-\varepsilon$ turbulence model within STAR-CD, which has known weaknesses, including its performance for flows with adverse pressure gradients. A total mesh size of approximately 500,000 cells was also used. In comparison the method used by this author utilised the SST turbulence model on grids of approximately 5M cells, increasing the potential accuracy of the fluid analysis. These improvements combine to generate the significant improvements in shape capture accuracy and the FSI correlation, seen by this author.

Chapter 6

Application of Viscous CFD and FSI to Full Scale Racing Yacht Sails

6.1. Introduction

In the previous chapters, an FSI model has been developed, capable of modelling the offwind performance of racing yacht sails at a level of accuracy not previously available. This chapter will start with the application of viscous CFD to full scale rigs, using the Volvo Open 70 yacht as the application, and then go on to investigate how various options for model simplification affect the results. It will also highlight some of the difficulties in modelling large, full scale sailing rigs.

The FSI model developed and validated in Chapter 5 is also applied to the full scale application, demonstrating the capabilities of the model to cope with the complex thread structures of modern laminated sails, multiple sails and complex rigs including masts and decks. The rigs include offwind sails, modelled with wind twist. The chapter also includes a parametric study, looking at the performance of a full scale code zero sail.

This chapter concludes by considering the potential of viscous FSI to model other applications.

6.2. The Volvo Open 70

The test case used within this chapter will be the rig from a full scale Volvo Open 70 (Volvo Open 70 rules, 2007). The Volvo Open 70 is an offshore class, designed for both robust and safe competition, whilst still maintaining excellent performance. It is the current class used in the round the world Volvo Ocean Race. During the 2008-09 race, a Volvo 70, 'Ericsson 4', broke the 24hr monohull record when she sailed an incredible 596.6 nautical miles (Ericsson Team Racing, 2009). The simulation models will be based on a code zero sail, similar in design to that used in the previous chapter, with a standard mainsail where appropriate. Unlike the scale models in Chapter 5, the sails will be created in full size and constructed from a composite stack, Figure 6.2.1. This consists of individually laid threads laminated between two layers of substrate, which fix the threads in place. For this type of sail, it is the threads, rather than the substrate, that are the major load bearing structure of the sail. This results in anisotropic material properties which need to be modelled by the structural solver for accurate results. Where required, the presence of a mast and or hull and decks are included. The hull used in the analysis is within the limits set within the Volvo Open 70 rules (Volvo Open 70 rules, 2007).

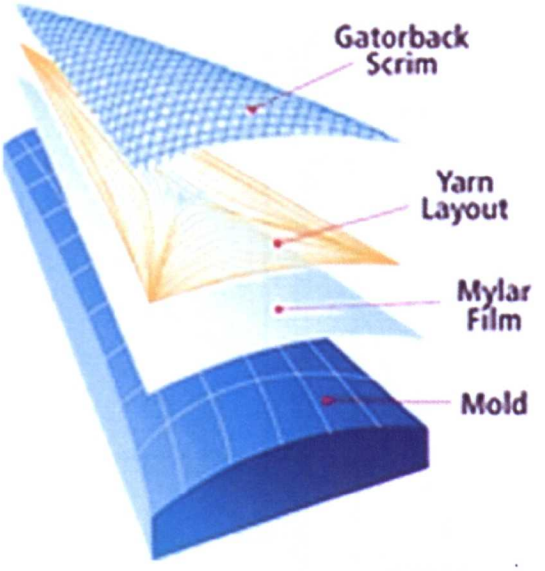

Figure 6.2.1 – North sails 3DL composite sail (image taken from http://www.uk.northsails.com)

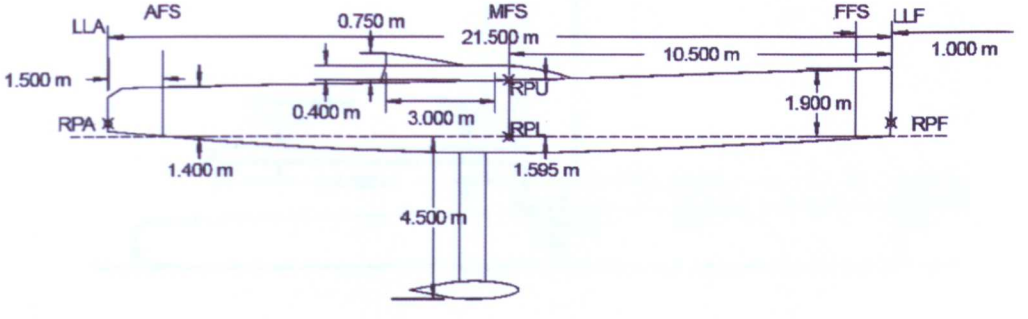

Figure 6.2.2- Volvo Open 70 hull dimensions (Volvo Open 70 rules, 2007)

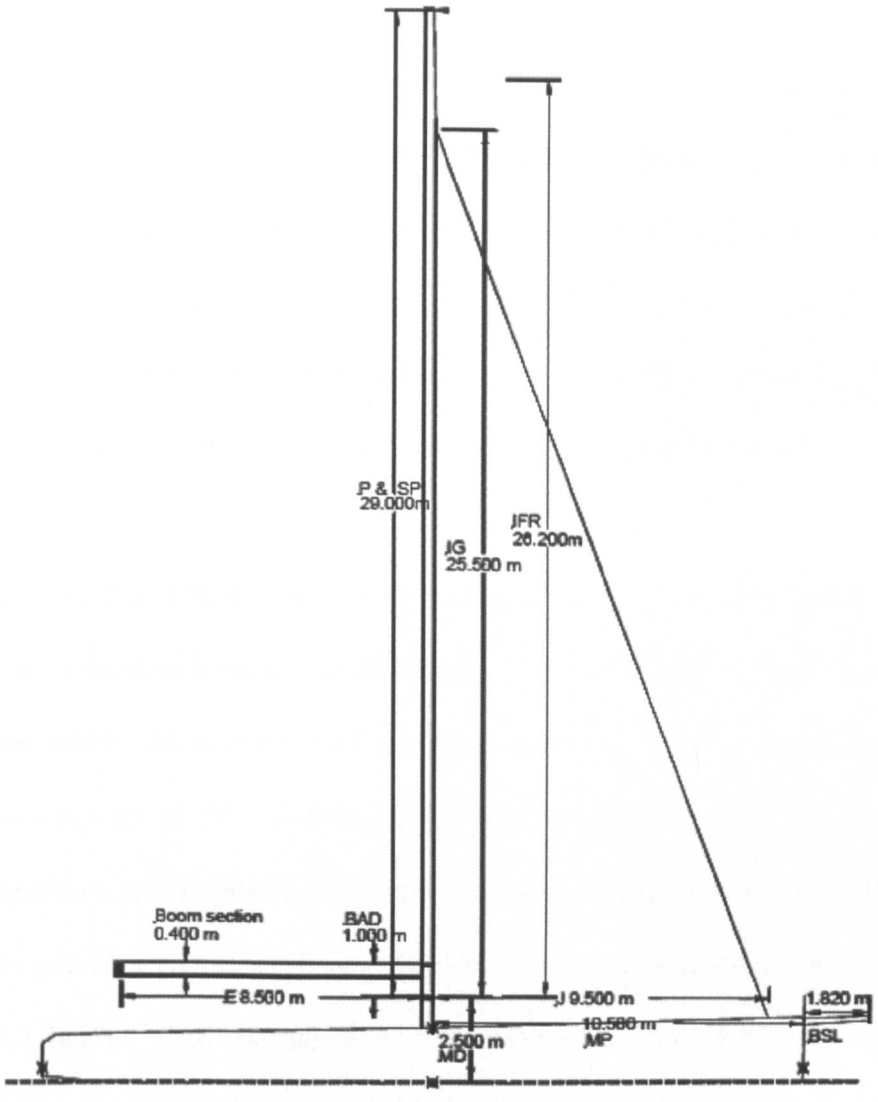

Figure 6.2.3 – Rig dimensions for a Volvo Open 70 yacht (Volvo Open 70 rules, 2007)

The rules are set to allow development, but yet control the costs needed for a successful and competitive campaign. Important hull dimensions are given in Figure 6.2.2 (Volvo Open 70 rules, 2007).

Within the Volvo Open 70 rules, sail design is an area of extensive research, with relatively few restrictions placed upon it. The rig however is given limitations, in addition to restraints on the number and types of sails allowed, Figure 6.2.3.

6.3. Volvo Open 70 CFD Model

The meshes created for the models within this section were all generated in ANSYS GAMBIT. The sail designs and CAD files were supplied by North Sails, UK. (North Sails were selected as suppliers by every team in the 2008-09 Volvo Ocean Race, (Ericsson Team Racing, 2009)). The sail mould shapes were provided in an IGES format. The thread layouts were supplied separately and had to be laid upon the mould shapes, ready for input to the structural solver.

As in Chapters 4 and 5, the models utilised prismatic boundary inflation mesh elements, combined with proximity size functions to control the element sizes and distribution within the domain, and in particular in the vicinity of the sail. A specific description of the construction of these meshes is not given here, to reduce repetition, except where significant differences are present to the methods used in the previous chapters. A summary of the mesh characteristics is given in Table 6.3.1 below. The techniques used within this chapter are similar to the meshes used in the previous chapters but over a larger scale, Chapter 5.

Surface and Boundary Layers Elements	First cell aspect ratio	10
	Growth rate	1.3
	Number of cells in the boundary layer (normal direction)	10
Sail Growth Function	First cell edge length	~0.01m (for y^+~100)
	Growth rate	1.08
	y^+	~4 (~100 for FSI simulations)
	Largest cell size	0.5m

Table 6.3.1 –Full scale Volvo Open 70 mesh characteristics

Careful placement of regions of mesh refinement can help provide sufficient levels of accuracy and maintain mesh independence, whilst providing an economical solution. This predominantly involves greater refinement in areas of flow separation and areas of large velocity gradients. A mesh expansion ratio of 1.1, expanding the cells away from the hull surfaces was used. This specifies that the edge length of adjacent cells increase at the rate of 1.1. Expansion factors of 1.08 were used away from the sails and mast surfaces, Figure 6.3.1. The results of the blended size functions can be seen in Figure 6.3.2, below.

In general a surface cell aspect ratio of less than 10 was achieved, but in certain circumstances this was allowed to reach 15 or 20, for the purposes of maintaining an acceptable cell count. The need to find a practical compromise became more of an issue for the cases presented in this chapter with multiple large sails. The need to maintain cell quality, in the region adjacent to the sails, and the need to maintain y^+ values leads to very large meshes. This is particularly true if an aspect ratio of 10 is strictly enforced. For example, a target first element height of 2mm would result in a 4 cm^2 face element size at an aspect ratio of 10. This in turn would result in 580,000 face elements and 5.8M prismatic volumes. If the aspect ratio is stretched to 20, this allows for a reduction in face cell count to 145,000, and a prismatic count of 1.45M, a more manageable cell count. Therefore, to limit the cell count to within acceptable limits of the resources available, such measures were taken where necessary. Cells of larger aspect ratio (up to 20) were allowed in regions of more uniform and steady flow such as mid chord. Throughout this thesis a maximum Y^+ of ~4 was achieved. The exception to this is the FSI model within this chapter. Due to the scale of the sails, the

inclusion of the rig and multiple sails it was necessary to increase the Y^+ to ~100 to reduce the computation expense. The mesh construction techniques remain the same but with larger first cell heights within the layered region.

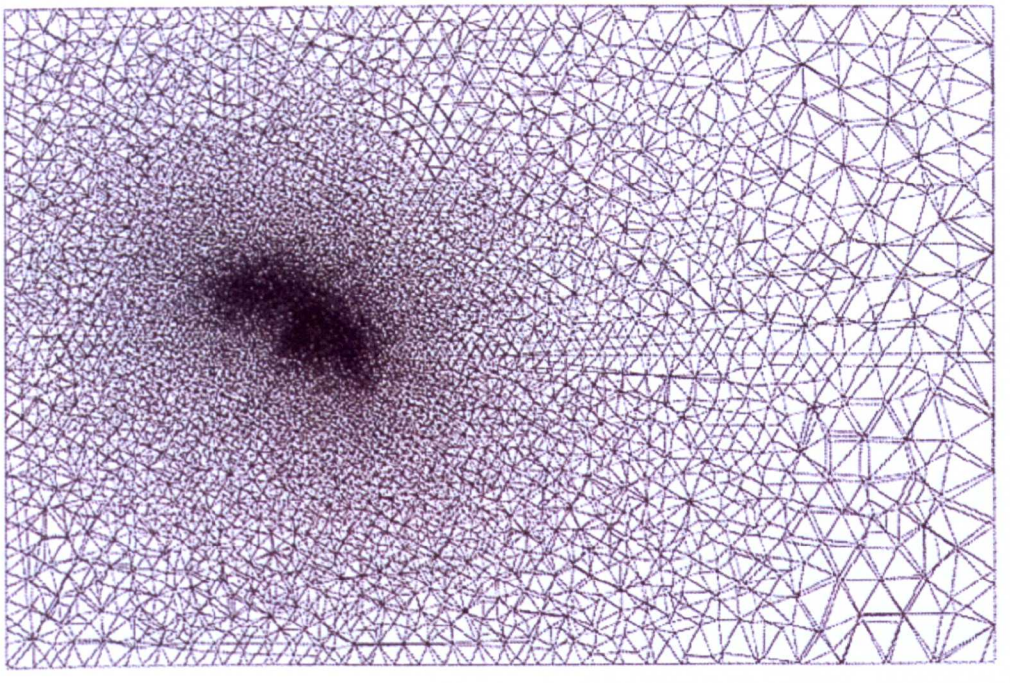

Figure 6.3.1 – Tet based mesh used throughout Chapter 6, showing increasing cell size with distance from sail surfaces.

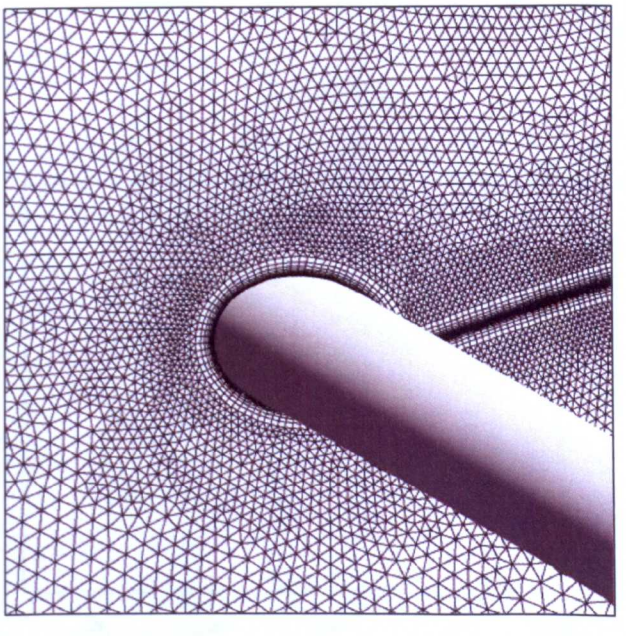

Figure 6.3.2 – Mesh refinement using boundary inflation elements and proximity size functions

An additional constraint placed upon the mesh generation strategy is stipulated due to the need to match the orientation of the model, in both the fluid and structural models. When this is combined with the need to provide a twisted wind profile, a slight change over the previous domain generation technique is needed. In Chapter 4, a turntable type approach was used to replicate the experimental method. In Chapter 5 the turntable approach had to be removed because of the orientation constraint of the fluid and structural models. This, combined with a need to model the wind tunnel walls, resulted in the creation of individual meshes for each wind angle. Within this chapter, the need to replicate the wind tunnel has been removed and the domain size increased. This has led to the use of multiple inlets and outlets as a way to minimise the need for remeshing, Figure 6.3.3. Two of the domain sides are inlets whilst the opposite faces are outlets. This type of analysis allows for changes in wind angle without the need for any manipulation of the mesh or a need for a complete remesh of the domain.

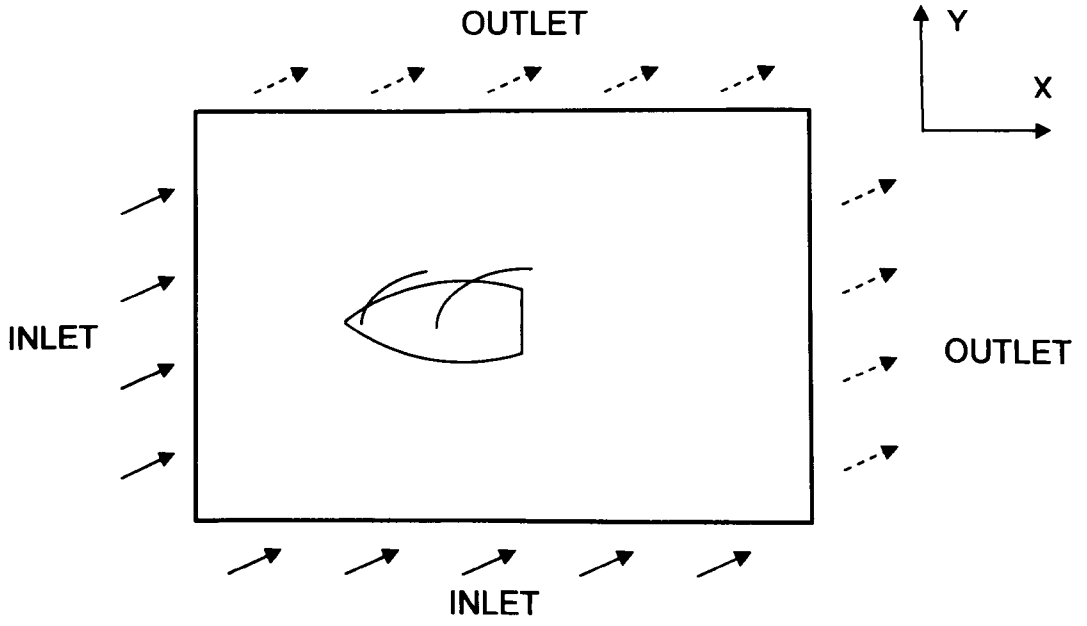

Figure 6.3.3 – Domain used for non wind tunnel full scale Volvo 70 FSI models (not to scale)

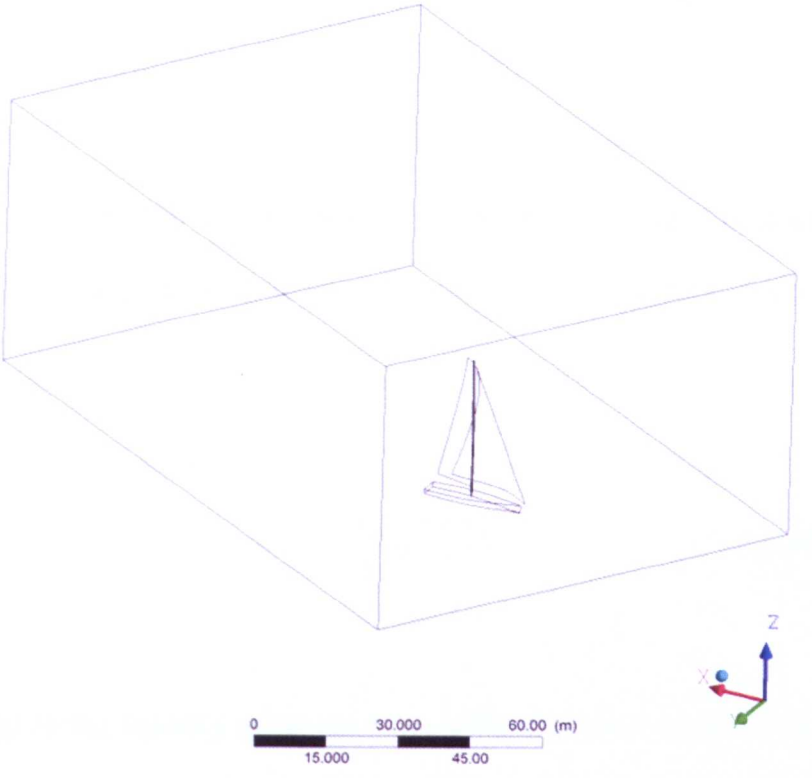

Figure 6.3.4 – Isometric view of a typical computational domain used throughout Chapter 6.

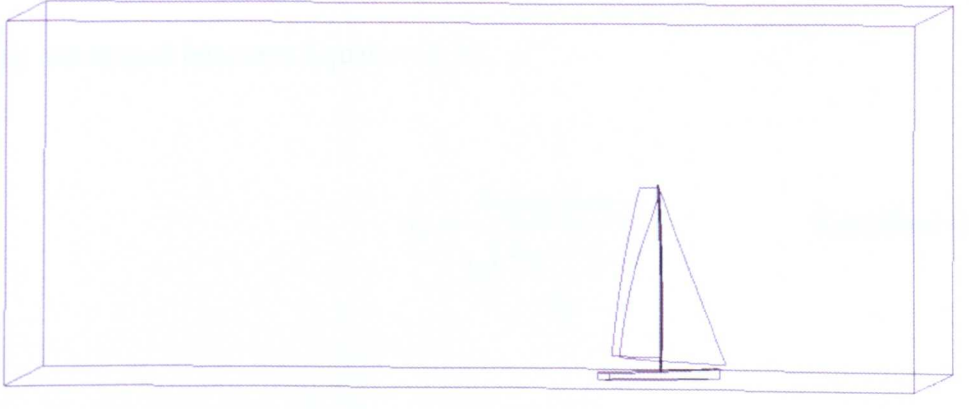

Figure 6.3.5 – Side view of a typical computational domain used throughout Chapter 6.

The domain is specified as shown in Figure 6.3.4 (not to scale). The domain consists of a pair of inlets and a pair of outlets. The velocity at the inlet is created

with the specification of Cartesian velocity components. The domain was 100m wide, 60m tall and 180m long, Figures 6.3.4-5. This also allows for the twisted flow to be applied as and when necessary, or even to be removed if and when needed for comparison.

The velocity profile in the atmospheric boundary layer can be modelled by equation 6.3.1 for a turbulent flow near a no-slip wall boundary (von Karman, 1930).

$$V(z) = \frac{u_*}{\kappa} \ln\left(\frac{z + z_0}{z_0}\right) \qquad \textbf{Equation 6.3.1}$$

Where *V(z)* is the velocity at height *z*, u_* is the friction velocity, *k* is the von-Karman constant and z_0 is the roughness height. A roughness height of 0.01m was chosen with an inlet turbulence intensity of 5%. The friction velocity can be found with the application of Equation 6.3.1 to a known velocity and height, which rearranged becomes Equation 6.3.2.

$$u_* = \frac{V(ref) \times \kappa}{\ln\left(\frac{z_{ref} + z_0}{z_0}\right)} \qquad \textbf{Equation 6.3.2}$$

Where *V(ref)* is the reference velocity at height z_{ref}. To create the twisted wind profile, this velocity then has to be combined with the apparent wind due to the boat velocity, Figure 6.3.6. Traditionally the reference height within the sailing industry is at the mast head. This is due to the majority of wind measurement

devices being located here. Further details on the application of the twisted wind profile can be found in Section 6.4.1.

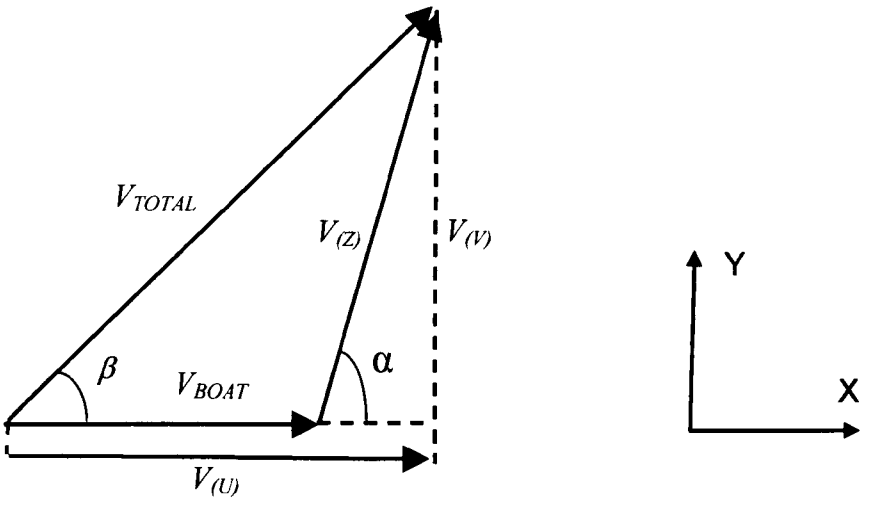

α = True Wind Angle, β = Apparent Wind Angle

Figure 6.3.6 – Twisted wind vectors

To create the total velocity vector, V_{TOTAL}, the wind vector due to the boat's velocity is combined with the velocity at height z, $V_{(Z)}$. The angle α, represents the true wind angle. The angle β, created between V_{TOTAL} and the x-axis, is the apparent wind angle. This creates the components of the twisted wind profile as shown in Equations 6.3.3-6.3.5.

$$V_{(U)} = V_{(BOAT)} + \left(V_{(Z)} \times \cos(\alpha)\right) \qquad \textbf{Equation 6.3.3}$$

$$V_{(V)} = \left(V_{(Z)} \times \sin(\alpha)\right) \qquad \textbf{Equation 6.3.4}$$

$$V_{(W)} = 0 \qquad \textbf{Equation 6.3.5}$$

The three equations above give the velocity components in the x, y and z directions respectively. This equates to directions parallel to the centreline of the

boat, at a right angle to the centreline of the boat, in the horizontal, and approximately parallel to the mast, in the vertical plane.

The changing of wind angle can be specified within the pre processor. Wind twist can also be included or excluded with the specification of a boat speed. Details of the implementation of this twisted wind model are given in Section 6.4.1.

The SST turbulence was used throughout this Chapter. The numerical simulations were carried out in a time dependent scenario, with a physical timestep of 0.02s. Drag and lift coefficient were monitored to ensure convergence in addition to the monitoring of the residuals to the solution equations. A maximum RMS residual of 10^{-4} was achieved. Convergence within each timestep of the transient loop was achieved within a maximum of 4 iterations.

6.4. Complete Model

With so many different decisions as to which features to include within a computational model, it is important to know the effect of removing various parts of the rig. Chapter 4 demonstrated that the rig is a complex collection of components, which interact with each other and need to be designed and modelled together. The more complex and inclusive the rig, the greater the complexity of the model and the more computationally expensive it becomes.

The list below details some of the considerations or options when deciding on the level of complexity of a model. These will be addressed individually within this section. Particular attention will be given to items that form part of the rig. CFD

models will be utilised to help determine their influence. The Volvo Open 70 will be used as the representative case of a realistic sailing rig.

The factors to be considered include:

- The use of twisted or non twisted flow.
- The modelling of individual or multiple sails.
- The inclusion of a mast or not.
- The inclusion of the decks and hull or not.

6.4.1. Twisted Flow

The modelling of wind twist is a fundamental and basic concept that was first discussed back in Chapter 1. The implementation of a twisted wind profile, in particular for offwind sailing, is essential and will be demonstrated in this section.

To illustrate the importance of the wind representation, the results from two simulations are presented. The first is a model created with a twisted wind profile and the second created from a model with the twisted flow omitted. For different vessels the twisted profile will be different and also highly dependent upon the True Wind Angle (TWA). The twisted model was created with an Apparent Wind Angle (AWA) of 38 degrees, an Apparent Wind Speed (AWS) of 11.24ms^{-1} and a boat speed of 7.0ms^{-1}. This was defined at a height of 25m. The non-twisted profile was set with similar values to the twisted model at 25m, but with constant wind vectors throughout changes in height. The variation in AWA between the foot of the sail and mast head is approximately 11.8 degrees (variation in AWA between a vertical height of 1m and 30m).

Figures 6.4.1.1-6.4.1.2 show streamlines created from the two different models. Both figures have been created with identical mainsail and code zero combinations, suitable for this AWA and AWS. The two models also contain the geometry for the hull and decks above the waterline. The figures are created with streamlines, started from identical upwind locations.

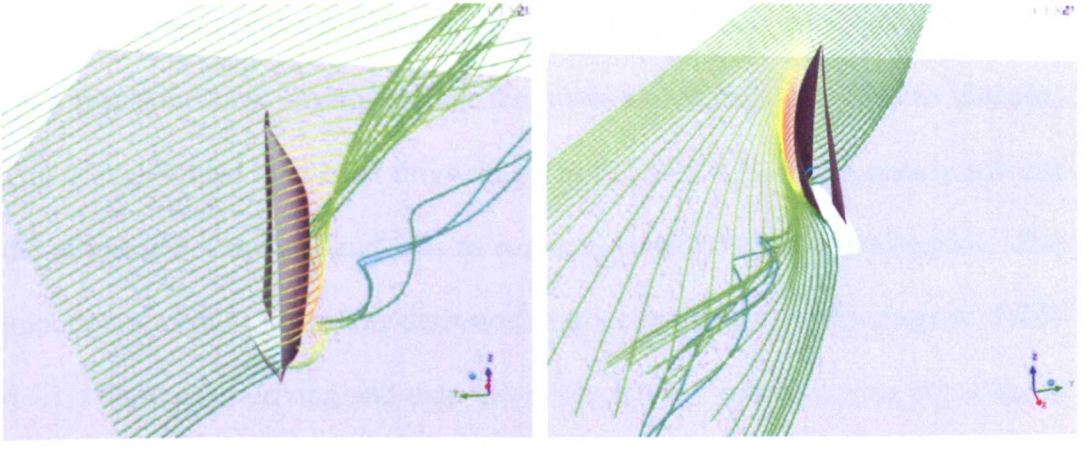

Figure 6.4.1.1– Streamlines around Volvo 70 rig created from a model with a twisted wind profile

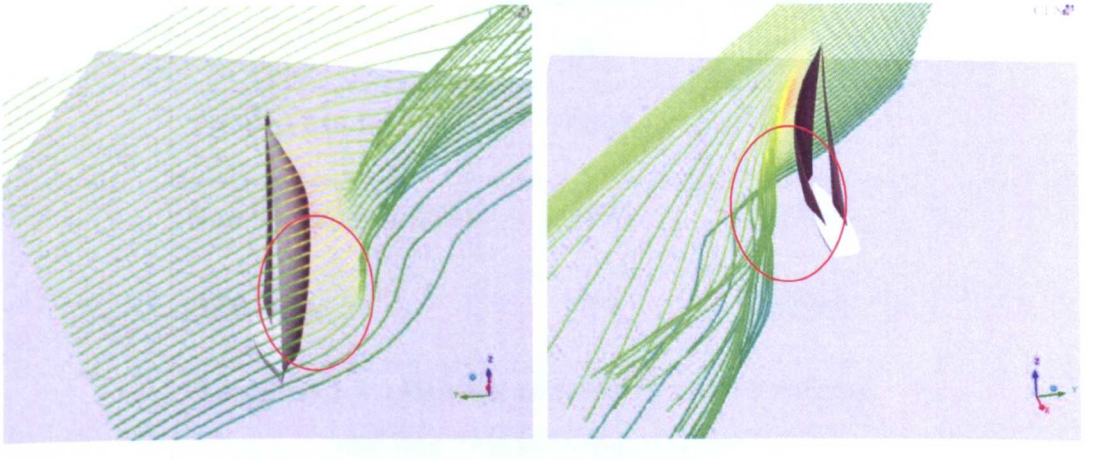

Figure 6.4.1.2– Streamlines around Volvo 70 rig created from a model without twisted wind profile

Figure 6.4.1.1 shows flow similar to that expected for a reasonably well trimmed sail configuration. The flow remains predominantly attached across the entire code zero leeward surface. Figure 6.4.1.2 shows streamlines from the non-twisted flow simulation. For this model the upper sections of the sail are also attached in a similar way to the twisted flow model. This is because at this height the flow is similar in direction and magnitude in both cases. For the lower sections of the sail the flow is approaching from a greater angle of attack than the twisted flow case. As a result the flow separates from the lower sail surface and fails to reattach. This is highlighted by the red rings shown in Figure 6.4.1.2. This greatly reduces the efficiency of the sail and fails to correctly predict its true performance. The importance of sail trim will be discussed in more detail later in this chapter. Table 6.4.1.1 shows the driving and side forces for the two models, with and without wind twist.

	Driving Force (N)	**Side Force (N)**
Twisted Model	17,068	44,712
Non-Twisted Model	13,093	36,863
Difference	23%	18%

Table 6.4.1.1 – Driving and side forces for twisted and non-twisted wind profiles

The forces from the two models are significantly different, which is perhaps to be expected from the flow visualisation and the streamlines shown in Figure 6.4.1.2. The figures highlight the necessity to correctly model the twisted wind profile.

For this case the difference in driving force is approximately 23% and the difference in side force is approximately 18%.

The twisted profile creates a fundamental difference between the operating conditions of plane wings and sails. The majority of plane wings are not required to fly at vastly different angles of attack, unlike sails which must be made to work with different angles of attack from root to tip (11.8 degrees in this example). To maintain an efficient rig, it is essential that the sails be trimmed to ensure they meet the flow at the required angle of attack. If an offwind sail is set too flat, i.e. the sail itself is set with little sail twist, it cannot be set optimally at all heights of the sail. If the sail is set for optimum performance of the lower sections, the upper sections will meet the oncoming flow at too high an angle of attack. This results in a stalled upper section of the sail. Conversely if the sail is set with too much twist the upper sections can often twist too far. The upper sections become 'flag like' and twist away in parallel to the wind.

These are the subtleties of sail trimming which can be overlooked by non-sailing engineers. Figure 6.4.1.3 is discussed next to illustrate this point. It shows a visualisation of an isosurface of velocity and streamlines for the non twisted flow model. The isosurface is set to show all regions that have a specified velocity; in this case it was set to a quarter of the freestream velocity. This figure then shows the regions adjacent to the sail surface, within the boundary layer, but also the areas in the separation bubble where the flow velocity is reduced. This, combined with the streamlines, shows how the flow for the upper half of the model remains attached. In contrast it also shows how the flow near the clew has separated. The

curvature in the sail has become too large, and attached flow cannot be maintained, creating the separation bubble. For this sail, the trimmer would need to move the clew away from the centreline to reduce the curvature and angle of attack. Care has to be taken in doing so, however, not to affect the attached flow at the upper surface.

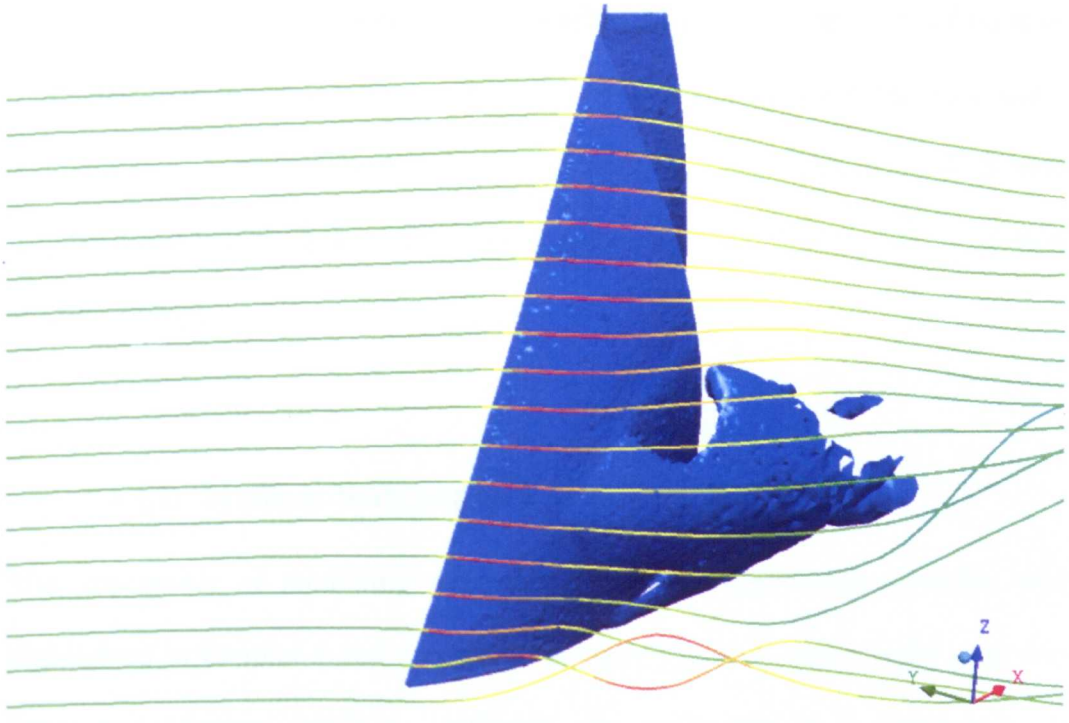

Figure 6.4.1.3 – Separation visualisation with an isosurface of velocity and streamlines

The twist of sails can also, in special occasions, be used to a trimmer's advantage. For example, to reduce healing force, more twist can be introduced into the sail. When such an increase is applied to a previously correctly trimmed sail, the lift from the upper section reduces. Introducing twist into a sail during real sailing conditions can also have different effects to those of the wind tunnel or CFD model. In real sailing applications, variations in wind and the influence of waves, result in an unsteady environment. A sail with twist can be a more forgiving sail.

This is because a flat sail (with little sail twist) can stall simultaneously up the luff. Conversely a twisted sail depowers or powers up gradually, helping to maintain smoother lift forces from the sails and hence a more stable environment. The importance of including a twisted wind profile is therefore essential in creating a more realistic simulation scenario. With no notable increase in computation times, the twisted profile should definitely be included in all models, unless trying to replicate specific cases, such as the wind tunnel model in Chapter 5. The flow visualisation is also a powerful tool for the education of both trimmers and sail designers, allowing them to see the physical effects of their changes in trim.

6.4.2. Multiple Sails and Sail Interaction

The importance of modelling sails in combination rather than isolation was highlighted in Chapter 4 and will not be covered further in this chapter (see also Paton and Morvan, 2007C). Although this study was in 2 dimensions, it highlighted the importance of the inclusion of both sails to create realistic results. It also highlighted the dangers of modelling in isolation as the driving force for both sails together was not the sum of the driving forces for the individual sails. The main feature of modelling sails independently was the lack of upwash created and the consequent separation for similar AWAs.

6.4.3. Mast Effects

The effects of the mast have been well documented for many years (Marchaj, 1964; Milgram, 1968; Wilkinson, 1983). These effects have also been

investigated in 2 dimensions by this author in Chapter 4 (see also Paton and Morvan, 2007). The simulations were set up as described in Section 6.4 with the same rig and sails as described in Section 6.4.1. The simulations were run at and AWA of 38 degrees, an AWS of 11.24ms^{-1} and a boat speed of 7.0ms^{-1}. This was defined at a height of 25m.

Figure 6.4.3.1 demonstrates the effects of the mast upon the overall flow and forces of the rig in 3 dimensions. The rig and mast are again typical of the Volvo Open 70 rig. The figure shows velocity slices through the domain when viewed from above. Also shown are velocity vectors.

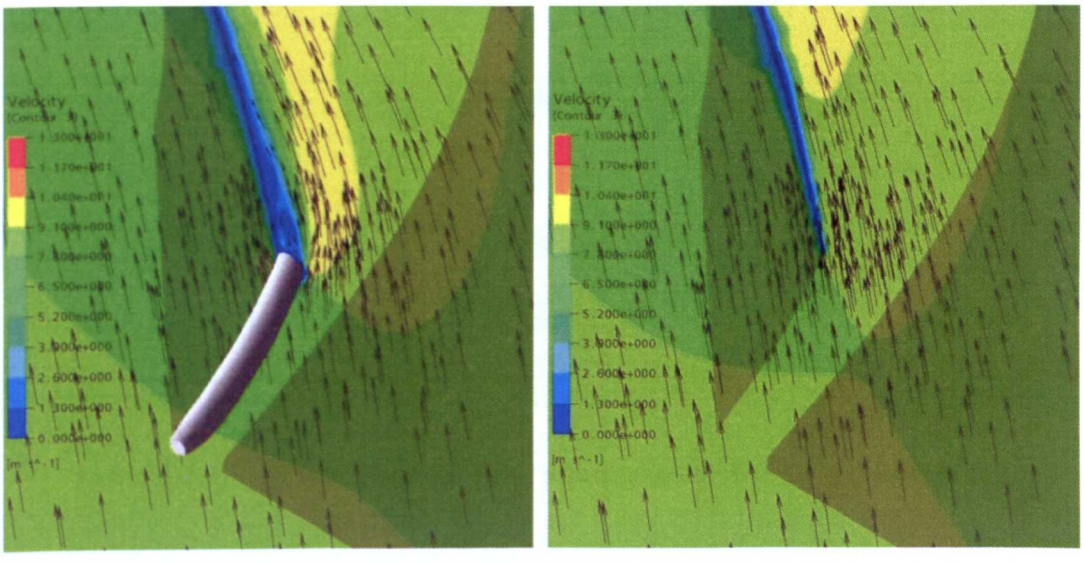

Figure 6.4.3.1 – Effect of mast inclusion upon velocity and flow field around a Volvo 70 rig

The images above represent identical views from above the rig looking down the mast. The shaded regions represent the outlines of the code zero and mainsail to help provide orientation. The immediate visible difference is the region of separation shown from the extended blue region in the rig with the mast. The flow fails to stay attached because of the highly curved nature of the mast. This

separation has an impact upon the mainsail's forces with differences in mainsail side force of approximately 3%. On the other hand, perhaps not surprisingly, the variations in the forces for the code zero were less than 0.5%, for both the driving force and side forces.

Table 6.4.3.1 shows a comparison of the total rig forces with and without a mast. Included in the table are columns showing total driving force, total side force and efficiency. The total driving force increases by 1.1% when the mast is removed. The side force reduces by 0.9%. The efficiency of the rig changes by a more significant 2%, as it combines the 2 changes seen in both the driving and side forces.

	Driving Force (N)	**Side Force (N)**	**Efficiency (Driving/Side)**
TOTAL RIG WITH MAST	15587.3	35386.2	0.440
TOTAL RIG WITHOUT MAST	15755.0	35067.6	0.449
% difference *(relative to with mast)*	1.06%	-0.91%	1.96%

Table 6.4.3.1 – Total rig forces for simulation with and without mast.

In conclusion, the area of influence of the mast is more significant on the mainsail and less so upon the code zero. As a result, if the tolerances suggested above are acceptable, the removal of the mast for studies focussed upon the code zero is acceptable. The increase in computation times to model the effects of the mast accurately are perhaps not outweighed by the potential gain of accuracy, considering the complexity their inclusion bears on the meshing procedure. The meshing of such models is considerably more intensive, with particular issues

involved with the interaction of the prism layers created from the masts and mainsail at larger AWAs.

For upwind sailing condition, where the slot size is reduced, the effects of the mast would be emphasised. The author suggests that the inclusion of the mast may add a factor of 2 to the time taken for the meshing process. Although the value of 3% was suggested as the percentage difference between mainsail forces, with and without mast, a parametric series of models would probably help remove some of these differences with similar trends predicted. For parametric studies the overall trends are often more significant in finding an optimum to improve performance, rather than the absolute values. This allows for optimum regions to be identified and more targeted work to be carried out.

In summary the influence of the mast upon results for the mainsail could be significant and should be included within studies focussing upon mainsails. The importance of the inclusion of masts within studies of offwind sails, where the focus is upon the foresail, is reduced significantly. However, if computation times and resources are not an issue, masts should be included to maximise the accuracy of the rig simulations.

6.4.4. Hull and Deck Effects

Within CFD models used for sail engineering, the hull and decks are often neglected. The following section gauges the impact of neglecting the deck and hull upon the forces and the underlying flow for the Volvo Open 70. The two models used are identical with the exception of the decks and above water line

hull. The model is again set at an AWA of 38 degrees and an AWS of 11.24m.s^{-1}. These are defined at a height of 25m. The twisted wind profile is also applied to both models. Although the deck geometry used is simplified and includes none of the features of equipment upon the deck itself, the impact of its modelling can be seen clearly from the following figures.

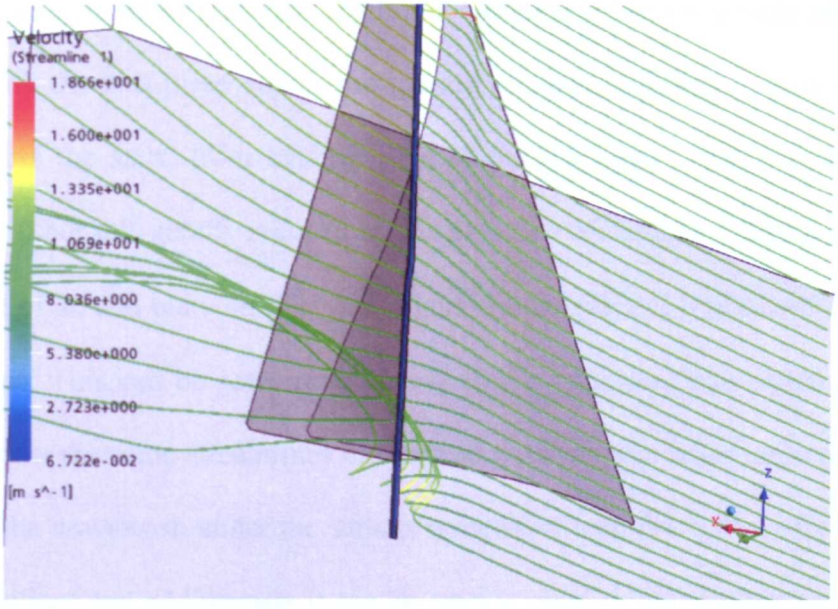

Figure 6.4.4.1 – Streamlines created from Volvo 70 simulation without hull and deck.

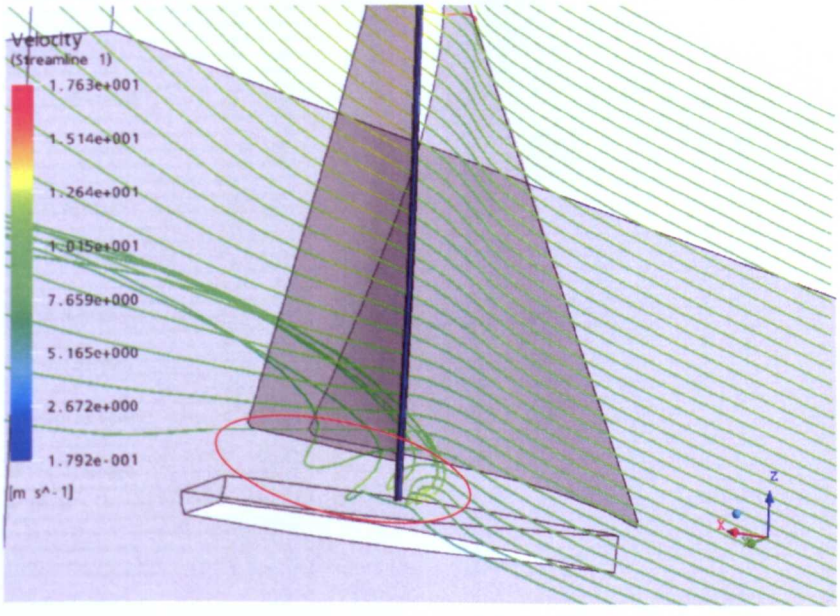

Figure 6.4.4.2 – Streamlines created from Volvo 70 simulation with hull and deck.

The effects can be clearly seen from the comparison of the streamlines between the two setups. The effect is particularly prominent at the foot of the code zero, highlighted by the red outline. Without the presence of the hull, the flow has a tendency to pass under the sails, creating a 'scrubbing' or downwash effect at its foot. With the hull these effects are greatly reduced, creating a more idealistic flow across the sails, from leading edge to trailing edge. There is still some downwash, but it is greatly reduced by the presence of the hull. This is similar to the effect of an end plate on a F1 car, where the endplate is introduced to reduce tip leakage. This can be seen more clearly in the following two figures. These figures show the same streamlines but instead from abeam. Here one can clearly see how the downwash under the sails is minimised with the hull present (shown by red outline) and additionally it can be seen to cause some upwash prior to the previously described downwash (shown by blue outline).

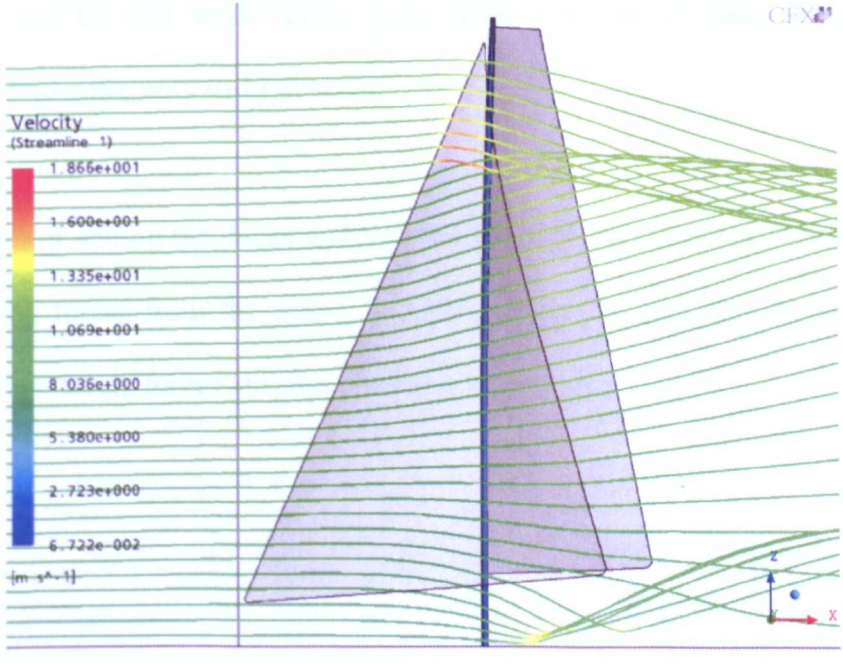

Figure 6.4.4.3 - Streamlines without deck from abeam

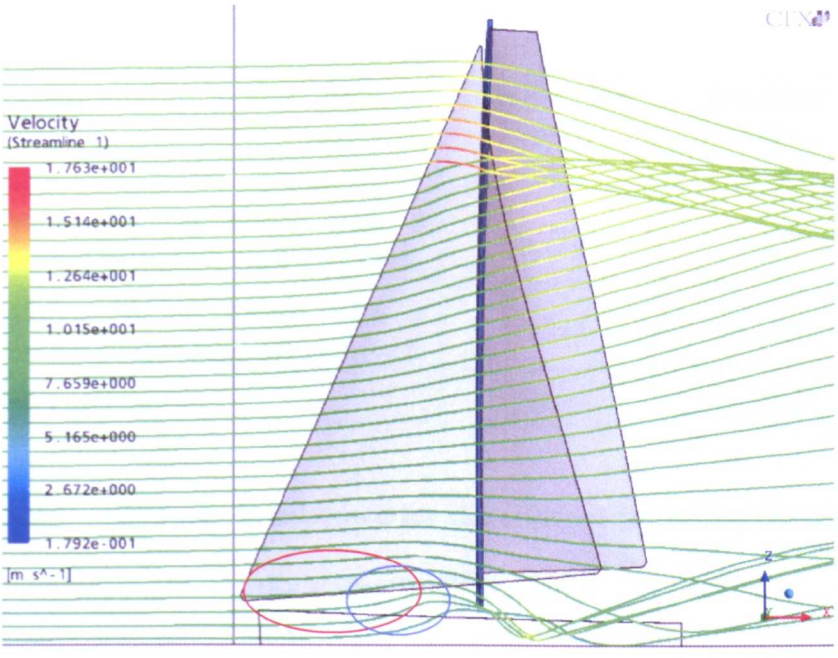

Figure 6.4.4.4 - Streamlines with deck from abeam

It is very likely that these effects would be further amplified if a realistic amount of heal was included within the model. For the models in this chapter it was decided to exclude any heal, to ensure consistency between models throughout this thesis and permit a better comparison. With a healed model, the upwash from the flow over the hull would 'carry' more of the flow onto the sails, thus reducing the flow under the sails still further.

The effect of adding the decks and hull has a beneficial effect upon the flow and the driving forces from the sails. A 5.1% increase in total rig driving force is seen. The total rig forces are summarised in Table 6.6.4.1.

	Rig Driving Force (N)	Rig Side Force (N)
Volvo 70 rig forces with a model including hull and deck	6,270	11,228
Volvo 70 rig forces with a model excluding hull and deck	5,949	11,118
% Difference	5.12%	0.98%

Table 6.6.4.1 – Rig force breakdown for the effect of including the hull within the Volvo 70 CFD model

The addition of the hull creates additional 'windage', the negative effect of wind on the hull, which could also be included in any analysis if needed. The modelling of the decks does increase the complexity of the meshing procedure but not unduly, and does have an important effect upon the results. It is therefore suggested that models should include decks and hulls where possible to obtain realistic performance predictions.

6.4.5. Summary

The previous subsection has considered the impact that different features have on the accuracy of the predicted forces on the rig. It is concluded that consideration of twisted flow, multiple sails and the hull and deck should always be included in any model. The effect of the mast can be excluded when studying off-wind foresails specifically, but otherwise it is worthwhile to include the mast also.

6.5. Volvo Open 70 FSI Model

Moving on from the viscous CFD models presented so far in Chapter 6, Sections 6.5-6.9 present results from the application of the FSI model developed in Chapter 5 to the Volvo 70 rig. Discussion on the convergence of the FSI solution is given for a two sail offwind sailing application. The section also discusses some of the issues surrounding the application of the FSI model to the Volvo 70 rig. A comparison to inviscid methods is made followed by a parametric analysis of carriage location and sheet length for the code zero sail.

This section begins with the description of the FSI model, including the details of the CFD and structural model for the Volvo Open 70. The structural model began with the recreation of the sails within a CAD scenario from the data supplied by North Sails, UK. This included the design shape of the mainsail, code zero, hull and mast. For commercial reasons, the details of the thread layouts and mould shapes are omitted due to the competitive sensitivity of the designs. For both sails, the individual threads were placed upon the intended mould shape within the CAD scenario. The sails physically consisted of a composite material, comprising two layers of substrate either side of 3 series of separate sets of threads. These are laid by a gantry, which position the threads in the directions requested by the sail designer. This is done for the three sets of yarn. The threads are designed to align with the stresses placed upon the sail.

As mentioned previously the details of the thread layouts cannot be given due to commercial sensitivity, but include:

- Threads between head and clew.

- Threads between head and tack.
- Threads between tack and clew.

The structural model was created with approximately 5,000 elements refined and aligned as necessary to create an accurate yet efficient mesh (Heppel, 2008, *personal communication*). Details of the initial rig and trim conditions were set in RELAX. Figure 6.5.1 shows the ease with which various trims can be dealt with by RELAX. The difficulties of obtaining appropriate trims have been discussed in Chapter 5. Although still an issue, the use of RELAX and its bespoke interface help minimise the complexity of a physically simple task, such as changing a sheet length. The dialogue box shown is relevant to a genoa and gives options for headstay tension, sheet length, carriage location etc. in addition to features such as mast bend.

As a result of the setup proposed in this thesis, it is only ever necessary to generate a single mesh for each sail scenario. Consequently, a model with a mainsail, code zero, mast and hull will only need one mesh, even if the sails are trimmed significantly. Changes to the structural elements can be made, providing the outline shape of the sail is not altered significantly, e.g. a thread layout could be altered provided the sail outline remains constant.

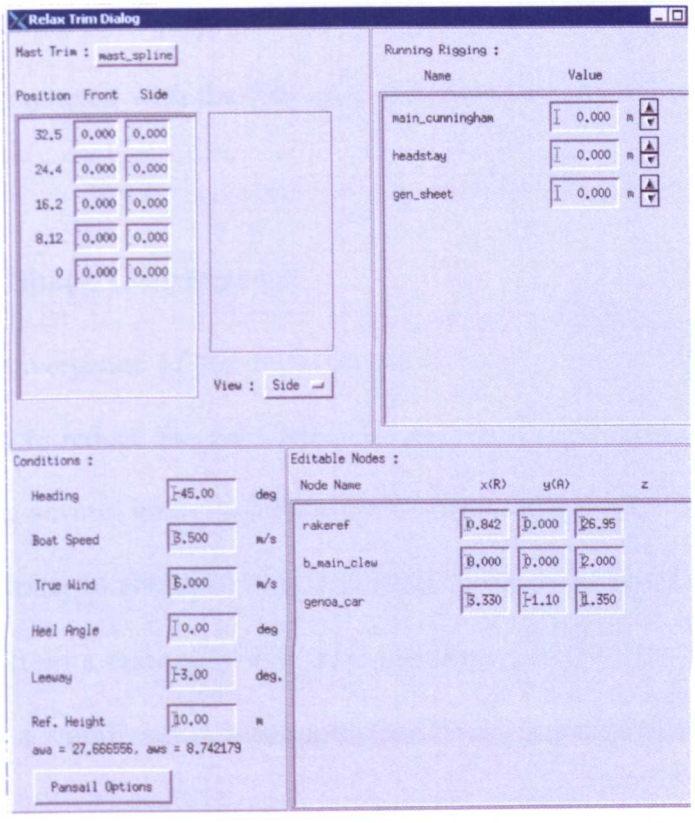

Figure 6.5.1 – RELAX trim dialog window for a foresail.

The CFD models were set up as detailed in Section 6.3. A twisted wind profile was used throughout. The SST turbulence model within ANSYS CFX was used. Transient simulations were used with a timestep of 0.2s.

6.6. Convergence

The rate of convergence of an FSI solution is one of the most important features of a successful scheme. The solution must be robust yet remain efficient. One of the disadvantages of using this type of multiple mesh FSI scheme is the potential for instabilities within the solution, due to interpolation and numerical rounding errors that occur as a result of the multiple routines used to transfer data and coordinates. The following section discusses convergence of the scheme, with

details of convergence of shapes, forces, and pressures. In addition, some of the difficulties encountered with the full scale application of the FSI scheme are also discussed.

6.6.1. Shape Convergence

The rate of convergence of the sails towards a steady flying shape is a major factor in trying to reduce the time taken for a complete FSI solution. With each CFD run taking several hours, reducing the number of FSI loops to a minimum is essential in helping to shrink turn-around times. The convergence study used in this section is from a main and code zero sail from a Volvo Open 70, where the code zero had a significant retrim applied to the sail (30 cm reduction in sheet length).

The sail shapes and pressures are plotted against the number of iterations, to show the adaptation of the sail shape over time. Figure 6.6.1.1 and Figure 6.6.1.2 show slices from the code zero at 5m and 25m above the water level. The slices represent sail shape, where the x-axis is parallel to the centreline of the boat and y-axis is perpendicular.

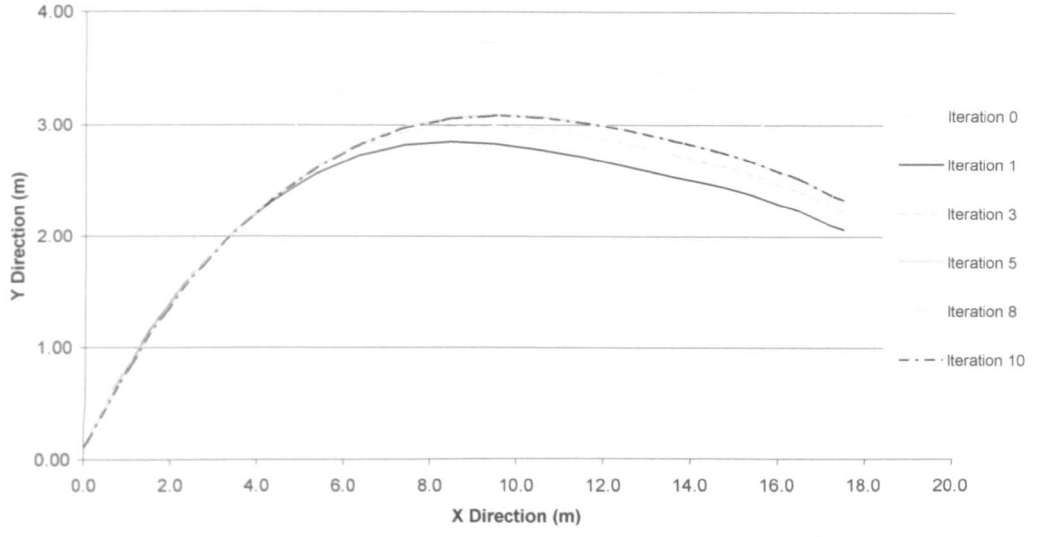

Figure 6.6.1.1 – Volvo 70 FSI convergence of 5m height sail chord

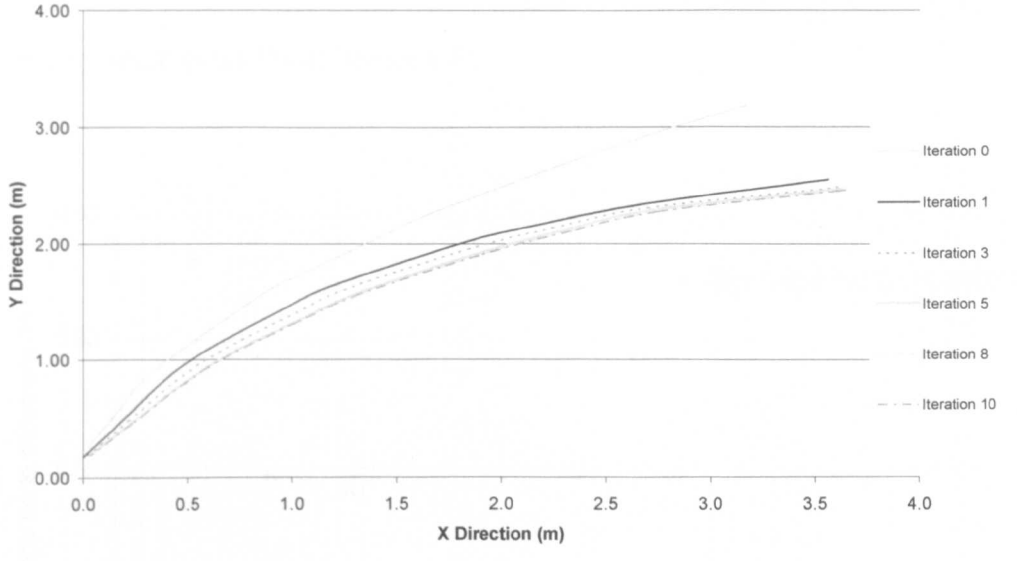

Figure 6.6.1.2 – Volvo 70 FSI convergence of 25m height sail chord

These figures illustrate the convergence to a steady flying shape for a code zero that has been retrimmed with a 30cm reduction in sheet length. Iteration 0 represents the initial flying shape that the CFD solution was given to create the mesh. The shapes converge quickly to a steady solution. By iteration 5, the shapes become barely distinguishable between iteration. For completeness, the figures also show data for 8 and 10 FSI iterations. It can be seen here that the two

are identical and very similar to that achieved at iteration 5. The mainsail included within the study has not been shown as no appreciable differences could be seen between iterations.

Figures 6.6.1.3 and 6.6.1.4 show the average node movement for slices at 5m and 25m above the waterline. Table 6.6.1.1 confirms the shapes have converged comprehensively by iteration 10. Table 6.6.1.1 shows the node movement per iteration, for 5, 15 and 25m slices. By iteration 8 the average node movement has reduced to less than 11 mm and by iteration 10 to less than 1 mm. When expressed as a percentage of the chord length (~18m), these numbers become relatively small (<0.61% at iteration 8).

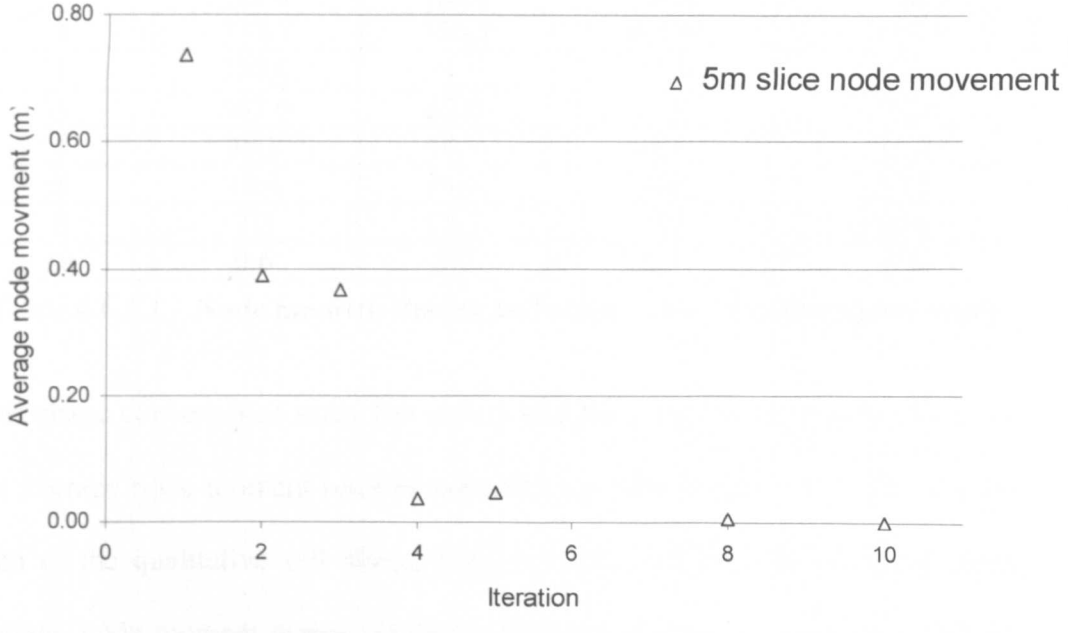

Figure 6.6.1.3 - 5m slice node convergence for FSI model of Volvo 70 rig

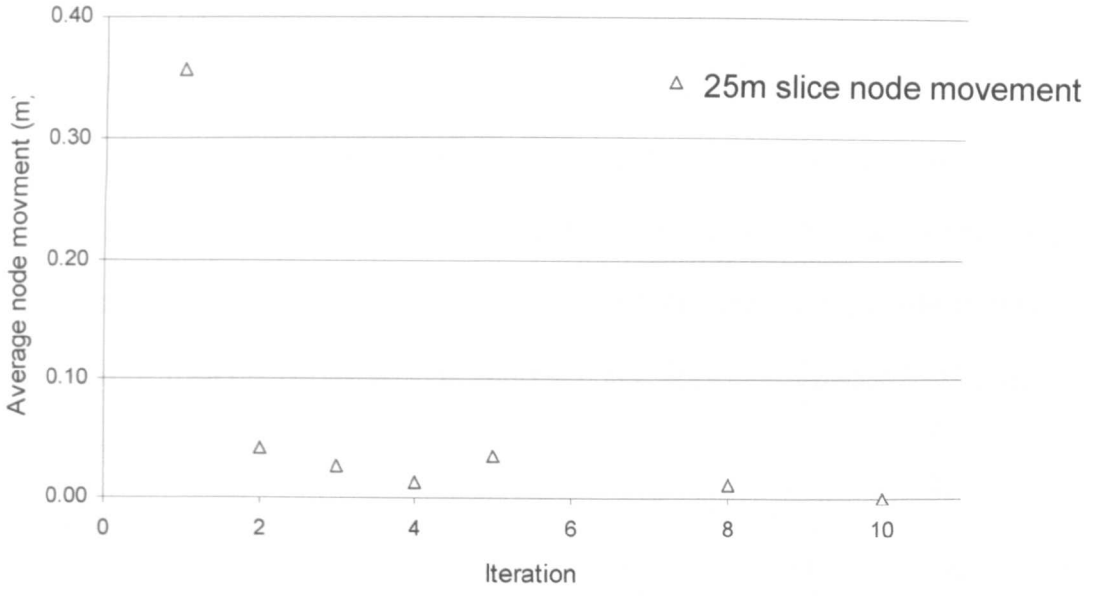

Figure 6.6.1.4 - 25m slice node convergence for FSI model of Volvo 70 rig

Iteration	Average node movement for 5m slice (mm)	Average node movement for 15m slice (mm)	Average node movement for 25m slice (mm)	Average Node movement across all slices (mm)
1	737.7	356.9	356.9	483.9
2	388.6	41.9	41.9	157.5
3	367.6	27.0	27.0	140.6
4	38.8	14.1	14.1	22.4
5	48.4	34.6	34.6	39.2
8	7.3	12.2	12.2	10.6
10	0.6	0.7	0.7	0.7

Table 6.6.1.1 – Node moment during full scale Volvo 70 convergence study.

This shape convergence study has shown that for a significant re-trim of the sail the average node moment reduces considerably after iteration 4. This was also seen in the qualitative sail slices, Figures 6.6.1.1-6.6.1.2. By iteration 10 the average node moment across all three slices was less than 1 mm for a full size Volvo 70 sail with a mast height of ~30m.

6.6.2. Convergence of Force and Pressure

From a sail design or naval architecture stand point, convergence of the forces is perhaps more important than the shape convergence. The following figures show the sail forces for the same model as in the previous shape convergence section, with a code zero and mainsail, subjected to a significant retrim (30cm reduction in sheet length). The figures show convergence of the forces against iteration for the mainsail and code zero.

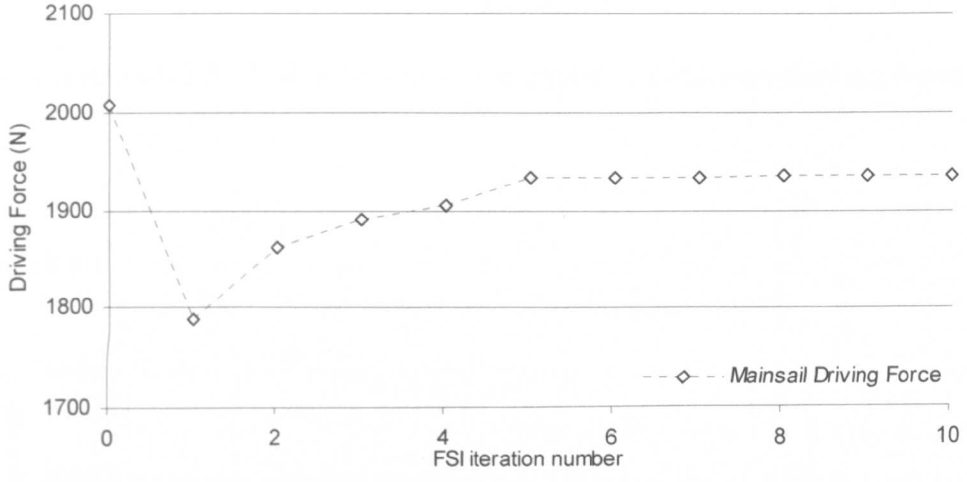

Figure 6.6.2.1 – Volvo 70 FSI convergence of mainsail driving force

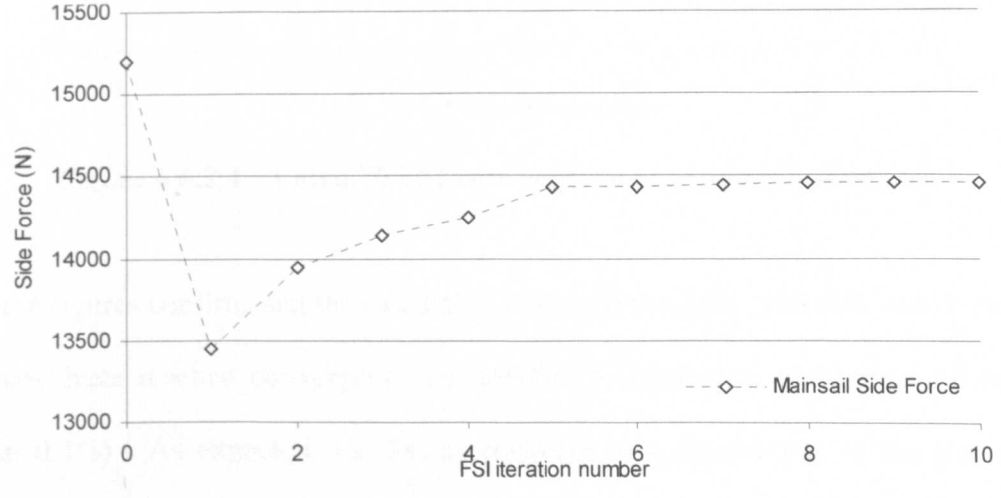

Figure 6.6.2.2 - Volvo 70 FSI convergence of mainsail side force

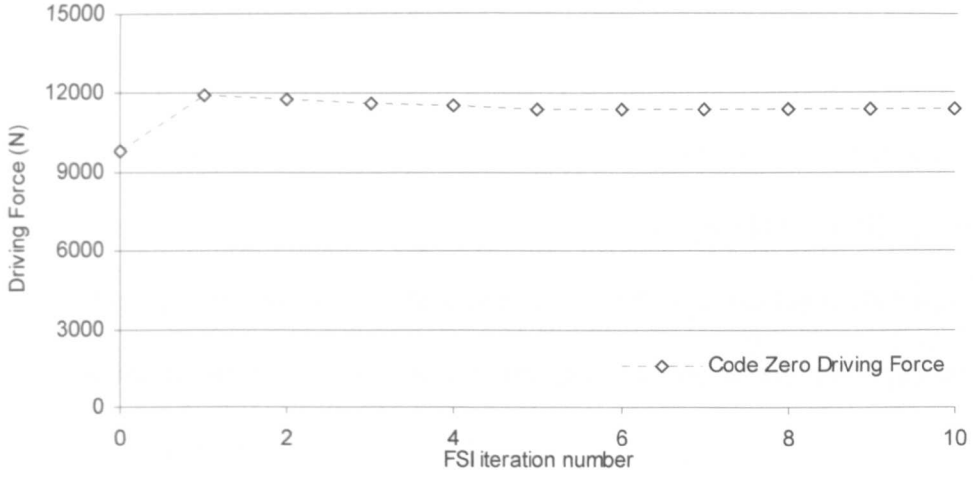

Figure 6.6.2.3 - Volvo 70 FSI convergence of code zero driving force

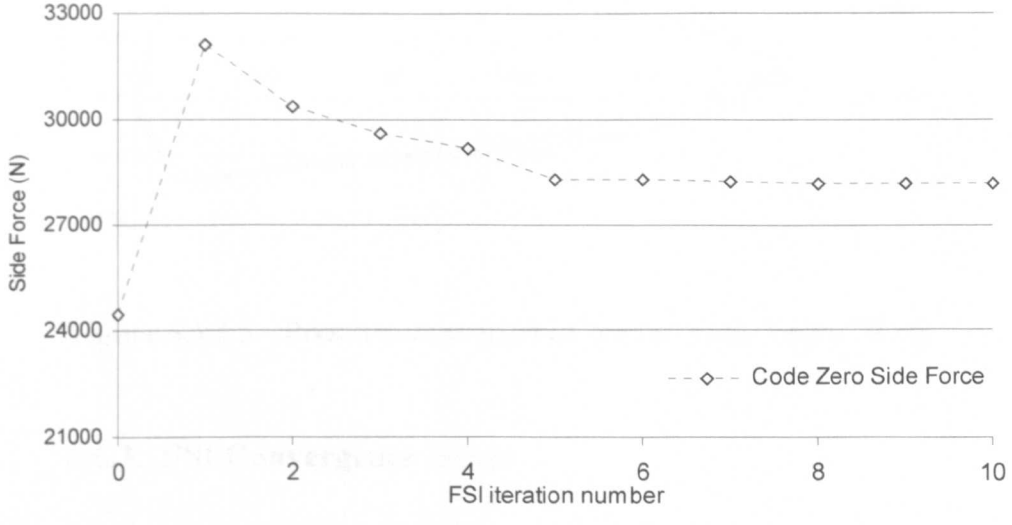

Figure 6.6.2.4 - Volvo 70 FSI convergence of code zero side force

These figures confirm that the calculated forces on the sails, both side and driving forces, have reached convergence by iteration 5 (Max error to iteration 10 less than 0.4%). As expected, the forces converge at a similar rate to the shapes, Figure 6.6.1.1 and 6.6.1.2. The maximum percentage difference at iteration 4 was

less than 3.5% when compared to the value at iteration 10, deemed converged. By iteration 8 the maximum difference was less than 0.3%.

Important for the stability of the FSI solution is the convergence of the pressure field. Figure 6.6.2.5 represents the convergence of the pressure profile along a 15m slice through the code zero. Here one can clearly see the rapid convergence of the pressure profiles. By iteration 5, the profiles are barely distinguishable from the iteration 10 profile.

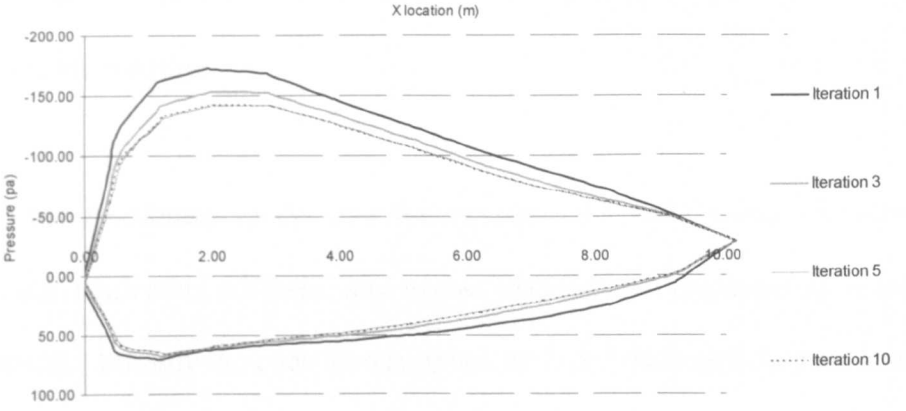

Figure 6.6.2.5 - Pressure convergence for full scale Volvo 70 rig

6.6.3. FSI Convergence Issues

It is worth noting at this stage that although the FSI approach presented in this thesis works well, it is susceptible to instabilities under certain circumstances, which are described below. These can be due to instabilities within either of the software codes and will be described within this section.

Within the structural solver, instabilities were encountered when modelling the extended foot of foresails. This area is similar to the extended leech area that

extends past the straight line between the tack and clew. For a sail designer, maximising the sail area at the foot is important, as it reduces 'scrubbing', increases the effective aspect ratio of the foresail, and creates driving force with relatively little healing moment. This extended area at the foot can become problematic from a modelling standpoint as the sail material model has no resistance to bending. A similar problem can be encountered at the leech, but battens are used to counteract the issue. For the sail designer, maximising the size of the area at the foot of the foresail is important and the natural stiffness of the laminate sails is used to help achieve this, in addition to the support from the decks and the guardrail.

Due to the membrane model and the assumptions made within the structural solver, e.g. neglecting stiffness, any excess material not supported by a batten is problematic. Initially the code zero supplied by North Sails included an 'extended foot', which created a fold along the foot. An example of this is shown in Figure 6.6.3.1 with an output from the structural post processor.

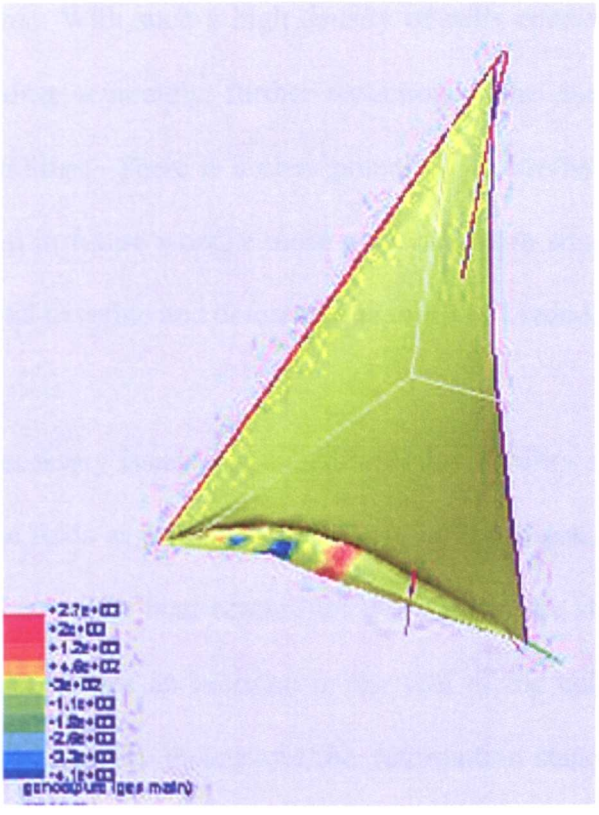

Figure 6.6.3.1 - Folded foot in RELAX

Although the structural model is capable of modelling creases within sails, the instabilities occur within the fluid solver. The coupling scripts deal with the fold by moving the nodes on the sail surface. It is the mesh deformation routine within the fluid solver that typically fails. This is due to the increased likelihood of inverted elements and therefore cells with negative volumes. To overcome this, it is necessary to ensure the mesh is locally fine enough to make certain the mesh can accurately represent the fold and the associated curvature of the geometry.

For similar reasons the fluid solver also has a tendency to return errors when the trims are extensively different to the shape used for the initial CFD model. This became particularly apparent when the code zero was sheeted in extensively beyond the initial shape, effectively squashing the cells between the mainsail,

mast and code zero. With such a high density of cells needed in this region to compute lift and drag accurately, further reduction of the distance between the sails caused instabilities. There is a clear potential for conflict here, and should folds be considered in future work, a more powerful mesh adaptation tool would need to be employed to refine and defeature the mesh as needed.

To overcome unnecessary issues associated with the inability of a given mesh to represent excessive folds as part of the FSI loop, an oversheeted initial sail shape (i.e. sail set too close to the boat centreline) was used as the starting point to the FSI analysis. This ensures an increase in the size of the cells within the slot, maintaining solution stability throughout the deformation stages toward the final flying shape. The trim within RELAX can then be adjusted towards the target trim, without the creation of negative or inverted elements.

Instabilities were also encountered when extremes of trim were set, usually outside the normal ranges of sailing. This often created extreme curvatures or regions where the sail shapes inverted, e.g. regions where the sail has luffed. Although these regions are within the capabilities of the FSI solution, it can be necessary in these cases to create an initial CFD model closer to the intended shape in order to compute a volume mesh with the correct local density of cells. An alternative to this approach can be to use an under relaxation factor, to reduce the sail movement between iterations within the structural solver. This approach is termed negative feedback within RELAX.

The negative feedback works by using a blend of the old and new pressures (Heppel, 2008, *personal correspondence*). It takes a parameter K, with a value between 0 and 1, to determine the ratio between the two pressures. A value of 0 means no feedback and a value of 1 implies 100% feedback, which is stable but infinitely slow. More formally the new pressure file with negative feedback is defined as in Equation 6.6.3.1.

$$DP = (DP(N-1)^* K) + (DP(N)^* (1-K)) \qquad \textbf{Equation 6.3.1}$$

Where DP is the pressure file, N is the loop number and K is the negative feedback constant. A value of 0.6, even in the most extreme cases, is found to be suitable to ensure convergence.

The FSI solution within this thesis proved to be robust. For example, for the parametric model shown later in this chapter, all FSI simulations within the matrix of cases (Table 6.8.1), were completed from a single initial CFD model. This allowed for batch files to be created within RELAX, for various trims. Each case within the matrix typically returned a solution in approximately 36 hours, for 7 FSI iterations on 16 processors. The ability of the automatic remeshing strategy used in this scheme is a major benefit over more simplistic solutions (Richter and Horrigan, 2003). Their process recreated the mesh from scratch following the structural solver using automated journals (a series of pre recorded commands to recreate a similar state). For large computation meshes this process could add several hours to the total simulation time. It also has the disadvantage of limiting

the meshing process to a single CPU, due to the limitation of GAMBIT their meshing software, resulting in the need for high memory workstations.

6.7. Full Viscous FSI vs. Simplified Models

The use of viscous CFD, within a FSI solution, has been questioned by some as to whether it can be a useful design tool, for either sail designers or naval architects (Elliot, 2008, *personal communication*; Claughton, 2008, *Personal communication)*. It has been argued that simplified inviscid methods can provide realistic sail shapes. The following section details a comparison between a simplified inviscid method and the viscous FSI model developed within this thesis.

6.7.1. Inviscid Method Comparison

This section details an inviscid FSI scheme and compares it to a viscous FSI model. The full viscous FSI scheme is compared to that of an inviscid code, Pansail (Fiddes and Gaydon, 1996), built into the RELAX software package. The known weaknesses of panel based methods, such as Pansail, include the poor prediction of forces, in particular drag (Lasher *et al.*, 2008). However the question that needs to be answered is 'whether inviscid methods can create realistic offwind sail shapes?'

Below are two figures showing a comparison of sail shapes created from the two separate methods at two different sail trims, Figures 6.7.1.1 and 6.7.1.2. The images represent outlines of the sails with two sail slices at 5 and 25m. The images are taken looking down from above the sails. The figures include an

outline of the sail shapes in addition to stripes at 5m and 25, to help show changes in curvature. The viscid method is provided by the CFX and RELAX FSI scheme. The second method is the inviscid coupling of Pansail and RELAX.

The sails are identical code zero sails, modelled in full scale. The two trims have been created with a change in carriage location, from 9.2m to 8.6m, both with similar sheet lengths. Figure 6.7.1.1 was created from a carriage location of 9.2m from a reference location. In Figure 6.7.1.2 the carriage has been moved forward to 8.6m, 0.6m further forward. The length of the sheet has been kept constant for both examples in addition to the AWA, kept at 38 degrees. Identical twisted wind profiles were used for all runs with both models. Run times for the two models were significantly different, with the inviscid solution solving in minutes, rather than hours for the full viscid solution.

For both trim conditions, the difference between the two models is clearly noticeable. The average error for the 5m and 25m quarter stripes over both trim conditions is 260mm, equivalent to a model scale error of 13mm. A breakdown of these numbers is given in Table 6.7.1.1. This was calculated with the same methodology as used in Chapter 5. In both trims, the inviscid method predicts a fuller shape with a more open leech. This highlights the difference in performance between the two models and challenges the validity of using panel methods for offwind flying shape predictions. The flatter sail shape, created from the further aft carriage location, provided closer results, with the inviscid code providing much closer sail shapes to the viscid code. The use of an inviscid code

for flatter sail shapes at lower angles of attack or for initial shapes for a FSI scheme, in these circumstances, seems to be justifiable.

	5m Stripe Error (full/model scale) (mm)	25m Stripe Error (full/model scale) (mm)	Average Stripe Error (full/model scale) (mm)
Inviscid Solution	122/6.1mm	400/20mm	262/13.1mm

Table 6.7.1.1 – Average node errors for both trim conditions for an inviscid method compared to a viscous FSI solution for Volvo 70 rig

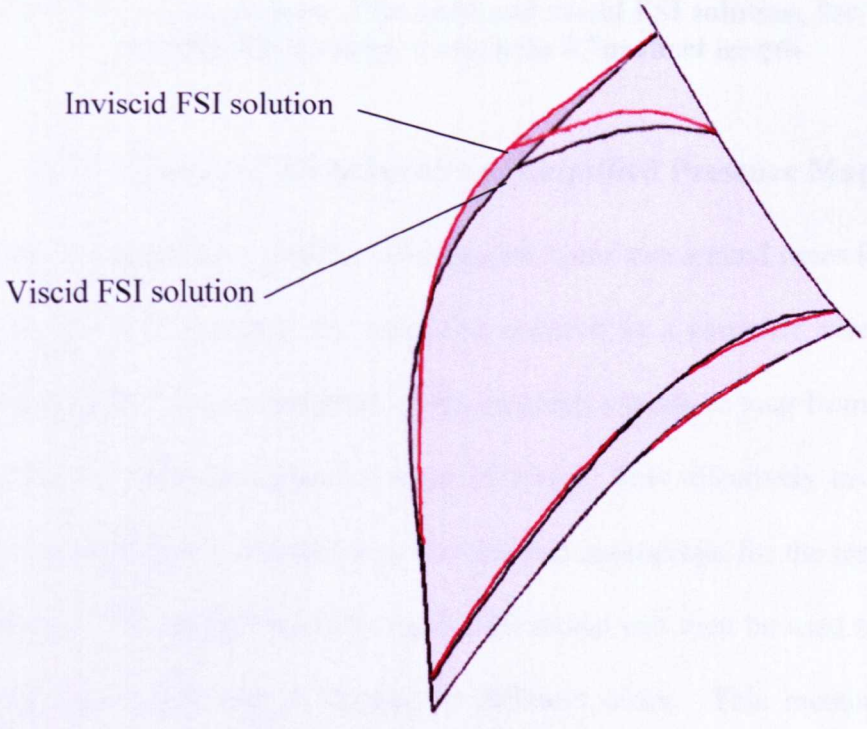

Figure 6.7.1.1 – Comparison of inviscid and viscid FSI solution for Volvo 70 application, carriage 9.2m, 0.7m sheet length.

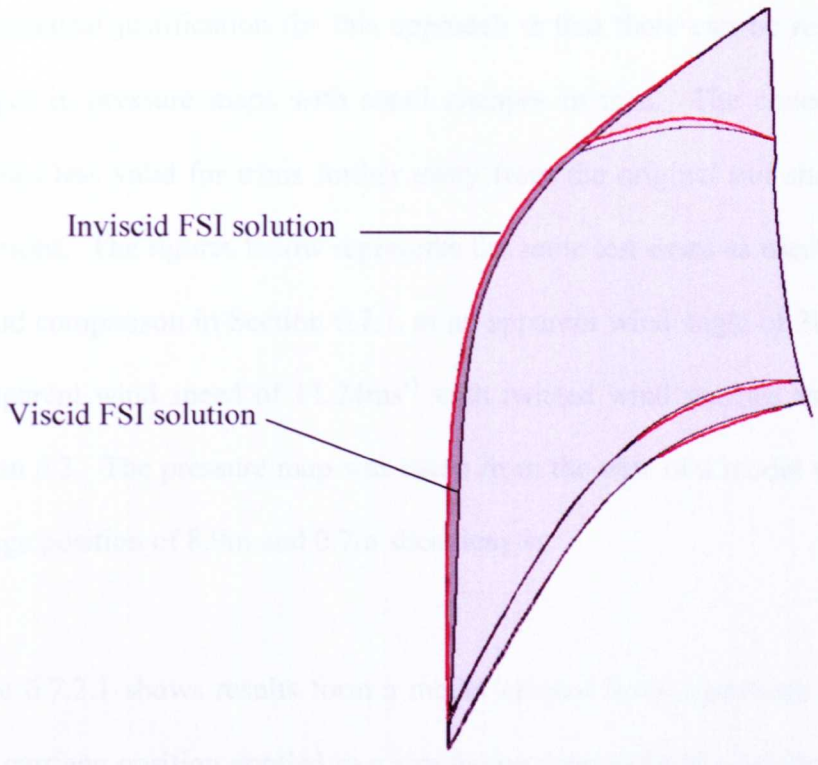

Figure 6.7.1.2 – Comparison of inviscid and viscid FSI solution, for Volvo 70 application, carriage 8.6m, trim 0.7m sheet length.

6.7.2. Viscous CFD Solution vs. Simplified Pressure Map Input

In an attempt to provide a quicker solution and faster turn around times for the sail designer or naval architect, an alternative solution to a complete viscous CFD solution and FSI loop is presented. This employs a pressure map from a similar trim condition used throughout a range of trims. This effectively involves the creation of a single CFD model at a trim deemed appropriate for the testing to be carried out. The results from this rigid CFD model can then be used to create a pressure map which can be applied to different trims. This method has the advantage of only needing the output of a single CFD simulation, thus reducing run times considerably.

The practical justification for this approach is that there can be relatively small changes in pressure maps with small changes in trim. The concept obviously becomes less valid for trims further away from the original sail shape and wind conditions. The figures below represents the same test cases as used for the panel method comparison in Section 6.7.1, at an apparent wind angle of 38 degrees and an apparent wind speed of $11.24ms^{-1}$ with twisted wind profiles as described in Section 6.3. The pressure map was taken from the trim of a model with a middle carriage position of 8.9m and 0.7m sheet length.

Figure 6.7.2.1 shows results form a model created from a pressure map from an 8.9m carriage position applied to a simulation created from a carriage position of 9.2m. Figure 6.7.2.2 uses a pressure map from the 8.9m carriage position and applies it to an 8.6m carriage position model.

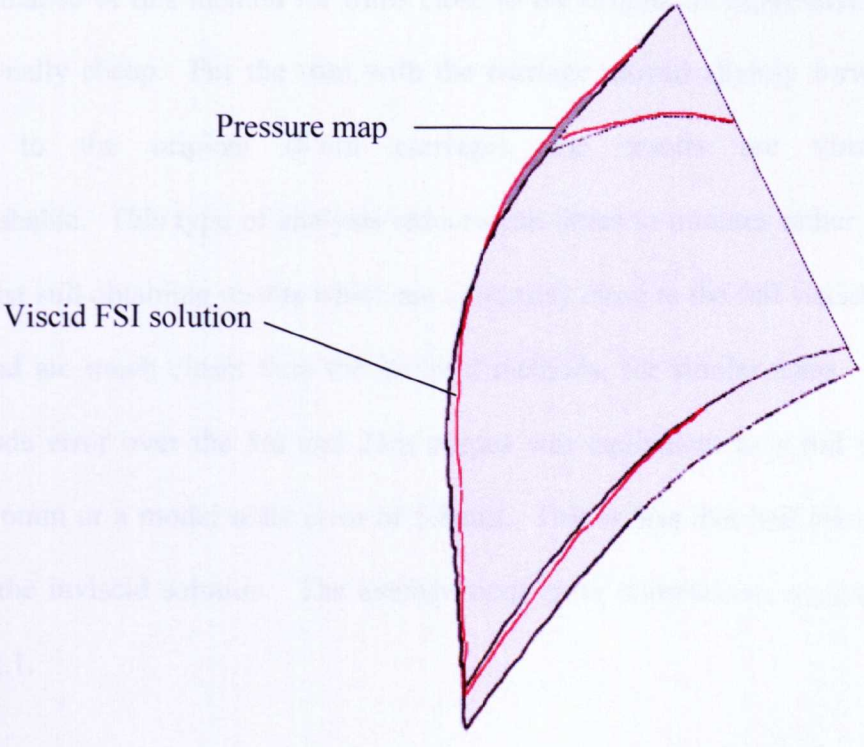

Figure 6.7.2.1 - Comparison of pressure map and viscid FSI solution, carriage 9.2m, 0.7m sheet length (red=pressure map)

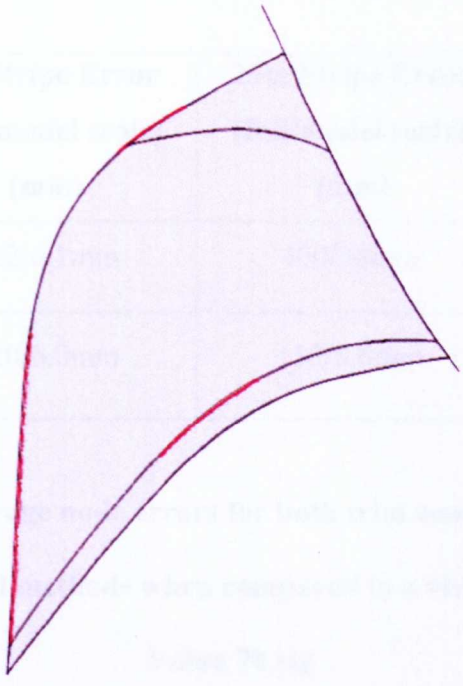

Figure 6.7.2.2 – Comparison of pressure map and viscid FSI solution, carriage 8.6m, 0.7m sheet length (red=pressure map)

The performance of this method for trims close to the original is impressive and computationally cheap. For the trim with the carriage moved slightly forward, compared to the original (8.6m carriage), the results are virtually indistinguishable. This type of analysis reduces run times to minutes rather than hours, whilst still obtaining results which are extremely close to the full viscid FSI solution and are much closer than the inviscid methods, for similar trims. The average node error over the 5m and 25m stripes was equivalent to a full scale error of 116mm or a model scale error of 5.8mm. This is less that *half the error* seen with the inviscid solution. The average node error comparison is given in Table 6.7.2.1.

	5m Stripe Error (full/model scale) (mm)	25m Stripe Error (full/model scale) (mm)	Average Stripe Error (full/model scale) (mm)
Inviscid Solution	122/6.1mm	400/20mm	262/13.1mm
Pressure map Solution	120/6.0mm	112/5.6mm	116/5.8mm

Table 6.7.2.1 – Average node errors for both trim conditions for pressure mapping and inviscid methods when compared to a viscous FSI solution for Volvo 70 rig

Even for the trims further from the reference shape, a reasonable shape prediction was seen, with improvements over the inviscid method. As a near instantaneous commercial solution for designers, this method may provide an economical alternative to the panel methods with acceptable accuracy.

This method relies upon the assumption that pressure maps are similar for small changes in trim. Although this is often the case it does not have to be so. The potentially significant change in pressure field with small changes in incidence angle make this method's performance unpredictable. An example of this would be the onset of a leading edge stall, significantly changing the pressure field. Another disadvantage of this technique is the lack of flow visualisation.

From the limited testing carried out, this method does appear to be able to outperform the inviscid simulations, for small changes in trim with similar flow fields.

6.7.3. Conclusions

The differences between simulations made with inviscid and viscid codes have been demonstrated for the range of trims detailed in Section 6.7.1 for a code zero sail at an AWA of 38 degrees. The modelling of sails using a single pressure map for similar trims has also been reported, with relatively good agreement to the full viscous scheme (average stripe error ~6mm). This gave improved performance in shape prediction over the inviscid simulations, whilst maintaining reduced run times. However, as discussed in Section 6.7.2, this method relies upon the assumption that the flow field does not change significantly for small changes in trim. For an industrial solution where quick turn around times are needed, a pressure map solution could provide acceptable results, with results in minutes rather than hours.

Where accuracy is important or during an optimisation process, there is no substitute for the full viscous FSI solution. This allows for flow visualisation for all changes in trim, leading to greater understanding and a higher level of accuracy for quantitative results. In certain circumstances, small changes in trim can lead to significant changes in flow patterns. An example of this would be the leading edge stall of the foresail, which can occur over a small range in AWA. A pressure map would struggle to accurately predict the forces in such a scenario, making the stall hard to predict.

The use of either of the alternative methods, either inviscid or a pressure map, for an initial flying shape for the FSI solution is recommended. This allows for an initial flying shape to be created quickly, which starts the FSI iteration closer to the final flying shape and reduces the corresponding run times. For accurate results of pressure, forces and sail shapes a converged full viscous FSI solution is needed.

6.8. Parametric Design Study

The following section uses the FSI solution to model a series of code zero trims. It focuses upon how this type of FSI tool can be useful in a design environment, with an emphasis upon performance. The section concentrates on the effects of sheet length and sheeting location upon sail shape, forces, moments and their overall performance.

The FSI model is that of the full scale Volvo 70 rig used throughout this chapter, with mainsail and code zero. The model did not have a mast or hull included within the simulation. The model includes a full twisted wind profile at an apparent wind angle of 38 degrees and an apparent wind speed of 11.2 ms^{-1}, both specified at a height of 25m. The code zero sail is trimmed using the primary two adjustments available to a foresail trimmer, the genoa sheet and the genoa carriage location. Other factors such as luff tension are kept constant. For this study no luff sag was allowed.

A series of different carriage positions has been chosen within the range, appropriate for the Volvo Open 70. These are at locations 8.6, 8.9, 9.2 and 9.5m from an undisclosed reference location[1]. A series of sheet lengths are then chosen to create a realistic range of flying shapes for the code zero. Again the sheet lengths included are not actual sheet lengths but relative sheet lengths, for commercially sensitive reasons. The table below shows the matrix of runs chosen to represent a range of trims and give a thorough testing of the FSI solution.

Sheet length (m)	**Carriage location (m)**			
	8.6	**8.9**	**9.2**	**9.5**
0.1	X			
0.4	X	X	X	X
0.7	X	X	X	X
1.0		X	X	X
1.3				X

Table 6.8.1 Sheet and carriage locations for the code zero parametric study.

The structural FE mesh used for the analysis is shown below in Figure 6.8.1. This highlights the refinement of the mesh in and around the 3 attachment locations. Approximately 5,000 structural elements are used for the structural analysis.

[1] NB: For commercially sensitive reasons the sheeting locations cannot be included within the thesis, by request of North Sails, UK.

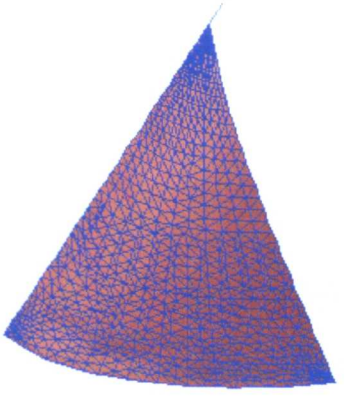

Figure 6.8.1 – RELAX meshing scheme for the code zero parametric study.

A meshing strategy similar to that used in Chapter 5 was used. Approximately 8 million cells are used for the CFD analysis with focus around the areas of interest for this study, the code zero. Inflation layers and size functions have been used as detailed in Table 6.8.2

Surface and Boundary Layers Elements	Growth rate	1.3
	Number of cells in the boundary layer (normal direction)	10
Sail Growth Function	First cell edge length	0.01-0.02m
	Growth rate	1.08
	Largest cell size	0.5m

Table 6.8.2 – Mesh details for Volvo 70 parametric design study

The variations in carriage location and sheet length serve to perform a complex process of controlling the shape, which in turn determines the forces placed upon the boat. The following sections discuss the ability of the FSI solution to replicate

the sail shapes and obtain useful information for the sail designer and naval architect.

6.8.1. Shape

The complexity of sail shapes, and their clear dependency on the sailing and trim conditions was shown in Chapter 5. This was highlighted by the difficulty in obtaining matching experimental and numerical trims of the scale code zero sail. The shape of the sail is sensitive to small changes in trim. Using the various controls the sailor can create different sail shapes. In reality this is limited to camber, location of maximum camber and the angle of attack. However due to the three dimensional nature of the sail, twist can also be added and controlled to create changes to the angle of attack with height. Sail trim is used to maximise the performance of the sails, whatever the objective, whether it be to maximise driving force or limit healing force. Detailed studies of sail trim e.g. Gladstone, 2007, have been well documented and will therefore not be covered in detail. The importance of being able to capture the subtleties of sail trim is essential if a FSI solution is to be useful to the sail designer or naval architect.

The influence of the two variables, sheet length and carriage location on sail shape, is essential for a trimmer to be able to obtain an efficient sail shape. For a trimmer, the goal is nearly always to maximise driving force within other restraints such as healing moment or boat balance. For a given sailing vessel, there is a maximum righting moment that the rig can withstand without it adversely affecting performance. As a result, the trimmer must change the shape to create a maximum amount of driving force, whilst containing healing moment, thereby maintaining a balanced vessel and not damaging the sails or rig.

The trimmer must use the sheet length and carriage location to control the sail camber, sail twist and sheeting angle. Moving the carriage forward creates more control of the leech and gives less control of the foot. This reduces the twist and introduces more depth to the sail. Conversely, movement of the carriage aft creates more control of the foot and less control in the leech. This creates flatter sails, with more twist. The use of the sheet helps control sheeting angle and the twist in the sails. As a sail is sheeted in further, more control is placed upon the leech as a greater proportion of the tension in the sheet goes into pulling the clew down rather than in. This section will discuss how the FSI solution copes with these subtle changes in trim.

Figures 6.8.1.1-2 show the impact of subtle changes in trim with examples from the converged FSI solutions. Figure 6.8.1.1 shows a comparison between two extreme trims from the matrix shown in Table 6.8.1. Included in Figure 6.8.1.1 is a trim with the carriage furthest aft with a relatively flat profile. In contrast, the figure also shows a relatively full and open shape. The carriage location and sheet lengths were 8.6m and 0.7m and 9.5m and 0.4m for the two respective shapes. Moving the carriage aft, flattened the sail, and in contrast the further forward carriage, created more depth combined with the eased sheet helped create the twist.

In contrast, Figure 6.8.1.2 shows how similar clew locations can create surprisingly different results. From an initial look the lower sail stripe and foot have similar maximum camber locations at similar angles of attack. However the

slight differences in location and trim cause one sail to twist off as height increases. Although the sail shapes are kept relatively similar, the angle of the sail relative to the wind changes. For the two sails in question the angle between the sail chord and boat centreline changes from 36.5° to 38.7° at 2/3 mast height. This variation could be enough to cause either of the sails to encounter enlarged regions of separation and as a result a decrease in efficiency.

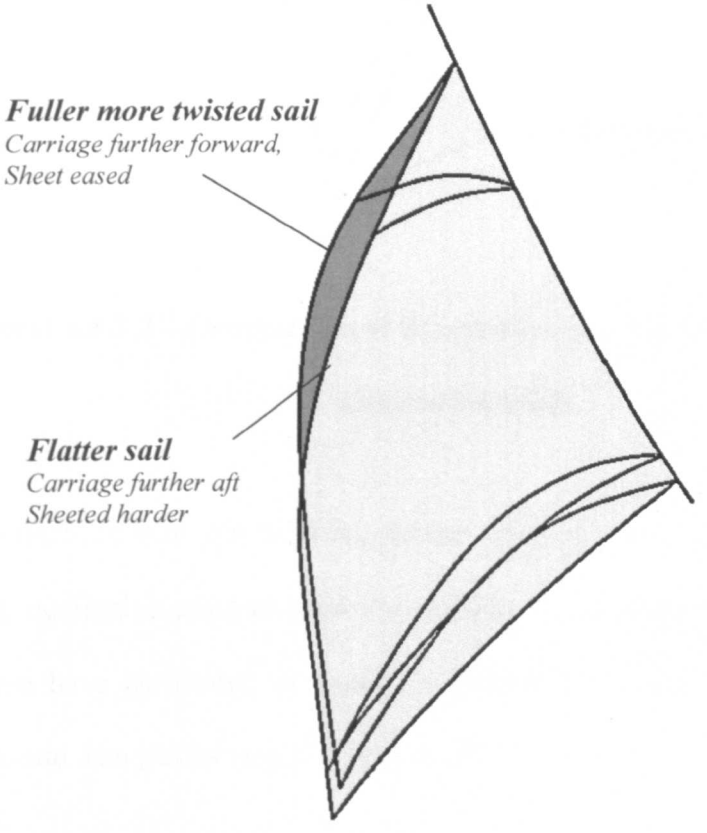

Figure 6.8.1.1 – Extremes of sail trim modelled in the Volvo 70 parametric study

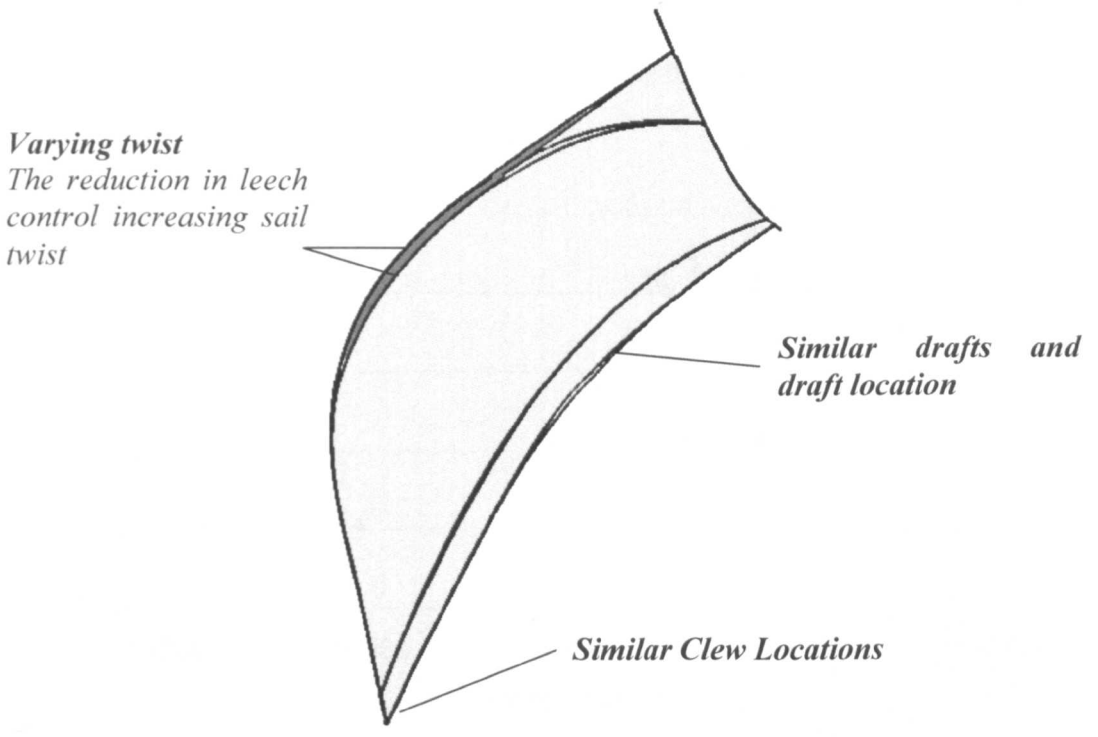

Figure 6.8.1.2 – Comparison of two similar sail trims within the Volvo 70 parametric study

The effects of trim and twist are further discussed later in the chapter. From a visual, qualitative point of view the changes in sail shapes generated by the FSI solution have performed as would be expected in comparison to experimental results and trim guides (e.g. *Gladstone, 2007).*

6.8.2. Drag and Lift

This section of the study is a demonstration of how this type of analysis can be used as a trimming tool to help improve performance or as part of a design study to help improve flying shapes. Figure 6.8.2.1 and Figure 6.8.2.2 show the various forces created from the different trims. Figure 6.8.2.1 represents a scatter plot of the family of trims showing side force vs. driving force. Each point represents a

single result from the trim matrix. It provides a ratio that is important to naval architects and which can be utilised when designing the keel and appendages.

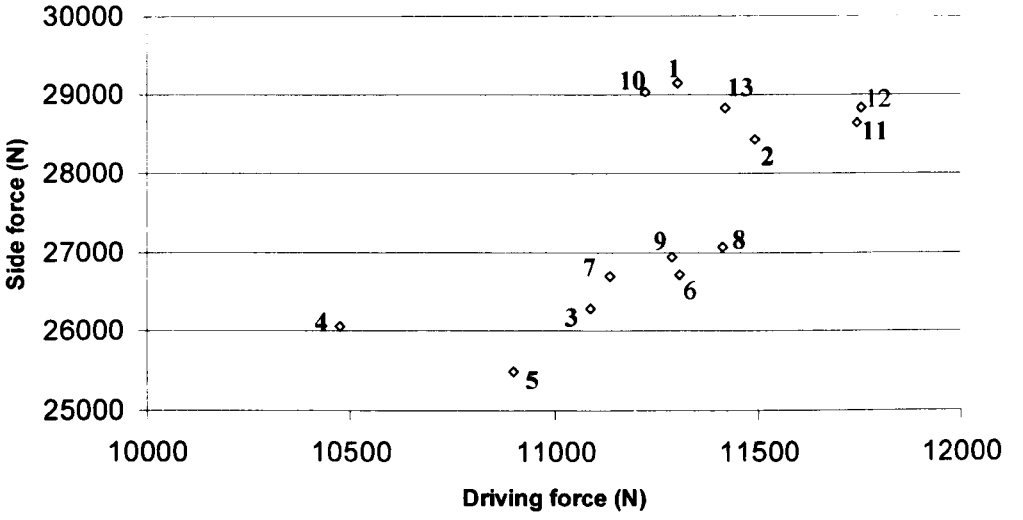

Trim (carriage location (m), sheet location (m))
1 (9.5, 1.3), **2** (9.5, 1), **3** (9.5, 0.7), **4** (9.5, 0.4), **5** (9.2, 1), **6** (9.5, 0.7), **7** (9.5, 0.4), **8** (8.9, 0.4), **9** (8.9, 0.7), **10** (8.9, 1), **11** (8.6, 0.1), **12** (8.6, 0,4), **13** (8.6, 0.7)

Figure 6.8.2.1 - Driving force vs. side force for varying trims within the parametric study

(each point=one trim)

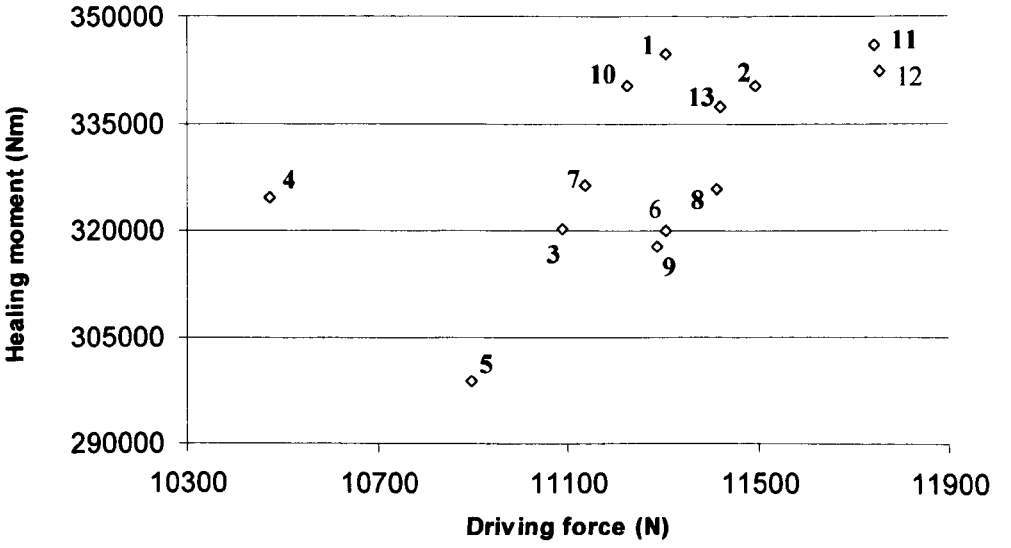

Trim (carriage location (m), sheet location (m))
1 (9.5, 1.3), **2** (9.5, 1), **3** (9.5, 0.7), **4** (9.5, 0.4), **5** (9.2, 1), **6** (9.5, 0.7), 7 (9.5, 0.4), **8** (8.9, 0.4), **9** (8.9, 0.7), **10** (8.9, 1), **11** (8.6, 0.1), **12** (8.6, 0,4), **13** (8.6, 0.7)

Figure 6.8.2.2 - Driving force vs. healing moment for varying trims within the parametric study

Figure 6.8.2.2 represents another key ratio, that of driving force and healing moment, essential when determining the amount of ballast necessary to compensate for the healing force generated from the rig for a given vessel. When sailing or designing a performance boat this ratio is key. The desire to maximise driving force within the available righting moment is a design objective and constraint.

This type of figure can also be used in a different manner when trying to optimise the performance of a vessel from a trimming standpoint. The goal for a trimmer, as mentioned previously, is to maximise the driving force. However, this has to happen within constraints, most obviously the maximum healing force. Each point on Figure 6.8.2.3 represents a trim within the continuum available to the trimmer. Each vessel has a specified, primarily pre determined, maximum and optimum righting moment. This, for a traditional vessel, is determined by the location and specification of the ballast, combined with the hull shape. The resultant righting moment will determine the optimum sail shape for the conditions.

Figure 6.8.2.3 attempts to demonstrate this, with data from the parametric study. If there were no limit placed upon the trimmer, and the vessel could cope with any healing moment without it being detrimental to boat speed, the trimmer should choose an 8.6m carriage location with a 0.4m sheet. However, due to detrimental effects of healing moment, it is more likely that a limit of healing moment is specified. In the example shown, a limit of 327,500 NM has been set as an upper limit. Within the limits of this healing moment, the overall aim for the trimmer is

to maximise the driving force, which, from Figure 6.8.2.3 is a 8.9m carriage location and a 0.4m sheet length. In contrast a trim created from a 9.5m carriage and a 0.4m sheet creates a similar healing moment but significantly less driving force and therefore less performance.

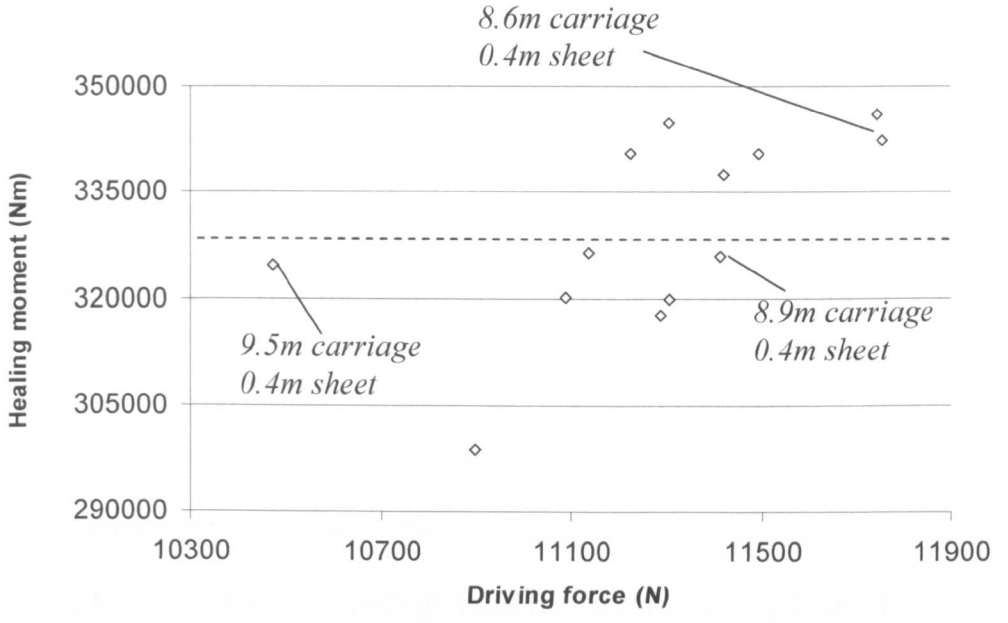

Figure 6.8.2.3 - Driving force vs. healing moment for varying trims within the parametric study

The potential for small changes in carriage location to affect performance so significantly is interesting. Figure 6.8.2.4 shows healing moment and carriage location in an attempt to find underlying trends. Here it can be seen a carriage location of 9.2m appears to generate the least healing moment with carriage locations either side generating more, as an underlying trend. This is perhaps not surprising as a carriage further aft, with the same sheet length, would flatten the sail, reducing its curvature and acting to reduce lift but increase the pressure of the windward side. Conversely a carriage location further forward would act to increase curvature and generate potentially more lift if the sail doesn't stall.

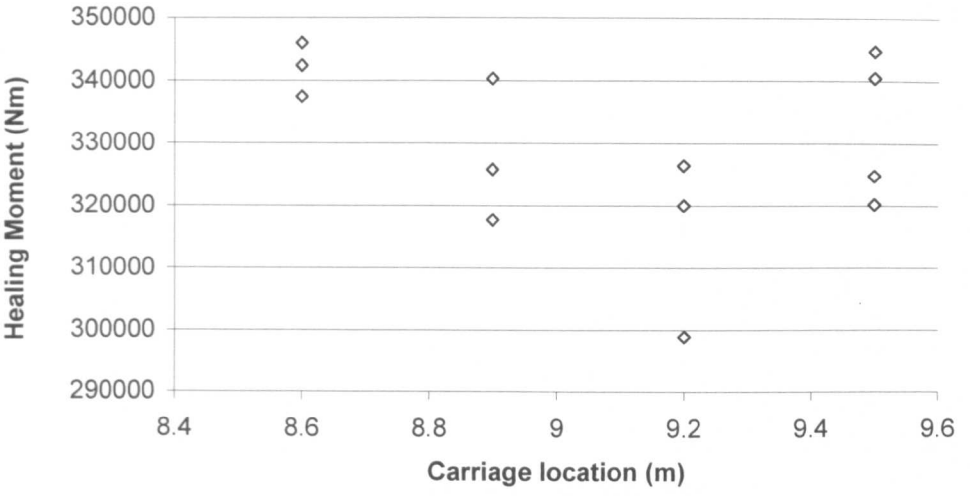

Figure 6.8.2.4 – Healing moment vs. carriage location for varying trims within the parametric study

The effect of carriage location upon driving force is shown in Figure 6.8.2.5. This shows similar general trends with a carriage location of 9.2m generating the least driving force. Moving the carriage location further forward is generally acting to increase curvature and driving force. An interesting feature of this graph is the increase in range of the 9.5m carriage location data, significantly more than the other carriages. This is likely to be due to the onset of stall. With a short carriage location and short sheet length the curvature of the sail will increase, increasing the likelihood of separation. This is confirmed in Figure 6.8.2.6 where sheet length is plotted against driving force, with a constant carriage location of 9.5m. Here the curve can clearly be seen with a maximum driving force at 1m. Reducing the sheet length past here reduces the driving force, which is likely to be due to the separation on the leeward side of the code zero.

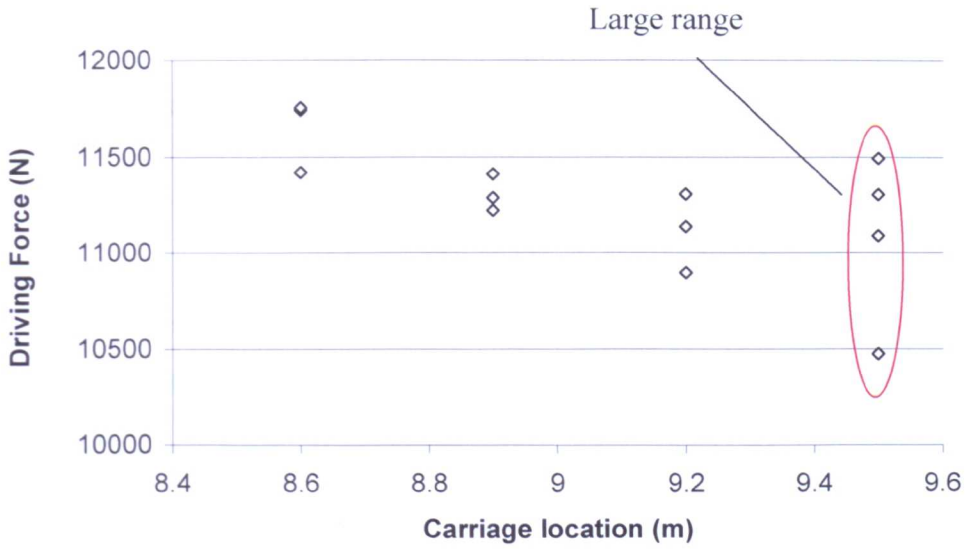

Figure 6.8.2.5 – Driving force vs. carriage location for varying trims within the parametric study

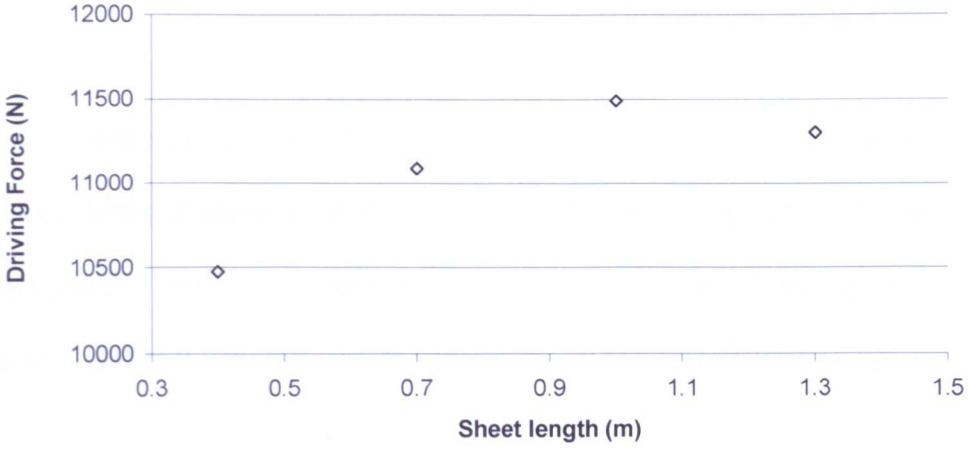

Figure 6.8.2.6 – Driving force vs. sheet length for varying trims within the parametric study with a constant carriage location of 9.5m

The figures within this section have given some insight into the potential for increasing performance and aiding trimming through viscous FSI simulations. However it is understood that this brief application of the method developed in this thesis is limited and the performance of a vessel cannot be determined with 3 performance objectives and 2 design parameters. However, the potential of such a

tool to increase the accuracy of a velocity prediction program (VPP) or aid in the design cycle has been shown.

6.9. Other Potential Applications

The focus of this chapter has been the use of the FSI model for the performance prediction of sailing vessels and in particular their sails. However, the FSI model has many potential other uses, a few of which are discussed below. The first could be as an aid in the training of personnel. This could be at any level, from sailor to sail designer or coach. CFD is used to that effect in other sports e.g. swimming (Morvan, 2008, *personal communication),* cycling (Lewis, 2009, *personal communication*) and other Olympic sports.

For sailors and sail makers alike, the FSI model is useful to help determine the effects of subtle changes in trim or design. The model can also help provide understanding of physical changes, such as an eased sheet or greater curvature in a sail design, and as a consequence, hopefully improving performance.

In a similar way simulation could help tune vessels to achieve their optimum performance. This is particularly true for novel vessels, with characteristics such as rotating masts (Paton and Morvan, 2007). To parametrically change mast rotation and sail camber to obtain optimum results could help reduce the time needed on the water to achieve maximum boat speed.

Finally, an application which may be practical in the future, although not realistic at present, is the development of a 'dash board type' FSI solution. This could help

take the current conditions, from onboard instruments such as AWA and AWS, and calculate the optimum sailing trim. A simplified version of this is often used by race teams at present to determine which sail plan to choose and which sails to hoist. This is usually in the form of a physical print out from a VPP, giving target boat speeds and the optimum sail plan. Developing this further and obtaining optimum real time sail trims could aid performance significantly.

6.10. Conclusions

The FSI tool developed within this thesis has been applied to real and complex offwind racing sails using the Volvo Open 70 as the application. Its use could be beneficial to both the sail designer and naval architect alike. The FSI solution has proved to be robust for a wide range of sailing conditions.

The model has been capable of detecting the subtleties of sail trim. The solution has also shown how it could determine optimum solutions within a range of sail trims, and could potentially help improve sail shape and design if implemented by racing teams and designers.

The method has also shown the potential for use in the training of crews and coaches. In real life sailing, the medium of air is not visible to the eye and so to be able to see virtually, in simulation, the effects of trim upon the flow is an extremely powerful aid and potentially useful to skippers, trimmers and designers alike.

Chapter 7

Concluding Remarks

7.1. Overview of the Work and Key Contributions

The nature of sail flow is complex. The flow around sails includes complicated features such as adverse pressure gradients and multiple regions of separation. The regions of separation, created from the presence of both the mast and the curvature of the sails, create a challenge for any computational method. Yet it is a proper understanding of these separation regions that is key to improving the performance of a sailing rig. As sails travel further offwind, their curvature needs to be increased to maximise performance, and with increased curvature comes the danger of flow separation. This increase in curvature and potential for separated regions poses a challenge to CFD techniques and turbulence models. The prediction of separation and the complex flow around offwind sails is beyond the capabilities of inviscid methods.

The use of viscous CFD is key to the accurate modelling of these complex flow conditions and forms the backbone of this thesis. Within this thesis the validation of the SST RANS based turbulence model of Menter (1993) has been carried out, for application to flow past sail sections. The validation was carried out against two *simplified* experimental cases, detailed in Chapter 4.

The first validation case was that of Collie, 2005. This involved the simulation of a circular arc section through a range of angles of attack, intended to represent offwind sail sections. The lift and drag coefficients at different angles of attack were used for validation. The viscous CFD model and the SST model performed well, predicting the general trends of the experimental results, in particular the onset of leading edge separation. This type of performance prediction would have been impossible with inviscid methods.

The 2nd validation case was that of Wilkinson, 1990. This involved the simulation of a more realistic sail section with the inclusion of a mast and mainsail section. For this validation case, pressure and velocity profiles were available. The SST RANS turbulence model performed well, predicting pressure profiles and boundary layer profiles for mast/sail flow. Qualitatively the model predicted very well the experimental results and the regions of separation detailed by Wilkinson, 1990. The numerical simulations correctly predicted the trends of the experimental data, even though some errors in quantitative values were observed. For the upper lifting section an error in the boundary layer profile of 11% was seen, Section 4.3.

Following the validation of the viscous CFD methodology, the method was then applied to rig sections to help improve the understanding of sail flow. The ability of viscous CFD to predict mast separation regions allowed the modelling of a range of mast shapes at varying rotations. The application demonstrated the potential of mast rotation to improve boat performance and reduce the drag

of rig sections by up to 65%. Again this would not have been possible with inviscid methods.

The next application was that of various rig configurations, including investigating the interaction between the foresail, mast and mainsail. Finally the effect of foresail sheeting angle was investigated, demonstrating and providing insight into the effect of under and over sheeting the foresail upon the performance of the rig.

Having put in place a robust CFD methodology for the modelling of yacht sails, the desire to extend rigid RANS based modelling to allow for the deformation and movement of the sails has been the primary focus of this thesis. A FSI solution has been presented, bringing together the RANS based CFD and a membrane structural solver, capable of modelling anisotropic offwind yacht sails. Bespoke coupling code was written to enable the transfer of data between the two solvers in an iterative partitioned approach. The FSI solution presented goes beyond FSI solutions previously presented in the field, giving the potential capability to model fully anisotropic sails, including offwind and downwind sails.

To validate the FSI solution a bespoke wind tunnel experiment was carried out for an offwind code zero sail, with support from North Sails UK. To facilitate the accurate, instantaneous capturing of the sail shapes, close range stereo photogrammetry was utilised. This is a significant improvement upon previous attempts at capturing sail shapes. The use of photogrammetry creates a non

intrusive instantaneous method that improves upon the performance of previous methods. Previously the use of intrusive methods such as the 'Romer' used by Mairs (2003) created a non-negligible effect on the flow and thus the sail shapes. The alternative to the use of an intrusive physical device is a laser scanner, but with this method being non instantaneous, a reduction in the potential accuracy is the direct consequence. The photogrammetry methods utilised in the present work provided instantaneous accurate capture of the sail shapes, within a statistical error of 1mm.

The FSI model performed well in recreating the shapes of a code zero sail within the wind tunnel. The validation exercise highlighted the difficultly in matching trims in the wind tunnel and the computational model. It also highlighted the importance of modelling complete rigs, including the physical characteristics of the rigging. In this case the importance of modelling the luff sag was essential in recreating accurate sail shapes at higher angles of attack. The model predicted the sail shapes to within an accuracy of 5.8mm, a significant improvement on previous published works, e.g. Mairs who reported 'bulk of the computational flying shape within a plus or minus 0.75 inch window of the experimental flying shape' (Mairs, 2003).

The viscous methodology was also utilised to model a realistic, full scale sailing scenario with multiple sails and additional elements of the rig built into the simulation. A Volvo Open 70 class yacht was recreated, using data provided by North Sails UK. The FSI model was shown to be capable of modelling multiple anisotropic laminate sails and predicting the changes in

performance with trim. A 2 parameter design space was created from changes in foresail carriage location and foresail sheet length. The parametric model provided an interesting insight into the potential of viscous FSI to help design and tune yachts. This type of viscous parametric FSI approach has never been applied to sails before and could become a useful tool for engineers and sailors.

The prediction of the overall rig performance allows the naval architect to further optimise their design, with more accurate data to feed into a velocity prediction program. As shown in the present work, the rig operates as a system and is not the sum of the performance of its individual components. The present contribution is therefore of high interest to the racing community.

The modelling of complete rigs has been stressed throughout this thesis. From the early validation against the Wilkinson test case (1983), the importance of the mast within sail analysis has been shown. The Wilkinson case showed the consequence of neglecting the mast within the analysis upon the prediction of velocity and pressures, both quantitatively and qualitatively. For the Wilkinson case the removal of the mast led to the under prediction of the drag coefficient by over 25% and to the overprediction of the lift coefficient by close to 8%. Later in this dissertation, the effects of neglecting the mast and deck were considered again, with significant changes to the flow field and performance clearly visible. To obtain highly accurate performance predictions and maximise the potential of optimisation, the inclusion of all parts of the rig should be strongly considered.

7.2. Future Work

There are many possible extensions to the current work and this area of research has by no means been exhausted. The modelling of downwind spinnakers, using the FSI technique presented, would be an interesting application, as it was not covered in this thesis. Although in theory this methodology should be capable of modelling spinnakers, it would present a challenge due to the highly flexible nature of this type of sail.

The improvement in the modelling of the fluid flow around sails from a fundamental turbulence modelling perspective is essential. Although this was not the focus of this thesis, improvements in the prediction of separation and reattachment points are needed to improve the computational accuracy of the numerical simulations. The movement away from RANS modelling towards LES would also be interesting, with DES as an obvious stepping stone (*Wright et al.*, 2010). This will happen shortly, with ever increasing computational power becoming available. However, pure computer power alone will not solve the problem in the mid-term, as improvements in methods still need to be made. For flow past sails and masts the ability of the method to accurately predict the separation points is key, the movement away from models that rely upon wall functions will be fundamental to improving correlation. This, in addition to capturing the transient nature of the flow, will be necessary before approaching downwind sails, with large transient separated regions.

The coupling between the two codes could also be investigated, with a closer coupled scheme examined to solve simultaneously rather than sequentially.

However, this is not possible with the current approach utilising separate, specialist solvers. In this author's opinion, the advantages of having two solvers with independent meshes and more advanced modelling capabilities currently outweigh the advantages of a closer coupled method.

The use of stereo close range photogrammetry is clearly an important step in advancing the shape capture of sails shown by the sudden influx of papers in that field (Paton *et al,* 2008; Renzsch *et al.*, 2008; Fossati *et al,* 2008). The progression of this technology to real time shape capture, particularly in full scale, would be significant, providing vastly improved feedback for trimmers and modellers. The extension of close range photogrammetry to full scale 'on the water' testing would also be worthwhile, improving upon the usual approach to shape capture of a single camera looking up or down.

7.3. Summary

The aim of this thesis and research was stated in Chapter 1 as:

> *"To develop a viscous fluid-structure interaction model for the accurate modelling of yacht sails, capable of modelling and predicting the performance of upwind and offwind sails."*

The thesis describes how this aim was successfully achieved, by detailing the creation and validation of a numerical FSI scheme capable of modelling the vast majority of sails, both upwind and offwind. The modelling of large downwind spinnakers using the viscous FSI solution developed in this thesis would be an interesting and challenging subject for further work. The ability of

viscous CFD to accurately predict performance has been shown with the use of rigid wind tunnel testing. The FSI model has created accurate predictions of flying shapes at wind tunnel scale. The technique has also been showcased at full scale for a complex real life rig of the Volvo Open 70. The FSI solution developed has advanced upon previous attempts of modelling anisotropic sails and predicting sail shapes. The research has also shown how viscous based CFD should be considered essential for all accurate and detailed modelling of sail flows.

REFERENCES

ABBOTT, H. and VON DOENHOFF, E., 1959, Theory of wing sections, Dover.

ARCARO, V., F., 2011A, A Simple Procedure for Shape Finding and Analysis of Fabric Structures', Available from www.arcaro.org/tension/main.htm, [Accessed May 29th 2011]

ARCARO, V., F., 2011B,Analysis of isotropic membrane structures, Available from www.arcaro.org/tension/main.htm, [Accessed May 29th 2011]

ANSYSa CFX, 2008. ANSYS CFX-SOLVER, Release 10.0: Theory. ANSYS.

ANSYS, 2009, Available from www.ansys.com/products/fluid-dynamics/cfx/ [Accessed 4th January 2009]

BARLOW, B., RAE, H. AND POPE, A., 1999. Low-speed wind tunnel testing,

John Wiley & Sons.

BARNES, M., 1977, *Form Finding and Analysis of Tension Structures by Dynamic Relaxation*, PhD thesis, The City University, London, 1977.

BARNES, M. 1994, Form and stress engineering of tension structures, *Structural Engineering Review, Vol 6, No 3-4 175-202.*

BARNES, M., 1999, Form Finding and analysis of structures by dynamic relaxation, *International Journal of Space Structures, Vol 14, Number 2.*

Bazilevs, Y., Calo, V.M.,. Zhang, Y., Hughes, T.J.R., 2006, Isogeometric fluid–structure interaction analysis with applications to arterial blood flow, *Comp. Mech.* 38 (2006) 310–322.

BETHWAITE, F., 2003, High performance sailing, Adlard Coles Nautical, London

CD-ADAPCO, 2009, Available from http://www.cd-adapco.com/ [Accessed 5January, 2009]

CHAPIN, V. G., JAMME, S., CHASSAING, P., 2005a, Viscous computational fluid dynamics as a relevant decision-making tool for mast-sail aerodynamics, *Journal of Marine Technology* , Vol 42, No. 1, 1-10.

CHAPIN, V. G., NEYHOUSSER, R., JAMME, S., DULLIAND, G. AND CHASSAING, P., 2005b, Sailing yacht rig improvements through viscous computational fluid dyanamics, *The 17th Chesapeake sailing yacht symposium, March 2005, Annapolis, Maryland.*

CHAPIN, V., NEYHOUSSER, R., DULLIAND, G. AND CHASSAING, P., 2006, Analysis, design and optimization of Navier-Stokes flows around interacting sails, *MDY06 International symposium on yacht design and production, March 2006, Madrid, Spain.*

CHAPMAN, D., KUEHN, D. and LARSON. H., 1957, Investigation of Separated Flows in Supersonic and Subsonic Streams with Emphasis on the Effect of Transition, *NACA-TN- 3869, NACA Rep. 1356.*

CHARVET, T., HAUVILLE, F. AND HUBERSON, S.,1996, Numerical simulation of the flow over sailsin real sailing conditions, *Journal of Wind Engineering and Industrial Aerodynamics*, 63, 111-129.

CLAUSS, G. AND HEISEN, W., 2005, CFD analysis on the flying shape of modern yacht sails, *12th international congress of the international association of the Mediterranean, 26-30 September 2005, Lisbon.*

COLLIE, S. J., GERRITSEN, M. AND JACKSON, P., 2001, A review of turbulence modelling for use in sail flow analysis, School of engineering report No. 603, Univeristy of Auckland, October 23, 2001.

COLLIE, S. J., JACKSON, P. S., GERRISTEN, M., AND FALLOW J. B., 2004, Two-dimensional CFD-based parametric Analysis of Downwind Sail Designs, International journal of small craft technology, 2004 part B.

COLLIE, S. J., 2005, *Application of computational fluid dynamics to two-dimensional downwind sails flow*, PhD Thesis, The University of Auckland.

COIRO, D. P., NICOLOSI, F., SCHERILLO, F. AND MAISTO, U., 2002, Numerical and experimental aeroelastic analysis of sails, *High performance yacht design conference, 4-6 December 2002 Auckland.*

DAY, A., 1966, Analysis of plates by dynamic relaxation with special reference to boundary conditions, *Symp. on the use of electronic digital computers in structural Engineering., University of Newcastle, July 1966.*

DAY, A. and BUNCE, J., 1969, The analysis of hanging roofs, *Arup Journal*, September , 1969. 30-31.

DOYLE, T., GERRITSEN, M. AND ICCARINO, G., 2002, Optimization of yard sectional shape and configuration for a modern clipper ship, 17th *Int. Sympo. on Yacht Design and Yacht Construction, Amsterdam 2002.*

DRELA, M. and GILES, M., 1987, Viscous–Inviscid Analysis of Transonic and Low Reynolds Number Airfoils. *AIAA Journal, 25* , 1347–1355.

ERICSSON TEAM RACING, 2009, Available from www.ericssonracingteam.com, [Accessed April 2009]

FALKNER, V., 1943, The Calculations of Aerodynamic Loading on Surfaces of any Shape, *Reports and Memoranda 1910, Aeronautical Research Council, London, Aug. 1943*

FALLOW, J., 1996, America's cup sail design, *Journal of wind engineering and industrial aerodynamics*, 63, 183-192.

FELIPPA, C. and Park, K., 2004, Synthesis Tools for Structural Dynamics and Partitioned Analysis of Coupled Systems, *Proceedings of NATO Advanced Research Workshop, Bled, Slovénie, 2004*

FIDES, S. P., AND GAYDON, J.H., 1996, A new vortex lattice method for calculating the flow past yacht sails, *Journal of wind engineering and industrial aerodynamics*, 63, 35-39.

FLAY, R. G. J., 1996, A twisted wind tunnel for testing yacht sails, *Journal of wind engineering and industrial aerodynamics*, 63, 171-182.

FLOW Solutions, (2007) [online], Available from www.flowsol.co.uk/products/pansail [Accessed 12th October 2007].

FLUENT, (2009), Available from www.fluent.com [Accessed 1st January 2009]

FOSSATI, F., MARTINA, F and MUGGIASCA, S., 2008, Experimental database of sails performance on flying shapes in upwind conditions, *Innovation in High Performance Sailing Yachts, Lorient, France (2008)*

FRIEDL, N., 2002, Membrane structures in unsteady potential flow, *Fifth world congress on computational mechanics, July 7-12, 2002, Vienna, Austria.*

GENTRY, A., 1973, How sails really work, *SAIL Magazine*, April 1973.

GENTRY, A., 1981, A review of modern sail theory, *Proceedings of the eleventh AIAA symposium on the aero/hydrodyanmics of sailing, September 12 , 1981, Seattle Washington.*

GENTRY, A., (2007). [Online], Available from www.arvelgentry.com [Accessed 11th October 2007].

GHANI, S., AROUSSI, A., and RICE, E., 2001, Simulation of road vehicle natural environment in a climatic wind tunnel, *Simulation Practice and Theory Volume 8, Issues 6-7, 15 March 2001, Pages 359-375*

GLADSTONE, B., 2007, *North U. TRIM*, 6th edition, North U., Madison CT.

GLUCK, M., BREUER, M., DURST, F., HALFMANN, A. AND RANK E, 2001, Computation of fluid–structure interaction on lightweight structures, *Journal of fluids and structures*, 89, 1351–1368

GLUCK, M., BREUER, M., DURST, F., HALFMANN, A. AND RANK E, 2003, Computation of wind-induced vibrations of flexible shells and membranous structures, *Journal of fluids and structures*, 17, 739-765.

HANSEN, H., JACKSON, P. and HOCHKIRCH, K., 2002, Comparison of wind tunnel and full-scale aerodynamic sail force measurements, *High performance yacht design conference, 4-6 December 2002 Auckland.*

HARGREAVES, D. AND MORVAN, H., 2007. Towards the validation of crosswind effects on a static high-sided vehicle, NAFEMS international journal of CFD case studies, 7.

De HART, J., PETERS, G., SCREURS, P and BAAIJENS, F., 2003, A three-dimensional computational analysis of fluid structure interaction in the aortic valve, *Journal of Biomechanics 36, 103–112*

HEDGES, K., RICHARDS, P. AND MALLINSON, G., 1996, Computer modelling of downwind sails, *Journal of Wind Engineering and Industrial Aerodynamics*, 63, 95-110.

HEPPEL, P., 2002, Accuracy in sail simulation: wrinkling and growing fast sails, *High performance yacht design conference, 4-6 Decemeber 2002 Auckland.*

HESS, J. L., 1990, Panel methods in computational fluid dynamics, Annual Review of Fluid Mechanics, 22, 255-74.

JACKSON, P. S. AND CHRISTIE, G. W., 1987, Numerical analysis of three-dimensional elastic membrane wings, *AIAA Journal*, 25, 676-682.

JONES, P. AND KORPUS, R., 2001, International America's Cup Class Yacht Design Using Viscous Flow CFD, *The 15th Chesapeake sailing yacht symposium, 2001, Annapolis.*

KAMAKOTI, R. AND SHYY, W., 2004, Fluid–structure interaction for aeroelastic applications, *Progress in Aerospace Sciences*, 40, 535–558

KORST, H., PAGE, R. and CHILDS, M., 1955, A theory for base pressures in transonic and supersonic flow. *University of Illinois. Engineering Experiment Station. Mechanical Engineering. Department, ME Tech. Note 392-2. March, 1955.*

KREBBER, B., AND HOCHKIRCH, K., 2006, Numerical investigation on the effects of trim for a yacht rig, *High performance yacht design conference, 14-16th February 2006 Auckland.*

LASHER, W.C., SONNENMEIER, J.R., FORSMAN, D.R. AND TOMCHO, J., 2005, The aerodynamics of symmetric spinnakers, *Journal of wind engineering and industrial aerodyanamics*, 93, 311-337.

LASHER C. W. AND RICHARDS P. J., 2007, Validation of Reynolds-averaged Navier-Stokes simulations for IACC spinnaker force coefficients in an atmospheric boundary layer, *Journal of ship research*, Volume 51, Number 1, 22-38.

LASHER C. W. AND SONNENMEIER J. R., 2008, An analysis of practical RANS simulations for spinnaker aerodynamics, *Journal of wind engineering and industrial aerodynamics*, 96, 143-165.

LAUNDER, B. and SPALDING, D., 1974. The numerical computation of turbulent flows. *Compuational Methods Applied Mechanical. Engineering*, 3:269-289, 1974.

LE MAITRE, O., HUBERSON, S. AND SOUSA DE CURSI, E., 1999, Unsteady model of sail and flow interaction, *Journal of fluids and structures*, 13, 37-59.

LUHMANN, T., ROBSON, S., KYLE, S. AND HARLEY, I., 2006, Close range photogrammetry principles, techniques and applications, Whittles Publishing, Caithness, Scotland.

LUI, F., CAI, J., ZHU, Y., TSAI, H. AND WONG, A., 2001, Calculation of wing flutter by a coupled fluid-structure method, *Journal of Aircraft*, 38

LIAW, K., 2005, *Simulation of flow around bluff bodies and bridge deck sections using CFD*, PhD thesis, University of Nottingham.

MADLIK, M., 2007 .Numerical Simulations of 3D Fluid-Structure interaction, *Computational Methods with Applications*, Harrachov August 21 2007

MAIRS, C., 2003, *Aerodynamic-structural model of offwind yacht sails*, Thesis (PhD). University of Maryland

MARCHAJ, C. A., 1964, *Sailing theory and practice*, , Dodd, Mead.

MARCHAJ, C. A., 2003, *Sail performance – techniques to maximise sail power*, Revised edition, McGraw-Hill.

MASSEY, B., 1998, *Mechanics of Fluids*, 7th edition, Stanley Thornes.

MASON, C., 2000, The best of SAIL trim, Sheridan house.

MASUYAMA, Y. AND FUKASAWA, T., 1997, Full scale measurement of sail force and the validation of numerical calculation method, *The 13th Chesapeake sailing yacht symposium, 1997, Annapolis.*

MASUYAMA, Y., TAHARA, Y., FUKASAWA, T. AND MAEDA, N., 2007. Database of sail shapes vs. sail performance and validation of numerical calculation for upwind condition. *The 18th Chesapeake sailing yacht symposium*, Annapolis, Maryland, March 2007.

McBEATH, S., 2006, *Competition car aerodynamics*, Haynes Publishing.

MENTER, F., 1993, Zonal Two Equation k-ω Turbulence Models for Aerodynamic Flows, *AIAA Paper 93-2906.*

MENTER, F., KUNTZ, M. AND LANGTRY, R., 2003, Ten Years of Industrial Experience with the SST Turbulence Model, *Turbulence, heat and mass transfer 4*, 2003.

MENTER, F. AND EGOROV, 2005, F., Scale-Adaptive Simulation Model using Two-Equation Models, *43rd AIAA Aerospace Sciences Meeting and Exhibit*, 10 - 13 January 2005, Reno, Nevada

MILGRAM, J.H., 1968, The aerodynamics of sails, *7th Symposium on Naval Hydrodynamics, 1968 Washington D.C.*

MILGRAM, J.H., 1971, Section data for thin highly cambered airfoils in incompressible flow, Technical Report CR-1767, NACA.

MILGRAM, 1978, The effects of masts of the aerodynamics of sail sections, *Marine Technology*, 15, 35-42.

MORVAN, H., STANGROOM, P., WRIGHT, N., 2007, Automated CFD analysis for multiple direction of flow over terrain, Wind and Structures, VOL 10; PART 2, pages 99-120.

MORVAN, H AND HARGREAVES, D., 2007, EC CRAFT project WEATHER: Final report towards WP2, Technical report submitted as part of the final project report to the EC, March 2007.

MPCCI, 2009, Available from http://www.mpcci.de/ [Accessed January 7th 2009]

MSC SOFTWARE, 2009, Available from www.mscsoftware.com/products/core_products.cfm [Accessed 6th January 2009]

MUTTIN, F., 1996, A finite element for wrinkled curved elastic membranes, and its application to sails, *Communication in numerical methods in engineering*, 12, 775-785.

NEW ZEALAND, 2009, Available from http://www.newzealand.com/travel /sights-activities/events-calendar/americas-cup-feature/about-americas-cup/americas-cup-history.cfm [Accessed April 2nd 2009]

NORRIS, S., 1993, The interaction of Yacht Sails in a Two-Dimensional Viscous Flow, *Master of Engineering*, University of Auckland, New-Zeeland, May 1993.

NORTH SAILS, 2008, *Sail design – North Sails and the technological development*, Available from http://www.northsails.co.uk [Accessed 7 January 2008].

OPENCFD, 2009, Available from http://www.opencfd.co.uk/ [Accessed 5 January, 2009]

OPTIMAL SOLUTIONS, 2009, Available from http://www.optimalsolutions.us/solutions/index.php [Accessed 12 December. 2009]

PANSAIL, 2007, Taken from *http://www.flowsol.co.uk/products/pansail/* July 2007

PATON, J. AND MORVAN, H., 2007, The effect of mast rotation and shape on the performance of sails, *International journal of marine engineering,2007*

PATON, J. AND MORVAN, H., 2007B, Yacht Sail Aerodynamics Using Computational Fluid Dynamics, *Marine 2007 – Computational methods in marine engineering, 5th-7th June 2007, Barcelona.*

PATON, J. AND MORVAN, H., 2007C, Using computational fluid dynamics to model main and foresail interaction - the 'slot effect' revisited, *Journal of wind engineering and industrial aerodynamics*, 2009, 540-547.

PATON, J., MORVAN, H., AND HEPPEL, P., 2008, Fluid structure interaction of yacht sails, *International conference on innovation in high performance sailing yachts, 29-30 May 2008, Lorient.*

PHA, 2009, Available from http://www.peterheppel.com/ [Accessed January 4th 2009]

PHOTOMETRIX, 2009, Available from http://www.photometrix.com.au/index.html [Accessed January 7th 2009]

PRANDTL, L., 1918, Tragfliigel Theorie, Nachrlcten van der Gesellschaft der Wissenschaften zu Gottingen, Ges-chaeftliche Mitteilungen, Klasse, Germany, 1918, pp. 451-477

PRANDTL, L. and BETZ, A., 1927, "Vier Abhandlungen zur Hydrodynamik und Aerodynamik," Gottingen Nachr., Gottingen, Selbstverlag des Kaiser Wilhelminstituts fur Stromungsforschung.

RANZENBACH, R. AND XU, Z., 2004, Fluid-structure interaction simulation of a code zero sail, *International symposium on yacht design and production, 25-26 March 2004 Madrid.*

RANZENBACH, R. AND XU, Z., 2005, Aero-structures: studying primary load paths and distortion, *Proc. of The 17th Chesapeake sailing yacht symposium, 2005 Chesapeake.*

RENZSCH H, MULLER O and GRAF K. FLEXSAIL, 2008, A Fluid Structure Interaction Program for the Investigation of Spinnakers. International Conference on Innovation in High Performance Sailing Yachts, Lorient, France (2008)
RHINO, 2009, Available from http://www.rhino3d.com/ [Accessed September 2008]

RICHARDS, P. J., JOHNSON, A. AND STANTON, A., 2001, America's Cup downwind sails – vertical wings or horizontal parachutes?, *Journal of wind engineering and industrial aerodynamics*, 89, 1565-1577.

RICHTER, H. AND HORRIGAN, K., 2003, Flying sails on the computer, *Fluent Newsletter* [Accessed online 3rd March 2009].

ROUX, Y., HUBERSON, S., HAUVILLE, F., BOIN, J., GUILBAUD, M., AND BA, M., 2002, Yacht performance prediction: towards a numerical VPP, *High performance yacht design conference, 4-6 December 2002 Auckland.*

RUMSEY, C. and GATSKI, T., 2001, Recent turbulence model advances applied to multi element airfoil applications, *Journal of Aircraft,* 38, 904-910

SCHOOP, H., BESSERT, N. AND TAENZER, L., 1998, On the elastic membrane in a potential flow, *International journal for numerical methods in engineering,* 41, 271-291.

SCHOOP, H. AND BESSERT, N., 2001, Instationary aeroelastic computation of yacht sails, *International journal for numerical methods in engineering,* 52, 787-803.

SCHLICHTING, H and GERSTEN, K., 2000, *Boundary-Layer Theory*, Springer.

SEIBERT, W. and LEWIS, R., 2004, Motor Sport Drives CFD Technology to a New Level, *Global Motorsports Conference*, Frankfurt, Germany, Nov. 2004

SHANKARAN, S., 2005, *Numerical analysis and design of upwind sails,* Thesis (PhD),

Stanford University.

SHANKARAN, S., DOYLE, T., GERRITSEN, M., ICCARINO, G. AND JAMESON, A., 2002, Improving the design of sails using CFD and optimization algorithms, *High performance yacht design conference, 4-6 December 2002 Auckland.*

SIEBER, G., 2001, Fluid-Structure interaction using loose coupling methods, MSc Dissertation, Technischen Universit Darmstadt

SMAR Azure Ltd, 2007, Available from www.smar-azure.com/CMS/Index.php?id=8 [Accessed 12th October 2007].

SMITH, M. and TAHA, A., 2009. Changes in camera calibration parameters of digital cameras with time, Optical 3-D measurement techniques IX (International Society For Photogrammetry and Remote Sensing, Commission V), Vienna, Austria 2009 21 -3 July.

SPALART, P., 2001, Young person's guide to detatched-eddy simulation grids, *Technical report NASA/CR-2001-211032.*

SPEER, T., 2007 [online], The aerodynamics of teardrop windmasts, Available from www.tspeer.com [accessed 12th October 2007].

SRIRAM, JAMESON, A. AND GERRITSEN, M. G., 2003, Numerical analysis and design of upwind sails, *21st AIAA applied aerodynamics conference, 23-26 June 2003 Orlando, Florida.*

VERSTEEG, W. AND MALALASEKERA, H., 2007, *An Introduction to Computational Fluid Dynamics: The Finite Volume Method,* Longman Publishing Grp.

VOLVO OPEN 70 RULES, Version 2, 16th May 2007, Volvo Event Management UK Ltd

VON KÁRMÁN, T., 1930, Mechanische Ähnlichkeit und Turbulenz, Nachrichten von der Gesellschaft der Wissenschaften zu Göttingen, Fachgruppe 1 (Mathematik) **5**: 58–76.

WHIDDEN, T. and LEVITT, M., 1998, *The art and science of sails*: A guide to modern materials, construction, aerodynamics, upkeep and use, Saint Martin's Press.

WILCOX, D., 1998, Turbulent modelling for CFD, DCW Industries, California.

WILKINSON, S., 1983, Investigations into 2D mast/sail interaction, *Conference on sail assisted commercial fishing vessels, 1983, 425-443.*

WILKINSON, S., 1984, *Partially separated flow around 2D masts and sails,* PhD Thesis, University of Southampton.

WILKINSON, S., 1987, A simple multi-layer panel method for partially separated flows around 2D masts and sails, *AIAA 19th fluid dynamics, plasma dynamics and lasers conference, 8-10 June 1987 Honolulu, Hawaii.*

WILKINSON, S., 1989, Static pressure distributions over 2d mast/sail geometries, *Marine technology, 26, 333-337.*

WILKINSON, S., 1990, Boundary layer explorations over a 2D mast/sail geometry, *Marine technology, 27, 250-256.*

WILLIAMS, P. AND BAKER, A., 1997, Numerical simulations of laminar flow over a 3d backward facing step, International journal for numerical methods in fluids, Vol 24, 1159-1183.

WRIGHT, A., CLAUGHTON, A., PATON, J. and LEWIS, R., 2010, Off-wind sail performance prediction and optimisation, *Innovsail 2010, 30 June - 1 July 2010, Lorient, France.*

XFOIL, 2007 [online], Available from http://web.mit.edu/drela/Public/web/xfoil [Accessed 12th October 2007]

APPENDIX